# Deterministic free surface multiple removal of marine seismic data

Rodney G.K. Johnston

B.Sc. Geophysics 1991
The University of Edinburgh

Le Diplôme d'Ingénieur 1993
L'École Nationale Supérieure du Pétrole et des Moteurs


Thesis submitted for the degree of
Doctor of Philosophy

The University of Edinburgh

2000

This thesis has been composed by myself and has not been submitted in any previous application for a degree. Except where stated to the contrary, the work reported within was executed by myself.

This thesis is dedicated to the memory of my father.

# ABSTRACT

This thesis presents a new method for sea surface multiple removal which includes in its solution the information at the source from the oscillating bubbles which generate the propagating wavefield. Arrays of interacting oscillating bubbles excite the earth with sound energy which is recorded as marine seismic reflection data. In the manipulation of the data to produce a detailed image of the earth's subsurface, the first task is the removal of multiple reflections related to the sea surface. The new formulation, in common with other wave-theoretical methods, requires a two-dimensional grid of receivers to record a two-dimensional grid of shots. Using the data themselves, and no information about the subsurface, all multiples are removed in a three-dimensional earth by calculating the plane wave reflection response in the frequency-wavenumber domain. Applying the plane wave concept to waves in three dimensions permits a complicated reflected wave to be decomposed into plane wave components. Each of these scattered upgoing plane wave components comprises primary and multiple reflections. The primaries result from a multiplication of an incident downgoing plane wave component with a plane wave reflection response, unique for the particular downgoing and upgoing plane wave components chosen. The multiples represent a sum of products of scattered downgoing plane wave components with plane wave reflection responses, related to the chosen downgoing and upgoing plane wave components. The result is a set of simultaneous equations whose unknowns form the three-dimensional reflection response. The wavefield from the oscillating bubbles produces the downgoing incident plane wave. There are various methods of measuring this input energy. They depend on the acquisition configuration being used, and the feasibility of placing hydrophones at certain distances from the sources of the oscillating bubbles. Consideration of the fluid dynamics of these oscillating bubbles, in isolation and together, and the wave propagation produced by them, reveals the requisite measurements to describe fully the acoustic output of the source. Real data examples related to three different source recording geometries show that the measurements are entirely feasible, and that they provide the information needed by the multiple removal scheme. Synthetic data examples in one and two dimensions illustrate the success of the sea surface multiple removal technique, both in the towed streamer configuration and the ocean bottom cable configuration.

# ACKNOWLEDGEMENTS

First of all I would like to thank my principal supervisor and my boss Anton Ziolkowski for all his enthusiasm, criticism, support and patience throughout the course of this work. It is often said that it's difficult having two bosses; sometimes it's tough doing two jobs for the same boss. As Fat Boy Slim once said "You've come a long way, baby".

Other people in the department of Geology and Geophysics have been of help during this work. I thank my second supervisor Bob Pearce for being around from afar, and my collegues, David Taylor for his knowledge of wave equations, modelling and everything mathematical, and Sergei Zatsepin for being a constant officemate, and not bad at maths either. I especially thank David for knocking together the modelling code I have used in chapter 8. Thanks also go to Margaret Penman, secretary to the Centre for Reservoir Geoscience for keeping everyone on track, and to the computing officers: Chis (?!), Shane, and Justin for trying to keep me happy.

To the people who read and commented on the chapters in this thesis I am indebted, for I hope their efforts make this an easier read. Thanks especially to my examiners Gary Hampson, Bruce Hobbs and Mike Warner for their thorough reading of the manuscript.

This work would not have been possible without the financial support of several organisations: Natural Environment Research Council (GR3/9064), Engineering and Physical Science Research Council (ROPA GR/L73524), Enterprise Oil plc, BHP Petroleum, Schlumberger Geco-Prakla, Saga Petroleum A/S and Texaco Britain Ltd. In the course of this sponsorship I have benefitted greatly from discussions with people in these organisations, and in others. In particular, I would like to thank Gary Hampson, Clement Kostov and Josef Paffenholz for their thoughtful insight into the multiple problem.

I thank Mike Saunders of Bolt Technology Corp. for permission to use Figure 3.1, and Floris Strijbos of Shell UK Expro for permission to use Figure 5.9. Thanks also go to Bolt Technology Corp., Enterpise Oil plc, and Richard Hobbs (Cambridge University), formerly of BIRPS, for providing the data used in chapter 6.

Finally, I would like to thank all my friends in Edinburgh and beyond who have helped me keep my head in one way or another, and have been an endless source of enjoyment and encouragement on the PhD road. Last, but not least, thanks to Caroline for agreeing to be my personal physician till the end, and for looking after me through the closing stages.

# CONTENTS

# CONVENTIONS, NOTATION AND DEFINITIONS

The conventions and notation presented in the thesis are given here. For specific definitions refer to the main text. SI units are used in general. In cases where an alternative system of units is more commonly employed, the SI equivalent is given.

### Scalar and Vector Quantities

Vector quantities are written in a bold typeface, for example $\mathbf{f}$, and scalar quantities in normal typeface, for example $f$.

### Space and Time

A right-handed Cartesian reference frame is used throughout the thesis, with the $z$-axis increasing downwards. Let $\mathbf{x} = (x, y, z)$ denote the position vector in the Cartesian reference frame, and $\mathbf{n} = (n_x, n_y, n_z)$ denote the unit basis vector so that

$$\mathbf{x} = n_x x + n_y y + n_z z. \tag{0.1}$$

Let $t$ denote time. The indicial notation is used for vectors with respect to the Cartesian reference frame. Thus $f_i$ represents the components of vector $\mathbf{f}$, where it is implied that $i$ takes the values $x$, $y$ and $z$. Further, the summation convention is used for repeated subscripts. Whenever a dummy subscript occurs twice in the same term, the term is summed over $x$, $y$ and $z$:

$$f_{kk} = f_{xx} + f_{yy} + f_{zz}. \tag{0.2}$$

### Special Functions

| | | |
|---|---|---|
| $\delta(x)$ | $\int_{-\infty}^{\infty} \delta(x-\eta) f(x) \mathrm{d}x = f(\eta)$ | the Dirac delta function |
| $\delta(\mathbf{x})$ | $\delta(x)\delta(y)\delta(z)$ | the three dimensional delta function |
| $\delta_{ij}$ | $\delta_{ij} f_j = f_i$ | the Kronecker delta |

### Integral transforms

The Fourier transform of $f(x,y,z,t)$ with respect to $t$ and transform parameter $\omega$ is

$$F(x,y,z,\omega) = \int_{-\infty}^{\infty} f(x,y,z,t)\exp\Big(+i[\omega t]\Big)\,\mathrm{d}t, \tag{0.3}$$

where the change of domain is indicated by the capital letter. The inverse transform is

$$f(x,y,z,t) = \frac{1}{2\pi}\int_{-\infty}^{\infty} F(x,y,z,\omega)\exp\Big(-i[\omega t]\Big)\,\mathrm{d}\omega. \tag{0.4}$$

The Fourier transform of $F(x_r,y_r,z_r,\omega)$ with respect to receiver coordinates $x_r, y_r$ and transform parameters $k_x^r, k_y^r$ is

$$\tilde{F}(k_x^r,k_y^r,z_r,\omega) = \iint_{-\infty}^{\infty} F(x_r,y_r,z_r,\omega)\exp\Big(-i[k_x^r x_r + k_y^r y_r]\Big)\,\mathrm{d}x_r\mathrm{d}y_r, \tag{0.5}$$

where the change of domain is indicated by the over-tilde. The inverse transform is

$$F(x_r,y_r,z_r,\omega) = \frac{1}{(2\pi)^2}\iint_{-\infty}^{\infty} \tilde{F}(k_x^r,k_y^r,z,\omega)\exp\Big(+i[k_x^r x_r + k_y^r y_r]\Big)\,\mathrm{d}k_x^r\mathrm{d}k_y^r. \tag{0.6}$$

The Fourier transform of $\tilde{F}(k_x^r,k_y^r,z_r,\omega,x_s,y_s,z_s)$ with respect to source coordinates $x_s, y_s$ and transform parameters $k_x^s, k_y^s$ is

$$\hat{\tilde{F}}(k_x^s,k_y^s,z_s,\omega,k_x^s,k_y^s,z_s) = \iint_{-\infty}^{\infty} \tilde{F}(k_x^r,k_y^r,z_r,\omega,x_s,y_s,z_s)\exp\Big(+i[k_x^s x_s + k_y^s y_s]\Big)\,\mathrm{d}x_s\mathrm{d}y_s, \tag{0.7}$$

where the change of domain is indicated by the over-hat. The inverse transform is

$$\tilde{F}(k_x^r,k_y^r,z_r,\omega,x_s,y_s,z_s) = \frac{1}{(2\pi)^2}\iint_{-\infty}^{\infty} \hat{\tilde{F}}(k_x^r,k_y^r,z,\omega,k_x^s,k_y^s,z_s)\exp\Big(-i[k_x^s x_s + k_y^s y_s]\Big)\,\mathrm{d}k_x^s\mathrm{d}k_y^s. \tag{0.8}$$

### Z-transforms

Discrete time series can be considered both in the time domain and in the frequency domain by taking their $Z$-transform. The $Z$-transform of a causal time series $f_t$ is defined by

$$F(Z) = \sum_{t}^{n} f_t Z^t = f_0 + f_1 Z + f_2 Z^2 + f_3 Z^3 + \ldots f_n Z^n, \tag{0.9}$$

where $Z$ is the unit delay operator between successive sample values, $f_0, f_1, f_2, \ldots$. The $Z$-transform of a non-causal time series has filter coefficients for negative powers of $Z$.

Evaluation of the Z-transform on the unit circle of the complex Z-plane, i.e. where $|Z| = 1$, occurs when

$$Z = e^{i\omega}. \tag{0.10}$$

Substitution of this value for $Z$ gives

$$F(\omega) = \sum_{t}^{n} f_t e^{i\omega t} \tag{0.11}$$

which is the discrete Fourier transform of $f_t$ (a frequency domain representation).

### Convolution

The convolution of $f(t)$ with $g(t)$, denoted by $\star$, is

$$f(\tau) \star g(\tau) = \int_{-\infty}^{\infty} f(t)g(\tau - t)\mathrm{d}t. \tag{0.12}$$

The Fourier transform of convolution is multiplication: $f(\tau) \star g(\tau) \leftrightarrow F(\omega)G(\omega)$. This is the convolution theorem. For discrete time series it relates Z-transforms, $f_\tau \star g_\tau \leftrightarrow F(Z)G(Z)$.

### SI Base Units

| Quantity | Unit | |
|---|---|---|
| | Name | Symbol |
| length | metre | m |
| mass | kilogramme | kg |
| time | second | s |
| plane angle | radian | rad |

### SI Derived Units

| Quantity | | Unit | |
|---|---|---|---|
| | Name | Symbol | Equivalent |
| electric potential | volt | V | $\mathrm{W\,A^{-1}}$ |
| energy | joule | J | $\mathrm{kg\,m^2\,s^{-2}}$ |
| frequency | hertz | Hz | $\mathrm{s^{-1}}$ |
| force | newton | N | $\mathrm{kg\,m\,s^{-2}}$ |
| power | watt | W | $\mathrm{J\,s^{-1}}$ |
| pressure | pascal | Pa | $\mathrm{N\,m^{-2}}$ |
| stress | pascal | Pa | $\mathrm{N\,m^{-2}}$ |
| velocity | metre per second | | $\mathrm{m\,s^{-1}}$ |
| wavenumber | per metre | | $\mathrm{m^{-1}}$ |

## Major symbols

| Symbol | Description | Units | First appears on page |
|---|---|---|---|
| $\mathbf{A}$ | two-way propagation operator | | 22 |
| $\mathbf{B}$ | decomposition operator | | 22 |
| $c$ | acoustic velocity of water | $\mathrm{m\ s^{-1}}$ | 15 |
| $c_{ijkl}$ | stiffness tensor | Pa | 13 |
| $\mathbf{C}$ | composition operator | | 22 |
| $D$ | source array dimension | m | 48 |
| $D$ | downgoing plane wave component | Pa | 22 |
| $\mathbf{e}$ | vector of wave variables | Pa | 23 |
| $\mathbf{E}$ | single layer propagator matrix | | 26 |
| $f$ | wave function | $\mathrm{m^3\ s^{-1}}$ | 38 |
| $\mathbf{f}$ | vector of field variables | | 22 |
| $\mathbf{f}$ | volume density of body force | $\mathrm{N\ m^{-3}}$ | 12 |
| $g$ | source density of bulk strain (volume injection) | % | 14 |
| $h$ | hydrophone sensitivity | $\mathrm{V\ Pa^{-1}}$ | 106 |
| $h$ | enthalpy | $\mathrm{J\ kg^{-1}}$ | 36 |
| $H$ | enthalpy in bubble | $\mathrm{J\ kg^{-1}}$ | 39 |
| $i^d$ | incident direct field | Pa | 89 |
| $i^r$ | incident ghost field | Pa | 89 |
| $I$ | incident plane wave component | Pa | 29 |
| $I^z$ | desired incident plane wave component | Pa | 95 |
| $\mathbf{I}$ | identity matrix | | 23 |
| $k$ | total wavenumber | $\mathrm{m^{-1}}$ | 16 |
| $k_{x,y}$ | horizontal wavenumbers | $\mathrm{m^{-1}}$ | 16 |
| $k^D_{x,y}$ | downgoing horizontal wavenumbers | $\mathrm{m^{-1}}$ | 81 |
| $k^U_{x,y}$ | upgoing horizontal wavenumbers | $\mathrm{m^{-1}}$ | 81 |
| $k_r$ | radial wavenumber | $\mathrm{m^{-1}}$ | 17 |
| $k_z$ | vertical wavenumber | $\mathrm{m^{-1}}$ | 18 |
| $K$ | bulk modulus | Pa | 14 |
| $m$ | hydrophone measurement | V | 106 |
| $\mathbf{n}$ | Cartesian basis vector | | 9 |
| $p$ | pressure difference | Pa | 10 |
| $p_b$ | dynamic pressure in water | Pa | 42 |
| $p_\infty$ | hydrostatic pressure | Pa | 36 |
| $p^0$, $p_0$ | pressure data without multiples | Pa | 68 |

| Symbol | Description | Units | First appears on page |
|---|---|---|---|
| $p^{inc}$ | incident pressure field | Pa | 88 |
| $p^{scat}$ | scattered pressure field | Pa | 77 |
| $p^{tot}$ | total pressure field | Pa | 88 |
| $P_B$ | dynamic bubble pressure | Pa | 34 |
| $\mathbf{P}$ | field variable propagator matrix | | 26 |
| $q$ | notional source | Pa | 89 |
| $\mathbf{Q}$ | wave variable propagator matrix | | 29 |
| $r$ | distance from source origin | m | 34 |
| $r^g$ | distance from virtual source origin | m | 106 |
| $r_i$ | local reflection coefficient | | 27 |
| $R$ | reflection response | | 77 |
| $R$ | dynamic bubble radius | m | 34 |
| $\dot{R}$ | dynamic bubble wall velocity | m s$^{-1}$ | 34 |
| $\ddot{R}$ | dynamic bubble wall acceleration | m s$^{-2}$ | 39 |
| $R_g$ | generalised reflection coefficient (including sea surface) | | 30 |
| $R_g^*$ | generalised reflection coefficient (excluding sea surface) | | 31 |
| $R_0$ | sea surface reflection coefficient | | 31 |
| $s$ | notional source-time function | Pa m | 2 |
| $s_A$ | distributed areal source | Pa | 128 |
| $s_E$ | effective source signature | Pa m | 128 |
| $S^z$ | desired source frequency spectrum | Pa | 95 |
| $t$ | time | s | 2 |
| $t_i$ | local transmission coefficient | | 27 |
| $\mathbf{t}$ | traction | Pa | 9 |
| $T_g$ | generalised transmision coefficient | | 30 |
| $\mathbf{u}$ | displacement | m | 10 |
| $U$ | upgoing plane wave component | Pa | 22 |
| $v$ | radial velocity | m s$^{-1}$ | 36 |
| $\mathbf{v}$ | velocity | m | 11 |
| $V_B$ | dynamic bubble volume | m$^3$ | 40 |
| $w$ | source density of strain rate (volume injection rate) | % s$^{-1}$ | 15 |
| $x_k$ | source array element coordinate | m | 89 |
| $x_r$ | receiver coordinate | m | 2 |
| $x_s$ | source coordinate | m | 2 |

| Symbol | Description | Units | First appears on page |
|---|---|---|---|
| $X^z$ | desired source $k_x$ spectrum | $m^{-1}$ | 95 |
| $y_k$ | source array element coordinate | m | 89 |
| $y_r$ | receiver coordinate | m | 2 |
| $y_s$ | source coordinate | m | 2 |
| $Y^z$ | desired source $k_y$ spectrum | $m^{-1}$ | 95 |
| $\mathcal{Y}$ | acoustic admittance | $m^2\ s\ kg^{-1}$ | 24 |
| $z_k$ | source array element coordinate | m | 89 |
| $z_r$ | receiver coordinate | m | 2 |
| $z_s$ | source coordinate | m | 2 |
| $\mathcal{Z}$ | acoustic impedance | $kg\ m^{-2}\ s^{-1}$ | 24 |
| $\varepsilon_{ij}$ | strain tensor | % | 11 |
| $\phi_i$ | downgoing propagation angle | rad | 81 |
| $\phi_j$ | upgoing propagation angle | rad | 81 |
| $\varphi$ | velocity potential | $m^2\ s^{-1}$ | 16 |
| $\lambda$ | wavelength | m | 44 |
| $\lambda$ | Lamé parameter | Pa | 13 |
| $\mathbf{\Lambda}$ | matrix of eigenvalues of $\mathbf{A}$ | | 22 |
| $\mu$ | Lamé parameter | Pa | 13 |
| $\rho$ | density | $kg\ m^{-3}$ | 11 |
| $\sigma_{ij}$ | source stress tensor | Pa | 14 |
| $\tau$ | discrete time | s | 101 |
| $\tau_{ij}$ | stress tensor | Pa | 10 |
| $\omega$ | angular frequency | $s^{-1}$ | 16 |
| $\sim$ | transform over receiver coordinates | | 77 |
| $\wedge$ | transform over source coordinates | | 81 |

# INTRODUCTION

*Chapter 1*

## 1.1 Motivation for the research: better earth images

The seismic reflection method has been a successful tool in the search for buried hydrocarbon deposits on the continental shelf over the last 30 years (e.g. Moreton, 1995). It has also been used to derive information of a more academic nature on the structure of the deep continental crust (e.g. Klemperer and Hobbs, 1991). Central to both of these aims has been the ability to form a coherent and detailed picture, or image, of the earth's subsurface by recording the passage of sound waves beneath a seismic survey line or grid. A major limiting factor in this *imaging* of the earth is, and has always been, reflections from the sea surface which contaminate and distort the picture of the subsurface. The concept is illustrated schematically in Figure 1.1, where some rays are drawn to indicate possible travel paths from the source to the receivers. The complexity introduced by the sea surface is obvious in Figure 1.1(a), which, due to sea surface reflections, contains more rays than Figure 1.1(b).

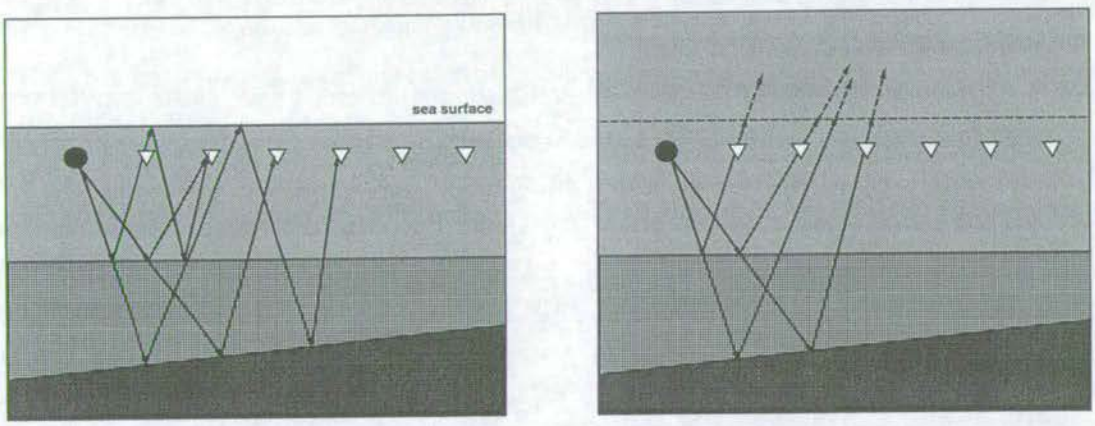


(a) With the sea surface.

(b) Without the sea surface.

Figure 1.1: The problem of sea surface multiple removal.

As seismic data acquisition and processing technology has advanced over the years, the earth images provided by the seismic reflection method have improved in resolution. As the earth has "come more into focus", so have the sea surface multiple reflections. Not surprisingly, the understanding of these multiple reflections and their methods of attenuation and

removal have, at the same time, increased in sophistication (for details, see chapter 4). Even with the state-of-the-art techniques available today, the removal or effective attenuation of sea surface multiple reflections is still considered an unsolved and challenging problem, for both economic and academic reasons.

## 1.2 Seismic reflection data: using the available information

In general terms, more data usually means more information. This is the case in seismology, in which there are a number of different wavetypes which propagate in the earth. For example, compressional ($P$) waves travel in liquids and solids whereas shear ($S$) waves travel in solids only. There are also surface waves. Each of these different waves has the potential to reveal unique information about the region of the earth through which it has travelled. Such wavetype information is gathered by different types of detectors. This point is returned to later in the chapter. More data can also mean denser coverage (more of the *same type* of data), both in terms of source locations and receiver locations. A well-defined theoretical limit provides the point at which more data no longer means more information. Put another way, the theoretical limit is the minimum amount of data required to extract all the information available with the seismic survey's input pulse waveform, or source signature. The minimum amount of data is generally not acquired (for economic reasons), but its importance is discussed throughout this thesis.

The source signature represents data which is usually ignored as a source of information. In the simplest of terms, a seismic reflection experiment creates a source of seismic waves, the input pulse, $s(x_s, y_s, z_s, t)$, the waves travel through the earth, $g(x_s, y_s, z_s, x_r, y_r, z_r, t)$, and are recorded at the receivers as the output pulse, $b(x_s, y_s, z_s, x_r, y_r, z_r, t)$. Note that these quantities depend on the source and receiver locations. The ability to construct a detailed picture of the subsurface is equivalent to obtaining a precise definition of the earth's impulse response $g$ from the measured output $b$. It is easier to extract $g$ knowing both $s$ and $b$ (input and output).

Historically, a lot of effort has been devoted to extracting the impulse response of the earth from the output data, while at the same time *estimating* the input pulse. One of the states-of-art in this regard is the latest generation of sea surface multiple removal techniques (Matson, 2000). However, it is possible to *measure* the input pulse independently. Thus an additional piece of data is available which can aid in obtaining a detailed picture of the earth. The source signature $s(x_s, y_s, z_s, t)$ is a required piece of information in the solution to removing sea surface multiple reflections. It is the latter option which is the subject of this thesis: a method of multiple removal which is exact, given adequate data, which calculates the earth's impulse response directly, using available information about the input pulse.

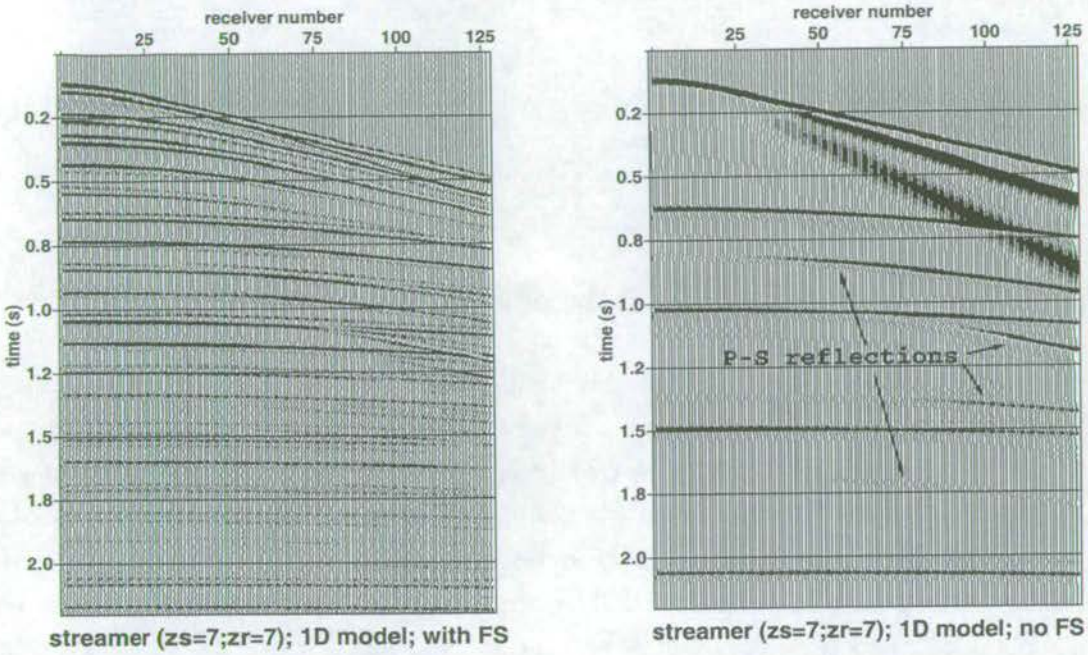


(a) With the sea surface.

(b) Without the sea surface.

Figure 1.2: The effect of the sea surface on 1D synthetic streamer data.

## 1.3 The problem of the sea surface

Seismic waves which travel into the earth are partially reflected when they encounter a change in material properties in the rock. The strength (or coefficient) of the reflection is related to how much the material properties change. Figure 1.1 schematically shows the rays of some possible reflections in a simple two-dimensional earth model. (Of course, the earth is really three-dimensional.) The open triangles denote hydrophone locations and the filled circle is a source location, both of which are in a layer of water. The interface between air and water represents a large change in material properties for a passing sound wave. For all practical purposes, the reflection coefficient at the sea surface is $-1$. This means that the air/water interface is a free surface at which the pressure deviation vanishes, and all upgoing energy is reflected back downwards. Thus, the primary reflections, produced by changes in the rock properties which the seismic reflection method seeks to define, are converted into multiple reflections by the sea surface. The primary and multiple reflections are recorded simultaneously, as can be seen in Figure 1.1(a). The upgoing and downgoing waves which comprise the recorded data both contain multiples.

The key to removing the multiples is the sea surface. In Figure 1.1(b) the upper half-space of air has been replaced with water so that there is no reflection from the notional boundary marked by the broken line. All the upgoing primary reflections which arrive from the earth are

| Depth(m) | P-wave (m/s) | S-wave (m/s) | density (kg $m^3$) |
|---|---|---|---|
| 75 | 1500 | 0 | 1000 |
| 575 | 2000 | 1155 | 2200 |
| 1075 | 2500 | 1443 | 2150 |
| 1775 | 3000 | 1732 | 2200 |
| 2775 | 3500 | 2021 | 2200 |
| $\infty$ | 4000 | 2309 | 2400 |

Table 1.1: One-dimensional elastic earth model.

recorded by the hydrophones and then pass on upwards and are never recorded again. There are no sea surface multiples. A complete sea surface multiple removal technique takes data recorded in the geometry of Figure 1.1(a) and converts it to data recorded in the geometry of Figure 1.1(b). Figure 1.2(a) shows the effect of the sea surface on synthetic data, calculated along a single line over a 1D earth using the reflectivity method (Fuchs & Müller, 1971). The elastic earth model is given in Table 1.1. (The direct wave from the source to the receivers has been omitted.) The sea surface multiple reflections dominate. In Figure 1.2(b), the synthetic data are modelled without the sea surface so that all upgoing energy is recorded once only, then continues upwards, as depicted in Figure 1.1(b). The primary *P* wave reflections are now clear, as are *P*-to-*S* converted waves which become *P* waves once more upon entering the water. In data contaminated by multiples, the relationship between the upgoing waves and the downgoing waves, at a notional boundary *below* the sea surface, yields explicitly the earth's impulse or reflection response *without* multiples.

Of course, the removal of sea surface multiples is only the first of many steps in the process of building a detailed picture of the subsurface. However, there are data processing algorithms whose major assumption is that multiples are not present. For example, migration, which aims to put reflections and diffractions into their correct subsurface position, and amplitude variation with offset (AVO) analysis, which seeks to detect subtle changes of reflection amplitude with offset, have a better chance of success on the data of Figure 1.2(b) than Figure 1.2(a).

## 1.4 Marine acquisition configurations

The most common marine acquisition geometry is towed streamer. It is illustrated in a two-dimensional cross-section in Figure 1.3. In this configuration the boat tows one or more streamers behind it, as well as the source array(s). The streamers contain pressure-sensitive hydrophones. This geometry is a fast and efficient method of data acquisition which means that costs are low (compared with other methods of acquisition at sea and on land). In terms of data coverage, the in-line direction is adequately sampled but the cross-line direction is usually undersampled. The reasons for this are: (1) it can be difficult, operationally, to tow the

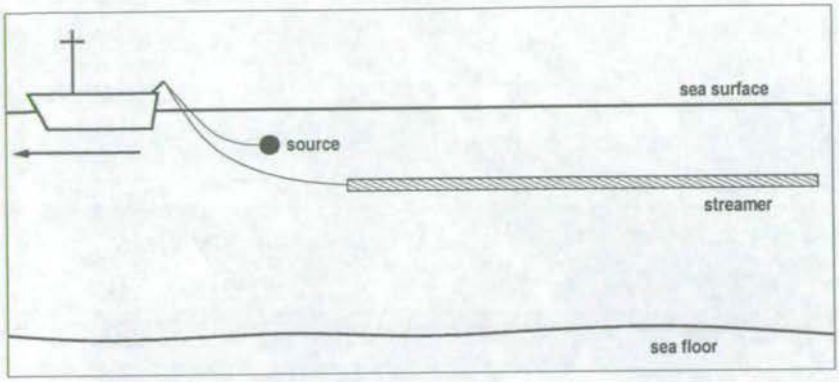


Figure 1.3: The streamer marine acquisition configuration.

streamers close enough together; (2) doing so increases the cost of data acquisition. Because the boat tows the streamer(s) behind the source(s), it records positive offsets only. (It is an engineering problem to deploy the source half-way down the cable to enable recording of negative offsets.) Due to prevailing currents, the cables can deviate considerably from the line of survey which complicates data processing. Measurements in the water record only $P$ waves. The data shown in Figure 1.2 are calculated for a towed streamer acquisition.

In a modern 3D survey up to 12 streamer cables and up two source arrays may be towed simultaneously behind a survey vessel to collect swaths of data over the subsurface. The survey is shot continuously except at line ends when the vessel has to turn around, enabling vast quantities of data to be collected very quickly. A combination of satellite, radio and acoustic positioning ties in the locations of all the survey elements in the water, and the desired survey location. In the last 5 years marine seismic surveying has come full circle since its humble beginnings as an adaptation of land-based acquisition (using cables of geophones in shallow water). It is now perceived (economically) advantageous to deploy cables on the sea floor containing geophones and hydrophones to measure more of the possible wavetypes which propagate in the earth.

The next most common marine geometry is ocean-bottom cable (OBC). This is shown schematically in Figure 1.4. The OBC lies on the sea floor—it may be trenched in, or simply dropped/dragged there. It is attached to a separate recording vessel (not shown), and the shooting vessel passes overhead. The OBC typically contains a hydrophone plus three geophones to measure the particle velocity in three orthogonal directions. Thus, the data which OBC collects are known as 4-component seismic data. The shooting vessel may shoot anywhere with respect to the OBC, enabling positive and negative offsets to be recorded. Several OBCs may be arranged on the sea floor to form a regular recording grid, allowing equal in-line and cross-line sampling. Because the cable contains geophones sitting on the sea floor it can record $S$ waves as well as $P$ waves, providing more information about the earth. On the down side are mainly economic reasons: the cables must be more robust because they

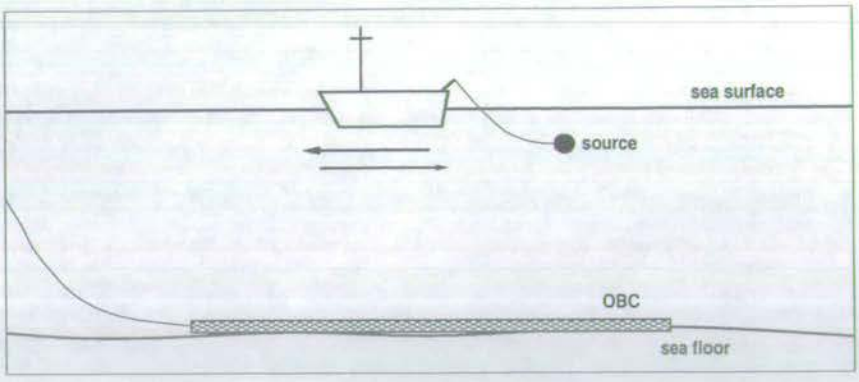


Figure 1.4: The ocean-bottom cable marine acquisition configuration.

are subjected to higher pressures; the cables contain more equipment; OBC deployment, and hence data acquisition, is slower, all of which cost more. The data shown in Figure 1.5 are calculated for hydrophones in an OBC acquisition configuration, using the same model as for Figure 1.2. The direct wave has not been modelled. With the OBC on the sea floor the hydrophones record a large amplitude interface wave known as a Stoneley wave. This is clearest in Figure 1.5(b) when the sea surface is absent. The amplitude of this wave decays exponentially with distance from the interface, so that by the time it travels to the sea surface it has diminished considerably. A comparison of Figures 1.2(b) and 1.5(b) shows this. In the streamer acquisition, although the hydrophones do register the passage of the Stoneley wave, the strongest amplitudes they record are from the reflections. However, in the OBC acquisition the Stoneley wave dominates the signal seen by the hydrophones.

A variation on deployment of seismic detectors on the sea floor is to plant individual 4-component sensors (nodes) using remote operated vehicles (ROVs). Because the nodes are planted robotically their coupling to the sea floor may be better. However, deployment is slow, and costs therefore are high.

A third marine geometry which has started to receive attention is vertical cable (VC). In this configuration a cable containing hydrophones is suspended vertically from a buoy and secured at the sea bottom with an anchor. Many cables may be arranged in a grid. This geometry will not be discussed further here.

## 1.5 Organisation of the thesis

Chapter 2 discusses the basic theory behind wave propagation, and generalises to the acoustic case. Chapter 3 explains the theory of bubble oscillations in water, and marine seismic sources in general. Chapter 4 reviews the vast literature of techniques which have been brought to bear on the sea surface multiple problem. Chapter 5 derives the theory specific to the new multiple removal technique. Chapter 6 deals with real data of source measurements in three differ-

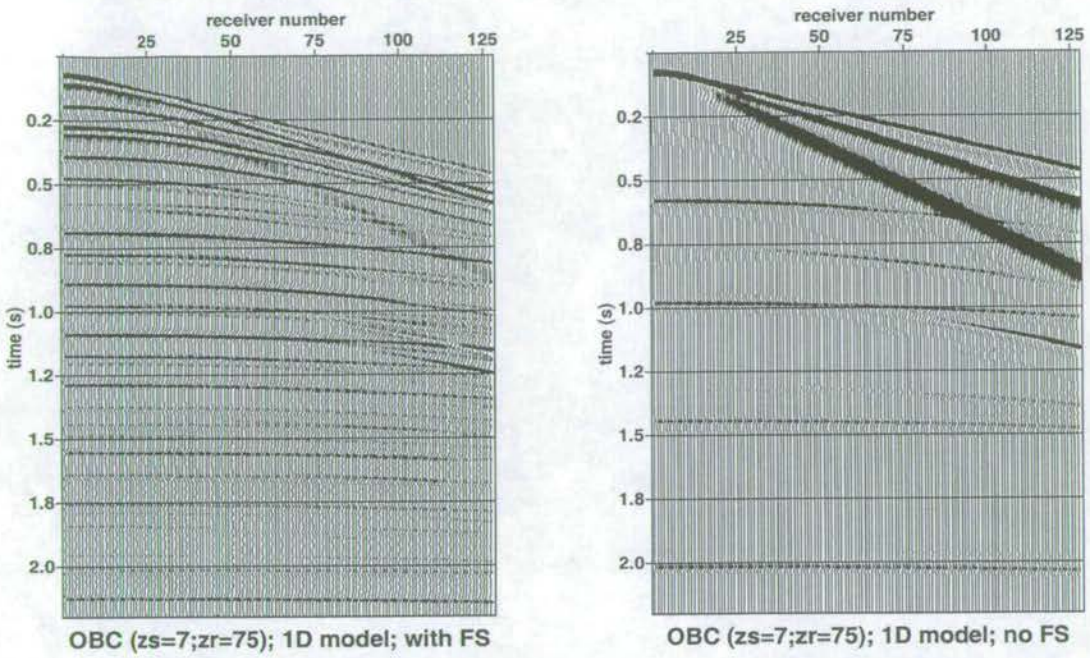


(a) With the sea surface.

(b) Without the sea surface.

Figure 1.5: The effect of the sea surface on 1D synthetic OBC data.

ent acquisition configurations, and reveals the processing necessary to derive the input pulse waveform in each case. Chapter 7 gives examples of the multiple removal scheme using one-dimensional synthetic data, and it examines the scheme's stability. Chapter 8 gives examples of multiple removal using two-dimensional synthetic data. Chapter 9 draws conclusions and makes recommendations for further research.

# THEORETICAL BACKGROUND

# *Chapter 2*

## 2.1 Introduction

Chapter 2 sets out the basic theory required to follow the rest of the thesis. Using elementary ideas of stress and strain, the first section of this chapter derives the wave equation for an ideal inviscid fluid, also know as the acoustic wave equation. The equation is given for pressure (stress). The next section goes on to show how wavefields, such as the one produced by an airgun and discussed in chapter 3, may be decomposed into plane waves. The final section discusses some key ideas from the analysis of plane waves in stratified media which are of use in the new theory of multiple removal presented in chapter 5.

## 2.2 The acoustic wave equation

Continuum mechanics is a convenient framework for defining the deformation of earth materials. Any material which is made up particles may be described as a continuum by assuming that the particles are close enough together to be devoid of empty spaces. This is valid for all but the smallest (inter-atomic) distances. The assumption ignores the molecular structure of the material and simplifies greatly the description of the field variables, such as pressure and displacement, which are expressed as piecewise continuous functions of space and time.

### Traction and the stress tensor

A material subjected to external forces transmits them from one part of the continuum to the next. At any one point $P$, enclosed in a surface element $\Delta S$ of the volume $V$, the resulting forces exerted by the material may be represented by a force and a moment at $P$ associated with a unit normal vector $\mathbf{n} = (n_x, n_y, n_z)$ directed outwards. The force at $P$ is called the traction. The Cauchy stress principle states that in the limit of vanishing surface element $\Delta S$, the moment tends to zero, and the traction divided by the area $\Delta S$ over which it acts is the stress associated with the unit normal $\mathbf{n}$ and $\Delta S$.

At an arbitrary point $P$ in the continuum the Cauchy stress principle associates a traction $\mathbf{t}$ with each unit normal vector $\mathbf{n}$. These normal vectors represent the orientations of all possible infinitesimal surface elements. The state of stress of the material is defined by all possible $\mathbf{t}$-$\mathbf{n}$ pairs. In fact (Love, 1927), it is sufficient to define the traction along three orthogonal planes; the traction on any other plane may then be derived by coordinate transformation. The traction

vector may be decomposed, thus

$$\begin{pmatrix} t_x \\ t_y \\ t_z \end{pmatrix} = \begin{pmatrix} \tau_{xx}n_x + \tau_{xy}n_y + \tau_{xz}n_z \\ \tau_{yx}n_x + \tau_{yy}n_y + \tau_{yz}n_z \\ \tau_{zx}n_x + \tau_{zy}n_y + \tau_{zz}n_z \end{pmatrix}, \tag{2.1}$$

or, writing the traction vectors more compactly with the indicial notation,

$$t_i = \tau_{ij}n_j. \tag{2.2}$$

The nine stress components required to define the traction vectors (and hence the state of stress) are known collectively as the stress tensor:

$$\boldsymbol{\tau} = \begin{pmatrix} \tau_{xx} & \tau_{xy} & \tau_{xz} \\ \tau_{yz} & \tau_{yy} & \tau_{yz} \\ \tau_{zx} & \tau_{zy} & \tau_{zz} \end{pmatrix}. \tag{2.3}$$

It can be shown that the stress tensor is symmetric (Love, 1927), $\tau_{ij} = \tau_{ji}$. The stress components perpendicular to each of the three orthogonal planes are the normal stresses (the diagonal elements of the tensor), and those parallel to these planes are the shearing stresses (the off-diagonal elements). The stress tensor may therefore be written as the sum of two parts, dilatational and deviatoric, representing changes of volume and shape, respectively:

$$\tau_{ij} = -p\delta_{ij} + \tau'_{ij}, \tag{2.4}$$

where $-p\delta_{ij}$ is the volumetric part, $\delta_{ij}$ is the Kronecker delta (which takes the value 1 when $i = j$, and 0 otherwise) and the deviatoric part is represented by

$$\tau'_{ij} = \tau_{ij}(1 - \delta_{ij}). \tag{2.5}$$

The volume changes are caused by the mean inward directed force acting on the particles, and are therefore related to the pressure by

$$p = -\frac{1}{3}\tau_{kk}, \tag{2.6}$$

where the repeated subscript implies a summation ($\tau_{kk} = \tau_{xx} + \tau_{yy} + \tau_{zz}$). In an ideal fluid, which cannot support changes in shape, or shear, only the dilatational stresses are present.

### Deformation and the strain tensor

Under the action of external forces a body tends to deform, and the particles within it move. The displacement of particles is denoted by $\mathbf{u} = (u_x, u_y, u_z)$. Displacement in itself does not

necessarily imply deformation, since the movement of all the particles in a body can be accommodated by a translation or rotation. Deformation occurs in response to differential displacement, i.e. to the variation of displacement between neighbouring particles within a body.

Consider two particles in a continuum, one at position $x_j$, the other at $x_j + \Delta x_j$ whose change in position is the displacement $u_i$. The first particle moves to $x_j + u_i(x_j)$, while the second moves to $x_j + \Delta x_j + u_i(x_j + \Delta x_j)$. Clearly deformation occurs if

$$|\Delta x_j + \Delta u_i| \neq |\Delta x_j|, \quad \text{where } \Delta u_i = u_i(x_j + \Delta x_j) - u_i(x_j). \tag{2.7}$$

The deformation is assumed arbitrarily small, so that the infinitesimal strain theory is applicable. Then $\Delta u_i$ may be expanded using Taylor's theorem, involving linear terms in the displacement gradients only. The infinitesimal strain tensor

$$\varepsilon_{ij} = \frac{1}{2}\left(\frac{\partial u_i}{\partial x_j} + \frac{\partial u_j}{\partial x_i}\right) \tag{2.8}$$

(e.g. Bullen, 1963) accounts for the deformation associated with the displacement $\Delta u_i$. Like the stress tensor, it is a symmetric 2nd order tensor.

### Conservation of mass and momentum

The conservation of mass states that the rate of increase of mass in an elemental volume $V$ is equivalent to the mass entering the surface $S$ enclosing $V$. From an Eulerian viewpoint, fixed in space with respect to the particle motion, and denoting particle velocity by $\mathbf{v} = (v_x, v_y, v_z)$, this is stated as

$$\frac{\partial}{\partial t}\int_V \rho dV = -\int_S \rho \mathbf{v}.\mathbf{n} dS. \tag{2.9}$$

Gauss's divergence theorem allows a surface integral to be replaced by a volume integral:

$$\int_V \nabla.\mathbf{g} dV = \int_S \mathbf{g}.\mathbf{n} dS, \tag{2.10}$$

which allows the mass balance (2.9) to be rewritten as

$$\frac{\partial}{\partial t}\int_V \rho dV = -\int_V \nabla.(\rho \mathbf{v}) dV. \tag{2.11}$$

Since the equation holds for any volume $V$, the equality holds for the integrand, wherever it is continuous,

$$\frac{\partial \rho}{\partial t} = -\frac{\partial(\rho v_i)}{\partial x_i} = -\nabla.(\rho \mathbf{v}). \tag{2.12}$$

This is the continuity equation in Eulerian coordinates.

Newton's second law of motion is a statement of conservation of momentum. In an Eulerian frame, the rate of change of momentum in a volume $V$ is equivalent to the momentum passing the surface $S$ enclosing $V$, plus all surface and body forces acting on the particles in $V$:

$$\frac{\partial}{\partial t}\int_V \rho v_i \mathrm{d}V = -\int_S (\rho v_i) v_j n_j \mathrm{d}S + \int_S t_i \mathrm{d}S + \int_V f_i \mathrm{d}V, \tag{2.13}$$

where $t_i$ is the traction on $S$, and $f_i$ is the volume density of external force. Using equation (2.2) and (2.10), the traction may be written as

$$\int_S t_i \mathrm{d}S = \int_S \tau_{ij} n_j \mathrm{d}S = \int_V \frac{\partial \tau_{ij}}{\partial x_j} \mathrm{d}V. \tag{2.14}$$

The remaining surface integral in equation (2.13) may be expressed as a volume integral using (2.10):

$$\int_S (\rho v_i) v_j n_j \mathrm{d}S = \int_V \frac{\partial}{\partial x_j}(\rho v_j v_i) \mathrm{d}V, \tag{2.15}$$

where the order of $v_i$ and $v_j$ has been reversed on the right-hand side. Thus, substitution of (2.14) and (2.15) in (2.13), and taking the spatial derivatives gives

$$\frac{\partial}{\partial t}\int_V \rho v_i \mathrm{d}V = -\int_V \left( v_i \frac{\partial(\rho v_j)}{\partial x_j} + \rho v_j \frac{\partial v_i}{\partial x_j} \right) \mathrm{d}V + \int_V \frac{\partial \tau_{ij}}{\partial x_j} \mathrm{d}V + \int_V f_i \mathrm{d}V. \tag{2.16}$$

Since the volume $V$ is arbitrary, the equality holds for the integrands. Expansion of the left-hand side of (2.16) gives

$$\rho \frac{\partial v_i}{\partial t} + v_i \frac{\partial \rho}{\partial t} = -v_i \frac{\partial(\rho v_j)}{\partial x_j} - \rho v_j \frac{\partial v_i}{\partial x_j} + \frac{\partial \tau_{ij}}{\partial x_j} + f_i, \tag{2.17}$$

from which it follows, with the aid of (2.12),

$$\rho \frac{\partial v_i}{\partial t} = -\rho v_j \frac{\partial v_i}{\partial x_j} + \frac{\partial \tau_{ij}}{\partial x_j} + f_i, \tag{2.18}$$

or

$$\rho \left( \frac{\partial \mathbf{v}}{\partial t} + (\nabla \mathbf{v}).\mathbf{v} \right) = \nabla.\boldsymbol{\tau} + \mathbf{f}. \tag{2.19}$$

In a Lagrangian frame, moving with the particles, equation (2.19) takes the form

$$\rho \frac{\mathrm{d}\mathbf{v}}{\mathrm{d}t} = \nabla.\boldsymbol{\tau} + \mathbf{f}, \tag{2.20}$$

in which $\frac{d}{dt}$ is the Lagrangian or total derivative. The material derivative on the left (often denoted by $\frac{D}{Dt}$ in hydrodynamics) follows the particle motion. In the linearised theory of elasticity the convective term $(\nabla \mathbf{v}).\mathbf{v}$ in (2.19) is negligible so that the Eulerian and Lagrangian descriptions are equivalent (Achenbach, 1973). In the linearised theory (i.e. not close to the source of the deformation) the velocity is related to the particle displacement simply by

$$v_i = \frac{\partial u_i}{\partial t}. \tag{2.21}$$

Equations (2.19) and (2.20) are therefore equivalent and may be written as

$$\rho \frac{\partial \mathbf{v}}{\partial t} = \nabla.\boldsymbol{\tau} + \mathbf{f}. \tag{2.22}$$

This is the linearised equation of motion in terms of the particle velocity.

The distinction between Lagrangian (total) and Eulerian (partial) derivatives is used in chapter 3 in the description of the wavefield produced by an oscillating bubble.

### Hooke's Law and the elastic constants

Linear elastic theory states that the stress is proportional to the strain, for weak deformation, such as that experienced by the passage of a seismic wave. Thus, a material returns to its original shape after the deformation. The constitutive law for elastic materials is a generalisation of Hooke's law, and linearly relates the stress and strain tensors,

$$\tau_{ij} = c_{ijpq}\varepsilon_{pq} \tag{2.23}$$

(see, for example, Aki and Richards, 1980). The stiffness tensor $c_{ijkl}$ has 81 components for a general anisotropic material (whose properties vary with direction). Symmetry arguments for the stress and strain tensors and energy considerations reduce this number to 21 (e.g. Brekhovskikh & Goncharov, 1982). In an isotropic material there are no preferred directions, and the stiffness tensor is characterised by 2 independent coefficients only, the Lamé parameters $\lambda$ and $\mu$. The latter of these parameters is known as the shear modulus.

For isotropy, the relationship between stress and strain is greatly simplified,

$$\tau_{ij} = \lambda \varepsilon_{kk}\delta_{ij} + 2\mu\varepsilon_{ij} \tag{2.24}$$

(e.g. Achenbach, 1973) where $\varepsilon_{kk} = \varepsilon_{11} + \varepsilon_{22} + \varepsilon_{33}$ is the volumetric strain or volume change. The normal stresses are found by setting $j = i$ in (2.24), and thus implying a summation:

$$\tau_{ii} = (3\lambda + 2\mu)\varepsilon_{ii}, \tag{2.25}$$

where $\tau_{ii} = \tau_{11} + \tau_{22} + \tau_{33}$ is the volumetric stress and $\delta_{ii} = \delta_{11} + \delta_{22} + \delta_{33} = 3$.

A special state of stress in a body is one in which the stress tensor has only one independent component—the pressure, $p$. It is known as hydrostatic pressure because it is satisfied by a fluid at rest. In an inviscid fluid the stresses are purely dilatational, thus, from (2.4),

$$\tau_{ij} = -p\delta_{ij}. \tag{2.26}$$

At all points in a fluid every axis is a principal axis, thus,

$$\begin{aligned} \tau_{xx} &= \tau_{yy} = \tau_{zz} = -p \\ \tau_{xy} &= \tau_{xz} = \tau_{yz} = 0. \end{aligned} \tag{2.27}$$

Equating (2.26) with (2.25) for the case $j = i$, the pressure is related to the strain by the incompressibility or bulk modulus $K$,

$$p = -K\varepsilon_{ii}, \quad \text{where } K = \lambda + \frac{2}{3}\mu. \tag{2.28}$$

Substitution of (2.8) into (2.28) allows the strain to be written in terms of displacement:

$$p = -K\frac{\partial u_i}{\partial x_i}. \tag{2.29}$$

When $K = \lambda$, equation (2.29) is an alternative statement of Hooke's Law for an ideal fluid.

When a source of deformation is present, $\sigma_{ij}$ denotes the stress distribution associated with it, analogous to the stress tensor $\tau_{ij}$. In a fluid this results in a source density of bulk strain (such as volume injection) denoted by $g$. Thus, in the presence of a seismic source (such as an airgun), (2.29) becomes

$$p = -K\frac{\partial u_i}{\partial x_i} - g. \tag{2.30}$$

### The wave equation

When a material allows only compressional motion, that is, a disturbance is propagated by volume changes, the governing equation for wave propagation is known as the acoustic wave equation. This is the case in an ideal fluid, for which there are no shearing stresses.

The two equations from which the wave equation derives are the equation of motion (Newton's 2nd law) and the equation of deformation (Hooke's law). To derive the wave equation they should both be written in terms of the same quantities. When equation (2.26) is

substituted into (2.22) the linearised equation of motion becomes

$$\rho \frac{\partial v_i}{\partial t} + \frac{\partial p}{\partial x_i} = f_i. \tag{2.31}$$

Taking the time derivative of (2.30) and substituting (2.21), the linearised equation of deformation *rate* is

$$\frac{1}{K}\frac{\partial p}{\partial t} + \frac{\partial v_i}{\partial x_i} = w, \tag{2.32}$$

where

$$w = -\frac{\partial g}{\partial t} \tag{2.33}$$

is the volume injection rate. Equations (2.31) and (2.32) are symmetrical equations. The wave equation is easily derived in terms of particle velocity or pressure by eliminating one of the dependent variables. Assuming constant density, the spatial derivative of (2.31) is

$$\rho \frac{\partial^2 v_i}{\partial x_i \partial t} + \frac{\partial^2 p}{\partial x_i^2} = \frac{\partial f_i}{\partial x_i}, \tag{2.34}$$

and the temporal derivative of (2.32) is

$$\frac{1}{K}\frac{\partial^2 p}{\partial t^2} + \frac{\partial^2 v_i}{\partial t \partial x_i} = \frac{\partial w}{\partial t}. \tag{2.35}$$

Multiplication of (2.35) by $\rho$ and subtraction of the result from (2.34) yields

$$\frac{\partial^2 p}{\partial x_i^2} - \frac{\rho}{K}\frac{\partial^2 p}{\partial t^2} = \frac{\partial f_i}{\partial x_i} - \rho \frac{\partial w}{\partial t}. \tag{2.36}$$

In an ideal fluid the body forces $f_i$ are zero, and (2.36) becomes

$$\frac{\partial^2 p}{\partial x_i^2} - \frac{1}{c^2}\frac{\partial^2 p}{\partial t^2} = -\rho \frac{\partial w}{\partial t}. \tag{2.37}$$

where

$$c = \sqrt{\frac{K}{\rho}} \tag{2.38}$$

is the velocity of wave propagation in the fluid. Equation (2.37) is the inhomogeneous acoustic wave equation for pressure. The acoustic source term $\rho \frac{\partial w}{\partial t}$ is discussed in detail in chapter 3.

In the absence of any sources (2.37) becomes the familiar homogenous acoustic wave

equation,

$$\nabla^2 p = \frac{1}{c^2}\frac{\partial^2 p}{\partial t^2}. \tag{2.39}$$

## 2.3 Decomposing spherical waves into plane waves

A key element in the multiple removal theory presented in this thesis is the idea of decomposing wavefields into plane waves. The theory of reflection and refraction of plane waves is well known, and permits a simple descripton of the sea surface multiples. Therefore, a derivation is given below, following Båth (1968), of expressing a spherical wave in terms of an infinite sum of plane waves.

Consider a source of spherical waves, such as the oscillating bubble produced by an airgun (discussed in chapter 3), centred on the origin. The acoustic velocity potential of such a source may be written as

$$\varphi = \frac{V_0}{4\pi}\frac{1}{R}\exp\left(i\omega\left[\frac{R}{c} - t\right]\right) \tag{2.40}$$

where $R = \sqrt{x^2+y^2+z^2}$ is the distance from the source and $\frac{V_0}{4\pi}$ represents the strength of the source.

To arrive at an expansion of a spherical wave into plane waves it is convenient to discard the parts of the potential which do not have a spatial dependence, namely the time dependence $\exp(-i\omega t)$, and the factor characterising the source strength. Consider the spherical wave in the plane $z = 0$. With these simplifications, the field of the spherical wave now takes the form

$$\frac{1}{r}\exp\left(i\omega\frac{r}{c}\right) = \frac{1}{r}\exp(ikr) \tag{2.41}$$

where $r = \sqrt{x^2+y^2}$ and $k = \frac{\omega}{c}$.

The field is now expanded in Fourier series along the $x$- and $y$-axes:

$$\frac{1}{r}\exp(ikr) = \frac{1}{(2\pi)^2}\iint_{-\infty}^{+\infty} A(k_x,k_y)\exp\left(+i\left[k_x x + k_y y\right]\right)\mathrm{d}k_x\mathrm{d}k_y, \tag{2.42}$$

where

$$A(k_x,k_y) = \iint_{-\infty}^{+\infty}\frac{1}{r}\exp(ikr)\exp\left(-i\left[k_x x + k_y y\right]\right)\mathrm{d}x\mathrm{d}y \tag{2.43}$$

represents the space to wavenumber Fourier transform and (2.42) is its inverse.

Now transform from Cartesian to polar coordinates with the following substitutions

$$\begin{aligned} k_x &= k_r\cos\theta; \qquad k_y = k_r\sin\theta; \qquad k_r = \sqrt{k_x^2+k_y^2}; \\ x &= r\cos\beta; \qquad y = r\sin\beta; \qquad \mathrm{d}x\mathrm{d}y = r\mathrm{d}r\mathrm{d}\beta, \end{aligned} \tag{2.44}$$

so that (2.43) becomes

$$\begin{aligned} A(k_x,k_y) &= \int_0^{2\pi}\int_0^{\infty}\frac{1}{r}\exp\left(+ikr\right)\exp\left(-i[k_r\cos\theta r\cos\beta + k_r\sin\theta r\sin\beta]\right)r\mathrm{d}r\mathrm{d}\beta \\ &= \int_0^{2\pi}\mathrm{d}\beta\int_0^{\infty}\exp\left(+ir[k-k_r\cos(\theta-\beta)]\right)\mathrm{d}r. \end{aligned} \tag{2.45}$$

The integral over $r$ may be evaluated by assuming that the medium is slightly attenuating such that $k$ has a positive imaginary part. Substitution of the upper limit of integration yields zero to give

$$\int_0^{\infty} e^{irB}\mathrm{d}r = \left[\frac{e^{irB}}{iB}\right]_0^{\infty} = -\frac{1}{iB} = \frac{i}{B},$$

where $B = [k-k_r\cos(\theta-\beta)]$. Evaluating the integral over $r$ in this way gives

$$A(k_x,k_y) = i\int_0^{2\pi}\frac{\mathrm{d}\beta}{k-k_r\cos(\theta-\beta)}. \tag{2.46}$$

Substituting $\delta_1 = \beta-\theta$ so that $\mathrm{d}\delta_1 = \mathrm{d}\beta$, equation (2.46) becomes

$$A(k_x,k_y) = i\int_{-\theta}^{2\pi-\theta}\frac{\mathrm{d}\delta_1}{k-k_r\cos(\delta_1)} = i\int_0^{2\pi}\frac{\mathrm{d}\delta_1}{k-k_r\cos(\delta_1)} \tag{2.47}$$

where it is noted that the integrand is even and $2\pi$-periodic. Further simplification yields

$$A(k_x,k_y) = \frac{i}{k}\int_0^{2\pi}\frac{\mathrm{d}\delta_1}{1+(-\frac{k_r}{k})\cos\delta_1}, \tag{2.48}$$

which may be evaluated with the standard integral (De La Vallée Poussin, 1938, p. 224),

$$\int_0^{2\pi}\frac{\mathrm{d}x}{1+a\cos x} = \frac{2\pi}{\sqrt{1-a^2}}$$

provided $a^2<1$, to give

$$A(k_x,k_y) = \frac{i}{k}\frac{2\pi}{\sqrt{1-\frac{k_r^2}{k^2}}} = \frac{i2\pi}{\sqrt{k^2-k_r^2}} = \frac{i2\pi}{\sqrt{k^2-k_x^2-k_y^2}},$$

where the value of $k_r$ has been substituted from (2.44). Thus, equation (2.42) becomes

$$\frac{1}{r}\exp(ikr) = \frac{i}{2\pi}\int_{-\infty}^{+\infty}\int \frac{\exp(+i[k_x x + k_y y])}{\sqrt{k^2 - k_x^2 - k_y^2}}\mathrm{d}k_x\mathrm{d}k_y \tag{2.49}$$

which is the plane wave decomposition of a spherical wave in the horizontal ($xy$-) plane $z = 0$.

Equation (2.49) may be generalised to three dimensions. Addition of the term $\pm ik_z z$ to the exponent in the integrand analytically continues the spherical-wave expansion into the $z$-direction, where

$$k_z^2 = k^2 - k_x^2 - k_y^2, \tag{2.50}$$

which is the dispersion relation. In the analytical continuation, the plus sign corresponds to points lying in the half-space $z > 0$, and to waves propagating in the positive $z$-direction. The minus sign corresponds to points for which $z < 0$, and waves travelling in the negative $z$-direction. The three-dimensional equation is therefore

$$\frac{1}{R}\exp(ikR) = \frac{i}{2\pi}\int_{-\infty}^{+\infty}\int \frac{\exp(+i[k_x x + k_y y \pm k_z z])}{k_z}\mathrm{d}k_x\mathrm{d}k_y, \tag{2.51}$$

where the $+$ sign is for $z > 0$, and the $-$ sign, for $z < 0$. (The generalisation from the $xy$- to the $xyz$-plane is valid since the right-hand side of (2.51) satisfies the wave equation and gives the correct value for the field at $z = 0$.)

Equation (2.51) gives the decomposition of a spherical wave into plane waves. It is known as the Weyl integral (Weyl, 1919). The exponent in the integrand represents a plane wave propagating in a direction given by the components $k_x$, $k_y$ and $k_z$ of the wave vector $k$. Once the explicit time dependence, $\exp(-i\omega t)$, is introduced into the integrand, it is clear that the plane wave

$$\exp(+i[k_x x + k_y y \pm k_z z - \omega t]) \quad \text{where } k_z = +\sqrt{\frac{\omega^2}{c^2} - k_x^2 - k_y^2} \tag{2.52}$$

propagates with the speed of the medium $c$.

Suppose $k_x$, $k_y$ and $\omega$ are all positive so that the plane wave is propagating in the positive $x$- and $y$-directions. The behaviour in the $z$-direction is determined by $\pm ik_z z$. When $k_z$ is real ($\frac{\omega^2}{c^2} > k_x^2 + k_y^2$) which corresponds to *homogeneous* waves, the choice of the sign dictates whether the wave propagates in the positive or negative $z$-direction. When $k_z$ is imaginary ($\frac{\omega^2}{c^2} < k_x^2 + k_y^2$) which corresponds to *inhomogeneous* or *evanescent* waves, the choice of sign dictates whether the wave exponentially grows or decays with increasing $z$. The evanescent waves are a necessary part of the plane wave decomposition of a spherical wave and ensure

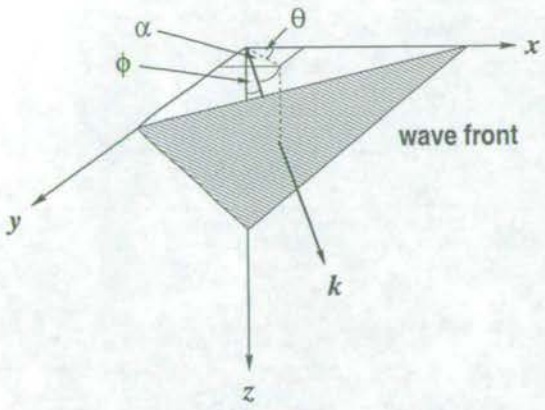


Figure 2.1: A homogeneous plane wave and its normal, the wavevector $k$, in spherical coordinates $\theta$ and $\phi$.

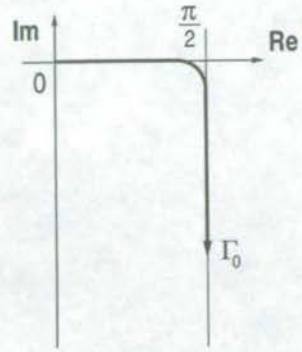


Figure 2.2: The path of integration over $\phi$ in the complex plane.

causality of the wavefield. Their inclusion guarantees the necessary singularity as $R \to 0$, and provides solutions to the wave equation which are bounded at all other points.

The direction of propagation of each of the plane waves may be expressed in terms of the angles of incidence $\phi$ and azimuth $\theta$ (see Figure 2.1). By making the following substitutions

$$k_x = k\sin\phi\cos\theta; \qquad k_y = k\sin\phi\sin\theta; \qquad k_z = k\cos\phi, \tag{2.53}$$

the integrals in equation (2.51) are evaluated in spherical coordinates with respect to $\theta$ and $\phi$ instead of $k_x$ and $k_y$. The integration w.r.t. $\theta$ is performed between 0 and $2\pi$, however, the integration w.r.t. $\phi$ must include complex angles due to the third substitution in (2.53). From equation (2.52), $k_z$ varies from $k_z = \frac{\omega}{c}$ when $k_x = k_y = 0$ to $k_z \to i\infty$ when $k_x \to \pm\infty$ or $k_y \to \pm\infty$. Thus, from (2.53), $\cos\phi = \frac{k_z}{k}$ and the integration w.r.t. $\phi$ is performed between 0 and $\frac{\pi}{2} - i\infty$. The path of integration over $\phi$ is the contour $\Gamma_0$ shown in Figure 2.2.

It may be shown (Båth, 1968, p. 190) that

$$\frac{1}{k_z}\mathrm{d}k_x\mathrm{d}k_y = k\sin\phi\,\mathrm{d}\phi\,\mathrm{d}\theta.$$

With these substitutions (2.51) becomes

$$\frac{1}{R}\exp(ikR) = \frac{ik}{2\pi}\int_0^{\frac{\pi}{2}-i\infty}\int_0^{2\pi}\exp\left(+i\left[k_x x + k_y y \pm k_z z\right]\right)\sin\phi\,\mathrm{d}\phi\,\mathrm{d}\theta, \tag{2.54}$$

where, in the exponent, the + sign corresponds with $z \geqslant 0$, and the − sign, with $z \leqslant 0$. Thus, in the expansion of a spherical wave, the homogeneous waves correspond to waves travelling

in all possible directions within the limits $0 \leqslant \theta \leqslant 2\pi$ and $0 \leqslant \phi \leqslant \frac{\pi}{2}$, whereas the evanescent waves correspond to complex values of $\phi$. Equation (2.54) may be expressed in terms of the angle of emergence $\alpha$ instead of the angle of incidence $\phi$ (see Figure 2.1) by making the following substitutions:

$$k_x = k\cos\alpha\cos\theta; \qquad k_y = k\cos\alpha\sin\theta; \qquad k_z = k\sin\alpha. \tag{2.55}$$

This gives for $z \geqslant 0$,

$$\frac{1}{R}\exp(ikR) = -\frac{ik}{2\pi}\int_{\frac{\pi}{2}}^{i\infty}\int_0^{2\pi}\exp(+i[k_x x + k_y y + k_z z])\cos\alpha\,\mathrm{d}\alpha\,\mathrm{d}\theta. \tag{2.56}$$

Equation (2.56) may be expressed in terms of cylindrical waves by changing from spherical coordinates to polar coordinates in the $xy$-plane, with the additional substitutions to (2.55):

$$\begin{aligned} k_r &= k\cos\alpha; \qquad \mathrm{d}\alpha = -\frac{\mathrm{d}k_r}{k\sin\alpha}; \qquad \sin\alpha = \frac{i\sqrt{k_r^2 - k^2}}{k} \\ x &= r\cos\beta; \qquad y = r\sin\beta. \end{aligned} \tag{2.57}$$

Thus, (2.56) becomes (for $z \geqslant 0$)

$$\begin{aligned} \frac{1}{R}\exp(ikR) &= -\frac{ik}{2\pi}\int_0^{\infty}\int_0^{2\pi}\exp\left(+i\left[k_r\cos\theta r\cos\beta + k_r\sin\theta r\sin\beta + iz\sqrt{k_r^2 - k^2}\right]\right)\cdot \\ &\qquad \frac{k_r}{k}\frac{-\mathrm{d}k_r}{i\sqrt{k_r^2 - k^2}}\mathrm{d}\theta \\ &= \frac{1}{2\pi}\int_0^{\infty}\mathrm{d}k_r\int_0^{2\pi}\frac{k_r}{\sqrt{k_r^2 - k^2}}\exp\left(irk_r\cos[\theta - \beta] - z\sqrt{k_r^2 - k^2}\right)\mathrm{d}\theta, \end{aligned} \tag{2.58}$$

which may be expressed in terms of a Bessel integral,

$$\frac{1}{R}\exp(ikR) = \int_0^{\infty}\frac{k_r J_0(k_r r)\exp\left(-z\sqrt{k_r^2 - k^2}\right)}{\sqrt{k_r^2 - k^2}}\mathrm{d}k_r \quad z \geqslant 0, \tag{2.59}$$

where $J_0$ is the Bessel function of zero order. Equations (2.58) and (2.59) can be found in Båth (1968), p. 191 and Aki & Richards (1980), pp. 198-199. Equation (2.59) gives the decomposition of a spherical wave into cylindrical waves. It is known as the Sommerfeld integral (Sommerfeld, 1909).

## 2.4 Waves in layered media

Waves travelling in layered media have been studied extensively (e.g. Ewing, Jardetsky & Press, 1957). The multiple removal scheme explained in chapter 5 is fully three-dimensional

in approach and does not require the earth to be horizontally stratified. However, it uses some concepts which have emerged from the studies of wave propagation in layered media. For this reason, certain elements of that analysis are presented here.

### Two-way wave equations

The homogeneous acoustic wave equation was derived in section 2.2. It is

$$\frac{K}{\rho}\nabla^2 p - \frac{\partial^2 p}{\partial t^2} = 0 \tag{2.60}$$

which is a *second-order* partial differential equation in $p(x,y,z,t)$. A similar expression may be derived for the particle velocity $\mathbf{v}(x,y,z,t)$. It is known as the two-way acoustic wave equation because it accounts for propagation both upwards and downwards (of course, waves actually travel in all directions).

The linearised equations of motion and deformation are *first-order* partial differential equations in $p$ and $\mathbf{v}$. In the absence of any sources they are

$$\rho\frac{\partial \mathbf{v}}{\partial t} = -\nabla p \tag{2.61}$$

$$\frac{1}{K}\frac{\partial p}{\partial t} = -\nabla.\mathbf{v}. \tag{2.62}$$

In layered media, the material properties are a function of depth only, such that

$$K(x,y,z) = K(z)\,; \quad \rho(x,y,z) = \rho(z).$$

Equations (2.61) and (2.62) may be transformed from $(x,y,z,t)$ to $(k_x,k_y,z,\omega)$ by making the substitution

$$\begin{aligned} p(x,y,z,t) &= P(k_x,k_y,z,\omega)\exp\left(-i[\omega t - k_x x - k_y y]\right) \\ \mathbf{v}(x,y,z,t) &= \mathbf{V}(k_x,k_y,z,\omega)\exp\left(-i[\omega t - k_x x - k_y y]\right). \end{aligned} \tag{2.63}$$

The step of transforming to the frequency-wavenumber domain allows the analysis of individual plane wave components. In effect, it performs a plane wave decomposition of the equations of motion and deformation. Thus, in the frequency-wavenumber domain, (2.61) and (2.62) become

$$-i\omega\rho\mathbf{V} = -ik_x P - ik_y P - \frac{\partial P}{\partial z} \tag{2.64}$$

$$-i\omega\frac{1}{K}P = -ik_x V_x - ik_y V_y - \frac{\partial V_z}{\partial z} \tag{2.65}$$

where, with the conventions used in this thesis,

$$\frac{\partial}{\partial t} \mapsto -i\omega\,; \quad \frac{\partial}{\partial x} \mapsto ik_x\,; \quad \frac{\partial}{\partial y} \mapsto ik_y.$$

Equating the $x$-components and the $y$-components of (2.64) allows $V_x$ and $V_y$ to be written in terms of pressure in (2.65):

$$-i\omega\frac{1}{K}P + \frac{ik_x^2}{\omega\rho}P + \frac{ik_y^2}{\omega\rho}P = -\frac{\partial V_z}{\partial z} \tag{2.66}$$

which may be written as

$$-\frac{i}{\omega\rho}\left(\frac{\omega^2}{c(z)^2} - k_x^2 - k_y^2\right)P = -\frac{\partial V_z}{\partial z}, \tag{2.67}$$

in which, from (2.52), the vertical wavenumber is identified as $k_z$, and $c(z)^2 = \frac{K(z)}{\rho(z)}$.

Equating the $z$-components of (2.64) gives

$$\frac{\partial P}{\partial z} = i\omega\rho V_z, \tag{2.68}$$

and (2.67) may be written as

$$\frac{\partial V_z}{\partial z} = \frac{ik_z^2}{\omega\rho}P. \tag{2.69}$$

Equations (2.68) and (2.69) relate material properties and the field variables, pressure and the vertical component of particle velocity, in stratified media. They may be combined into a single matrix equation:

$$\frac{\partial}{\partial z}\begin{bmatrix} P \\ V_z \end{bmatrix} = \begin{bmatrix} 0 & i\omega\rho \\ \frac{ik_z^2}{\omega\rho} & 0 \end{bmatrix}\begin{bmatrix} P \\ V_z \end{bmatrix}, \tag{2.70}$$

or

$$\frac{\partial \mathbf{f}}{\partial z} = \mathbf{A}\mathbf{f}. \tag{2.71}$$

Equations (2.71) represent a set of coupled *first-order* partial differential equations in $P$ and $V_z$, both a function of $(k_x, k_y, z, \omega)$. They account for propagation both upwards and downwards. They may be solved by diagonalising $\mathbf{A}$, which depends only on the material properties of the earth and the plane wave under consideration, and decomposing $\mathbf{f}$ into upgoing and downgoing waves to produce uncoupled one-way wave equations. A one-way wave equation accounts for propagation either upwards or downwards.

### One-way wave equations

Following Claerbout (1976), the eigenvalue decomposition of **A** is achieved as follows

$$\mathbf{A} = \mathbf{C}\Lambda\mathbf{B}, \tag{2.72}$$

where

$$\mathbf{C} = \begin{bmatrix} 1 & 1 \\ -\frac{k_z}{\omega\rho} & \frac{k_z}{\omega\rho} \end{bmatrix} \tag{2.73}$$

is the matrix of column eigenvectors of **A**, and

$$\mathbf{B} = \frac{1}{2}\begin{bmatrix} 1 & -\frac{\omega\rho}{k_z} \\ 1 & \frac{\omega\rho}{k_z} \end{bmatrix} \tag{2.74}$$

is the matrix of row eigenvectors of **A**, normalised so that

$$\mathbf{CB} = \mathbf{BC} = \mathbf{I}. \tag{2.75}$$

The diagonal matrix $\Lambda$ in (2.72) is given by

$$\Lambda = \mathbf{BAC} = \begin{bmatrix} -ik_z & 0 \\ 0 & ik_z \end{bmatrix}, \tag{2.76}$$

where the two eigenvalues of **A** lie on the diagonal.

A vector **e** may be defined which contains the upgoing and downgoing plane wave components, called here the wave variables,

$$\mathbf{e} = \begin{bmatrix} U \\ D \end{bmatrix}, \tag{2.77}$$

and which is obtained from the field variables using the *decomposition* matrix **B**:

$$\mathbf{e} = \mathbf{Bf}, \tag{2.78}$$

or

$$\begin{bmatrix} U \\ D \end{bmatrix} = \frac{1}{2}\begin{bmatrix} 1 & -\frac{\omega\rho}{k_z} \\ 1 & \frac{\omega\rho}{k_z} \end{bmatrix}\begin{bmatrix} P \\ V_z \end{bmatrix}. \tag{2.79}$$

Similarly, the field variables **f** may be obtained from the wave variables using the *composition*

matrix **C**:

$$\mathbf{f} = \mathbf{C}\mathbf{e}, \tag{2.80}$$

or

$$\begin{bmatrix} P \\ V_z \end{bmatrix} = \begin{bmatrix} 1 & 1 \\ -\frac{k_z}{\omega\rho} & \frac{k_z}{\omega\rho} \end{bmatrix} \begin{bmatrix} U \\ D \end{bmatrix}. \tag{2.81}$$

The eigenvectors in **B** and **C** are normalised such that the dimensions of **e** are pressure. Thus, the sum of upgoing and downgoing plane wave components is simply the pressure. The particle velocity is the difference of these components, scaled by the admittance of the medium, $\mathcal{Y}$:

$$\mathcal{Y} = \frac{k_z}{\omega\rho} = \frac{\cos\phi}{\rho c}, \tag{2.82}$$

where $\phi$ is the incidence angle of the wave with the interface, and

$$\cos\phi = \frac{ck_z}{\omega}, \qquad \sin\phi = \frac{c}{\omega}(k_x + k_y). \tag{2.83}$$

The admittance is the inverse of the impedance, $\mathcal{Z}$:

$$\mathcal{Z} = \frac{\omega\rho}{k_z} = \frac{\rho c}{\cos\phi}. \tag{2.84}$$

Substitution of (2.80) into (2.71) gives

$$\begin{aligned} \frac{\partial}{\partial z}(\mathbf{C}\mathbf{e}) &= \mathbf{A}\mathbf{C}\mathbf{e} \\ &= \mathbf{C}\frac{\partial \mathbf{e}}{\partial z} + \mathbf{e}\frac{\partial \mathbf{C}}{\partial z}. \end{aligned} \tag{2.85}$$

Equating the right-hand sides of equation (2.85) and simplifying with the help of (2.75) and (2.76) yields

$$\begin{aligned} \mathbf{B}\mathbf{A}\mathbf{C}\mathbf{e} &= \mathbf{B}\mathbf{C}\frac{\partial \mathbf{e}}{\partial z} + \mathbf{B}\mathbf{e}\frac{\partial \mathbf{C}}{\partial z} \\ \Rightarrow \frac{\partial \mathbf{e}}{\partial z} &= \mathbf{\Lambda}\mathbf{e} - \mathbf{B}\mathbf{e}\frac{\partial \mathbf{C}}{\partial z}. \end{aligned} \tag{2.86}$$

The second term on the right in (2.86) represents the coupling between the wave variables $U$ and $D$. If the material is homogeneous then, since **C** is non-singular if $k_z \neq 0$, $\frac{\partial \mathbf{C}}{\partial z} = 0$ and

equation (2.86) simplifies to

$$\frac{\partial \mathbf{e}}{\partial \mathbf{z}} = \mathbf{\Lambda e}. \tag{2.87}$$

Equally, equation (2.87) may be written as

$$\frac{\partial}{\partial z}\begin{bmatrix} U \\ D \end{bmatrix} = \begin{bmatrix} -ik_z & 0 \\ 0 & ik_z \end{bmatrix}\begin{bmatrix} U \\ D \end{bmatrix}, \tag{2.88}$$

which represents a separate problem for each component of $\mathbf{e}$, due to the diagonal property of the matrix of eigenvalues $\mathbf{\Lambda}$. Thus, the original problem of coupled first-order differential equations (2.71) has been decomposed into two uncoupled differential equations. The upgoing and downgoing waves propagate independently without interaction as long as the material properties are constant within a layer. They obey *one-way* wave equations. Note that the decomposition breaks down for $k_z = 0$ which represents waves which propagate horizontally. The general solution of (2.87) has the form

$$\mathbf{e} = \exp(\mathbf{\Lambda} z)\,\mathbf{e}_0 \tag{2.89}$$

where $\mathbf{e}_0$ is a constant.

### Propagator matrices

Consider now a system of $N-1$ plane layers in which the subscript $i$ denotes the properties of a layer between depths $z_i$ and $z_{i+1}$, shown schematically in Figure 2.3, and the superscripts $t$ and $b$ denote the top and bottom of a layer, respectively. From (2.89) it follows that

$$\mathbf{e}_i^b = \exp(\mathbf{\Lambda}_i \Delta z_i)\mathbf{e}_i^t, \tag{2.90}$$

where

$$\Delta z_i = z_{i+1} - z_i \tag{2.91}$$

is the distance between the top and bottom of layer $i$, where $\mathbf{e}$ takes the values $\mathbf{e}_i^t$ and $\mathbf{e}_i^b$, respectively. Equation (2.90) propagates the wavefield (the upgoing and downgoing plane wave components) within a single homogeneous layer.

Premultiplying equation (2.90) by $\mathbf{C}_i$, and using (2.78) and (2.80) gives

$$\mathbf{f}_{i+1}^t = \mathbf{f}_i^b = \mathbf{C}_i\mathbf{E}_i\mathbf{B}_i\mathbf{f}_i^t, \tag{2.92}$$

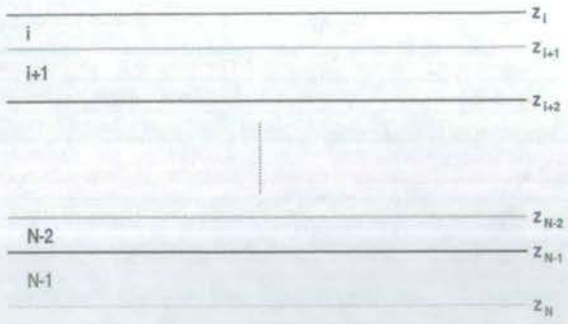


Figure 2.3: A stack of $N-1$ plane layers whose top surface is at depth $z_i$.

where

$$\mathbf{E}_i = \exp(\mathbf{\Lambda}_i \Delta z_i), \tag{2.93}$$

and the continuity of stress and the vertical component of particle velocity is imposed across the interfaces ($\mathbf{f}_{i+1}^t = \mathbf{f}_i^b$). This is a prescription for the field variables at the top of the $i+1$th interface, given those at the top of the $i$th. This may be written as

$$\mathbf{f}_{i+1}^t = \mathbf{P}_i \mathbf{f}_i^t, \tag{2.94}$$

where $\mathbf{P}_i$ is known as a propagator matrix (Gilbert and Backus, 1966), which, on expanding $\mathbf{C}_i\mathbf{E}_i\mathbf{B}_i$ in (2.92), takes the form

$$\mathbf{P}_i = \begin{bmatrix} \cos(k_{z_i}\Delta z) & \frac{i\omega\rho_i}{k_{z_i}}\sin(k_{z_i}\Delta z) \\ \frac{ik_{z_i}}{\omega\rho_i}\sin(k_{z_i}\Delta z) & \cos(k_{z_i}\Delta z) \end{bmatrix}. \tag{2.95}$$

The matrix $\mathbf{P}$ accounts for propagation of the field variables from one interface to the next. In this way, the field variables at the top of the first layer ($z = z_1$) are related to those at the top of the last layer ($z = z_{N-1}$) by $N-2$ multiplications:

$$\begin{aligned} \mathbf{f}_{N-1}^t &= [\mathbf{C}_{N-2}\mathbf{E}_{N-2}\mathbf{B}_{N-2}][\mathbf{C}_{N-3}\mathbf{E}_{N-3}\mathbf{B}_{N-3}]\ldots[\mathbf{C}_2\mathbf{E}_2\mathbf{B}_2][\mathbf{C}_1\mathbf{E}_1\mathbf{B}_1]\mathbf{f}_1^t \\ &= \prod_{i=1}^{N-2} \mathbf{P}_i \mathbf{f}_1^t, \end{aligned} \tag{2.96}$$

where the $\mathbf{P}$s, in general, are different for each layer.

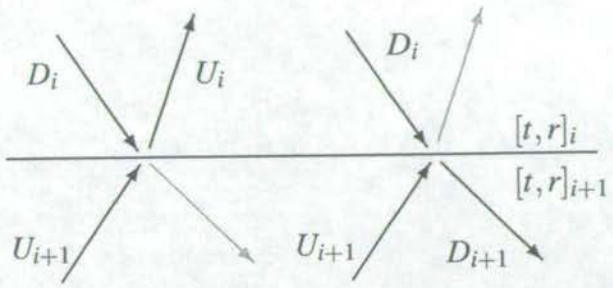


$$U_i = t_{i+1}U_{i+1} + r_i D_i \quad D_{i+1} = r_{i+1}U_{i+1} + t_i D_i$$

Figure 2.4: Upgoing and downgoing waves at a single interface.

### Local reflection coefficients

The matrix (2.95) propagates field variables through a single layer, based on the material properties of that layer. The product of the **P**s in (2.96) propagates pressure and particle velocity across many layers. To understand what happens locally, at the interfaces between the layers, it is necessary to examine the wave variables on either side of a single interface. Multiplication of (2.92) by $\mathbf{B}_{i+1}$ and substituting (2.78) and (2.90) gives

$$\mathbf{e}^t_{i+1} = \mathbf{B}_{i+1}\mathbf{C}_i\mathbf{e}^b_i \tag{2.97}$$

which relates the wave variables at the top of layer $i+1$ to those at the bottom of layer $i$. Consider now the upgoing and downgoing waves which make up the **e**s at a single interface, as shown in Figure 2.4. The reflection and transmission coefficients at the interface are denoted by $r$ and $t$, respectively, with the subscript indicating which side they refer to. The upgoing wave in layer $i$ and the downgoing wave in layer $i+1$ may be expressed in terms of the waves scattered by the interface:

$$\begin{bmatrix} U_i \\ D_{i+1} \end{bmatrix} = \begin{bmatrix} t_{i+1} & r_i \\ r_{i+1} & t_i \end{bmatrix} \begin{bmatrix} U_{i+1} \\ D_i \end{bmatrix}.$$

Rearrangement of this expression, by putting the wave variables from either side of the interface on either side of the equation, gives

$$\begin{bmatrix} U_{i+1} \\ D_{i+1} \end{bmatrix} = \frac{1}{t_{i+1}} \begin{bmatrix} 1 & r_{i+1} \\ r_{i+1} & 1 \end{bmatrix} \begin{bmatrix} U_i \\ D_i \end{bmatrix}, \tag{2.98}$$

(Claerbout, 1976). Now this relates the wave variables on either side of an interface through the reflection and transmission coefficients. Returning to equation (2.97), the product $\mathbf{B}_{i+1}\mathbf{C}_i$ relates the wave variables on either side of the interface. Using (2.73), (2.74) and (2.84) this

product becomes

$$\mathbf{B}_{i+1}\mathbf{C}_i = \frac{1}{2}\begin{bmatrix} 1 & -Z_{i+1} \\ 1 & Z_{i+1} \end{bmatrix}\begin{bmatrix} 1 & 1 \\ -\frac{1}{Z_i} & \frac{1}{Z_i} \end{bmatrix}, \tag{2.99}$$

which may be simplified to give

$$\mathbf{B}_{i+1}\mathbf{C}_i = \frac{Z_i + Z_{i+1}}{2Z_i}\begin{bmatrix} 1 & \frac{Z_i - Z_{i+1}}{Z_i + Z_{i+1}} \\ \frac{Z_i - Z_{i+1}}{Z_i + Z_{i+1}} & 1 \end{bmatrix}. \tag{2.100}$$

Substitution of (2.100) in (2.97) gives

$$\mathbf{e}_{i+1}^t = \frac{Z_i + Z_{i+1}}{2Z_i}\begin{bmatrix} 1 & \frac{Z_i - Z_{i+1}}{Z_i + Z_{i+1}} \\ \frac{Z_i - Z_{i+1}}{Z_i + Z_{i+1}} & 1 \end{bmatrix}\mathbf{e}_i^b, \tag{2.101}$$

which, when compared with (2.98), allows the reflection and transmission coefficients of the interface to be identified. Using (2.84), the reflection coefficient *from below* is

$$r_{i+1} = \frac{\frac{\omega\rho_i}{k_{z_i}} - \frac{\omega\rho_{i+1}}{k_{z_{i+1}}}}{\frac{\omega\rho_i}{k_{z_i}} + \frac{\omega\rho_{i+1}}{k_{z_{i+1}}}} = \frac{\rho_i c_i/\cos\phi_i - \rho_{i+1}c_{i+1}/\cos\phi_{i+1}}{\rho_i c_i/\cos\phi_i + \rho_{i+1}c_{i+1}/\cos\phi_{i+1}}, \tag{2.102}$$

which degenerates to the well-known result for normal incidence when $\phi = 0$. The transmission coefficient for propagation from layer $i+1$ to layer $i$ is

$$t_{i+1} = \frac{2\frac{\omega\rho_i}{k_{z_i}}}{\frac{\omega\rho_i}{k_{z_i}} + \frac{\omega\rho_{i+1}}{k_{z_{i+1}}}} = \frac{2\rho_i c_i/\cos\phi_i}{\rho_i c_i/\cos\phi_i + \rho_{i+1}c_{i+1}/\cos\phi_{i+1}}. \tag{2.103}$$

Equations (2.102) and (2.103) represent *local* properties of the earth. They are unique to a single interface and do not take into account waves elsewhere in the earth.

### Generalised reflection coefficients

A single plane wave incident on a stack of layers gives rise to many plane waves which propagate as upgoing and downgoing plane wave components in the layered system. The layers cause the waves to interfere.

Now suppose a stack of $N-1$ layers is bounded above and below by half-spaces (see Figure 2.5), and that in the upper half-space there is an incident (downgoing) plane wave $I$, and a reflected (upgoing) plane wave $U_0$, while in the lower half-space there is a transmitted (downgoing) plane wave $D_N$ only. Thus, the wave variables, $\mathbf{e}_0^b$ in the upper half-space and

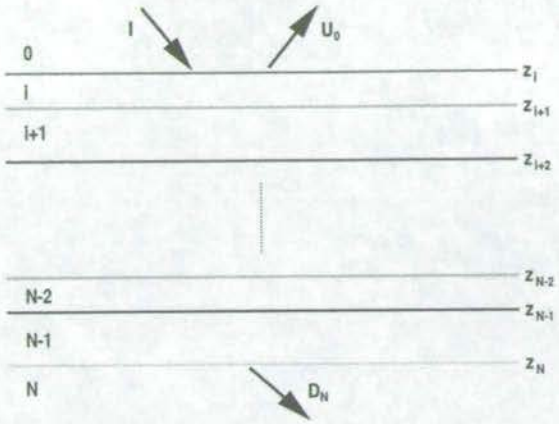


Figure 2.5: A stack of $N-1$ plane layers bounded above and below by half-spaces, in which plane waves propagate.

$\mathbf{e}_N^t$ in the lower half-space, are given by

$$\mathbf{e}_0^b = \begin{bmatrix} U_0 \\ I \end{bmatrix}, \qquad \mathbf{e}_N^t = \begin{bmatrix} 0 \\ D_N \end{bmatrix}. \tag{2.104}$$

The wave variables at the top of layer 1 are related to those at the bottom of half-space 0 by

$$\mathbf{f}_1^t = \mathbf{f}_0^b = \mathbf{C}_0 \mathbf{e}_0^b. \tag{2.105}$$

To propagate the field variables to the top of half-space $N$ requires $N-1$ multiplications. Thus, equation (2.96) becomes

$$\mathbf{f}_N^t = \prod_{i=1}^{N-1} \mathbf{P}_i \mathbf{f}_1^t. \tag{2.106}$$

Premultiplying (2.106) by $\mathbf{B}_N$ and substituting (2.105) gives

$$\mathbf{e}_N^t = \mathbf{B}_N \prod_{i=1}^{N-1} \mathbf{P}_i \mathbf{C}_0 \mathbf{e}_0^b, \tag{2.107}$$

or

$$\mathbf{e}_N^t = \mathbf{Q} \mathbf{e}_0^b, \tag{2.108}$$

where $\mathbf{Q}$ is a 2x2 matrix which accounts for the propagation of the wave variables through all of the layers, from the bottom of the upper half-space to the top of the lower half-space.

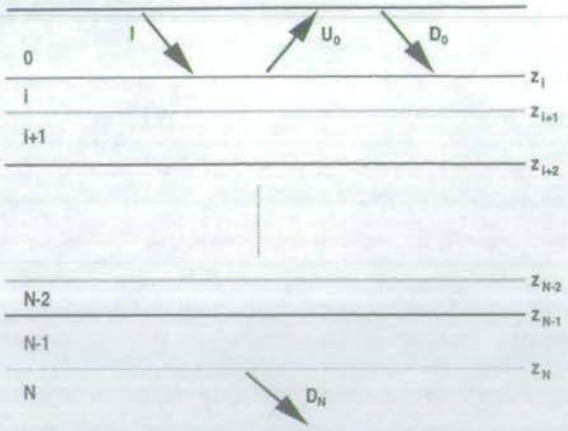


Figure 2.6: A stack of $N-1$ plane layers bounded above by a layer with a free surface and below by a half-space, in which plane waves propagate.

Substitution of (2.104) in (2.108) yields

$$\begin{bmatrix} 0 \\ D_N \end{bmatrix} = \begin{bmatrix} \mathrm{Q}_{11} & \mathrm{Q}_{12} \\ \mathrm{Q}_{21} & \mathrm{Q}_{22} \end{bmatrix} \begin{bmatrix} U_0 \\ I \end{bmatrix}, \tag{2.109}$$

from which it may be deduced that

$$U_0 = -\frac{\mathrm{Q}_{12}}{\mathrm{Q}_{11}} I = R_g I, \tag{2.110}$$

and

$$D_N = \left( \mathrm{Q}_{22} - \frac{\mathrm{Q}_{12}\mathrm{Q}_{21}}{\mathrm{Q}_{11}} \right) I = T_g I. \tag{2.111}$$

in which, $R_g$ and $T_g$ are the generalised reflection and transmission coefficients, respectively. They can be calculated knowing the material properties of all the layers. They are more difficult to compute than the local reflection and transmission coefficients because they are *global*, and account for the effect of the whole layer stack at once.

The generalised reflection coefficient $R_g$ is described later in the thesis as the *reflection response* of the earth. It is defined by (2.110) in a stack of layers between two half-spaces. To relate these results to what follows later in the thesis, assume that the upper half-space is water. Equation (2.110) then defines the earth's reflection response in the absence of a sea surface.

### Introducing a free surface

When the stack of layers is bounded by a water layer with a free surface, there are upgoing $U_0$ and downgoing $D_0$ scattered plane waves in the upper layer, as well as the incident plane wave

$I$, as shown in Figure 2.6. The upgoing and downgoing waves both contain the sea surface multiples. In this case the generalised reflection coefficient of the stack of layers is defined by

$$R_g = \frac{U_0}{I + D_0}, \tag{2.112}$$

which is a function of $(k_x, k_y, z, \omega)$. In the presence of a sea surface, the wave variables, $\mathbf{e}_0^b$ in the upper water layer and $\mathbf{e}_N^t$ in lower half-space, are

$$\mathbf{e}_0^b = \begin{bmatrix} U_0 \\ I + D_0 \end{bmatrix}, \qquad \mathbf{e}_N^t = \begin{bmatrix} 0 \\ D_N \end{bmatrix}. \tag{2.113}$$

Substitution of (2.113) in (2.108), yields

$$\begin{bmatrix} 0 \\ D_N \end{bmatrix} = \begin{bmatrix} \mathsf{Q}_{11} & \mathsf{Q}_{12} \\ \mathsf{Q}_{21} & \mathsf{Q}_{22} \end{bmatrix} \begin{bmatrix} U_0 \\ I + R_0 U_0 \end{bmatrix}, \tag{2.114}$$

where $D_0 = R_0 U_0$ at the surface, and $R_0$ is the sea surface reflection coefficient (assumed to be $-1$). It follows from (2.114) that the generalised reflection coefficient $R_g^*$ in the presence of the sea surface is

$$R_g^* = -\frac{\mathsf{Q}_{12}}{\mathsf{Q}_{11} + R_0 \mathsf{Q}_{12}}. \tag{2.115}$$

Equation (2.115) expresses the reflection response in terms of the layer parameters. Equally, in terms of the plane waves, the response in the presence of the free surface is defined by

$$R_g^* = \frac{U_0}{I}, \tag{2.116}$$

which is essentially a deconvolution by the source term. Dividing the definitions for $R_g$ and $R_g^*$ given by (2.110) and (2.115), the reflection response in the presence of the sea surface may be expressed as a function of the reflection response in the absence of the sea surface, and vice-versa:

$$\begin{aligned} R_g^* &= \frac{R_g}{1 - R_0 R_g} = R_g(1 + R_0 R_g + (R_0 R_g)^2 + (R_0 R_g)^3 + \ldots), \\ R_g &= \frac{R_g^*}{1 + R_0 R_g^*} = R_g^*(1 - R_0 R_g^* + (R_0 R_g^*)^2 - (R_0 R_g^*)^3 + \ldots). \end{aligned} \tag{2.117}$$

These relations were derived by Koehler and Taner (1977) for vertically-propagating waves in a stack of homogeous layers. The factor $\frac{1}{1-R_0 R_g}$ generates the multiples in the reflection response, and $\frac{1}{1+R_0 R_g^*}$ removes them. When there is no free surface, $R_0 = 0$ and there are no multiples.

## 2.5 Conclusions

This chapter of basic theory provides the foundations of wave propagation in acoustic media used later in the thesis. The main points covered are: (1) derivation of the acoustic wave equation in the time domain; (2) decomposition of spherical waves into plane waves and cylindrical waves; (3) derivation of the acoustic wave equation for pressure and particle velocity in the frequency domain. (4) Manipulation of the acoustic wavefield in plane wave components within a stack of layers to: (5) extract upgoing and downgoing waves as separate solutions of the one-way wave equation; (6) derive the local reflection and transmission coefficients at an interface separating two plane layers; and (7) derive expressions for the generalised reflection and transmission coefficients of the whole stack.

# THE MARINE SEISMIC SOURCE

*Chapter 3*

## 3.1 Introduction

The seismic source is one of the most important elements of the seismic reflection method. Without it, there would be no reflections. This chapter discusses the marine seismic source. The most commonly-used marine seismic source is the airgun (Ewing & Zaunere, 1964). It has been in commerical use in the U.S. since 1966 (Giles, 1968). The mechanics of how this source produces sound waves has evolved from the study of sources which were first used on land. The original marine seismic source was dynamite, which, on land, is a very impulsive source. At sea, however, due to the displacement of water by the explosion, a long and complicated signal is produced due to oscillation of the resulting bubble of air produced.

Marine surveys were conducted between the 40s and 60s using dynamite as a sound source (Lugg, 1979). In practice, explosive charges were placed near to the surface, to dissipate the energy produced by the explosion (by venting at the surface) after the initial peak in pressure due to the passing shock wave. This practice was damaging to marine life, which was the main reason for developing alternative sound sources. Experimental studies (Lavergne, 1970) showed that smaller charges at greater depths below the surface could produce as much energy in the seismic bandwidth as the commonly-used larger charges at shallow depth, and with less environmental impact. This was due to less destructive interaction between the free surface (ghost) reflection and the direct pulse, but at the expense of generating bubble oscillations.

A large study of underwater explosions (Kramer *et al.*, 1968) provides a good qualitative description of bubble oscillations, although the physics of the bubble behaviour has never been fully explained. The purpose of this chapter is to describe how the bubble oscillations produced by a marine seismic source such as an airgun act as a source of seismic energy.

First, the chapter begins with a brief description of the mechanical operation of an airgun. Second, follows a derivation of the exact non-linear wave equation. Third, I derive the equation of motion of an oscillating bubble under various approximations, to obtain a solution to the wave equation which provides expressions for the pressure and particle velocity in the water. The solution (after Ziolkowski, 1998) retains the essential features of the fluid flow near to the bubble wall and the linear acoustic approximation far from it. An examination of the different zones of wave propagation produced by an oscillating bubble reveals the requisite measurements to describe fully the acoustic output of the source. Finally, the effect of combining many airguns into an array is examined. Since this is the mode of deployment

of the airgun as a practical sound source, the chapter ends with an explanation of the extra complexity that this introduces.

## 3.2 The operation of an airgun

An airgun produces sound waves by rapidly ejecting compressed air, typically at pressures of 2,000 psi (14 MPa), into the surrounding water. A diagram of an airgun is given in Figure 3.1. The upper chamber (UC) fills with air from the top of the gun, then passes through an orifice in the centre of the shuttle to fill the lower chamber (LC). Because the tiggering piston (TP) is larger than the firing piston (FP), the gun remains closed due to the net downward force. A solenoid valve, once opened, allows high pressure air to hit the underside of TP which is sufficient to upset the force balance on the two pistons. The air in the LC forces the shuttle upwards past the gun ports, and the air races out into the water. In the cross-section of Figure 3.1, two ports out of four are visible.

The explosive discharge of the air into the water creates the initial pressure pulse due to the displacement of the surrounding water. The pressure difference which develops between the inside and the outside of "the bubble" drives a series of bubble oscillations in expansion and contraction which continue until the bubble pressure is in equilibrium with the water. These bubble oscillations reinforce the low frequency seismic energy which is used to image the earth, since the high frequencies in the initial sharp pulse are attenuated by the earth.

## 3.3 The wavefield of an oscillating bubble

The particle motion produced by a bubble oscillating in water causes a pressure build-up and acoustic waves to be radiated. The interest in this thesis is in how to make measurements of the pressure to characterise the source of the acoustic waves. To do so involves understanding any linear and non-linear behaviour of the particle motion which produces pressure waves in the water. A description of the wavefield in the water is possible by considering the elementary motion of the fluid particles.

In the following analysis, the effect of gravity is neglected, and a single bubble is considered, oscillating in an infinite volume of water as shown in Figure 3.2. The bubble is assumed to be spherical and small, at the wavelengths of sound generated. This is in contrast to the real bubble, which at optical wavelengths can be more irregular as indicated in Figure 3.2. The pressure within the bubble is assumed to be uniform, and is denoted by $P_B(t)$; outside the bubble, it is governed by the fluid flow and the acoustic radiation ahead of the bubble wall. The pressure is continuous at the bubble wall, but the pressure gradient is not. The bubble radius is denoted by $R(t)$, and the bubble wall velocity, by $\dot{R}(t)$. The pressure and particle velocity are measured at a distance $r$ from the centre of the bubble (gun ports).

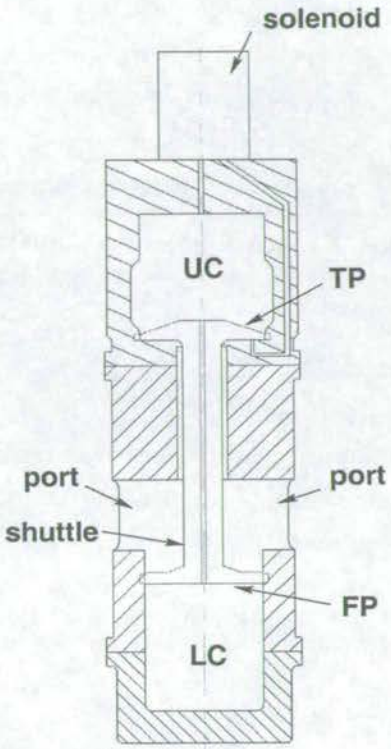


Figure 3.1: Section through an airgun (courtesy of Bolt Technology Corporation), primed ready to fire.

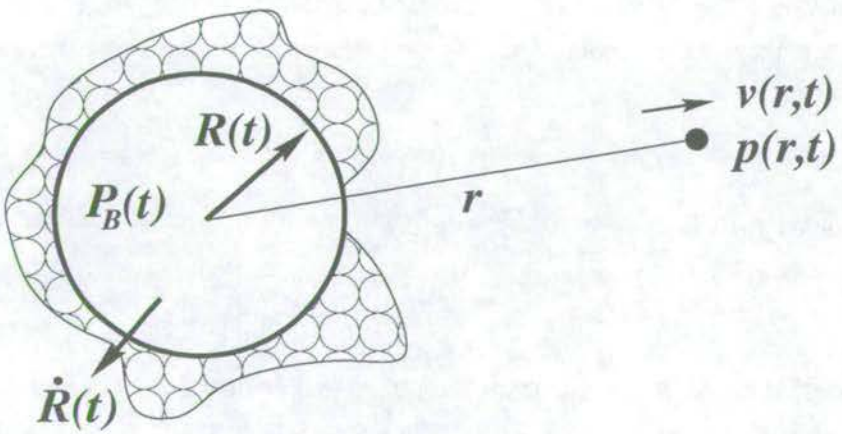


Figure 3.2: Schematic of the bubble model at an instant $t$ of time.

### Frames of reference

It was noted in chapter 2 (page 13) that in Eulerian and Lagrangian frames of reference, temporal derivatives are equal only if the amplitude of the particle displacement is small compared with the wavelength of the spatial disturbance it produces. This is satisfied in a linearised theory of motion. It is not satisfied by the motion very close to the bubble wall.

In the Lagrangian description, which follows the particle motion, the (total) temporal derivative is denoted by

$$\frac{\mathrm{d}}{\mathrm{d}t} = \frac{\mathrm{D}}{\mathrm{D}t} = \frac{\partial}{\partial t} + v\frac{\partial}{\partial r}. \tag{3.1}$$

In the Eulerian description, which is fixed in space with respect to the particle motion, the (partial) temporal derivatives are simply $\frac{\partial}{\partial t}$. Thus, the Eulerian and Lagrangian derivatives are related by the chain rule, with $v = \frac{\partial r}{\partial t}$.

### Non-linear wave equation

The fluid is assumed to be inviscid and the motion is spherically symmetric. The flow is therefore irrotational, and the radial velocity, $v$, is the gradient of a particle velocity potential $\varphi$ (Lamb, 1923),

$$v = -\frac{\partial \varphi}{\partial r}, \tag{3.2}$$

where the minus sign indicates $\varphi$ is the potential that *starts* the flow $v$ from rest. The exact equation of motion for spherical waves was first derived by Lamb (1923). Following his steps, the pressure in the water is a definite function of the density, such that the enthalpy is

$$h = \int_{p_\infty}^{p} \frac{\mathrm{d}p}{\rho} = \int_{\rho_\infty}^{\rho} c^2 \frac{\mathrm{d}\rho}{\rho}, \tag{3.3}$$

where $p_\infty$ and $\rho_\infty$ are the undisturbed pressure and density, respectively, in the water, and

$$c^2 = \frac{\mathrm{d}p}{\mathrm{d}\rho}. \tag{3.4}$$

Since the flow is radial, all equations are expressed in spherical polar coordinates. The principle of conservation of mass gives rise to the equation of continuity,

$$\frac{1}{\rho}\left(\frac{\partial \rho}{\partial t} + v\frac{\partial \rho}{\partial r}\right) = -\nabla \mathbf{v} \tag{3.5}$$

which, upon substitution of (3.4), becomes

$$\frac{1}{\rho}\left(\frac{\partial p}{\partial t}+v\frac{\partial p}{\partial r}\right)=-c^2\left(\frac{\partial v}{\partial r}+\frac{2v}{r}\right). \tag{3.6}$$

The two terms on the right-hand side arise from the divergence of the radial velocity. The second of the terms on the left-hand side is due to the frame of reference. This convective term arises from the Lagrangian, total, derivative of pressure with respect to time, of a point moving with the fluid. Equation (3.6) is known as the kinematic equation.

The principle of conservation of momentum is expressed by Newton's second law of motion, and gives rise to the equation of motion,

$$\frac{\partial v}{\partial t}+v\frac{\partial v}{\partial r}=-\frac{1}{\rho}\frac{\partial p}{\partial r}. \tag{3.7}$$

The integral of equation (3.7) is a form of Bernoulli's equation, and is called the dynamic equation. Carrying out the integration from $r$ to $\infty$, and substituting for (3.2) and (3.3), gives

$$\frac{\partial \varphi}{\partial t}-\frac{v^2}{2}=h=\frac{\partial \varphi}{\partial t}-\frac{1}{2}\left(\frac{\partial \varphi}{\partial r}\right)^2, \tag{3.8}$$

where $\varphi=0$, and $v=0$ at $\infty$. The partial derivatives of (3.8) with respect to $t$ and $r$ are

$$\frac{\partial h}{\partial t}=\frac{\partial^2\varphi}{\partial t^2}-\left(\frac{\partial \varphi}{\partial r}\right)\frac{\partial^2\varphi}{\partial t\partial r}, \qquad \frac{\partial h}{\partial r}=\frac{\partial^2\varphi}{\partial t\partial r}-\left(\frac{\partial \varphi}{\partial r}\right)\frac{\partial^2\varphi}{\partial r^2}. \tag{3.9}$$

Substitution of (3.9) into (3.6) yields the exact non-linear wave equation for radial flow in terms of the velocity potential,

$$\frac{\partial^2\varphi}{\partial t^2}-2\frac{\partial \varphi}{\partial r}\frac{\partial^2\varphi}{\partial r\partial t}+\left(\frac{\partial \varphi}{\partial r}\right)^2\frac{\partial^2\varphi}{\partial r^2}=c^2\left(\frac{\partial^2\varphi}{\partial r^2}+\frac{2}{r}\frac{\partial \varphi}{\partial r}\right). \tag{3.10}$$

It was first derived by Lamb (1923) and has no (known) analytical solution. To find a solution requires approximations. Equation (3.10) may be rewritten in the following form (with $v^2=(\frac{\partial \varphi}{\partial r})^2$)

$$\frac{\partial^2\varphi}{\partial r^2}\left(1-\frac{v^2}{c^2}\right)+\frac{2}{r}\frac{\partial \varphi}{\partial r}\left(1+\frac{r}{c^2}\frac{\partial^2\varphi}{\partial r\partial t}\right)-\frac{1}{c^2}\frac{\partial^2\varphi}{\partial t^2}=0, \tag{3.11}$$

where the non-linear terms are now obvious in the brackets as higher-order corrections to the particle motion. If the velocity of the fluid is small compared with the velocity of sound, the higher-order terms are small compared with the rest of the terms in the equation.

### Linear acoustic approximation

Linearisation of equation (3.10) is achieved by assuming infinitely small particle motions. The non-linear (convective) terms in the Lagrangian derivatives in (3.6) & (3.7) are therefore zero, which implies that the total derivative following the particle motion is the same as the partial derivative fixed in space. The linearised mass, momentum and dynamic equations are then

$$\frac{1}{\rho}\frac{\partial p}{\partial t} = -c^2\left(\frac{\partial v}{\partial r} + \frac{2v}{r}\right), \qquad \frac{\partial v}{\partial t} = -\frac{1}{\rho}\frac{\partial p}{\partial r}, \qquad \frac{\partial \varphi}{\partial t} = h. \tag{3.12}$$

Eliminating $h$ between the dynamic and kinematic equations yields the linearised (inexact) wave equation,

$$\frac{\partial^2 \varphi}{\partial t^2} = c^2\left(\frac{\partial^2 \varphi}{\partial r^2} + \frac{2}{r}\frac{\partial \varphi}{\partial r}\right), \tag{3.13}$$

which may be written as

$$\frac{\partial^2 (r\varphi)}{\partial t^2} = c^2\left(\frac{\partial^2 (r\varphi)}{\partial r^2}\right). \tag{3.14}$$

The well-known solution to this equation is

$$\varphi = \frac{1}{r} f\left(t - \frac{r}{c}\right), \tag{3.15}$$

where $f(r,t)$ is some unknown wave function, and the solution for inward-travelling waves has been excluded using the Sommerfeld radiation condition. The solution states that the quantity $r\varphi$ propagates outwards with fixed velocity $c$ and constant amplitude.

The approximation of seeking a velocity potential which satisfies the linear acoustic wave equation was addresed by Lamb (1923). By considering the incompressible flow approximation, he found that the higher-order terms required in equation (3.11) are negligible for the pressures used today in air guns (Ziolkowski, 1998). Therefore, (3.15) is a good approximation to the true velocity potential at large distances from the origin, from which a description of the acoustic radiation may be derived.

At small distances from the source, the linear acoustic approximation is inadequate. To see this, assume that the quantity $r\frac{\partial \varphi}{\partial t}$ propagates outwards with fixed velocity $c$ and constant amplitude. Therefore, from (3.15) it follows that

$$\frac{\partial}{\partial t}\left(r\frac{\partial \varphi}{\partial t}\right) = f''\left(t - \frac{r}{c}\right) = -c\frac{\partial}{\partial r}\left(r\frac{\partial \varphi}{\partial t}\right), \tag{3.16}$$

where $'$ denotes differentiation w.r.t. the argument. Using equations (3.3) and (3.12), and

observing that linearisation has made the partial and total derivatives equivalent, (3.16) gives

$$r\frac{\mathrm{D}v}{\mathrm{D}t} = \frac{r}{c}\frac{\mathrm{D}h}{\mathrm{D}t} + h \tag{3.17}$$

for the equation of motion of the fluid. At the bubble wall, where $r = R$, this becomes

$$R\ddot{R} = \frac{R}{c}\dot{H} + H, \tag{3.18}$$

where $H = \frac{p_B - p_\infty}{\rho_\infty}$, and the overdot indicates the time differential following the particle motion. The terms on the right relate to the bubble. The first of these is the radiated acoustic energy, and the second is the pressure, or potential energy, in the bubble. The term on the left is the potential energy of the water. In the linear acoustic approximation, the water has no kinetic energy, there are no oscillations, and the bubble continues to expand. Thus, a description of the fluid flow is required to explain the bubble oscillations.

### Non-linear fluid flow

The linear acoustic approximation is generally assumed when dealing with conventional marine seismic data which records the acoustic wavefield at large distances from the bubble origin. In this regime the particle velocities are small and the recorded data approximately obey the linear acoustic wave equation.

To understand the physics of the oscillating bubble, which is necessary to make meaningful measurements very close to the bubble origin, it is necessary to describe the fluid flow. This is a contentious issue, and has seen publication of many models for the fluid compressibility which governs how a disturbance is propagated through the fluid. Knowledge of the compressibility is important close to the bubble wall where the particle velocity is highest. A good explanation of these models is provided by Knapp *et al.* (1970).

### Incompressible flow approximation

The original work was done by Rayleigh (1917) when he considered the collapse of a spherical cavity, using the assumption of an incompressible fluid. The density is constant in an incompressible fluid, particles propagate instantaneously, and the velocity of sound is infinite. Therefore, no sound waves are radiated and the bubble oscillations go on forever. However, the theory provides a good description of the fluid flow close to the bubble.

Using the incompressible flow approximation, the equation of motion of the bubble wall is derived below. The continuity equation, which expresses fluid compressibility, becomes

$$\frac{1}{\rho}\left(\frac{\partial \rho}{\partial t} + v\frac{\partial \rho}{\partial r}\right) = 0 = \frac{\partial v}{\partial r} + \frac{2v}{r}, \tag{3.19}$$

which may be integrated to find an expression for the particle velocity,

$$v = \frac{F(t)}{r^2} = -\frac{\partial \varphi}{\partial r}, \tag{3.20}$$

where $F(t)$ is some function of time. Further integration yields the particle velocity potential,

$$\varphi = \frac{F(t)}{r}. \tag{3.21}$$

The unknown time function is obtained from (3.20), substituting $r = R$

$$F(t) = R^2 \dot{R}, \tag{3.22}$$

so that the particle velocity has the correct value at the bubble wall,

$$v = \frac{R^2 \dot{R}}{R^2} = \dot{R}. \tag{3.23}$$

The derivative of the bubble radius, $\dot{R}$, is taken on the moving bubble wall, and is necessarily the total derivative. $F(t)$ is related to the bubble volume $V_B$ by

$$F(t) = \frac{\mathrm{D}}{\mathrm{D}t}\left(\frac{R^3}{3}\right) = \frac{1}{4\pi}\frac{\mathrm{d}V_B}{\mathrm{d}t} \tag{3.24}$$

where $V_B = \frac{4}{3}\pi R^3$. Thus, by comparing equations (3.15) and (3.21), it is clear that for the incompressible flow approximation $F(t) = f(t)$.

Substituting (3.20) & (3.21) for $v$ and $\varphi$ into the dynamic equation, (3.8), and using (3.3) and (3.22) gives

$$\frac{R^2\ddot{R} + 2R\dot{R}^2}{r} - \frac{R^4\dot{R}^2}{2r^4} = \frac{P_B - p_\infty}{\rho_\infty}, \tag{3.25}$$

which is the equation of motion of the fluid. At the bubble wall, where $r = R$, it becomes

$$R\ddot{R} + \frac{3\dot{R}^2}{2} = \frac{P_B - p_\infty}{\rho_\infty}. \tag{3.26}$$

This equation of motion of the bubble wall was first derived by Rayleigh (1917). The second term on the left is the kinetic energy of the water, which causes the oscillations. Note, however, that there is no radiated energy term on the right, and no sound waves are generated. It is therefore difficult to reconcile this approximation of the particle motion with the linear acoustic approximation, which is itself a good description at large distances from the bubble.

### Non-linearly compressible flow approximation

It is desirable to have a description of the fluid flow close to the bubble which is valid to the same level of accuracy as the linear acoustic approximation far from the bubble. For then, there is a smooth transition from one theory to the other.

The analysis presented here is used in Trilling (1952) and Ziolkowski (1998) to get expressions for the particle velocity and pressure fields in the water. The model of Ziolkowski (1998) described below, which he terms the non-linear acoustic approximation, links the description of the bubble oscillations to the acoustic radiation with the same set of approximations.

The particle velocity potential which satisfies the linear acoustic approximation, given by (3.15), propagates outwards with constant velocity $c$. In this non-linearly compressible approximation, the time derivative of the particle velocity potential is also assumed to propagate outwards with constant velocity $c$. Its value is found from the non-linear dynamic equation (3.8),

$$\frac{\partial \varphi}{\partial t} = \frac{1}{r} f'\left(t - \frac{r}{c}\right) = h + \frac{v^2}{2}. \tag{3.27}$$

Therefore, as in the linear acoustic case,

$$\frac{\partial}{\partial t}\left(r\frac{\partial \varphi}{\partial t}\right) = f''\left(t - \frac{r}{c}\right) = -c\frac{\partial}{\partial r}\left(r\frac{\partial \varphi}{\partial t}\right). \tag{3.28}$$

Substitution from (3.27) in (3.28) and taking the derivatives yields

$$rv\frac{\partial v}{\partial t} + r\frac{\partial h}{\partial t} + \frac{cv^2}{2} + crv\frac{\partial v}{\partial r} + ch + cr\frac{\partial h}{\partial r} = 0. \tag{3.29}$$

This equation is expressed in terms of (Eulerian) partial derivatives fixed in space. To describe the motion of the fluid requires (Lagrangian) total derivatives following the particle motion. Using the following expressions,

$$\frac{\mathrm{D}h}{\mathrm{D}t} = \frac{\partial h}{\partial t} + v\frac{\partial h}{\partial r}, \qquad \frac{\mathrm{D}v}{\mathrm{D}t} = \frac{\partial v}{\partial t} + v\frac{\partial v}{\partial r}, \tag{3.30}$$

and equations (3.6) and (3.7), equation (3.29) may be expressed as

$$r\frac{\mathrm{D}v}{\mathrm{D}t}\left(1 - \frac{2v}{c}\right) + \frac{3}{2}v^2\left(1 - \frac{4v}{3c}\right) = \frac{r}{c}\frac{\mathrm{D}h}{\mathrm{D}t}\left(1 - \frac{v}{c} + \frac{v^2}{c^2}\right) + h, \tag{3.31}$$

which is the equation of motion of the fluid incorporating compressibility. When the equation is evaluated at the bubble wall with $h = \frac{p_B - p_\infty}{\rho_\infty}$, the equation derived by Trilling (1952) results. However, he went on to make further approximations and never used it in this form. For the peak pressures experienced with conventional airguns, $\frac{v}{c}$ is small so the $\frac{v^2}{c^2}$ term may be

neglected (Ziolkowski, 1998). At the bubble wall, where $r = R$, this becomes

$$R\ddot{R}\left(1-\frac{2\dot{R}}{c}\right)+\frac{3}{2}\dot{R}^2\left(1-\frac{4\dot{R}}{3c}\right)=\frac{R}{c}\dot{H}\left(1-\frac{\dot{R}}{c}\right)+H, \tag{3.32}$$

where the enthalpy at the bubble wall is found from the dynamic equation

$$H(t)=\frac{\partial\varphi}{\partial t}-\frac{v^2}{2}. \tag{3.33}$$

Equation (3.33) links the enthalpy at the bubble wall arising from the oscillations to the wave function (3.15) obeying the linearised wave equation, and the acoustic propagation in the water. From equation (3.32) an expression for the particle acceleration at the bubble wall, $\ddot{R}$, may be derived. In the absence of compressibility, (3.32) reduces to Rayleigh's result (3.26). When it is linearised, it reduces to (3.18).

### Pressure and particle velocity

The particle velocity in the water is found by substituting the linear acoustic solution (3.15) into the particle velocity potential defined by equation (3.2),

$$v(r,t)=-\frac{\partial\varphi}{\partial r}=\frac{1}{rc}f'\left(t-\frac{r}{c}\right)+\frac{1}{r^2}f\left(t-\frac{r}{c}\right). \tag{3.34}$$

The enthalpy at a point in the water is found from the non-linear dynamic equation (3.8), using the wave function which satisfies the linear acoustic approximation (3.15). The pressure is obtained from the enthalpy by assuming that the density is constant, to give

$$\frac{p_b(r,t)-p_\infty}{\rho}\doteq\frac{\partial\varphi}{\partial t}-\frac{v^2}{2} \tag{3.35}$$

where $p_b(r,t)$ is the pressure in the water caused by the oscillating bubble and $p_\infty$ is hydrostatic pressure. This assumption, though not at all necessary, is consistent with the level of accuracy that the non-linear acoustic approximation gives (Ziolkowski, 1998). Denoting the pressure difference in the water simply by $p(r,t)$ gives

$$\frac{p(r,t)}{\rho}=\frac{1}{r}f'\left(t-\frac{r}{c}\right)-\frac{v^2(r,t)}{2}. \tag{3.36}$$

## 3.4 The zones of propagation of a monopole source

The oscillating bubble produced by an airgun may be several tens of centimetres in diametre, at its maximum. At optical wavelengths it may not appear spherical. However, the wavelengths of sound generated by such a bubble are of the order of tens of metres, for an upper frequency of 125 Hz. The bubble is small compared with the wavelengths of sound it ra-

diates. It behaves as a monopole source, and, consequently, has a spherically-symmetric radiation pattern. From section 3.3 it is clear that the wavefield of a monopole source has linear and non-linear zones of wave propagation. By considering the pressure and the particle velocity, and the relative influence of the terms they comprise, three distinct regimes of wave propagation may be defined: non-linear near field, linear near field and far field.

### The non-linear near field or "zero" field

The zone closest to the bubble wall is where the particle velocities are highest, and a linear theory of wave propagation is inadequate. A complete description of the wavefield in this zone of non-linear propagation requires measurements of both the pressure and the particle velocity,

$$p(r,t) = \frac{\rho}{r} f'\left(t - \frac{r}{c}\right) - \frac{\rho v^2(r,t)}{2}, \tag{3.37}$$

$$v(r,t) = \frac{1}{rc} f'\left(t - \frac{r}{c}\right) + \frac{1}{r^2} f\left(t - \frac{r}{c}\right). \tag{3.38}$$

The non-linear zone is known as the "zero" field (Walter, pers. comm.; Ziolkowski, 1999). In the zero field, the non-linear pressure term represents "afterflow" (Cole, 1948), which is a consequence of the bubble oscillations moving the water back and forth.

A measurement in the zero field may be anywhere between the centre of the bubble and approximately 1m. A measurement made inside the bubble, as opposed to in the water, must make use of the equation of motion of the bubble (3.32) to describe the pressure on the bubble wall, and hence in the water. This is discussed in more detail in an example with some experimental data in chapter 6.

### The linear near field

At about 1m from the bubble origin, the linear near field begins. At this distance, the particle velocities are moderate enough to allow the linear acoustic approximation to describe the motion adequately. The pressure propagates linearly and is composed of a single term,

$$p(r,t) = \frac{\rho}{r} f'\left(t - \frac{r}{c}\right). \tag{3.39}$$

The particle velocity, however, is still composed of two terms,

$$v(r,t) = \frac{1}{rc} f'\left(t - \frac{r}{c}\right) + \frac{1}{r^2} f\left(t - \frac{r}{c}\right). \tag{3.40}$$

The second term on the right, inversely proportional to the square of the radius, is more important closer to the source than the first term, which decays linearly with distance. Transformation of equation (3.40) to the frequency domain (noting that $\frac{\partial}{\partial t} \mapsto -i\omega$ with the present conventions) gives

$$V(r,\omega) = F(\omega)\left[\frac{-i\omega}{rc} + \frac{1}{r^2}\right]\exp\left(i\omega\frac{r}{c}\right), \tag{3.41}$$

from which it is clear that the two terms are 90° out of phase. The particle velocity may be written in terms of the pressure, by transforming (3.39) to the frequency domain

$$P(r,\omega) = \frac{-i\omega\rho}{r}F(\omega)\exp\left(i\omega\frac{r}{c}\right), \tag{3.42}$$

and substituting it in (3.41) to give

$$V(r,\omega) = \frac{P(r,\omega)}{\rho c}\left(1 + \frac{i\lambda}{2\pi r}\right). \tag{3.43}$$

The two terms in the particle velocity are therefore equal when $r = \frac{\lambda}{2\pi}$. The linear near field exists where the out-of-phase term is significant, which is for distances up to about one wavelength. In the linear near field, the particle velocity is constantly changing shape with distance from the source; the pressure simply scales inversely with distance.

A point source is therefore completely characterised by a pressure measurement at a known distance in the linear near field; the pressure elsewhere may be extrapolated knowing the geometry. (In fact, the particle velocity in the far field may be evaluated from a pressure measurement in the near field (see below).) A measurement of particle velocity, however, records a mix of two components—the wave function and its derivative. It does not allow the pressure or the particle velocity to be calculated elsewhere, without additional information.

### The far field

At distances greater than about one wavelength, the pressure and the particle velocity propagate linearly, and are very nearly in phase with each other. They are each composed of one term only,

$$p(r,t) = \frac{\rho}{r}f'\left(t - \frac{r}{c}\right), \tag{3.44}$$

$$v(r,t) = \frac{1}{rc}f'\left(t - \frac{r}{c}\right). \tag{3.45}$$

Thus, if either the particle velocity or the pressure is measured, the other may be calculated elsewhere in the far field, knowing the distance $r$ and the material properties of water, $c$ and

$\rho$.

## 3.5 The airgun array

The bubble oscillations produced by an underwater source result in a pressure signature which is long and complicated. In the frequency domain this is manifested by peaks and notches in the amplitude spectrum, as shown in Figure 3.3. Any single bubble has a characteristic period of oscillation which is a function of its initial conditions.

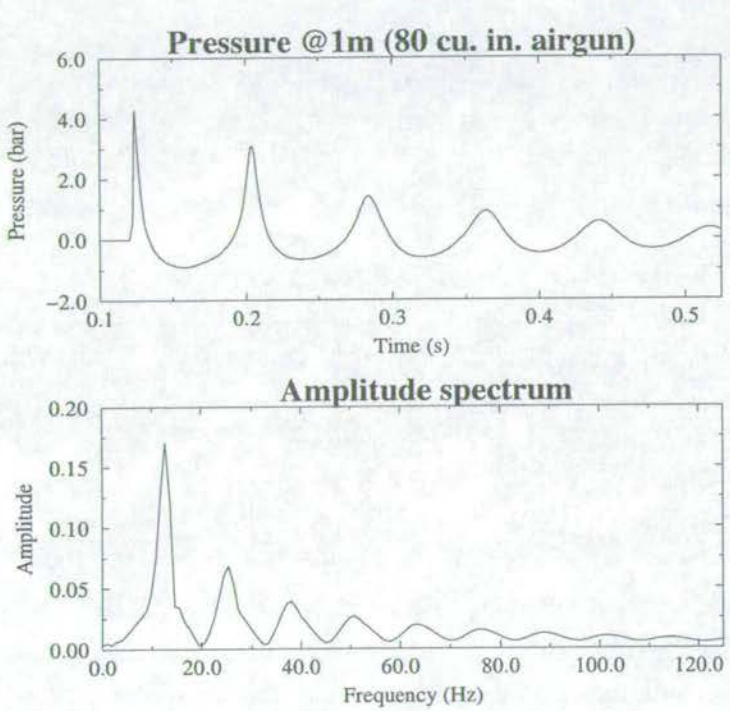


Figure 3.3: (a) The pressure measured by the oscillating bubble produced by an 80 cu. in. airgun fired at 5m depth and 2000 psi. (b) The amplitude spectrum of (a) containing the peaks and notches produced by the oscillations.

Rayleigh (1917), when considering the problem of a spherical bubble in an incompressible fluid, derived the time of collapse of the bubble. Equation (3.26), written again here for convenience,

$$R\ddot{R} + \frac{3\dot{R}^2}{2} = \frac{P_B - p_\infty}{\rho_\infty}, \tag{3.46}$$

may be integrated to give

$$R^3\dot{R}^2 = \frac{2}{3}\frac{p_\infty}{\rho_\infty}(R_m^3 - R^3), \tag{3.47}$$

where $R_m$ is the maximum bubble radius, and it is assumed that $P_B = 0$. Denoting $\dot{R}$ by $\frac{dR}{dt}$, the equation may be integrated further to yield the time to collapse $t_c$,

$$t_c = 0.915 R_m \left( \frac{\rho_\infty}{p_\infty} \right)^{\frac{1}{2}}. \tag{3.48}$$

Assuming the time to collapse is the same as the time of expansion, as it is in an incompressible fluid, the period of bubble oscillation $T = 2t_c$. Willis (1941), when considering underwater explosions, proposed that the potential energy $E_p$ of a spherical cavity is proportional to its radius $R_m$ and the hydrostatic pressure:

$$E_p = \frac{4}{3} \pi R_m^3 p_\infty. \tag{3.49}$$

Substituting for $R_m$ from (3.49) in (3.48) for an expansion-contraction cycle yields the Rayleigh-Willis formula

$$T = 1.14 \rho^{\frac{1}{2}} E_p^{\frac{1}{3}} p_\infty^{-\frac{5}{6}}. \tag{3.50}$$

Now, further assuming that $E_p$ is proportional to the pressure $P_G$ and volume $V_G$ of air in the gun yields the modified Rayleigh-Willis formula. This is

$$T = \kappa P_G^{\frac{1}{3}} V_G^{\frac{1}{3}} p_\infty^{-\frac{5}{6}}, \tag{3.51}$$

where $\kappa$ is a constant which depends on the units used for the quantities in the equation, and is related to the source of the oscillations. The important point for airguns, is that the bubble period scales as the cube root of the gun volume.

Thus, if guns of varying volumes are fired at the same depth and pressure, their bubble oscillations interfere destructively, while the initial peaks interfere constructively. The principle is illustrated in the time domain in Figure 3.4. This is know as "tuning", and has been employed in airgun arrray design since the 70s (Giles & Johnston, 1973). The result in the frequency domain is that peaks in the amplitude spectrum of one gun fill in the notches of another, such that the combined effect tends towards a flatter amplitude spectrum over the bandwidth of interest. Typically, guns are arranged in a linear or areal array.

## 3.6 The zones of propagation of an extended source

An airgun array can be considered to be an extended source (distinct from a monopole source) if its largest dimension is of the same order as the wavelength of sound it radiates. The radiation pattern from an extended source is not spherically symmetric, but is, in general, angle- and frequency-dependent. The zones of propagation for an extended source are defined

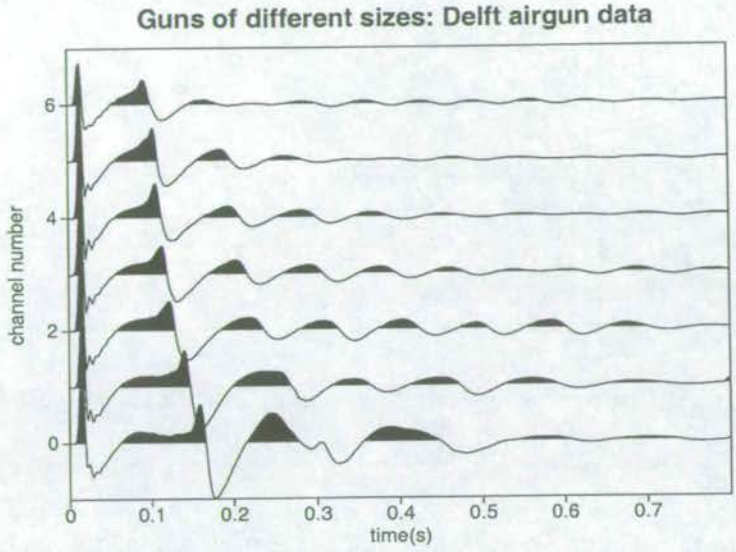


Figure 3.4: The pressure signatures from seven airguns in an array whose volumes increase from top to bottom. Notice how the initial peaks only are in phase.

below.

### The non-linear near field (zero field)

The zero field refers to the non-linear zone of fluid flow very close to a single bubble (section 3.3). This definition is unchanged but there is now a zero field for each element in an array. Often airguns are arranged in clusters—several guns are positioned so close together that their bubbles coalesce, and the guns effectively act as a single element. In this case it is more complicated: the zero field extends between the guns in the cluster and envelops them, out to a distance of about 1m.

### The linear near field

The near field is that part of the radiation field of an array where the effects of each individual source are felt, as well as the interference pattern which develops between them. In the near field, with increasing distance from the array, the signal changes both shape and amplitude. There is a direct analogue in Fraunhoffer diffraction in optics: at moderate distances from a slit, the physical size of the slit is experiencied in the near field. At distances large compared with the slit, it is the interference pattern caused by the diffraction slit which is felt. In the far field, the pressure and the particle velocity do not feel the effects of the individual sources. They show, more simply, that there is an extended source with a radiation pattern which varies with angle and azimuth.

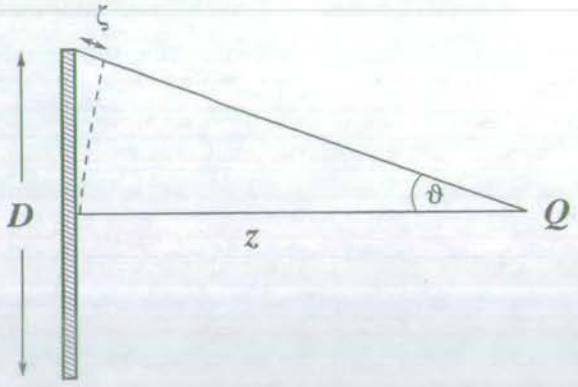


Figure 3.5: The geometry used to estimate the near and far fields of an extended array of dimension $D$.

Consider point $Q$ in Figure 3.5, on the axis of a line array of dimension $D$. $Q$ is just in the near field when the path differences between the various elements of the source array and its axis do not vary by more than about one half-wavelength. This corresponds to the onset of destructive interference. The greatest path difference is at the end of the array, thus the path difference $\zeta$ is such that

$$\zeta = \frac{D}{2}\sin\vartheta > \frac{\lambda}{2}. \tag{3.52}$$

Thus, from Pythagoras's theorem,

$$z^2 + \left(\frac{D}{2}\right)^2 = (z+\zeta)^2, \tag{3.53}$$

and substituting $\frac{\lambda}{2}$ for $\zeta$ gives for the point $Q$ to be in the near field,

$$z < \frac{D^2}{4\lambda} - \frac{\lambda}{4} \lesssim \frac{D^2}{4\lambda}. \tag{3.54}$$

### The far field

When the signal at a point $Q$, a distance $z$ from the centre of an an array, ceases to change shape with increasing distance, $Q$ is said to be in the far field. The amplitude of the signal in the far field decreases with increasing distance in any one direction. In general, a different signal is received in every direction from the source. Equation (3.54) is an approximate result which defines the distance just in the near field. There is a transition between the near field and far field. Consequently, a point of observation $Q$ is said to be in the far field of an array

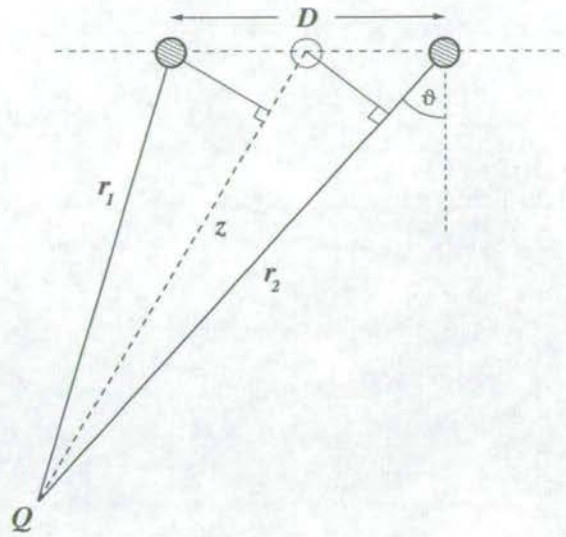


Figure 3.6: The geometry used to derive the radiation characteristics of a two-point extended array of dimension $D$.

at ranges of $z$,

$$z > \frac{D^2}{\lambda}. \tag{3.55}$$

Thus, a single measurement of pressure in the far field of an array characterises the radiation of the array in that direction. It cannot be used to calculate the pressure in any other direction. To know the the pressure output of the array in all directions would require an infinite number of far-field measurements. An example of measuring the vertical far-field signature is described in chapter 6.

## 3.7 Directivity and interaction

An array of airguns has a radiation pattern which varies with direction. The variation is known as directivity. It is a geometric effect. The wavefield from an airgun is produced by a bubble oscillating in a background pressure. When the oscillations from one gun affect the oscillations of a neighbouring gun, the phenomenon is called interaction. It is a physical effect.

### Directivity

Consider two non-interacting identical monopole sources, separated by a distance $D$ as shown in Figure 3.6. Their combined pressure output at a distance $z$ is

$$\frac{p(z,t)}{\rho} = \frac{1}{r_1} f'\left(t - \frac{r_1}{c}\right) + \frac{1}{r_2} f'\left(t - \frac{r_2}{c}\right), \tag{3.56}$$

which, on transformation to the frequency domain, is

$$\frac{P(z,\omega)}{\rho} = \frac{1}{r_1}F'(\omega)\exp\left(i\omega\frac{r_1}{c}\right) + \frac{1}{r_2}F'(\omega)\exp\left(i\omega\frac{r_2}{c}\right). \tag{3.57}$$

If the point $Q$ is in the far field, such that $z \gg D$, then the spherical divergence experienced by both sources is approximately the same: $r_1 \approx z \approx r_2$. Retaining the phase dependencies ($\pm\frac{D}{2}\sin\vartheta$) gives

$$\frac{P(z,\omega)}{\rho} = \frac{1}{z}F'(\omega)\exp\left(i\omega\frac{z}{c}\right). \tag{3.58}$$
$$\left[\exp\left(i\omega\left[-\frac{D\sin\vartheta}{2c}\right]\right) + \exp\left(i\omega\left[+\frac{D\sin\vartheta}{2c}\right]\right)\right],$$

which may be expressed as

$$\frac{P(z,\omega)}{\rho} = \underbrace{\frac{1}{z}F'(\omega)\exp\left(i\omega\frac{z}{c}\right)}_{\text{monopole}} \overbrace{2\cos\left(\frac{\pi D\sin\vartheta}{\lambda}\right)}^{\text{directivity}}. \tag{3.59}$$

The term marked by the underbrace is the output of a monopole placed between the two sources. The cosine term is the directivity factor of the two-point array, which depends on $\frac{\lambda}{D}$, the array's beamwidth.

Arrays are usually tuned so that they produce an impulsive-looking pulse in the vertical direction. Conservation of energy states that the signal which interferes destructively in the vertical direction must add up constructively in other directions. Thus tuned arrays are more directional than untuned arrays, and can have quite undesirable far-field signatures in directions away from the vertical.

A similar expression is obtained for sources in a vertical array

$$\frac{P(z,\omega)}{\rho} = \frac{1}{z}F'(\omega)\exp\left(i\omega\frac{z}{c}\right)2\cos\left(\frac{\pi D\cos\vartheta}{\lambda}\right). \tag{3.60}$$

Note that if the sources are of opposite polarity, the directivity factor becomes

$$2i\sin\left(\frac{\pi D\cos\vartheta}{\lambda}\right),$$

which is the case for a source at depth $\frac{D}{2}$, and its virtual image in the sea surface. On substitution of (2.83) for $\cos\vartheta$, in the frequency-wavenumber domain, the factor becomes

$$2i\sin\left(k_z\frac{D}{2}\right). \tag{3.61}$$

### Interaction

A simple consideration of energy conservation leads to the requirement for interaction (Ziolkowski *et al.*, 1982). Consider two identical monopole sources separated by a distance $D$, and oscillating in a constant hydrostatic pressure $p_\infty$. The far-field radiated energy $E_r$ associated with each monopole in isolation is

$$E_r = 4\pi r^2 \int_0^\infty p(r,t).v(r,t)\mathrm{d}t, \tag{3.62}$$

so that their combined energy, by linear superposition, is $2E_r$. If the separation between the sources is reduced such that $D \ll \lambda$ then, together, they behave as a single monopole with spherical symmetry. The new monopole has twice the strength of the original monopole, and its radiated energy is

$$E_{rn} = 4\pi r^2 \int_0^\infty 2p(r,t).2v(r,t)\mathrm{d}t, \tag{3.63}$$

so the new combined energy is $4E_r$. Clearly both results cannot be correct.

The problem is with the (assumed) linear superposition of sources. If two independent pressure measurements are each a solution of the linear acoustic wave equation (3.14), linear superposition states that their sum is also a solution. When $D > \lambda$ superposition gives the correct energy: The two monopoles together constitute an extended source which has a directivity pattern. This ensures that there is the correct conservation of energy through a balance of constructive and destructive interference. When $D \ll \lambda$, the sources do not act as they do in isolation. In particular, each bubble no longer oscillates in a constant background pressure. Linear superposition of their "in-isolation" pressure signatures therefore violates the conservation of energy. In order to solve the problem, the signatures must be found which describe each bubble oscillating in the presence of others, in a constant background pressure. Linear superposition applies to such signatures.

Figure 3.7 illustrates the problem. The top panel shows the signature of an 80 cu. in. airgun firing in isolation. The middle panel shows the signature of the same gun when 5 other guns fire at the same time. Note in particular that the signature of the interacting source has an irregular bubble period.

The interaction problem was solved by Ziolkowski *et al.*, (1982) and Parkes *et al.*, (1984). Consider the pressure at a hydrophone $i$ in the near field of a single gun

$$p_i(t) = p_b(t) - p_e, \tag{3.64}$$

where the external pressure is $p_e = p_\infty$, and the pressure in the water caused by the oscillating bubble is $p_b(t)$. When another gun fires simultaneously, which is a distance less than $\lambda$ away,

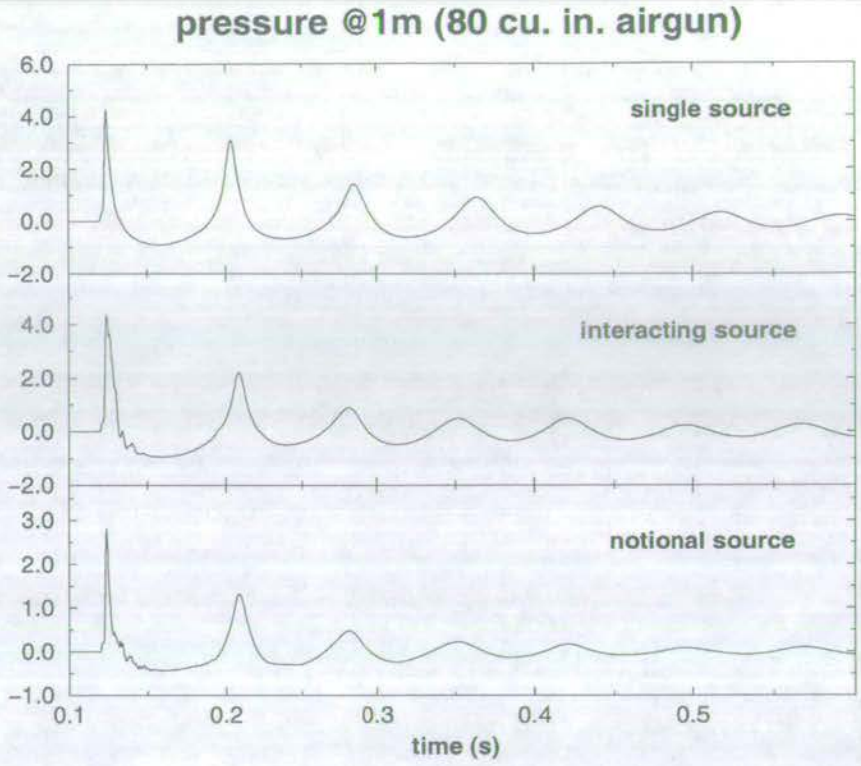


Figure 3.7: The pressure produced by an oscillating bubble: (top) single source; (middle) interacting source; (bottom) notional source.

there is interaction between the guns. The pressure experienced by hydrophone $i$ is now

$$p_i'(t) = p_b(t) - p_e' \tag{3.65}$$

where $p_i'(t)$ is different from the pressure with a single gun firing, because $p_e' = p_\infty + p_{mi}(t)$, and $p_{mi}(t)$ is the modulation on hydrostatic pressure experienced at the hydrophone. If many guns are firing, $p_{mi}(t)$ accounts for the modulation at hydrophone $i$ caused by all the guns. Equation (3.65) may be written as

$$p_i'(t) = p_b(t) - p_{mi}(t) - p_e, \tag{3.66}$$

and, by denoting $p_b'(t) = p_b(t) - p_{mi}(t)$, this gives

$$p_i'(t) = p_b'(t) - p_e. \tag{3.67}$$

Thus, the actual situation of a bubble oscillating in a modulated background pressure (3.65) is replaced with the conceptual situation of a bubble of modulated internal pressure oscillating in a constant background pressure (3.67). The new bubbles, referred to as "notional" sources,

may be linearly superposed. The bottom panel of Figure 3.7 gives an example of such a notional source which is from a six element array.

To solve the problem in practice, $n$ near-field hydrophones are required for $n$ guns. A method and example of measuring the source signature taking this effect into account is described in chapter 6.

## 3.8 Conclusions

It is possible to find an approximate solution to the non-linear wave equation which is appropriate for the oscillating bubble produced by a marine seismic source, such as an airgun. The expressions for pressure and particle velocity which derive from that solution show which measurements are required to fully characterise the source signature, at all ranges from a single airgun. A consideration of the complexity introduced by an extended source reveals the measurements required at all ranges from an array of interacting or non-interacting airguns.

# SEA SURFACE MULTIPLE ATTENUATION TECHNIQUES

*Chapter 4*

## 4.1 Introduction

Multiple removal is a long-standing problem in controlled-source seismology; the multiples have been around for as long as the seismic method itself. Their discussion in the literature is almost as old. In 1946 a workshop was organised by the Society of Exploration Geophysicists (SEG) on the subject of multiple reflections. In 1997 another workshop (not the second) was organised by the SEG on the subject of multiple attenuation techniques. The multiples are still with us.

This chapter discusses the main classes of sea surface multiple attenuation: those used today in routine processing; and those considered to be state-of-the-art. The different methods (and their degrees of approximation) are presented with a consistent notation so that they may be compared and contrasted more easily. The chapter covers the following material: (1) The various effects classified as multiples which are due to reflection at the sea surface; methods of multiple attenuation which are (2) Velocity-based; (3) Statistical; and (4) Wave-theoretical; and finally, (5) Conclusions.

## 4.2 The sea surface effects

The sea surface gives rise to many events on seismic data which are categorized simply as different types of "multiples". With the plethora of techniques available for suppressing multiples, it is often confusing which part of the whole multiple problem is being attacked. It is worthwhile, therefore, to discuss the different effects produced by the free surface at the air/water interface, in order to understand how the techniques described in this chapter compare. Several classes of multiples are depicted in Figure 4.1 and are discussed in this section, in increasing order of complexity and difficulty of removal.

### The receiver ghost

Consider a streamer at depth $z = z_r$ in the water, as depicted in Figure 4.2. An upward-travelling plane wave is depicted by the ray which is normal to the wavefront. It is measured by the receiver, reflected in the sea surface, and measured again. The combined effect for the

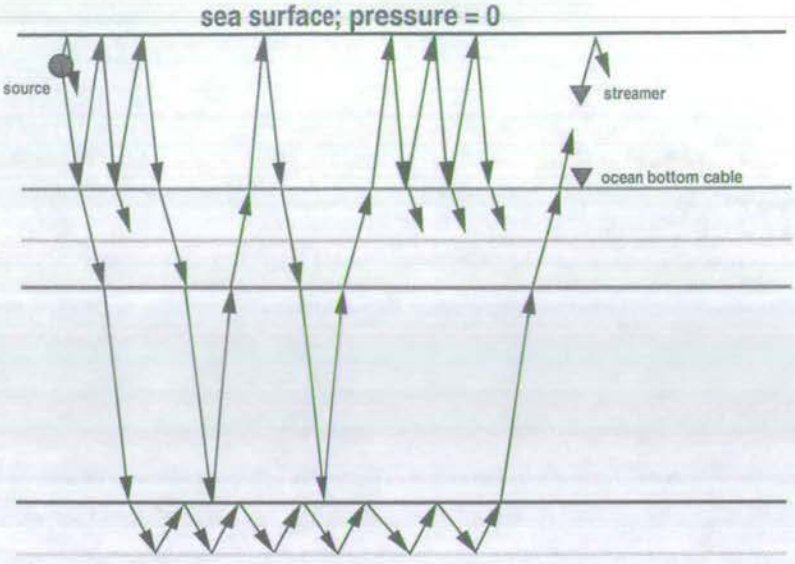


Figure 4.1: Different multiple raypaths associated with the sea surface.

receiver is that it "sees" a wave travelling in the negative $z$-direction originating somewhere below it, and a wave travelling in the positive $z$-direction which originates above the sea surface. This latter wave is the receiver "ghost" reflection and occurs during recording. (The same phenomenon occurs, during the emission of energy, at the source side.)

The net effect of the two waves travelling in opposite directions can be decomposed into the upward-travelling wave and a modulation due to the sea surface given by (see section 3.7, p. 50)

$$\left| 2\sin\left(\frac{\omega z_r \cos\phi}{c}\right)\right|, \tag{4.1}$$

where $\phi$ is the angle of propagation with respect to the vertical, $c$ is the velocity of sound in water, and $\omega$ is the angular frequency. The upgoing plane wave is a reflection from the earth—its complexity depends on the earth model. This point will be returned to later.

Figure 4.3 shows a plot of (4.1) for vertical incidence and various receiver depths. The notches in the ghost spectrum, at frequencies (Hertz):

$$f = \frac{nc}{2z_r \cos\phi}; \quad \text{where } n = 0,1,2,\ldots, \tag{4.2}$$

reduce the available bandwidth of the data as the depth of the receiver is increased. Filling in the amplitude spectrum at the ghost notch frequencies and correcting the $\pi$ phase change introduced by the sea surface reflection is known as *deghosting*. One possible method of deghosting is to deconvolve the receiver ghost from the measured data. Because the ghost is dependent on angle, it can be removed properly only by treating each angle, or plane wave,

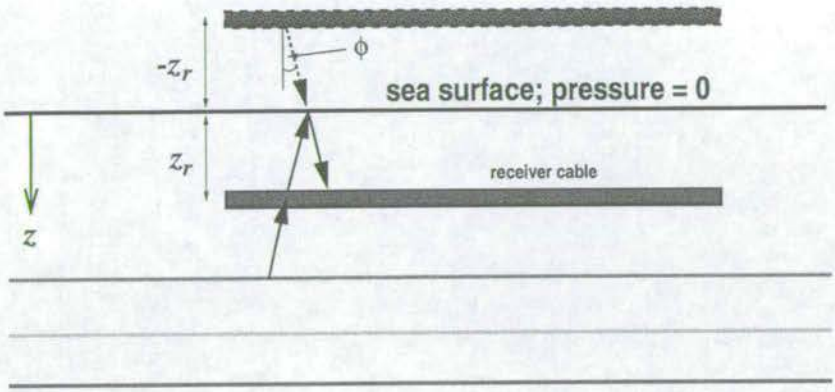


Figure 4.2: The raypath geometry for the receiver ghost.

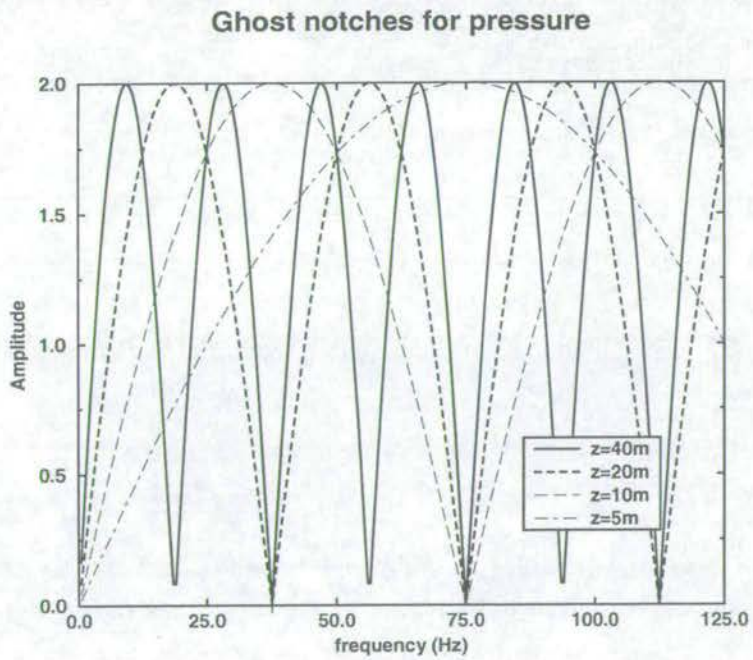


Figure 4.3: Ghost notches for a pressure detector.

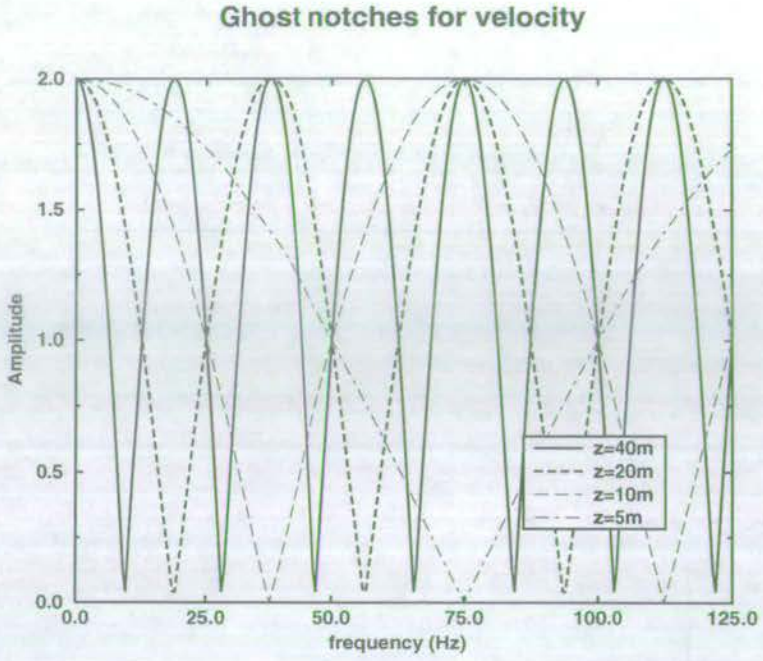


Figure 4.4: Ghost notches for a particle velocity detector.

separately. In the frequency-wavenumber ($\omega$-$k$) domain the receiver response, which includes the factor in (4.1) becomes

$$1-\exp(ik_z[2z_r]), \tag{4.3}$$

where $k_z = \sqrt{\omega^2/c^2 - k_x^2 - k_y^2}$. Successful recovery of the energy at the notch frequencies is dictated by the stability of the complex division by (4.3) which goes to zero when $\exp(ik_z[2z_r]) = +1$. Removing the receiver ghost in this way from pressure data yields the upgoing wave.

It is interesting to note that the ghost modulation for particle velocity, plotted in Figure 4.4 and given by

$$\left|2\cos\left(\frac{\omega z_r \cos\phi}{c}\right)\right|, \tag{4.4}$$

is not the same as for pressure. The reason is that the sea surface is pressure-free, and hence the sea surface reflection coefficient for particle velocity ($+1$) has the opposite polarity to that for pressure ($-1$). The notches in the spectrum for particle velocity occur at frequencies,

$$f = \frac{nc}{4z_r \cos\phi}; \quad \text{where } n = 1, 2, \ldots. \tag{4.5}$$

A comparison of the curves in Figure 4.3 and Figure 4.4 shows that a suitable combination

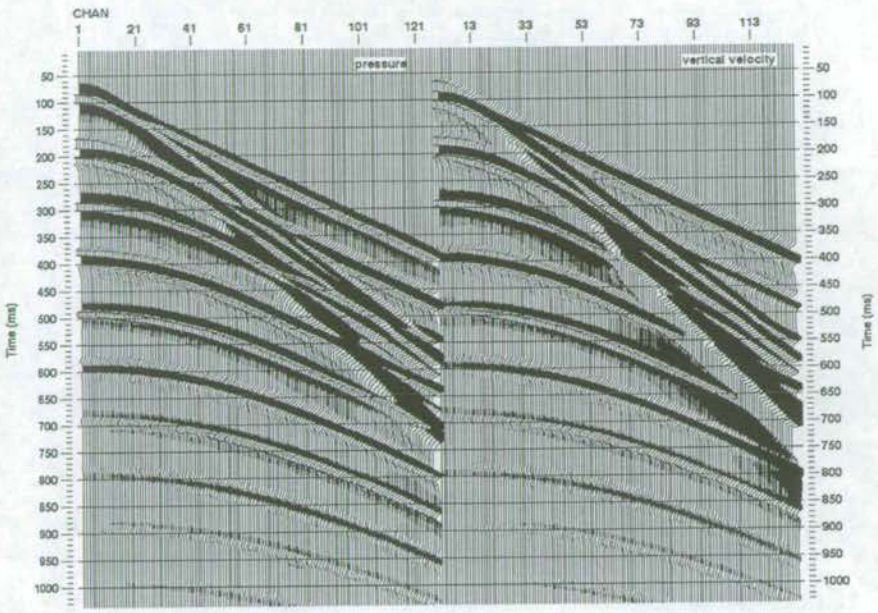


Figure 4.5: A line source over a layered earth with no incident field. The gather on the left is the pressure; the gather on the right is the normal component of particle velocity.

of pressures *or* velocities from two depths, or pressure *and* velocity from the same depth, results in a flatter spectrum (Haggerty, 1954). Equations derived in chapter 2 describe how to combine pressure and particle velocity at the same depth.

These are possible methods of removing the receiver ghost. There are several others. What is left, however, after deghosting, is the upgoing wavefield in the water. This wavefield may be of abitrary complexity, as noted earlier, and it still contains all other multiples indicated in Figure 4.1.

Receiver deghosting is illustrated in the following example. Figure 4.5 shows the scattered fields of the pressure and the vertical component of particle velocity, modelled using the reflectivity method (Fuchs & Müller, 1971), for the simple model of a water layer overlying an elastic half-space (Figure 4.6). Figure 4.7 shows the plane-wave combination of pressure and the vertical component of particle velocity, using the theory derived in section 2.4 (equations (2.79)), which yields the upgoing and downgoing pressure waves in the water. Note that while the receiver ghost has been eliminated from the panel on the left, the multiples have not been cancelled and are present in both wavefields.

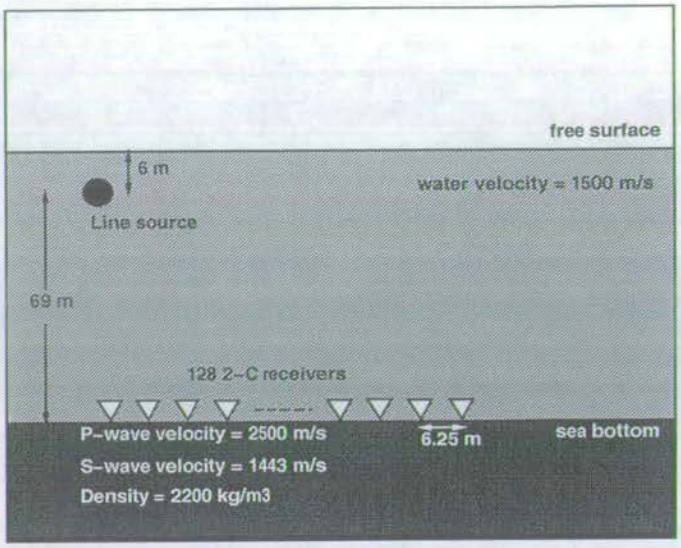


Figure 4.6: Earth model of a water layer overlying an elastic half-space. The model properties are such that a $P$-wave source in the water excites a $P$-wave reflection, a $P$-wave refraction, a (Stoneley) interface wave, and many multiples of these.

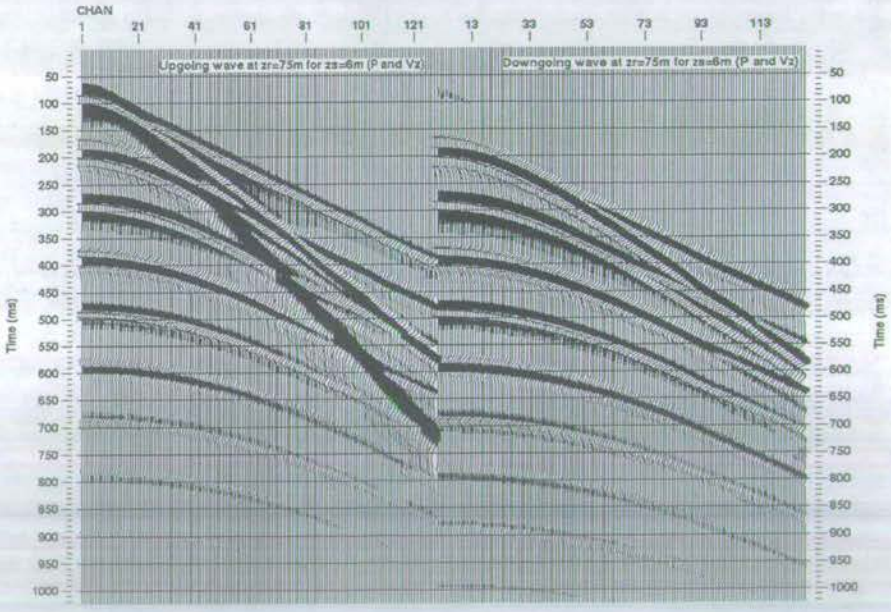


Figure 4.7: Separating upgoing and downgoing wavefields with the scattered pressure and particle velocity: Upgoing pressure wave on the left; downgoing pressure wave on the right.

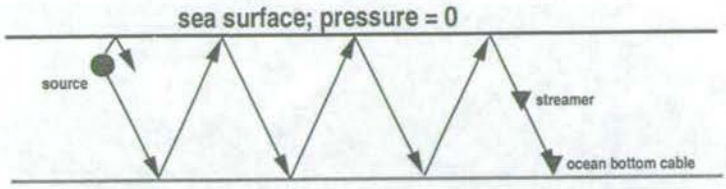


Figure 4.8: The raypath geometry for water layer reverberations.

### Water layer reverberations

Energy which is trapped between the sea surface and the sea floor gives rise to water layer reverberations on the seismic record. The multiples which persist after receiver deghosting in Figure 4.7 are therefore water-layer reverberations. Pure water layer multiples are depicted in Figure 4.8, while so-called water-layer "peg-legs" are depicted in Figure 4.9. Note that the latter exist at both source and receiver side. Removing these reverberations requires an estimate of the sea floor reflectivity. When the receivers are on the sea floor as in OBC acquisition, the receiver ghost arrives at the same time as the receiver-side reverberations.

The sea surface and a strong impedance contrast at the sea floor (relative to a solid/solid interface) present a wave guide for the propagation of sound (Burg *et al.*, 1951). The problem was treated by Backus (1959) using linear filter theory, in a classic paper on multiple elimination. His one-dimensional solution states that the water-layer reverberation filter has the $Z$-transform

$$F_{rev}(Z) = \sum_{i=0}^{\infty}(-r_1 Z)^i = \frac{1}{1+r_1 Z}, \tag{4.6}$$

where $r_1$ is the seafloor reflection coefficient, $Z$ is the unit delay operator for two-way travel in the water column, and the sea surface has a reflection coefficient of $-1$. The filter operates on the recorded wavefield twice: at the source side when energy penetrates the sediments as the downgoing wave; and at the receiver side when energy penetrates the water as the upgoing wave. The operator, $F^B_{derev}$, which removes this effect is clearly

$$F^B_{derev}(Z) = (1+r_1 Z)^2 = 1+2r_1 Z+r_1^2 Z^2. \tag{4.7}$$

This concept was extended by Morley & Claerbout (1983) with the Split-Backus model which accommodates differences in multiple period at source and receiver locations (due for example to a dipping sea floor (Levin & Shah, 1977)). Their operator, $F^{SB}_{derev}$, is an intuitive generalisation of Backus's original filter:

$$F^{SB}_{derev}(Z) = (1+r_1^s Z^s)(1+r_1^r Z^r), \tag{4.8}$$

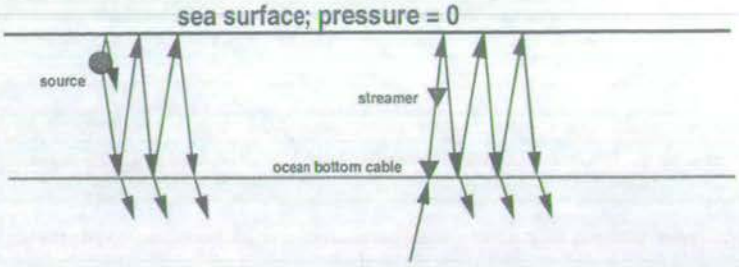


Figure 4.9: The raypath geometry for source and receiver side peg-leg reverberations.

where $r_1^s$ and $r_1^r$ are the reflection coefficients, and $Z^s$ and $Z^r$ are the delay operators, at the source and receiver locations, respectively. Although decoupling of the reverberations at the source and receiver side allows non-zero offset primary reflections, the method is still inherently one-dimensional and requires the multiples in the water to propagate at normal incidence. Note that in both dereverberation filters, an estimate of the seafloor reflection coefficients is required. This is usually obtained by the minimisation of an error function which accounts for the energy left after subtracting the multiples from the data. In addition the two-way traveltimes in the water must be estimated.

Since the advent of OBC recording there has been a lot of work published which uses both pressure and particle velocity. A much-popularised approach is that of Barr & Sanders (1989) who treat the problem in one dimension using dual sensor data (pressure and the vertical component of particle velocity). They exploit the fact that reverberations have opposite polarity on the two sensors to eliminate them at the receiver side. Consider a unit impulse travelling upwards through the sea floor into the water column, and its passage past a pressure-sensitive detector; for simplicity's sake, suppose the detector is mid-way between the sea surface and the sea floor. Time zero is triggered when the impulse first passes the detector. The sea surface reflection coefficent is $-1$ for pressure, while the acoustic reflection and transmission coefficients at the sea floor are $r_1$ and $t_1$, respectively. The detector records upgoing and downgoing waves which travel between the sea surface and the sea floor. Denoting these waves by $u(t)$ and $d(t)$, their time series are

$$\begin{aligned} u(t) &= t_1, \quad -r_1 t_1, \quad +r_1^2 t_1, \ldots \\ d(t) &= \quad -t_1, \quad +r_1 t_1, \quad -r_1^3 t_1, \ldots, \end{aligned} \tag{4.9}$$

where $d(t)$ lags $u(t)$ by the one-way travel time in the water. If the detector is now positioned on the sea floor, the upgoing and downgoing waves are recorded simultaneously. The Z-

transform of each of the waves is

$$\begin{aligned} U(Z) &= t_1 - r_1 t_1 Z + r_1^2 t_1 Z^2 - r_1^3 t_1 Z^3 + \cdots = \frac{t_1}{1+r_1 Z}, \\ D(Z) &= \quad -t_1 Z + r_1 t_1 Z^2 - r_1^2 t_1 Z^3 + \cdots = \frac{-t_1 Z}{1+r_1 Z}, \end{aligned} \tag{4.10}$$

in which Backus's reverberation filter is obvious. The sums and differences of these waves are

$$\begin{aligned} U(Z)+D(Z) &= \quad t_1\Big(1-(1+r_1)Z+(1+r_1)r_1 Z^2 - \ldots\Big) \\ D(Z)-U(Z) &= -t_1\Big(1+(1-r_1)Z-(1-r_1)r_1 Z^2 + \ldots\Big), \end{aligned} \tag{4.11}$$

which are related to the pressure and particle velocity in the frequency-wavenumber domain via equations (2.81). In the time domain the pressure and the vertical component of particle velocity may be written as

$$\begin{aligned} p(t) &= \Big(u(t)+d(t)\Big) \\ v_z(t) &= \Big(d(t)-u(t)\Big)\frac{\cos\phi}{\rho c}. \end{aligned} \tag{4.12}$$

Thus, the ghost and the water-layer reverberations at the receiver side are cancelled by a combination of $p(t)$ and $v_z(t)$:

$$p_0(t) = p(t) - f_{bs} v_z(t) = \frac{2t_1}{1-r_1}, \tag{4.13}$$

where $p_0(t)$ is reverberation-free, and the Barr & Sanders filter $f_{bs}$ is

$$f_{bs} = \frac{\rho c}{\cos\phi}\frac{1+r_1}{1-r_1}. \tag{4.14}$$

The method assumes vertical angles of propagation in a 1D earth, and requires that the seafloor reflection coefficient be estimated.

Osen *et al.* (1999) present a method of multiple-removal that involves separating upgoing and downgoing plane waves just below the sea floor. Their formulation is analogous to that given in section 2.4, but for the elastic case. It includes separation into upgoing and downgoing waves for all four components of an OBC receiver. Their multiple removal step for pressure may be written in the frequency-wavenumber domain as,

$$U = \frac{1}{2}(P - F_{osen} V_z) \tag{4.15}$$

where $U$ is the desired "multiple-free" upgoing pressure, and the $(k_x, k_y, z, \omega)$ dependence is assumed. The filter $F_{osen}$ depends on the density and $P$- & $S$-wave velocities of the sea floor, as well as on the plane wave under consideration. Although the wavefield separation is performed *below* the sea floor, and hence requires the estimation of more parameters, the upgoing wave which is left still contains most of the multiples. The receiver-side water-layer reverberations only have been eliminated. Thus, it is similar in scope to the approach of Barr & Sanders (1989), but is correct for all angles of propagation. The method assumes that the sea floor is locally flat.

## 4.3 Velocity-based methods

A key step in multi-channel seismic data processing which was first used to attenuate multiples is stacking (Mayne, 1952 & 1960; Schneider *et al.*, 1965). This technique, like all *velocity-based* multiple attenuation methods, relies on there being sufficient *moveout difference* between primary and multiple reflections to discriminate between them. If the velocity in the sediments is higher than the velocity in the water layer, then the multiples will tend to have have a lower stacking velocity than the primaries, because they have spent more time travelling in the water. When data within a common midpoint (CMP) gather are normal moveout (NMO)-corrected with a velocity appropriate for the primaries, then stacked, the multiples will tend to be suppressed as they are not as coherent horizontally as the primaries.

Stacking is less effective the more complicated the geology becomes because of its simple underlying model of a 1D earth and hyperbolic moveout curves to preferentially attenuate multiples. By definition stacking cannot be applied pre-stack. However, there are a number of approaches which make better use of possible moveout differences. In general, these methods transform the data into a domain where the primaries and multiples are more separable. An example is the method of Ryu (1982) which applies an NMO correction with a velocity between that of primaries and multiples: The primaries are over-corrected (concave hyperbolas–negative dip), and the multiples are under-corrected (convex hyperbolas–positive dip). On Fourier transformation to the $\omega$-$k$ domain, the primaries map into the negative half of the $\omega$-$k$ spectrum, while the multiples map into the positive half, and can be muted. On transformation back to the time-space domain and reverse NMO correction, primaries only should remain. Because there is less moveout at zero offset, multiple energy will be least well removed at the apex of the hyperbolas, and an inner trace mute is often required prior to stacking.

A variation on the approach of Ryu (1982) is to NMO correct the data with the velocity field of the multiples. This renders the multiples approximately flat and they may be removed in the $\omega$-$k$ domain with a $k = 0$ notch filter.

Another popular transform associated with multiple removal is the discrete Radon trans-

form (DRT) (Beylkin, 1987). The DRT can take many guises depending on what is used as the basis functions. It assumes a 1D earth and is normally applied to CMP gathers, which approximate common shot gathers over a horizontally-layered earth. Like the $\omega$-$k$ method above, the goal is to obtain separabilty in the transformed domain. The basis functions can be chosen such that either the primaries or the multiples are well described by them, and become very localised in the transform domain. It is then easy to isolate the primaries and inverse transform to get multiple-free seismograms, or to isolate the multiples and inverse transform to get a multiple model for subtraction from the multiple-contaminated data.

Thorson & Claerbout (1985) were first to describe the DRT as a least-squares problem in their inverse velocity stacking algorithm for modelling hyperbolic reflections. They find a set of weights, or transform coefficients, which enable the model they find to describe the data they start with, while simultaneously minimising the misfit, in a least-squares sense. Hampson (1986) uses this approach to suppress multiples by transforming NMO-corrected gathers with the parabolic Radon transform. Foster & Mosher (1992) describe another implementation of the transform involving hyperbolic transforms and NMO-corrected gathers. In both of these Radon transform approaches the conclusions are the same: *if* enough velocity discrimination exists between primaries and multiples, the multiples will be effectively suppressed at all offsets equally.

## 4.4 Statistical methods

The common element to all statistical methods is that the multiples are assumed to be *periodic*, and therefore predictable. The data model for these statistical techniques is that the earth is one dimensional, and conforms to one of several statistical models. Important contributions in the statistical approach to multiple elimination include Robinson (1957), Backus (1959), Watson (1965), Silverman & Sparks (1965), Kunetz & Fourman (1968), which have led to what is now called *predictive deconvolution* (Peacock & Treitel, 1969).

The seismic convolutional model (Robinson, 1954) underlying predictive deconvolution states

$$x(t) = w(t) \star g(t) + n(t) \tag{4.16}$$

where $x(t)$ is the seismic trace, $w(t)$ is the seismic wavelet, $g(t)$ is the (unpredictable) reflectivity (or "geology") and includes absorption here, and $n(t)$ is (Gaussian) noise. In this model, the wavelet is given by

$$w(t) = m(t) \star s_c(t) \tag{4.17}$$

where $m(t)$ is the (predictable) multiples, and $s_c(t)$ includes all convolutional effects at the

source and receiver: commonly the source signature, the source and receiver ghosts, and the receiver and recording responses.

Various assumptions are imposed on all of the elements in equation (4.16) so that multiples can be predicted and subtracted using only knowledge of $x(t)$. These are discussed in general in Ziolkowski (1984), and in the context of predictive deconvolution in Ziolkowski, Underhill & Johnston (1998) and Ziolkowski, Johnston & Underhill (1999).

The problem with predictive deconvolution as a multiple attenuation technique is that it is only one dimensional. Even in a one-dimensional earth the multiples are periodic for the zero offset trace only, and become less so with offset. The problem is exacerbated by complex geologies. Taner (1980) describes a multi-channel procedure which exploits radial traces. It relies on multiples reverberating in the water layer with a constant angle of reflection, so that they lie on a straight line which passes through the origin in the time-space domain. A primary event at $(t_1, x_1)$ on a particular trace is used to predict the multiples of it on other traces at $(2t_1, 2x_1)$, $(3t_1, 3x_1)$, and so on.

A change of domains from time-space to intercept time-slowness ($\tau$-$p$) via a linear DRT, extends the usefulness of traditional single-channel predictive deconvolution to non-zero offsets. For a 1D medium multiples are periodic with respect to intercept time for all slownesses and can be removed more effectively (Tatham *et al.* (1983), Tatham, (1989)). Taner *et al.* (1995) describe the same extension to non-zero offsets explicitly in the time-space domain. The two approaches are equivalent.

When the sea floor is dipping, predictive deconvolution (both $t$-$x$ and $\tau$-$p$) fails because the multiples are no longer periodic. Hartley *et al.* (1998) solve this problem by defining a transformation which depends on sea floor dip and renders multiples periodic with the same wavelet stretch on each trace within a shot gather. Predictive deconvolution then has more chance of success.

Lokshtanov (1995) adopts a data model which expresses the reflection response in terms of different types of multiples, as suggested by Kennett (1983). He then applies predictive deconvolution in the $\tau$-$p$ domain to remove water-layer reverberations and peg-leg multiples for a locally 1D sea floor. A single channel version removes source- and receiver-side peg-legs over 1D structures, however, the multi-channel version for 2D geologies fails to fully remove source-side peg-leg multiples. The seafloor reflection coefficients are estimated in the process by minimising the energy in the processed data.

## 4.5 Wave-theoretical methods

The most sophisticated methods of multiple attenuation are wave theoretical. That is, they take account of wave propagation in the earth. The most complete methods effectively replace the sea surface with a non-reflecting boundary so that the material above the boundary is

water, not air. All multiples, no matter how complex, involving at least one upwards reflection against the sea surface, are removed. The data acquisition requirements for such a task are high: a full 2D array of shots, each of which must be recorded by a full 2D array of receivers. All offsets are required, positive, negative and zero. Both shot and receiver coordinates must be adequately sampled such that the full 3D wavefield is recorded.

Assuming the water layer is homogenous and isotropic, the simplest wave equation any sea surface multiple attenuation technique must honour is the constant density acoustic wave equation. With this in mind, all possible solutions to the problem must be related, as shown below. They may, however, differ in their assumptions and their implementations.

### Wavefield continuation

A method based on the wave equation which removes multiples related to a particular interface, such as the water bottom, is the method of explicit wavefield extrapolation and subtraction (Wiggins, 1988). The data at the surface are a sum of upgoing and downgoing waves. After separating these waves, the method uses the wave equation to extrapolate the downgoing wave forward ($D$), and the upgoing wave backward ($U$), to the water bottom. The forward extrapolation through the water predicts the multiples which are already in the backward-extrapolated data. At the horizon the following statement holds

$$U_0 = U - rD, \tag{4.18}$$

where $r$ is a short operator which represents the reflectivity of the water bottom, or the horizon generating the multiples, and $U_0$ is the upgoing wave without the multiples, essentially just below the water bottom. The wave equation is used again to propagate the wavefield $U_0$ (without water-bottom multiples) back to the surface. Energy minimisation of the difference between $U_0$ and $U$ at the reflector provides an estimate of $r$.

### "Noah's" deconvolution

The first wave theoretical approach to multiple removal is a 2D formulation proposed by Riley & Claerbout (1976) in the time domain. They write in a caption to a figure of a submarine performing a seismic experiment deep below the sea surface, "Noah believed that the large problem with multiple reflections was due mainly to the presence of the sea surface. By effectively removing the sea surface Noah eliminated the disturbing amount of multiple energy associated with reflections off the sea surface". They formulate the problem first of all in 1D with,

$$p_t^0 = p_t - w^{-1} \star \sum_{k=1}^{t-1} p_k^0 p_{t-k} \tag{4.19}$$

where $p_t^0$ is the data without multiples, $p_t$ the data with multiples, $w^{-1}$ the inverse of the wavelet, and $\star$ denotes convolution. In the absence of any other deterministic means, they propose estimating $w^{-1}$ directly from the data by requiring that $p(t)$ in (4.19) is minimised (in a least-squares sense) over a window where multiples only exist. This is an energy-minimisation criterion. Alternatively, equation (4.19) can be written as

$$p_0 = p + p_0 N p \tag{4.20}$$

where $N$ accounts for the wavelet inverse, the sea surface effect and the convolution.

They go on to describe the forward and inverse problems for 2D multiples using a finite difference approach, and restricting wave propagation to near-vertical. The inverse solution (multiple removal) involves propagating upgoing and downgoing wavefields downwards, to remove multiples and image reflectors simultaneously. They conclude that imperfections in their multiple removal result arise principally from inaccuracies in estimating the source wavelet inverse.

### Reflection response

An exact 1D solution is formulated by Kennett (1979) in the $\omega$-$k$ domain for a line or point source at the surface, or just below it. He formulates the problem by recovering the plane-wave reflection response of the earth. To do this requires detailed knowledge of the source time function and its directivity, and the properties of the medium between source and the surface. The multiple-free solution is found by effectively deconvolving for the source effect and performing an algebraic transformation of the data.

### Feedback loop

The problem of the free surface in 2D is formulated in the $\omega$-$x$ domain as a feedback loop by Berkhout (1982). (Earlier work on the feedback approach by Koehler *et al.* (1974) provides an exact result in the time domain for an impulsive plane wave in 1D.) The formulation is limited to the scattered field only, and assumes dipole line sources at the sea surface and line receivers just below the surface. The method is developed in Verschuur (1991), Verschuur *et al.* (1992) and Berkhout & Verschuur (1997).

Using wave theory they begin by describing the forward model of seismic data with dipole sources at a non-reflecting surface and wave propagation operators for upgoing and downgoing waves. Introducing the free surface they argue that the upgoing data at the surface is repeatedly multiplied by the sea surface reflection coefficient and added back to the downgoing data in the form of a feedback loop. The expression for seismic data with multiples is then inverted to isolate the part which contains the primaries only.

They express the data with multiples as (for one frequency):

$$P = P_0 - P_0 A P, \tag{4.21}$$

where $P$ is the recorded data, $P_0$ is the data without multiples, and $A$ defines a "surface operator" which includes the source (signature) & receiver effects (all deterministic in theory). $P_0$ and $P$ are matrices which are a function of source and receiver offset. From equation (4.21) it follows that the data without multiples are given by

$$P_0 = P + P_0 A P. \tag{4.22}$$

The contributions from different orders of multiples are explicit if this expression is rewritten as $P_0 = P/(1 - AP)$ and expanded into a Taylor series:

$$P_0 = P\Big(1 + (AP) + (AP)^2 + (AP)^3 + \ldots\Big). \tag{4.23}$$

All multiples can be removed by subtracting higher and higher order terms if the surface operator $A$ is known. Alternatively equation (4.22) can be written in terms of a recursion (Berkhout & Verschuur (1997)):

$$P_0^n = P + P_0^{n-1} A P, \tag{4.24}$$

where implicitly $P_0^0 = P$. With each iteration, successively higher orders of multiples are predicted and subtracted from the recorded data. Repeated application of (4.24) is equivalent to (4.23). It is also suggested that a first-pass multiple attenuation result using another technique can be used as the starting estimate for the multiple-free result.

In all the published implementations of this method, knowledge of the source signature and the acquisition geometry are ignored. Instead, a least-squares estimate of the operator $A$ (or a variant thereof) is found by minimising the energy in the multiple-free upgoing wavefield (Verschuur *et al.*, 1989 and Verschuur & Berkhout, 1997). Finally, $A$ now accounts for the deterministic effects mentioned above, plus any and all algorithmic deficiencies which result from the data not satisfying the initial assumptions: using total field instead of scattered field, using 3D data instead of 2D data, limited spatial aperture effects, data sampling effects, and so on. It remains to be proven that all the inadequecies in the method can be parameterised in this way.

### Acoustic reciprocity

An exact solution to the full 3D problem for point sources and point receivers has been derived by Fokkema & van den Berg (1990, 1993) using Rayleigh's reciprocity theorem. The method

was developed by van Borselen *et al.* (1996) and explicitly includes the incident and scattered fields.

Fokkema & van den Berg begin by defining two non-identical "states" in a data domain, and consider their interaction. One state is identified with the actual situation where the sea surface is present; the other state is the desired situation where the sea surface is absent. Using the Rayleigh reciprocity theorem, an integral equation is derived which expresses the desired pressure field in an unbounded medium in terms of the actual measured pressure in a bounded medium incorporating the free surface. In the $\omega$-$x$-$y$ domain they write (for one frequency):

$$p^0 = p^{deg} + \int p^0 B p^{deg} \mathrm{d}x\mathrm{d}y, \tag{4.25}$$

where $p^0$ is the data without multiples, $p^{deg}$ is the deghosted wavefield, and $B$ includes the effects of the source signature and the obliquity factor (which accounts for a correct decomposition into plane waves to enable deghosting). Each of these quantities is a function of source and receiver coordinates ($x$ & $y$). Van Borselen *et al.* (1996) formulate the problem in the double Radon domain, but the form of the equations is the same.

Equation (4.25) represents an integral equation of the second kind, and can be written as

$$P_0 = P^{deg} + P_0 B P^{deg}, \tag{4.26}$$

or expanded into a Taylor series as,

$$P_0 = P^{deg}\left(1 + (BP^{deg}) + (BP^{deg})^2 + (BP^{deg})^3 + \ldots\right). \tag{4.27}$$

As before, the inclusion of higher-order terms in the series removes higher order multiple terms.

The source signature is required for a proper implementation of equation (4.26) as matrix inversion, or (4.27) as prediction and subtraction. The authors note that the matrix inversion is accomplished faster in the double Radon domain where numerical techniques can take advantage of data symmetries and data clustering. Van Borselen *et al.* (1994) formulate the problem of free surface multiple removal, when the source signature is unknown, as an optimisation problem. They use a modified conjugate gradient algorithm in the frequency domain to minimise the energy in their multiple-free result and deliver the inverse of a wavelet. At each step in the optimisation causality is enforced in the wavelet. The authors stress in their conclusions that their results do not prove the validity of the energy-minimisation criterion.

### Inverse scattering

Based on a scattering theory description of the reflection process (e.g. Moses, 1956), Carvalho *et al.* (1991, 1992) and Weglein *et al.* (1997) derive an inverse scattering series solution to the

2D problem for line sources and line receivers. The method applies to the scattered field only.

They begin by describing the forward scattering problem in which seismic data are expressed as propagation in a reference medium (for the free-surface case this is a half-space of water; for the no-free-surface case this is a whole space of water), plus a perturbation due to scattering at points in the earth where the medium properties depart from those of the reference. The full inverse scattering problem is to find the perturbations (the earth properties) given the seismic data. By analysing the infinite series in the forward problem, they identify the terms responsible for producing free surface multiples. This subseries of terms is required in the particular inverse scattering problem which removes sea surface multiples. Each higher order scattering term in the inverse series removes a higher order of sea surface multiple. In the $\omega$-$x$ domain they write (for one frequency):

$$P_0 = P^{deg} + P_0 C P^{deg}, \tag{4.28}$$

where $P_0$ is the data without multiples, $P^{deg}$ is the deghosted wavefield, and $C$ is a factor which includes the effect of the source signature and the obliquity factor. $P_0$ and $P^{deg}$ are matrices which are a function of source and receiver offset. Equation (4.28) can be expanded as a Taylor series,

$$P_0 = P^{deg}\left(1 + (CP^{deg}) + (CP^{deg})^2 + (CP^{deg})^3 + \ldots\right). \tag{4.29}$$

As before, in the methods listed above, the solution is formulated, without knowledge of the source signature, as an optimisation problem. A search is performed for the "effective wavelet" which minimises the energy in the multiple-free upgoing wavefield. Carvalho *et al.* (1994) and Ikelle *et al.* (1997) propose two more approaches to this same problem. Carvalho *et al.* (1994) propose using a simulated annealing algorithm at a user-specified number of frequencies to define an amplitude scale factor, a time shift and a phase rotation. Ikelle *et al.* (1997) suggest that the wavelet should be estimated by removal of first order multiples only. They formulate the problem in the frequency-wavenumber domain and seek to find a wavelet which may vary with direction and with offset.

### Kirchhoff integral

Another approach, somewhat related to the feedback method (inspired by Verschuur *et al.* (1988)), has been developed by Dragoset (1993), Dragoset & MacKay (1993) and Dragoset & Jeričević (1998) for the 2D problem of line sources and line receivers. They use Kirchhoff diffraction theory to select the correct traces which may be considered as primaries in the construction of a particular multiple. These traces are used to predict the multiple event in a wave-theoretical sense. The method applies to the scattered field only.

Their version of the multiple-free solution states (for one frequency):

$$P_0 = P + P_0 DP, \tag{4.30}$$

where $P_0$ is the data without multiples, $P$ is the recorded data, and $D$ is a factor which includes the effect of the source signature and the obliquity factor. Equation (4.30) can be expanded as a Taylor series,

$$P_0 = P\Big(1 + (DP) + (DP)^2 + (DP)^3 + \ldots\Big), \tag{4.31}$$

which allows solution by predicting the multiples and adaptively subtracting them, by searching for the inverse of the wavelet contained in $D$ through some kind of optimisation.

In the latest version of this method (Dragoset, 1999), an approximate wavelet is used in a first step to predict the multiples using the terms in the expansion in (4.31), then, in a second step, "adapative noise cancellation" is performed which matches the predicted multiples to the actual multiples by time- and offset-dependent filtering. The adaptive cancellation speeds up the computation and filters algorithmic and acquisition approximations out of the data.

## 4.6 Conclusions

There are too many multiple removal schemes to cover individually. This chapter illustrates the different multiples associated with the sea surface, and the range of techniques which have been used to remove and attenuate them.

The most routine methods require the multiples to be periodic (statistical approach), or for the sediments to have significantly higher velocities than the the water layer (velocity-based approach). Most of these techniques rely on an underlying one-dimensional model which limits their usefulness in areas with 2D and 3D geology. Newer methods which exploit particle velocity as well as pressure to eliminate reverberations are still limited to locally 1D sea floors. Apart from the velocity-based approaches, all of these methods must somehow estimate the acoustic or elastic properties of the sea floor. These methods affect the amplitude of the primaries as well as removing multiples.

The latest generation of techniques is fully-wave theoretical, and can attack all classes of multiples due to the sea surface without any knowledge of the sub-surface. In principle they can deal with fully 3D geologies given adequate data. However, most of the techniques described in section 4.5 are derived for the 2D situation only. Since the problem is the same for all, the different solutions can be cast in a similar way. They also have one thing in common: they all require the source signature to be known. This requirement is akin to knowledge of the sea floor reflection coefficient for the less complete, statistical, methods above. In the absence of any knowledge of the source signature, the wave-theoretical methods are reformulated to

use an energy minimisation criterion to estimate an effective wavelet which removes all the multiples in a statistical sense. In theory, these methods preserve primary energy. However, with the energy-minimisation to find the wavelet, this is no longer always the case.

# MULTIPLE-FREE DATA AS A REFLECTION RESPONSE

*Chapter 5*

## 5.1 Introduction

The earth's plane wave reflection response is well-known in a layered medium (Thomson, 1950; Haskell, 1953). The reflection response at a depth level $z$ defines the reflection properties of the layered medium below that level. If the response is calculated below the free surface, it therefore excludes all multiples related to that free surface.

In a three-dimensional earth, the reflection response concept may be applied to non-plane waves: a complicated reflected wave may be decomposed into plane wave components. Each of these scattered upgoing plane wave components comprise primary and multiple reflections. The primaries result from a multiplication of an incident downgoing plane wave component with a generalised reflection coefficient, or reflection response, unique for the particular downgoing and upgoing plane wave components chosen. The multiples represent a sum of products of scattered downgoing plane wave components with generalised reflection coefficients, related to the chosen downgoing and upgoing plane wave component. Applying this argument to marine seismic reflection data recorded over a 3D earth results in a set of simultaneous equations whose unknowns form the three-dimensional reflection response. The data themselves contain all the information required to remove the effect of the sea surface. The trick is how to manipulate them to do so.

The chapter opens with an analytical example in 1D which shows how data in the presence of sea surface multiples can be manipulated to yield the reflection response. The analytical result is recast as a ratio of upgoing to downgoing plane waves. The plane wave reflection response in terms of this ratio is then generalised to three dimensions, resulting in the simultaneous equations described in the paragraph above. The subsequent sections go on to describe how to manipulate the measured data to obtain the requisite plane wave components with which to express the three-dimensional reflection response. Once the equations have been solved it is necessary to construct multiple-free seismograms via a forward modelling step. After explaining this last step, the chapter closes with some conclusions.

## 5.2 The concept of the reflection response

The concept of the reflection response has been used for many years to account for propagation of plane waves within an acoustic or elastic earth, composed of homogeneous or inhomogeneous layers (for example: Thomson (1950); Haskell (1953); Goupillaud (1961); Kunetz and d'Erceville (1962); Treitel and Robinson (1966); Gilbert and Backus (1966)).

Comprehensive reviews of wave propagation in layered media are provided in Kennett (1983) and Ursin (1983). Contained therein are analytical results which relate layer properties to generalised reflection coefficients. These coefficients account for the reflection properties of all the layers at once *below* the level at which they are calculated (including conversions between different propagation modes and inter-layer multiples). The generalised reflection coefficients, or plane wave reflection responses, represent transfer functions which convert the incident plane waves into scattered plane waves. The relations for the acoustic case are derived in chapter 2. The reflection response does not contain free surface multiples, such as those related to the sea surface, because it excludes all the effects *above* the level at which it is evaluated (Ross and Shah, 1987).

It is relatively straight-forward to see how plane waves propagate in plane layers. Once the layers are no longer planar, or interfaces assume complicated geometries, as in a three-dimensional earth, plane waves cease to have an obvious meaning. However, complicated waves may be decomposed into a multitude of plane wave *components*, each of which travels in a different direction. Thus, a number of transfer functions may be defined which convert the same incident plane wave into many scattered plane wave components. The more complicated the earth, the more numerous are the required transfer functions to describe the reflection process fully. This is the approach to sea surface multiple removal described in this chapter.

## 5.3 The reflection response in 1D

### In the absence of the free surface

Section 2.4 derives the reflection response of a stack of homogeneous acoustic layers bounded above and below by half-spaces. It is derived in terms of propagator matrices which depend on the material properties of the layers traversed, and the plane wave under consideration. These generalised reflection coefficients are equal to the ratio of the plane waves propagating in the upper half-space.

For a 1D model with no free surface there only two plane waves—a downgoing incident wave and an upgoing scattered wave, as shown in Figure 5.1. The reflection response is defined simply by

$$\tilde{U} = \tilde{R}\tilde{I}. \tag{5.1}$$

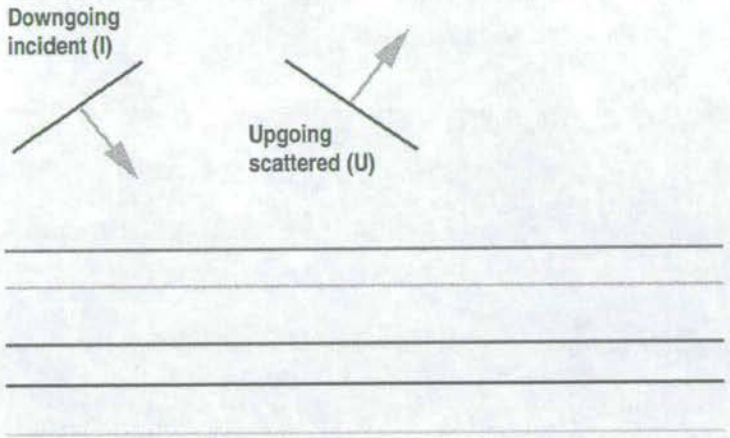


Figure 5.1: Plane waves propagating in a 1D medium in a half space of water.

In a seismic reflection experiment, a seismic source creates spherical waves, which may be decomposed mathematically into plane waves. The next part of this section goes on to describe an analytical result in 1D in which the upper half-space is replaced with a water layer whose upper surface is pressure-free, and in which a monopole source emits spherical waves.

### In the presence of the free surface

In the critical reflection theorem, Fokkema and Ziolkowski (1987) position a monopole source emitting spherical waves at $(x_s, y_s, z_s)$ in a water layer of thickness $z_e$, bounded above by a free surface. They consider the wavefield, reflected by a series of acoustic layers, arriving at the receivers at $(x, y, z)$ in the water, and decompose it into plane wave components. Equations (29) and (31) of Fokkema and Ziolkowski are combined and rewritten in terms of wavenumbers instead of slownesses to give an expression for the field scattered by the layers,

$$\tilde{P}^{scat} = \frac{i}{2k_z} S(\omega). \qquad (5.2)$$
$$\frac{\left[1-\exp\left(ik_z[2z_s]\right)\right]\left[1-\exp\left(ik_z[2z]\right)\right]\tilde{R}\exp\left(ikz[2z_e-z-z_s]\right)}{1+\tilde{R}\exp\left(ik_z[2z_e]\right)}.$$

Note that although the analysis of Fokkema and Ziolkowski is for an acoustic layered half-space, this expression for the scattered field is valid for an elastic layered half-space with an acoustic layer on top, in which the sources and receivers reside. This is the configuration for

the acquisition of marine seismic data.

Taking to the front a phase factor which accounts for propagation from the source to the receivers, equation (5.2) may be written as

$$\tilde{P}^{scat} = \frac{i}{2k_z} S(\omega) \exp\Big(ik_z|z - z_s|\Big). \\ \frac{\Big[1 - \exp\Big(ik_z[2z_s]\Big)\Big]\Big[1 - \exp\Big(ik_z[2z]\Big)\Big]\tilde{R}\exp\Big(ik_z[2z_e - 2z]\Big)}{1 + \tilde{R}\exp\Big(ik_z[2z_e]\Big)}. \tag{5.3}$$

With the following substitutions,

$$\begin{aligned} S' &= \frac{i}{2k_z} S(\omega) \exp\Big(ik_z|z_r - z_s|\Big) \quad \text{(direct "source" term)} \\ G_s &= 1 - \exp\Big(ik_z[2z_s]\Big) \quad \text{(source ghost)} \\ G_r &= 1 - \exp\Big(ik_z[2z]\Big) \quad \text{(receiver ghost)} \\ V &= \exp\Big(ik_z[2z_e - 2z]\Big) \quad \text{(phase factor)} \\ W &= \exp\Big(ik_z[2z_e]\Big) \quad \text{(phase factor)} \\ X &= \frac{W}{V} = \exp\Big(ik_z[2z]\Big) \quad \text{(phase factor),} \end{aligned} \tag{5.4}$$

the scattered pressure field may be expressed more compactly by

$$\tilde{P}^{scat} = \frac{S' G_s G_r \tilde{R} V}{1 + \tilde{R} W}. \tag{5.5}$$

In the absence of a free surface, (suppose for example the seismic reflection experiment is performed deep in an ocean trench, with a submarine instead of a boat towing all the equipment; the sea surface is far enough away to produce no reflections within the time window of interest, as envisaged by "Noah" in Riley and Claerbout (1976)), the hypothetical scattered field, $\tilde{P}^0$, is

$$\tilde{P}^0 = S' \tilde{R} V. \tag{5.6}$$

Comparing equations (5.5) and (5.6), the sea surface effect is clear: it produces the ghost reflections $G_s$ and $G_r$, and the factor $\frac{1}{1+\tilde{R}W}$ which produces all the multiples, as noted in section 2.4. The hypothetical recording is simply the reflection response, referred to the receiver level, multiplied by an incident field which accounts for propagation of the source to the receivers.

The goal for sea surface removal is to find an expression for the reflection response $\tilde{R}$ from

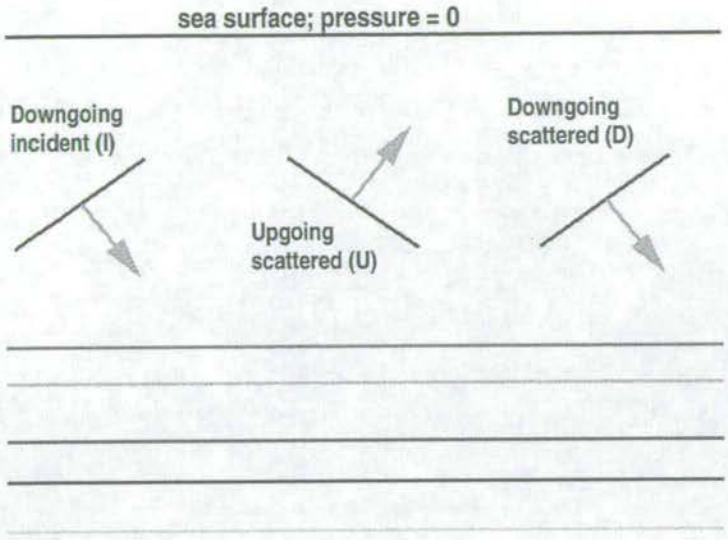


Figure 5.2: Plane waves propagating in a 1D medium in a water layer.

the data. An algebraic transformation of equation (5.5) gives

$$\tilde{R}V = \frac{\tilde{P}^{scat}}{S'G_sG_r - \tilde{P}^{scat}X}. \tag{5.7}$$

This is essentially the same approach used by Kennett (1979) to replace the sea surface with a non-reflecting boundary. The reflection response is referred to a plane at a depth $z$ below the surface, and excludes all effects above this level, including the sea surface itself.

Equation (5.7) describes the reflection response in terms of measureable quantities only; the right-hand side of the equation is independent of any earth parameters. Thus, the data themselves contain all the required information to remove the multiples. This is true in 3D as well, as shown later. However, the manipulation of the data is slightly more complicated.

A simpler form for the response can be found by dividing throughout by the source and receiver terms, $S'G_sG_r$,

$$\tilde{R}V = \frac{\tilde{P}^{dec}}{1 - \tilde{P}^{dec}X}, \tag{5.8}$$

where $\tilde{P}^{dec}$ is the scattered field deconvolved for source and receiver effects. Expanding the denominator in a Taylor series gives

$$\tilde{R}V = \tilde{P}^{dec}(1 + \tilde{P}^{dec}X + (\tilde{P}^{dec}X)^2 + (\tilde{P}^{dec}X)^3 + \ldots), \tag{5.9}$$

from which it is obvious that addition of successive terms refines the removal of higher and higher order multiples from $\tilde{P}^{dec}$. (The multiplications of the data with themselves correspond, in the time-space domain, to convolutions which apply time and offset phase shifts

which align the data with successively higher orders of multiples in themselves.) To predict and subtract all orders of multiples correctly requires all the terms in the series. The form of equation (5.9) is basically the same as the wave-theoretical approaches described in chapter 4.

Another form for the response can be obtained from (5.7) by dividing throughout by the receiver ghost $G_r$,

$$\tilde{R}V = \frac{\tilde{P}^{scat}/G_r}{S'G_s - \tilde{P}^{scat}X/G_r}. \tag{5.10}$$

In section 4.2 it was established that receiver deghosting of the scattered pressure gives the upgoing wave. Therefore, in accordance with equation (2.112) of section 2.4, equation (5.10) is equivalent to

$$\tilde{R}V = \frac{\tilde{U}}{\tilde{I}+\tilde{D}}. \tag{5.11}$$

Equation (5.11) gives the reflection response for a single plane wave in terms of the upgoing and downgoing scattered and incident plane wave components. This numerical description is equivalent to the analytical description of equation (5.10) for a one-dimensional earth.

Given a wavefield recorded over a complex three-dimensional earth, it is possible to decompose the recorded data into upgoing and downgoing plane wave components numerically. This generalisation to 3D of the result given above for 1D is the approach adopted in the formulation of Ziolkowski, Taylor and Johnston (1999) (abbreviated to ZTJ from now on). The following section describes the general three-dimensional method of multiple-removal.

## 5.4 The reflection response in 3D

In ZTJ's analysis of a generalised (3D) reflection response there are a number of key steps. First, source measurements are used to isolate the scattered field from the total measured field. Second, in the presence of a two- or three-dimensional earth, a complicated non-plane wave is reflected in response to a single incident plane wave. It is assumed that this reflected wave can be decomposed into plane wave components as depicted in Figure 5.3. The complicated wave is most faithfully represented as the number of plane wave components approaches infinity. The number of plane waves is ultimately limited by the discretisation of the data: by the shot location spacing to stimulate the earth with energy, and by the receiver spacing and temporal sampling to record the wavefield. Third, the generalised reflection response is referred to a plane boundary within the water column, at a depth below the sources. The relationship between the upgoing and downgoing waves at this notional interface acts as a lower boundary condition to the problem, and defines the three-dimensional reflection response.

The formulation in the frequency-wavenumber domain is essentially the same for the 2D and 3D problems. The 3D problem introduces two new coordinates compared with the

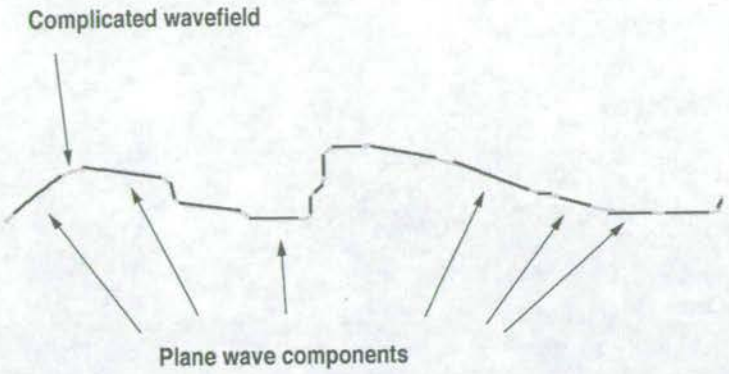


Figure 5.3: Decomposing a non-plane wave into plane wave components. Note that the plane wave components are infinitely long, but for the sake of clarity are drawn here only where they constructively interfere to reproduce the complicated wavefield.

2D problem. For 2D data, which corresponds to line sources perpendicular to recorded dip lines of receivers, Fourier transforms are applied over source and receiver $x$-coordinates. For 3D data, which corresponds to point or areal sources over recorded areal patches of receivers, Fourier transforms are applied over source and receiver $x$- *and* $y$-coordinates. Thus, to record 3D data requires adequate sampling of *five* dimensions: 2 source directions, 2 receiver directions, and time. In practice, a two-dimensional grid of receivers must record a two-dimensional grid of shots.

### In the absence of the free surface

Consider the situation of a three-dimensional earth, with a plane wave propagating in an upper half-space of water, as depicted schematically in Figure 5.4.

A single downgoing incident wave denoted symbolically by $\hat{\hat{I}}$ is reflected by the earth to yield a complicated upgoing scattered wave $\hat{\hat{U}}$. Suppose the plane wave is incident at an angle $\phi_i$, which is defined in terms of the downgoing horizontal wavenumbers using (2.83):

$$k_x^D + k_y^D = \frac{\omega \sin \phi_i}{c}. \tag{5.12}$$

Let this combination of $(k_x^D, k_y^D, \omega)$ be denoted simply by the subscript $i$. Thus, the particular downgoing plane wave is $\hat{\hat{I}}_i$. The non-plane scattered wave may be decomposed into upgoing plane wave components, each of which is characterised by its angle of propagation $\phi_j$, defined by upgoing horizontal wavenumbers

$$k_x^U + k_y^U = \frac{\omega \sin \phi_j}{c}, \tag{5.13}$$

and denoted simply by the subscript $j$, a unique combination of $(k_x^U, k_y^U, \omega)$. Thus, for every

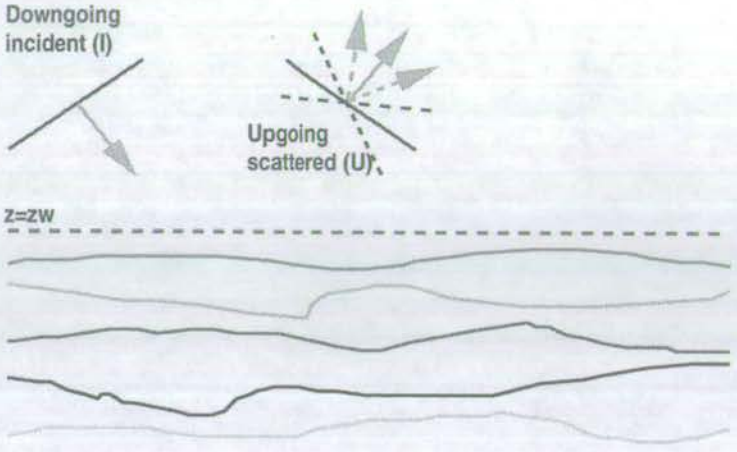


Figure 5.4: Plane waves propagating in a 3D medium in a half space of water.

downgoing plane wave $\hat{\hat{I}}_i$ incident on the three-dimensional earth, there are an infinite number of upgoing plane wave components $\hat{\hat{U}}_{ji}$ scattered by it. In the frequency-wavenumber domain, for a single plane wave arriving at an angle $\phi_i$, the reflection response is defined for the multitude of scattered angles $\phi_j$ by

$$\hat{\hat{U}}(k_x^U, k_y^U, z_w, \omega, k_x^D, k_y^D, z_s) = \hat{\hat{R}}(k_x^U, k_y^U, z_w, \omega, k_x^D, k_y^D, z_s)\hat{\hat{I}}(k_x^D, k_y^D, z_w, \omega, z_s). \tag{5.14}$$

In the more compact notation, (5.14) becomes,

$$\hat{\hat{U}}_{ji} = \hat{\hat{R}}_{ji}\,\hat{\hat{I}}_i,\ j = 1, \ldots, N, \tag{5.15}$$

where $N$ is the number of plane wave components per upgoing wave. Equation (5.15) is repeated with different $i$ for all of the $N$ possible downgoing incident plane waves.

The reflection response is referred to a plane $z = z_w$ above the sea floor and below the sources. To do this, the plane wave components in $\hat{\hat{I}}$, $\hat{\hat{U}}$ and $\hat{\hat{D}}$ must be referred to $z_w$. This is discussed later. The 3D nature of the earth is obvious by comparison with the 1D case: $N$ plane wave reflection responses are recovered per incident plane wave. The upgoing scattered plane wave components contain only primaries and internal multiples, so recovering the $\hat{\hat{R}}_{ji}$ for the 3D earth essentially deconvolves the source signature.

### In the presence of the free surface

When the the free surface is introduced, a more complicated picture results as shown in Figure 5.5. Any downgoing incident wave arriving at an angle $\phi_i$ is reflected from the 3D earth

resulting in many scattered plane wave components, travelling upwards and downwards. Both the upgoing and downgoing waves contain the primaries and the multiples. The free surface reflects an upgoing plane wave $\hat{\hat{U}}_{ji}$ into a downgoing plane wave component $\hat{\hat{D}}_{ji}$. However, there are many other downgoing scattered plane waves $\hat{\hat{D}}_{ki}$, propagating at an angle denoted by $\phi_k$ and defined by

$$k_x + k_y = \frac{\omega \sin \phi_k}{c}. \tag{5.16}$$

These downgoing plane wave components arise from the reflection of the incident wave $\hat{\hat{I}}_i$ from the plane wave component of the 3D reflection response denoted by $\hat{\hat{R}}_{ki}$. The reflection response is defined in terms of these plane wave components as

$$\begin{aligned}\hat{\hat{U}}(k_x^U, k_y^U, z_w, \omega, k_x^D, k_y^D, z_s) &= \hat{\hat{R}}(k_x^U, k_y^U, z_w, \omega, k_x^D, k_y^D, z_s)\hat{\hat{I}}(k_x^D, k_y^D, z_w, \omega, z_s) \\ &+ \frac{1}{(2\pi)^2}\int\int_{-\infty}^{\infty} \hat{\hat{R}}(k_x^U, k_y^U, z_w, \omega, k_x, k_y, z_s)\hat{\hat{D}}(k_x, k_y, z_w, \omega, k_x^D, k_y^D, z_s)\mathrm{d}k_x\mathrm{d}k_y.\end{aligned} \tag{5.17}$$

By comparison with (5.14), the primaries are obvious in the first term of (5.17). The second term represents the multiples, which are a result of all the downgoing plane wave components reflected from the different plane wave components of the three-dimensional reflection response.

Alternatively, the discretised version of equation (5.17) is

$$\hat{\hat{U}}_{ji} = \hat{\hat{R}}_{ji}.\hat{\hat{I}}_i + \frac{\Delta k_x \Delta k_y}{(2\pi)^2}\sum_{k=1}^{N} \hat{\hat{R}}_{jk}.\hat{\hat{D}}_{ki}, i = 1, \ldots, N, \tag{5.18}$$

where now the upgoing wave, the $j$th of $N$ possible plane wave components, is fixed, and $i$ is varied over the possible downgoing incident plane waves which contribute to it. Equations (5.18) are a set of simultaneous equations for every upgoing ($j$th) plane wave component, in terms of all the possible downgoing plane wave components (the $i$s), where the $\hat{\hat{R}}_{ji}$ are the unknown plane wave components of the three-dimensional reflection response. Equations (5.18) may be rewritten in matrix form, in which the structure is more obvious:

$$\begin{pmatrix} \hat{\hat{U}}_{j1} \\ \hat{\hat{U}}_{j2} \\ \vdots \\ \hat{\hat{U}}_{jN} \end{pmatrix} = \begin{pmatrix} \hat{\hat{I}}_1 + \hat{\hat{D}}'_{11} & \hat{\hat{D}}'_{21} & \cdots & \hat{\hat{D}}'_{N1} \\ \hat{\hat{D}}'_{12} & \hat{\hat{I}}_2 + \hat{\hat{D}}'_{22} & \cdots & \hat{\hat{D}}'_{N2} \\ \vdots & \vdots & \vdots & \vdots \\ \hat{\hat{D}}'_{1N} & \hat{\hat{D}}'_{2N} & \cdots & \hat{\hat{I}}_N + \hat{\hat{D}}'_{NN} \end{pmatrix} \begin{pmatrix} \hat{\hat{R}}_{j1} \\ \hat{\hat{R}}_{j2} \\ \vdots \\ \hat{\hat{R}}_{jN} \end{pmatrix}, \tag{5.19}$$

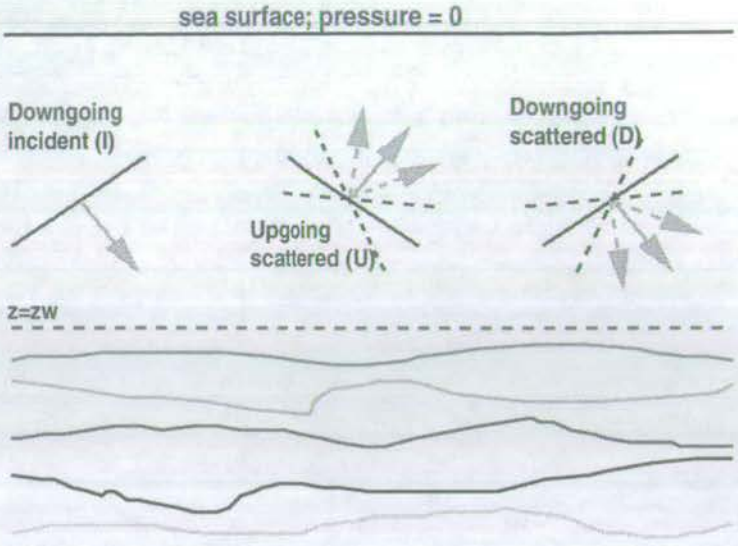


Figure 5.5: Plane waves propagating in a 3D medium in a water layer.

where

$$\hat{\hat{D}}'_{ki} = \frac{\Delta k_x \Delta k_y}{(2\pi)^2} \hat{\hat{D}}_{ki}. \tag{5.20}$$

Equations (5.19) are solved for every upgoing plane wave component $j$. The 1D solution is found in the leading diagonal terms. The off-diagonal terms represent the three-dimensionality of the earth. In words, the equations state: each $j$th upgoing plane wave component is the product of the $i$th incident downgoing plane wave with the $ji$th plane wave component of the reflection response, plus a sum of products (over $k$) of all the $ki$th scattered downgoing plane wave components with the $jk$th plane wave components of the reflection response.

The remainder of the chapter is devoted to an explanation of how the terms in equations (5.17) may be extracted from the measured data. Finally, the forward modelling step to produce multiple-free seismograms is discussed.

## 5.5 Separating the total field into constituent parts

In the analysis presented in section 5.4 a clear distinction is made between *incident* and *scattered* plane waves. To do so in practice requires a consideration of the measured data.

Figure 5.6 compares two hypothetical acquisition scenarios. In Figure 5.6(a) there is a source and a number of receivers in a half-space of water. The receivers measure the *incident* field only since there is no earth to produce a *scattered* field. In Figure 5.6(b), in which the earth is now present below a water layer, the receivers measure the *total* field, which is the sum of the incident and scattered fields. The incident field travels directly from the source to

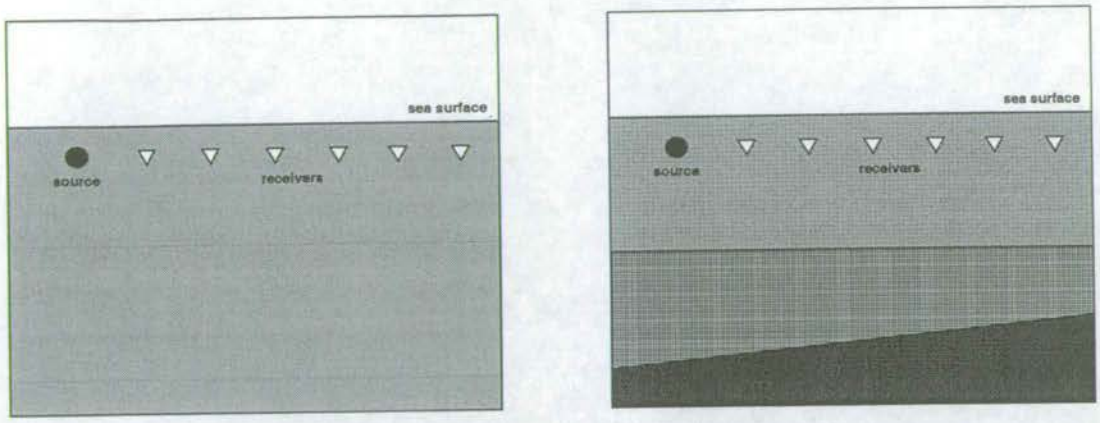


(a) Recording of the incident field.

(b) Recording of the total field.

Figure 5.6: Configurations for defining different parts of the recorded wavefield.

the receivers (the direct wave including the source ghost). The scattered field is all the energy reflected from the subsurface.

Before the analysis of section 5.4 may be applied, it is necessary to remove the incident field from the total field. There are several ways in which the incident field may be removed to yield the scattered field, some of which are explained below.

### Time-space domain muting

The incident field can be muted in the time-space domain, by multiplying by the filter

$$f_m(x,y,t) = \begin{cases} 0 & \text{while incident field exists,} \\ 1 & \text{otherwise.} \end{cases} \tag{5.21}$$

If the sources and receivers are far enough from the subsurface, as is the case with conventional streamer acquisition in deep water, this approach can be satisfactory. The concept is illustrated in Figure 5.7 with a shot record from the Rockall Trough, West of the United Kingdom (the source signature for this survey is discussed in section 6.4). The linear event starting near $t = 0$ is the direct arrival at the hydrophones. Because the water is deep the first primary reflections don't arrive at the hydrophones until about 4s. The first order multiple reflections are clearly visible around 8s.

The energy from the source dies away to the noise level by the time the hydrophones start recording the first reflections from the earth. For streamer data recorded in shallow water, or OBC data, time-space domain muting is difficult to apply because the incident field from the source interferes directly with the scattered field from the earth. Any attempt to mute the

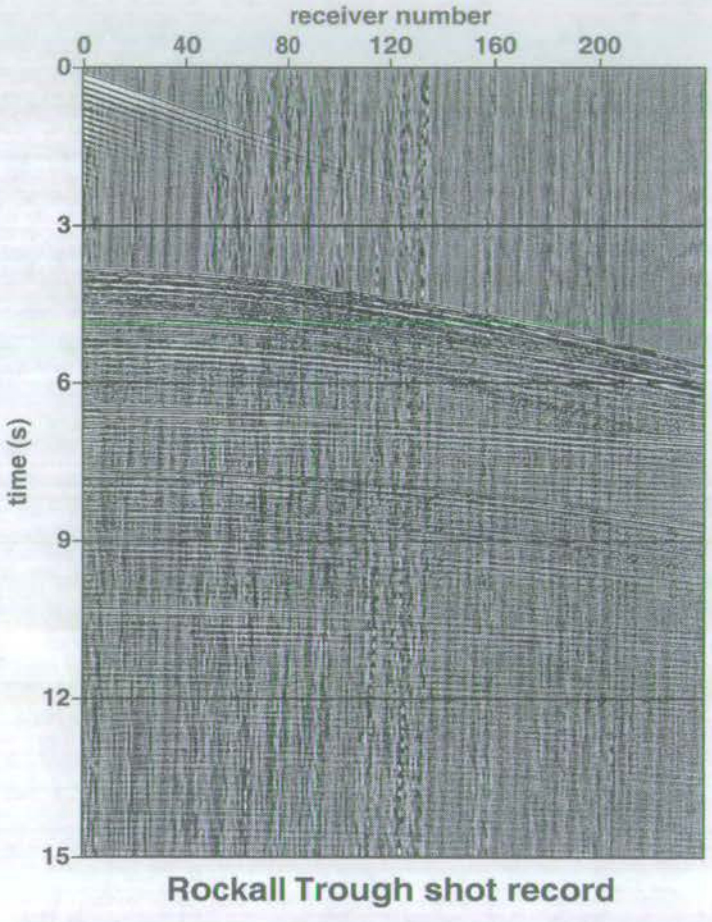


Figure 5.7: A common shot gather recorded in deep water, in which the incident field arrives at the hydrophones before the scattered field.

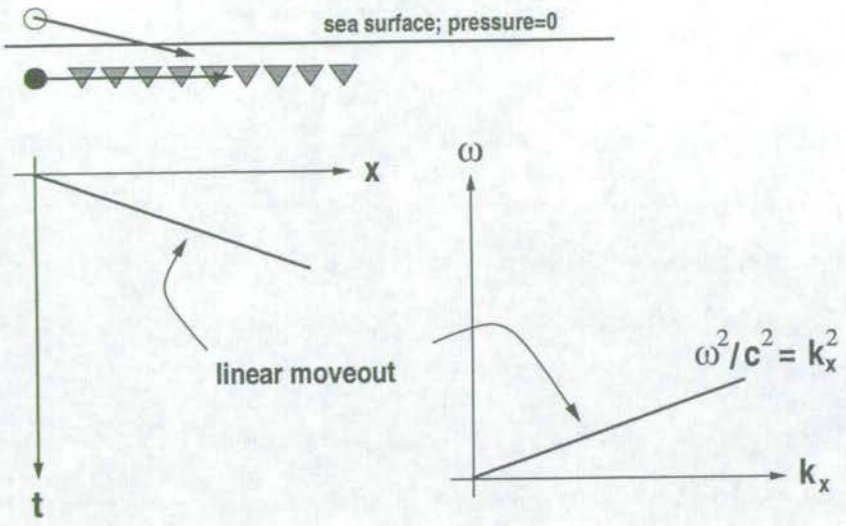


Figure 5.8: The upper part of the diagram shows the travel paths at the sea surface for the incident field from the source and its ghost to the receivers. The lower part shows the resulting linear moveout which plots as a straight line in the $(t,x)$ domain and the $(\omega,k_x)$ domain.

incident field removes some of the scattered field, which is required to accurately recover the reflection response and remove the multiples.

### Frequency-wavenumber domain filtering

It can be muted in the frequency-wavenumber domain. This is a plausible solution for streamer data with sources and receivers at the same depth, as shown in the upper part of Figure 5.8. The source and its ghost are denoted by the circles, and the receivers, by the triangles. The incident field travels through the water horizontally from source to receivers (true for the direct arrival, and approximately so for the ghost arrival). It gives rise to simple linear moveout in the time-space domain as indicated in the lower part of Figure 5.8.

In the frequency-wavenumber domain the incident field lies along the line $\frac{\omega^2}{c^2} = k_x^2 + k_y^2$, where $c$ is the velocity of sound in water. Figure 5.8 shows the 2D case, for which $k_y = 0$. This line corresponds to horizontally-travelling energy and may be removed with a carefully-constructed notch filter. There is always the possibility, however, that some of the required scattered field is removed as well.

It is not possible to do this with OBC data because the incident field has non-linear moveout in the time-space domain, which means the energy is spread out in the frequency-wavenumber domain.

### Modelling and subtraction

The airgun array can be modelled and an incident field calculated, and then subtracted from the field data in the time-space domain. Experience suggests that modelling does not ac-

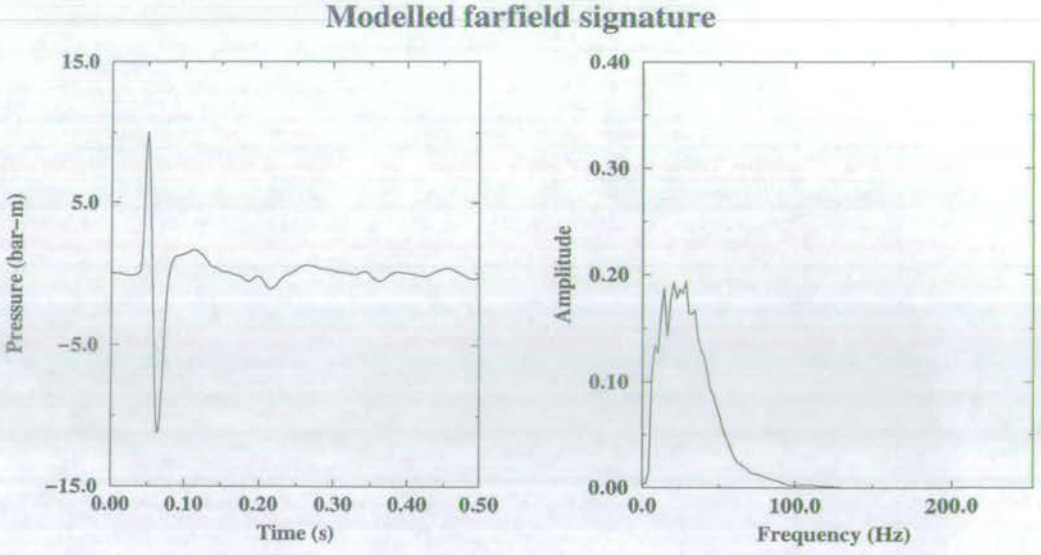


Figure 5.9: Vertically-travelling farfield wavelet estimated by modelling, and high-cut filtered to simulate the earth's attenuation (Courtesy of Shell UK Expro).

curately represent the pressure output of the guns under the field conditions that the arrays operate in. Figures 5.9 and 5.10 allow a comparison between a modelled vertically-travelling farfield wavelet and one constructed from source signature measurements. The wavelets have been filtered with a 40Hz high-cut filter to simulate the attenuating effect of the earth. Note that the modelled wavelet is deficient in low frequencies, and has significant phase differences from the deterministic wavelet. If the field data are not properly calibrated in units of pressure (they are usually voltages on tape), a discrepancy arises in scaling, due to airgun array modelling programs providing units of pressure. This makes subtraction more difficult.

### Measurement and subtraction

The source wavefield can be measured in the field, during acquisition of the total field data. The incident field may then be calculated and subtracted from the data to leave the scattered field. Chapter 3 explains the theory of how these measurements may be made in principle, and chapter 6 shows how they are made in practice, for several acquisition configurations.

Since the source signature is an integral part of the solution for the reflection response, this last method is the preferred way to isolate the scattered field. Section 5.6 describes the construction of the incident field from the source elements which make up a typical airgun array. The scattered field is then

$$p^{scat}(x,y,z,t,x_s,y_s,z_s) = p^{tot}(x,y,z,t,x_s,y_s,z_s) - p^{inc}(x,y,z,t,x_s,y_s,z_s), \tag{5.22}$$

where *scat*, *tot* and *inc* denote scattered, total, and incident fields, respectively.

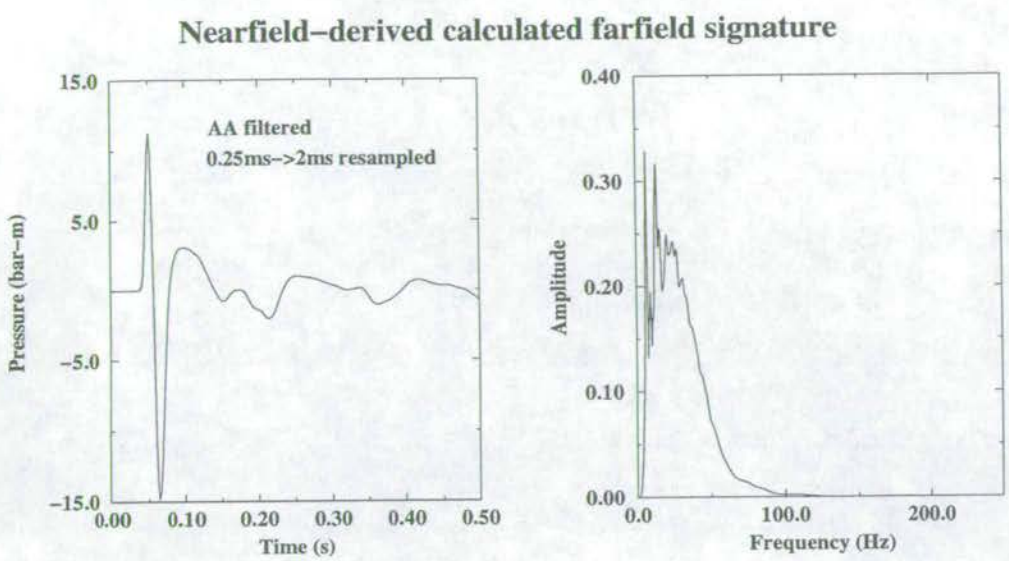


Figure 5.10: Vertically-travelling farfield wavelet constructed from measurements, and high-cut filtered to simulate the earth's attenuation.

## 5.6 Constructing the incident field

The incident field is defined in the presence of the sea surface, but in the absence of any reflectors as shown in Figure 5.6(a). The wavefield $p^{inc}(x,y,z,t,x_s,y_s,z_s)$ at the receivers at $(x,y,z)$, arriving from the source at $(x_s,y_s,z_s)$, is therefore composed of two parts: The direct wave is $i^d(x,y,z,t,x_s,y_s,z_s)$ and its reflection in the sea surface or ghost wave is $i^r(x,y,z,t,x_s,y_s,-z_s)$. The direct and ghost arrivals are related by the free surface boundary condition of vanishing pressure *at the receiver*, which is

$$i^d(x,y,z=0,t,x_s,y_s,z_s) = -i^r(x,y,z=0,t,x_s,y_s,-z_s). \tag{5.23}$$

The direct wave satisfies the inhomogeneous acoustic wave equation:

$$\nabla^2 i^d - \frac{1}{c^2}\frac{\partial^2 i^d}{\partial t^2} = -\sum_{k=1}^{n} q_k, \tag{5.24}$$

where

$$q_k = s_k(t)\delta(x-x_s-x_k)\delta(y-y_s-y_k)\delta(z-z_k) \tag{5.25}$$

is the $k$th notional monopole source, and $c$ is the velocity of sound in water. The monopole source and the source array are discussed in detail in chapters 3 and 6.

In a common shot gather the wavefield measured at each receiver is the point response from the source array. Fourier transformation over horizontal receiver coordinates and time decomposes the point response at the receivers into plane wave components. The incident

field transforms to

$$\tilde{I}^d(k_x,k_y,z,\omega,x_s,y_s,z_s)=\iiint_{-\infty}^{\infty} i^d(x,y,z,t,x_s,y_s,z_s)\exp(+i[\omega t-k_x x-k_y y])\mathrm{d}t\mathrm{d}x\mathrm{d}y, \tag{5.26}$$

so that (5.24) becomes

$$\left(-{k_x}^2-{k_y}^2+\frac{\partial^2}{\partial z^2}+\frac{\omega^2}{c^2}\right)\tilde{I}^d=\left({k_z}^2+\frac{\partial^2}{\partial z^2}\right)\tilde{I}^d=-\sum_{k=1}^{n}Q_k \tag{5.27}$$

where the vertical wavenumber is $k_z=\sqrt{\frac{\omega^2}{c^2}-{k_x}^2-{k_y}^2}$, and

$$Q_k=S_k(\omega)\exp(-ik_x[x_s+x_k])\exp(-ik_y[y_s+y_k])\delta(z-z_k). \tag{5.28}$$

The solution of (5.27) is

$$\tilde{I}^d(k_x,k_y,z,\omega,x_s,y_s,z_s)=\frac{i}{2k_z}\sum_{k=1}^{n}\tilde{Q}_k(z) \tag{5.29}$$

where

$$\tilde{Q}_k(z)=S_k(\omega)\exp(-ik_x[x_s+x_k])\exp(-ik_y[y_s+y_k])\exp(+ik_z|z-z_k|). \tag{5.30}$$

The solution (5.29) is a sum of $n$ plane wave decompositions. The decomposition is discussed in chapter 2. The $\frac{i}{2k_z}$ is known as the "obliquity factor" from diffraction theory in optics, which arises in the plane wave decomposition of a spherical wave. Each of the notional sources in the source array emits a spherical wave which is decomposed by the Fourier expansion along the receiver $x$- and $y$-axes.

The ghost wave results from the direct wave scattering off the sea surface. It therefore satisfies the homogeneous wave equation, which in the frequency-wavenumber domain is

$$\left(\frac{\omega^2}{c^2}-k_x^2-k_y^2+\frac{\partial^2}{\partial z^2}\right)\tilde{I}^d=0. \tag{5.31}$$

The solution is

$$\begin{aligned}\tilde{I}^r(k_x,k_y,z,\omega,x_s,y_s,-z_s)&=\tilde{I}^r(k_x,k_y,z=0,\omega,x_s,y_s,-z_s)\exp(+ik_z z)\\&=-\tilde{I}^d(k_x,k_y,z=0,\omega,x_s,y_s,z_s)\exp(+ik_z z),\\&=-\frac{i}{2k_z}\sum_{k=1}^{n}\tilde{Q}_k^r(z),\end{aligned} \tag{5.32}$$

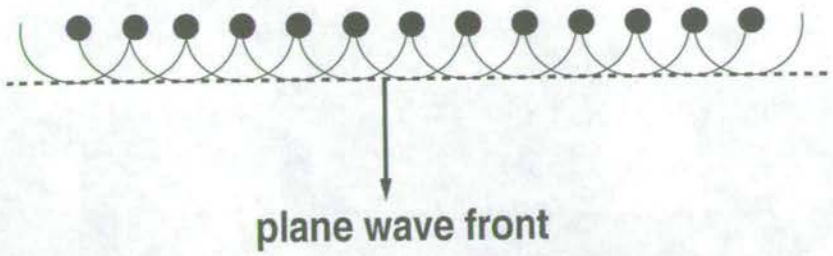


Figure 5.11: Simulation of a vertically-travelling plane wave by firing many closely spaced sources simultaneously.

where

$$\tilde{Q}_k^r(z) = S_k(\omega)\exp(-ik_x[x_s+x_k])\exp(-ik_y[y_s+y_k])\exp(+ik_z[z+z_k]). \tag{5.33}$$

Note that in the solution (5.32) to the homogenous wave equation there are no upgoing scattered waves, since, in this analysis, there are no scatterers below the receivers.

The incident field is the sum of the direct and ghost arrivals,

$$\tilde{I}(k_x,k_y,z,\omega,z_s,y_s,z_s) = \frac{i}{2k_z}\sum_{k=1}^{n}\tilde{Q}_k(z)\Big(1-\exp(ik_z[2z_k])\Big), \tag{5.34}$$

and inverse Fourier transformation over horizontal receiver coordinates and frequency yields $p^{inc}(x,y,z,t,x_s,y_s,z_s)$, the incident field arriving at the receivers in a common shot gather. This can be subtracted from the total field to yield the scattered field.

## 5.7 Creating a downgoing incident plane wave

A vertically-travelling plane wave may be constructed in the field by firing many sources simultaneously as shown in Figure 5.11. The plane wave front, indicated by the dashed line, is simulated by the constructive interference of the spherical waves from the closely spaced sources. If time delays are introduced to the firing times of each source, then plane waves at any angle may be generated. This is sometimes known as beam steering an array. Fortunately it is not necessary to resort to such a complicated, and error-prone, operational procedure to create plane waves. Fourier analysis of a wavefield allows different angles to be constructed mathematically.

The incident field for a single shot is defined in plane wave components by (5.34). To relate this to a notional boundary $z = z_w$ in the water requires an additional vertical phase

shift,

$$\tilde{I}(k_x,k_y,z_w,\omega,z_s,y_s,z_s)=\frac{i}{2k_z}\sum_{k=1}^{n}\tilde{Q}_k(z_w)\Big(1-\exp(ik_z[2z_k])\Big), \tag{5.35}$$

where

$$\tilde{Q}_k(z_w)=S_k(\omega)\exp(-ik_x[x_s+x_k]\exp(-ik_y[y_s+y_k]\exp(+ik_z|z_w-z_k|). \tag{5.36}$$

To construct incident plane waves for all angles (real and imaginary) requires all the sources to be summed up with the appropriate phase shifts corresponding to their spatial locations. Formally, the sumation is as follows

$$\hat{\tilde{I}}(k_x^D,k_y^D,z_w,\omega,z_s)=\int\int_{-\infty}^{\infty}\tilde{I}(k_x,k_y,z_w,\omega,x_s,y_s,z_s)\exp(+i[k_x^Dx_s+k_y^Dy_s])\mathrm{d}x_s\mathrm{d}y_s, \tag{5.37}$$

which is a Fourier tranformation over horizontal source coordinates. The incident plane waves described by (5.37) are required in equations (5.17) for the 3D reflection response.

## 5.8 Separating the scattered field into constituent parts

Section 5.4 gives an expression for the reflection response in terms of upgoing and downgoing plane wave components. However, after subtraction of the incident field the scattered field remains, containing upgoing and downgoing waves.

There are several ways to extract the upgoing and downgoing scattered waves, depending on the measurements available. Some of these are discussed in chapter 4. However, all of the techniques for wavefield separation essentially follow from the solution of the acoustic homogeneous wave equation. In the frequency-receiver wavenumber domain this is the Helmholtz equation:

$$\frac{\partial^2\tilde{P}^{scat}}{\partial z^2}+k_z^2\tilde{P}^{scat}=0, \tag{5.38}$$

where the scattered wavefield is

$$\tilde{P}^{scat}(k_x,k_y,z,\omega,x_s,y_s,z_s)=\int\int\int_{-\infty}^{\infty}p^{scat}(x,y,z,t,x_s,y_s,z_s)\exp(+i[\omega t-k_xx-k_yy])\mathrm{d}t\mathrm{d}x\mathrm{d}y, \tag{5.39}$$

and $k_z=\sqrt{\frac{\omega^2}{c^2}-k_x^2-k_y^2}$. The well-known solution of (5.38) is a sum of upgoing and down-

going waves, which may be expressed as

$$\tilde{P}^{scat}(k_x,k_y,z,\omega,x_s,y_s,z_s) = \tilde{U}(k_x,k_y,z=0,\omega,x_s,y_s,z_s)\exp(-ik_z z) + \tilde{D}(k_x,k_y,z=0,\omega,x_s,y_s,z_s)\exp(+ik_z z). \quad (5.40)$$

Key to separating the upgoing and downgoing waves is the free surface boundary condition: the wavefield is zero at the sea surface, and thus the upgoing and downgoing waves must exactly cancel. At the receivers below the surface, the upgoing and downgoing waves are out of phase and unequal.

A number of techniques have been developed which rely on pressure measurements at two depth levels, as in a dual streamer configuration (e.g. Sonneland *et al.* (1986); Monk (1990)). Section 4.2 explains how this deghosting works in principal. The methods used here are applied to individual plane wave components, which involves Fourier transformation over horizontal receiver coordinates and time.

### Ocean bottom cable acquisition

If pressure and the normal component of particle velocity are measured at the sea floor, the additional information provided by the particle velocity may be exploited, in much the same way as a second pressure measurement at another depth level. The up/down separation using these two measurements is derived in terms of an eigenvalue decomposition in chapter 2 in the analysis of waves in layered media. An alternative derivation is presented here, in brief, for completeness.

The pressure and particle velocity are related by the equation of motion, which in the frequency-wavenumber domain may be written as

$$\frac{\partial \tilde{P}}{\partial z} = i\rho\omega\tilde{V}_z, \quad (5.41)$$

in which the dependence on $(k_x,k_y,z,\omega,x_s,y_s,z_s)$ is understood. This dependence is written explicitly below only where necessary. From equation (5.41) follows the upgoing and downgoing waves of the vertical component of particle velocity in terms of the pressure:

$$\tilde{U} = -\frac{\rho\omega}{k_z}\tilde{U}_v, \quad \tilde{D} = +\frac{\rho\omega}{k_z}\tilde{D}_v, \quad (5.42)$$

where the subscript $v$ denotes that the wavefields are related to the particle velocity. Using equation (5.40), the analogous relation for the vertical component of particle velocity, plus equations (5.42), the upgoing and downgoing pressure waves may be separated:

$$2\tilde{U} = \tilde{P}^{scat} - \frac{\rho\omega}{k_z}\tilde{V}_z^{scat}, \quad 2\tilde{D} = \tilde{P}^{scat} + \frac{\rho\omega}{k_z}\tilde{V}_z^{scat}. \quad (5.43)$$

Equations (5.43) are implicitly evaluated at the receiver level at depth $z$. To refer these plane wave components to the notional boundary $z = z_w$ below the source requires the following phase shifts

$$\begin{aligned}\tilde{U}(k_x,k_y,z_w,\omega,x_s,y_s,z_s) &= \tilde{U}(k_x,k_y,z,\omega,x_s,y_s,z_s)\exp\left(-ik_z[z_w-z]\right),\\ \tilde{D}(k_x,k_y,z_w,\omega,x_s,y_s,z_s) &= \tilde{D}(k_x,k_y,z,\omega,x_s,y_s,z_s)\exp\left(+ik_z[z_w-z]\right).\end{aligned} \tag{5.44}$$

### Streamer acquisition

If pressure only is measured, the free surface boundary condition gives

$$\tilde{U}(k_x,k_y,z=0,\omega,x_s,y_s,z_s) = -\tilde{D}(k_x,k_y,z=0,\omega,x_s,y_s,z_s). \tag{5.45}$$

Use of (5.45) to substitute for the downgoing wave in equation (5.40) gives

$$\tilde{U}(k_x,k_y,z,\omega,x_s,y_s,z_s) = \frac{\tilde{P}^{scat}(k_x,k_y,z,\omega,x_s,y_s,z_s)}{1-\exp\Big(ik_z[2z]\Big)}, \tag{5.46}$$

whereas substitution for the upgoing wave gives

$$\tilde{D}(k_x,k_y,z,\omega,x_s,y_s,z_s) = -\frac{\tilde{P}^{scat}(k_x,k_y,z,\omega,x_s,y_s,z_s)\exp\Big(+ik_z[2z]\Big)}{1-\exp\Big(ik_z[2z]\Big)}. \tag{5.47}$$

Alternatively, the downgoing wave may be obtained from the scattered pressure and the upgoing wave directly

$$\tilde{D}(k_x,k_y,z,\omega,x_s,y_s,z_s) = \tilde{P}^{scat}(k_x,k_y,z,\omega,x_s,y_s,z_s) - \tilde{U}(k_x,k_y,z,\omega,x_s,y_s,z_s). \tag{5.48}$$

To refer these upgoing and downgoing plane wave components to the notional boundary $z = z_w$, the phase shifts given in (5.44) must be applied. The separation is achieved through deconvolution of the scattered pressure by the receiver ghost. This is similar to the approach presented by Levy and Stinson (1986).

Both of the principles described here for separating upgoing and downgoing waves are discussed in chapter 4 with reference to the different effects of the sea surface.

## 5.9 Analysis of the scattered field response to plane waves

To calculate the scattered field response to a *single shot*, the data are Fourier analysed with respect to horizontal receiver coordinates. This is the step performed in section 5.8. In the

frequency-receiver wavenumber domain the upgoing and downgoing plane wave components of the response are separated.

In section 5.4, however, the reflection response is defined in terms of upgoing and downgoing plane wave components in response to an incident *plane wave*. To derive the scattered field response to plane waves, the data must be reordered from common shot gathers to common receiver gathers, and then Fourier analysed with respect to the horizontal source coordinates:

$$\hat{\tilde{U}}(k_x,k_y,z_w,\omega,k_x^D,k_y^D,z_s)=\int\!\!\int_{-\infty}^{\infty}\tilde{U}(k_x,k_y,z_w,\omega,x_s,y_s,z_s)\exp(+i[k_x^Dx_s+k_y^Dy_s])\mathrm{d}x_s\mathrm{d}y_s,$$

$$\hat{\tilde{D}}(k_x,k_y,z_w,\omega,k_x^D,k_y^D,z_s)=\int\!\!\int_{-\infty}^{\infty}\tilde{D}(k_x,k_y,z_w,\omega,x_s,y_s,z_s)\exp(+i[k_x^Dx_s+k_y^Dy_s])\mathrm{d}x_s\mathrm{d}y_s. \tag{5.49}$$

The upgoing and downgoing plane wave components in equations (5.49) are the quantities required for equations (5.17).

Clearly, the transform over shot position does not affect the up/down separation in section 5.8, which depends on upgoing wavenumbers only. Therefore, the transforms over source coordinates may be applied to the scattered field(s), prior to separation into upgoing and downgoing plane wave components.

## 5.10 From the reflection response to multiple-free data

The reflection response in the five-dimensional transform domain is essentialy broadband, in frequency and in wavenumber. The directivity of the source array and the signatures of the firing elements comprising it are a common factor in $\hat{\tilde{U}}$, $\hat{\tilde{D}}$ and $\hat{\tilde{I}}$ of equations (5.19). Solution of the equations for $\hat{\tilde{R}}$ removes the directivity and the signatures associated with the array.

A new incident field is required which has desirable characteristics in the absence of the sea surface. By analogy with the direct part of the incident field, given by equations (5.29) and (5.30), the desired incident field $\tilde{I}^z$ is

$$\tilde{I}^z(k_x,k_y,z_w,\omega,x_s,y_s,z_s)=\frac{i}{2k_z^D}S^z(\omega)X^z(k_x^D)Y^z(k_y^D)\exp(+ik_z^D[z_w-z_s]). \tag{5.50}$$

The factor $S^z(\omega)$ has a smooth amplitude spectrum which results in a short wavelet with good resolving power in the time domain. To control the amplification of noise outside the signal bandwidth, it should ideally be based on the amplitude spectrum of the original signal (Ziolkowski, Underhill and Johnston, 1998). The factors $X^z(k_x^D)$ and $Y^z(k_y^D)$ perform a similar role for the wavenumber amplitude spectra in the $x$- and $y$-directions, replacing the extended array with something more localised in space.

The new downgoing incident plane waves containing the desired incident field are composed, as before, by summing over the horizontal source coordinates,

$$\hat{\tilde{I}}^z(k_x^D,k_y^D,z_w,\omega,z_s)=\int_{-\infty}^{\infty}\int\tilde{I}^z(k_x,k_y,z_w,\omega,x_s,y_s,z_s)\exp(+i[k_x^D+k_y^D])\mathrm{d}x_s\mathrm{d}y_s. \tag{5.51}$$

To produce seismograms, a downgoing incident plane wave must be propagated from a chosen level $z=z_s$ to the notional boundary $z=z_w$, where it is multiplied with the reflection response. The band-limited reflection response is now the scattered field response to a plane wave—it contains upgoing primary energy only. This upgoing plane wave may then be propagated back to the receiver level $z$ with an additional phase shift:

$$\hat{\tilde{P}}^0(k_x^U,k_y^U,z,\omega,k_x^D,k_y^D,z_s)=\hat{\tilde{R}}(k_x^U,k_y^U,z_w,\omega,k_x^D,k_y^D,z_s)\hat{\tilde{I}}^z(k_x^D,k_y^D,z_w,\omega,z_s)\exp(ik_z^U[z_w-z]), \tag{5.52}$$

where $\hat{\tilde{P}}^0$ denotes the multiple-free data. In the compacted notation this procedure is

$$\hat{\tilde{P}}^0_{ji}=\hat{\tilde{R}}_{ji}\hat{\tilde{I}}^z_i\exp(ik_z^U[z_w-z]). \tag{5.53}$$

It is carried out for all $j$ components of the reflection response. The downgoing plane wave is changed and the process is repeated.

Finally, the data are summed over source wavenumbers to isolate the contributions from each individual source position,

$$\tilde{P}^0(k_x^U,k_y^U,z,\omega,x_s,y_s,z_s)=\frac{1}{(2\pi)^2}\int_{-\infty}^{\infty}\int\hat{\tilde{P}}^0(k_x^U,k_y^U,z,\omega,k_x^D,k_y^D,z_s)\exp(-i[k_x^Dx_s+k_y^Dy_s])\mathrm{d}k_x^s\mathrm{d}k_y^s, \tag{5.54}$$

and then summed over receiver wavenumbers and frequency to recompose the spherical wave time signatures,

$$p^0(x,y,z,t,x_s,y_s,z_s)=\frac{1}{(2\pi)^3}\int_{-\infty}^{\infty}\iint\tilde{P}^0(k_x^U,k_y^U,z,\omega,x_s,y_s,z_s)\exp(-i[\omega t-k_x^Ux-k_y^Uy])\mathrm{d}\omega\mathrm{d}k_x\mathrm{d}k_y. \tag{5.55}$$

The data without multiples are $p^0(x,y,z,t,x_s,y_s,z_s)$.

## 5.11 Conclusions

Sea surface multiples can be removed by calculating plane wave reflection responses below the sea surface. In constructing these responses, the data themselves contain the information

required to eliminate the multiples. In addition to the reflection data at a two-dimensional grid of receivers, in response to a two-dimensional grid of shots, the spatial and temporal signature of the source array must be measured. As a result, the formulation deals explicitly with realisitic source arrays, such as those described in chapters 3 and 6.

The formulation is carried in the frequency-wavenumber domain where the problem and its solution are most easily conceptualised. By generalising the idea of plane waves in layered media, the data are manipulated to construct plane waves, and to analyse the plane wave response to these waves. In this domain, the multiples are eliminated with a direct solution, as opposed to the iterative method employed by most other wave-theoretical methods (see chapter 4).

# MARINE SEISMIC WAVEFIELD MEASUREMENTS

*Chapter 6*

## 6.1 Introduction

A key element in the multiple removal scheme is knowledge of the source signature. This signature is the source-time function at the source location, where the convolution with the impulse response of the earth occurs.

The acoustic wavefield generated by an oscillating bubble is isotropic because the bubble is a monopole at seismic frequencies. Thus, the dimensions of the physical bubble are small compared with the wavelengths of sound it radiates. However, it has non-linear and linear zones of wave propagation. The acoustic wavefield generated by an array of oscillating bubbles is, in general, directionally-dependent, because the dimensions of the array are comparable with the wavelengths generated. In this chapter two different methods of measuring the pressure wavefield of an array of airguns are presented with field data. The steps necessary to extract the source signature from the measurements are discussed in the context of constructing the incident field required in the multiple removal scheme (see chapter 5). A third approach is presented which allows the pressure and particle velocity wavefield to be determined for a single monopole airgun source, using experimental data. The three techniques differ in their measurement requirements.

## 6.2 Measurement of the wavefield in the zero field

A method for measuring the wavefield of an airgun array using pressure sensors situated in the non-linear zone of wave propagation has recently been published (Ziolkowski, 1998). The sensor may simultaneously measure the firing time of the gun relative to the time break, the pressure output performance of the gun with time, and the manifold pressure (Ziolkowski, 1999). Such measurements in the non-linear zone of wave propagation are referred to as being in the "zero field" (Walter, pers. comm.; Ziolkowski, 1999). The data in this section result from a study performed in collaboration with Bolt Technology Corporation, using a prototype zero-field pressure sensor called the Bolt Stainless Steel (BSS) sensor. A single air gun was used in the experiment. The data were shot in Seneca Lake NY, USA, in 1994.

A theory of source signature measurement which allows pressure sensors to be located

close to the airgun ports is given in Ziolkowski (1998). What follows here is a summary of the theory presented in that paper, and its relation to the experimental data from Seneca Lake published in Ziolkowski and Johnston (1998).

In the zero field, in the absence of the free surface and any other reflections, the pressure recorded by a single hydrophone at $(x,y,z)$ in response to a single air gun at $(x_s,y_s,z_s)$ is given by

$$p(r,t) = \frac{\rho}{r} f'(t-\frac{r}{c}) - \frac{\rho v^2(r,t)}{2}, \tag{6.1}$$

and the particle velocity is given by

$$v(r,t) = \frac{1}{rc} f'(t-\frac{r}{c}) + \frac{1}{r^2} f(t-\frac{r}{c}), \tag{6.2}$$

where $r = \sqrt{(x-x_s)^2+(y-y_s)^2+(z-z_s)^2}$, $\rho$ and $c$ are, respectively, the density and velocity of sound in water. $f'(t)$ is essentially the source-time function, or "source signature" and, in the incompressible case (see chapter 3), it is the time derivative of the wave function,

$$f(t) = \frac{1}{4\pi} \frac{dV_B}{dt}, \tag{6.3}$$

where $V_B$ is the bubble volume. (Multiplying $f'(t)$ by $\rho$ gives units of pressure $\times$ distance.) Thus, the source-time function is proportional to the rate of change of the bubble volume velocity. These expressions are derived in chapter 3.

Substitution of (6.2) into (6.1), and neglecting terms in $(rc)^{-2}$, yields

$$p(r,t) = \frac{\rho}{r} f'(t-\frac{r}{c}) - \frac{\rho}{2r^4} f^2(t-\frac{r}{c}). \tag{6.4}$$

In equations (6.1), (6.2) & (6.4), the second term on the right reflects the non-linear nature of the wave propagation associated with the bubble motion. This "afterflow" term (Cole, 1948) is negligible at distances greater than approximately 1m for pressure (Ziolkowski and Johnston, 1997); and at distances greater than about one wavelength for particle velocity (Stoffa and Ziolkowski, 1983). (See chapter 3 for details.) At distances much less than 1m, in the zero field, the afterflow is important. Hence, useage of pressure measurements at distances of less than 1m requires knowledge of the particle velocity. Put more precisely, a complete description of the wave propagation is provided by the wave function $f(t)$ and its first derivative $f'(t)$, as in equations (6.1) and (6.2). Therefore, once these quantities have been found, the pressure (and particle velocity) may be evaluated anywhere in the water.

A problem with measuring the wavefield in the zero field is that sometimes the sensor is in the water, and at other times it is inside the airgun bubble: a measurement made in the water is related to the pressure elsewhere in the water through the acoustic wave equation; a

measurement made inside the bubble is related to the pressure outside in the water through the equation of motion of the bubble wall. The theory of Ziolkowski (1998) provides a description of the bubble dynamics to a level of accuracy that is commensurate with the description of the non-linear acoustic wave propagation in the water, in the vicinity of the bubble wall. This allows a recursive scheme to be developed which calculates $f(t)$ and $f'(t)$ in the water by numerically integrating the bubble radius and the particle velocity. When the pressure sensor is outside the bubble (as determined from the dynamic bubble radius—see below), the particle velocity is evaluated at the sensor using the acoustic wave equation. When the sensor is inside the bubble, the particle velocity at the bubble wall is evaluated by integrating the equation of motion of the bubble.

### Outside the bubble

Assuming an initial value for the particle velocity $v(r,t)$ at time $t=\tau$, the values of $f(t)$ and $f'(t)$ may be found by rearranging equations (6.2) and (6.1):

$$f(\tau-\frac{r}{c}) = r^2\left(v(r,\tau) - \frac{p(r,\tau)}{\rho c} - \frac{v^2(r,\tau)}{2c}\right) \qquad (6.5)$$
$$f'(\tau-\frac{r}{c}) = r\left(\frac{p(r,\tau)}{\rho} + \frac{v^2(r,\tau)}{2}\right).$$

The value of the particle velocity at a subsequent time $v(r,\tau+\Delta\tau)$ may be found by numerical integration using a truncated Taylor series expansion:

$$v(r,\tau+\Delta\tau) = v(r,\tau) + v'(r,\tau)\Delta\tau + v''(r,\tau)\frac{\Delta\tau^2}{2}. \qquad (6.6)$$

Similarly, assuming an initial bubble radius $R(t)$ at time $t=\tau$, the value at a subsequent time is

$$R(r,\tau+\Delta\tau) = R(\tau) + \dot{R}(\tau)\Delta\tau + \ddot{R}(\tau)\frac{\Delta\tau^2}{2}. \qquad (6.7)$$

The purpose of the scheme is to calculate $f(t)$ and $f'(t)$ on a sample-by-sample basis, stepping forward by $\Delta\tau$, using equation (6.6) to update the particle velocity, and using equation (6.7) to follow the movement of the bubble.

Equation (6.6) requires $v'(r,\tau)$ and $v''(r,\tau)$ which may be found by successive differentiation of equation (6.2). This, in turn, requires $f'(\tau-\frac{r}{c})$, $f''(\tau-\frac{r}{c})$ and $f'''(\tau-\frac{r}{c})$ which may be found by successive differentiation of equation (6.1). The pressure measurement $p(r,t)$ may be differentiated to get $p'(r,t)$ and $p''(r,t)$.

Evaluation of $v(r,\tau)$ and $v'(r,\tau)$ at the bubble wall (using (6.2) and its derivative), gives the $\dot{R}(\tau)$ and $\ddot{R}(\tau)$ required for equation (6.7). Evaluation of equation (6.1) at the bubble wall

provides the dynamic bubble pressure $p(R,\tau)$, which is the difference between the pressure in the bubble and hydrostatic pressure. The absolute pressure in the bubble is simply

$$P_B(\tau) = p_\infty + p(R,\tau), \tag{6.8}$$

where $p_\infty$ is hydrostatic pressure.

### Inside the bubble

Assuming initial values for the bubble radius $R(t)$ and the bubble wall velocity $\dot{R}(t)$ at time $t = \tau$, the values of the wave function and its first derivative at the bubble wall are (neglecting the time delay $R/c$)

$$f(\tau) = R^2\left(\dot{R}(\tau) - \frac{p(\tau)}{\rho c} - \frac{\dot{R}^2(\tau)}{2c}\right) \tag{6.9}$$

$$f'(\tau) = R\left(\frac{p(\tau)}{\rho} + \frac{\dot{R}^2(\tau)}{2}\right).$$

The value of the bubble radius $R$ and the bubble wall velocity $\dot{R}$ at a subsequent time may be found by numerical integration:

$$R(\tau+\Delta\tau) = R(\tau) + \dot{R}(\tau)\Delta\tau + \ddot{R}(\tau)\frac{\Delta\tau^2}{2}, \tag{6.10}$$

$$\dot{R}(\tau+\Delta\tau) = \dot{R}(\tau) + \ddot{R}(\tau)\Delta\tau + \dddot{R}(\tau)\frac{\Delta\tau^2}{2}. \tag{6.11}$$

The purpose of the scheme is to compute $f(t)$ and $f'(t)$ at the bubble wall, and hence the pressure anywhere in the water. The instantaneous pressure in the bubble is calculated as the bubble moves back and forth. The key assumption here, as in equation (6.8) above, is that the pressure is uniform throughout the bubble, including at the bubble wall, and decays with distance away from the bubble wall. This implies that knowledge of the pressure at the bubble wall connects the advancing pressure wave in the water with the absolute pressure inside the bubble.

Equations (6.10) and (6.11) require the bubble wall acceleration $\ddot{R}$, and its derivative $\dddot{R}$. These can be found from the equation of motion of the bubble wall, equation (3.32).

### The Seneca Lake experiment

An experiment was conducted to measure the pressure in the non-linear zero field using Bolt's gun-mounted BSS sensor, and in the near and far fields using conventional hydrophones. The BSS had previously been used to measure the internal time break of the gun, but the gun had

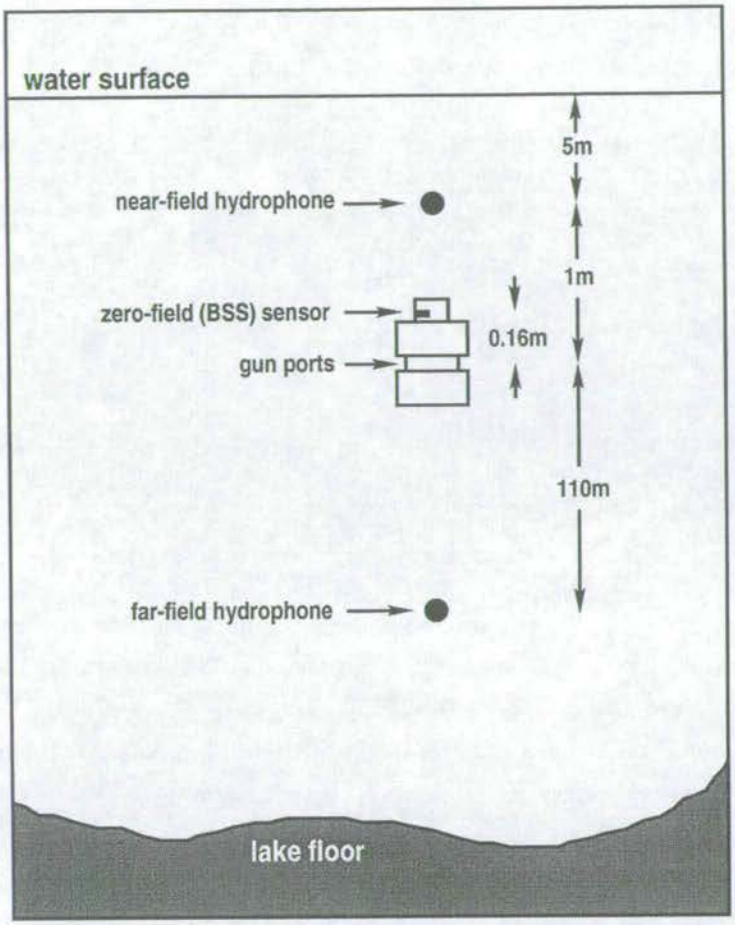


Figure 6.1: The acquisition set-up for the test in Seneca Lake.

been modified to allow the sensor to measure the pressure in the water instead. The purpose of the experiment was to test the feasibilty of the BSS as a means of measuring the source signature. Using the zero-field measurement, it is possible to predict the pressure at any distance from the gun, such as at the near- or far-field hydrophones, where the computation can be checked.

Figure 6.1 shows the acquisition set-up for this experiment. A single air gun is deployed 6m below the lake surface. A near-field hydrophone is situated 1m above the gun ports; the zero-field sensor is attached to the gun 0.16m from the gun ports; and a far-field hydrophone is situated approximately 110m below the gun. The measurements at the three sensors are shown in Figure 6.2. Note that the two hydrophone measurements have units related to pressure, whereas the zero-field sensor has units of volts. The hydrophones were calibrated. Each is of a known sensitivity which is independent of frequency. However, the sensitivity of the BSS is frequency dependent. Table 6.1 shows results of a sensitivity and phase analysis performed on the sensor after the Seneca Lake experiment. The analyis is for the 6-40 Hz frequency

range only, and the phase estimates were unreliable due to the noise floor of the sensor being too high. Figure 6.3(a) shows the data points from Table 6.1 in the 6-40 Hz range for

| frequency (Hz) | sensitivity (volts/Pa) | phase (degrees) |
|---|---|---|
| 6 | 0.007 | 60 |
| 8 | 0.0085 | 55 |
| 10 | 0.01 | 50 |
| 12 | 0.011 | 46 |
| 14 | 0.011 | 38 |
| 16 | 0.012 | 35 |
| 18 | 0.0115 | 32 |
| 20 | 0.0125 | 25 |
| 30 | 0.013 | 18 |
| 40 | 0.014 | 15 |

Table 6.1: Sensitivity and phase analysis of the BSS sensor.

amplitude (above) and phase (below), plotted as squares. Through these points is constructed a possible amplitude and phase spectrum. The amplitude spectrum includes an anti-alias recording filter, and the phase is constrained to be minimum. The resulting time-domain response corresponding to this amplitude and phase is shown in Figure 6.3(b). Deconvolution of the BSS measurement for this response should yield the pressure at the BSS which could then be used in the scheme described above. Unfortunately the response shown in Figure 6.3 is not accurate enough to obtain the true pressure at the BSS.

### Pressure in the near field

Starting with the measurement at the near-field hydrophone, it is possible to apply the theory given above to predict the pressure in the zero field. This necessarily calculates the non-linear acoustic radiation near to the gun ports, as well as the motion of the bubble wall and the pressure inside the bubble.

The first step in the procedure is to remove any DC signal from the measurement by calculating the mean value and removing it. DC signal corresponds to energy at zero frequency, which clearly should not exist, but often is introduced by recording circuits. The second step is to resample to a higher sampling interval. Because the scheme described above is recursive, propagation of errors could be a problem. Transforming the data to the frequency domain and increasing the Nyquist frequency by a factor of 4 with zero padding is adequate (see below).

The measurement at the hydrophone (where the afterflow term is negligible) is

$$m(r,t) = h\Big[\frac{\rho}{r(t)} f'(t - \frac{r(t)}{c}) - \frac{\rho}{r^g(t)} f'(t - \frac{r^g(t)}{c})\Big], \tag{6.12}$$

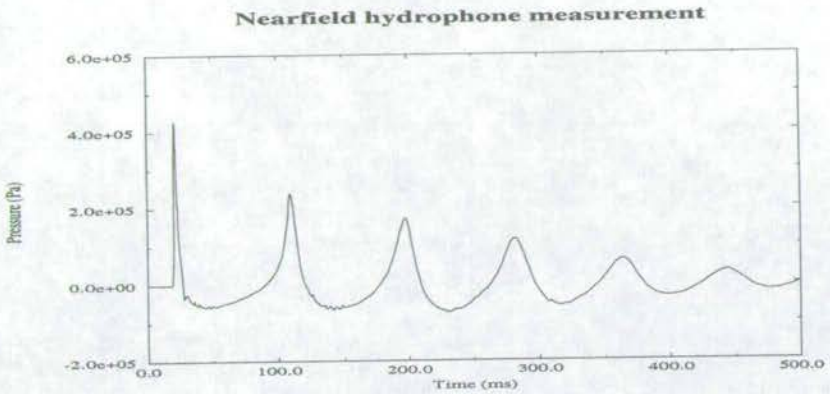


(a) The pressure recorded at the near-field hydrophone.

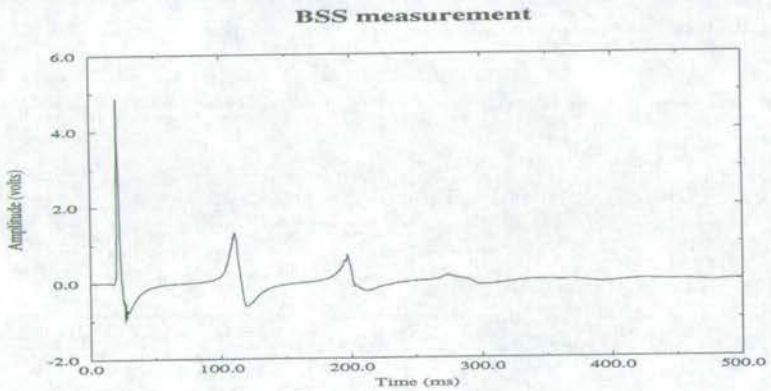


(b) The voltage recorded at the zero-field sensor.

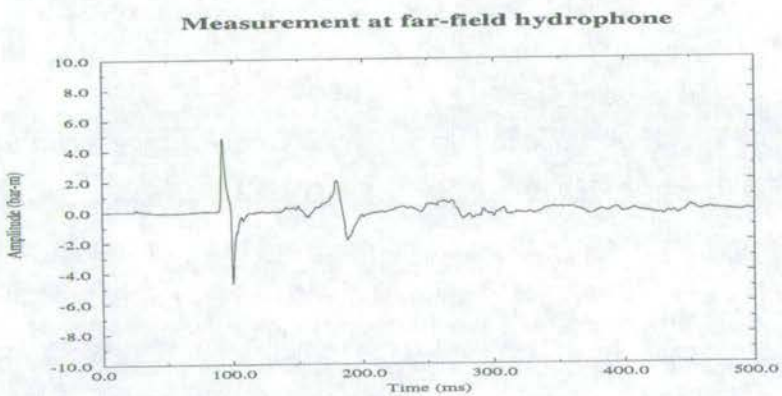


(c) The pressure recorded at the far-field hydrophone.

Figure 6.2: The Seneca Lake data for one air gun pop.

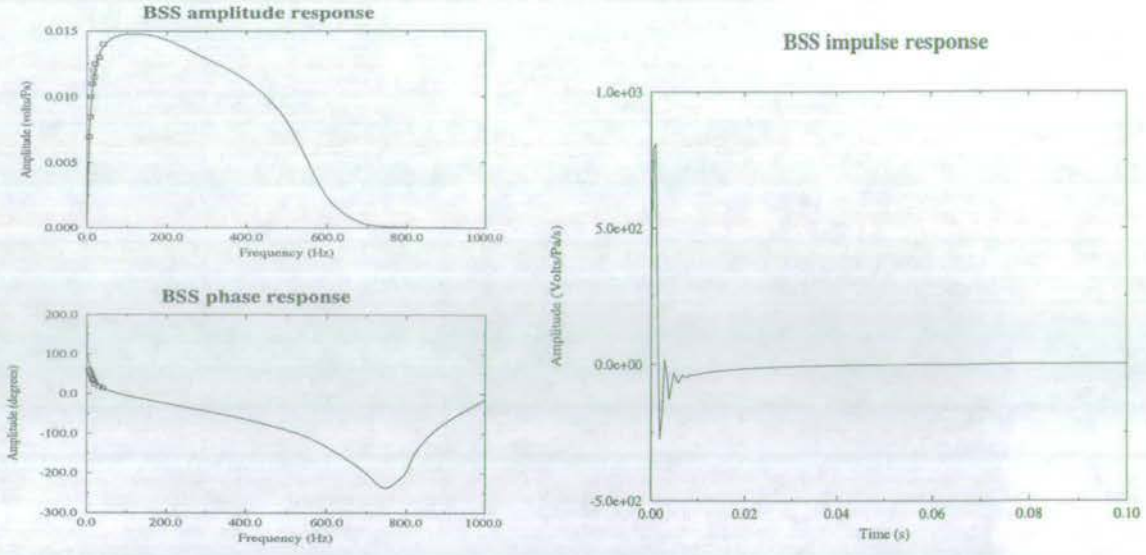


(a) Frequency domain

(b) Time domain

Figure 6.3: Impulse response of the BSS sensor. (b) is the Fourier transform of (a).

where $h$ is the (known) sensitivity of the hydrophone, and

$$r(t) = \sqrt{(x-x_s)^2+(y-y_s)^2+(z-[z_s-v_z t])^2} \tag{6.13}$$
$$r^g(t) = \sqrt{(x-x_s)^2+(y-y_s)^2+(z+[z_s-v_z t])^2}$$

are the time-dependent distances for the direct and ghost arrivals, caused by the bubble rising towards the surface with constant velocity $v_z$. The bubble rise velocity is typically around $-1.0\text{ms}^{-1}$ (Ziolkowski and Johnston, 1997). Note that equation (6.12) is different from the theoretical expression (6.1), and includes the reflection in the sea surface of the outward-travelling wave from the bubble.

At 1m the afterflow term in (6.1) is negligible, and the outgoing pressure from the bubble is obtained from the measurement at the hydrophone as

$$p(r,t) = \frac{m(r,t)}{h} + \frac{\rho}{r^g(t)} f'(t - \frac{r^g(t)}{c}). \tag{6.14}$$

The addition of the term on the right removes the source ghost. The source ghost arrives at a time $\tau = \frac{r^g(t)-r(t)}{c}$ after the direct arrival. Therefore, causality ensures that the data exist, which do not include, or have already been corrected for, the ghost term, to use as the corrections on the right-hand side of equation (6.14). The time $\tau$ is, in general, a non-integer value, and the required values of $f'(t)$ are found by interpolation of the previously recorded values, as shown in Figure 6.4. The pressure at the hydrophone at 1m and the deghosted pressure are

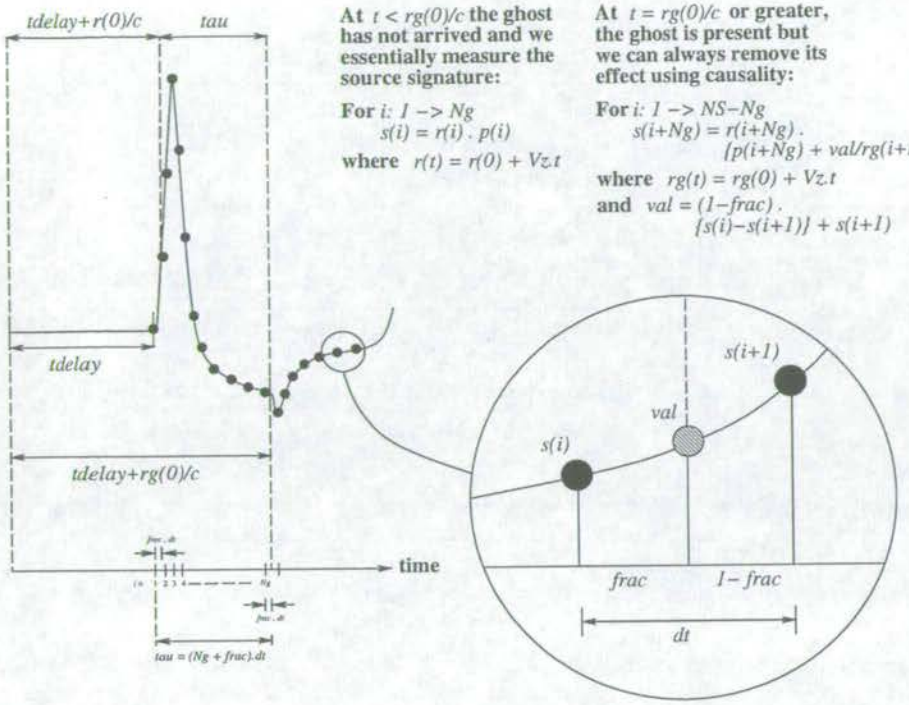


Figure 6.4: The time-varying interpolation used to remove the source ghost reflection.

shown in Figure 6.5.

The first and second derivatives of the outward-travelling pressure wave (Figure 6.5(b)) are required to calculate $p'(t)$ and $p''(t)$. These are calculated with a time-domain finite difference scheme and are shown in Figure 6.6. Resampling the data by the factor of 4 described above, permits $p(t)$ to be reconstructed faithfully from $p'(t)$ and $p''(t)$ using the truncated Taylor series expansion as an integration scheme.

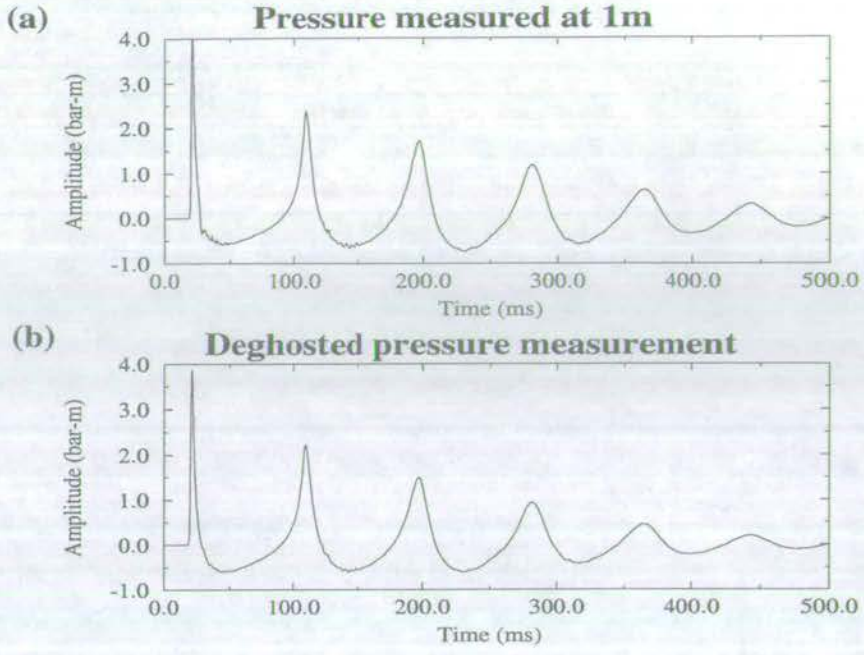


Figure 6.5: The pressure at 1m: (a) with ghost; (b) without ghost.

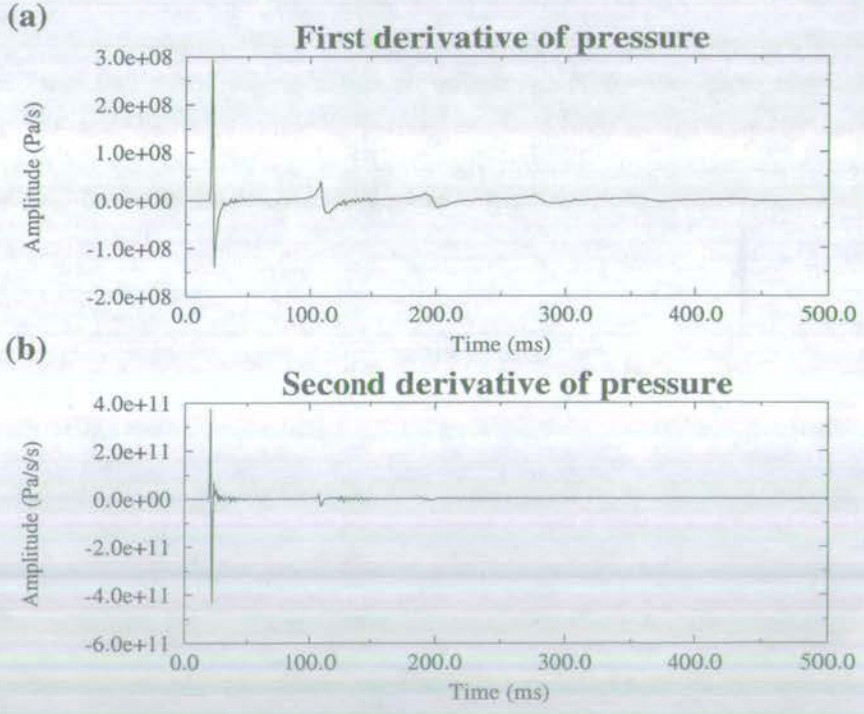


Figure 6.6: (a) The first derivative; (b) the second derivative, of the deghosted near-field pressure.

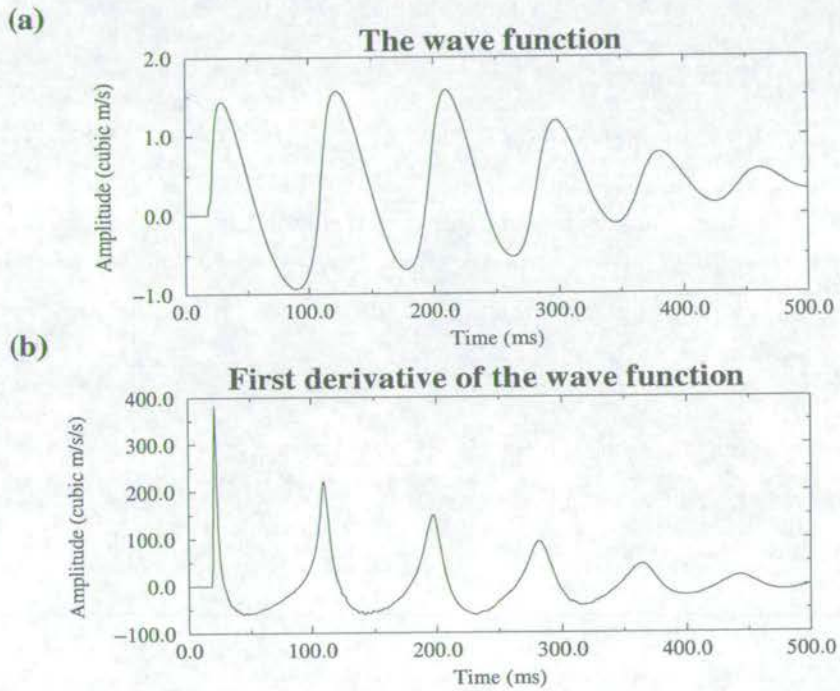


Figure 6.7: (a) The wave function $f(t)$; (b) the first derivative of the wave function $f'(t)$.

### Pressure in the zero field

The next step in the scheme recursively computes the values of the material quantities associated with the fluid flow and the acoustic radiation caused by the bubble motion. This requires two constants to integrate each of, the particle velocity $v(r,\tau)$, and the bubble radius $R(\tau)$. These are found by trial-and-error, by predicting the pressure at a second location. The second location was chosen to be the pressure at the BSS (zero-field) sensor. The constants of integration are adjusted until the peak amplitude predicted in the zero field matches the measurement there.

The initial particle velocity at the hydrophone was found to be $0.13\text{ms}^{-1}$, which allowed the wave function to be integrated using equations (6.5) and (6.6). The wave function and its first derivative are shown in Figure 6.7.

The initial bubble radius was found to be 0.133m. This value begins a recursion which permits calculation of the bubble radius, bubble wall velocity and internal pressure of the bubble. The bubble radius and bubble wall velocity are essentially integrated using the two constants of integration. The bubble properties are plotted in Figure 6.8. Monitoring the dynamic bubble radius is important for knowing at which times the zero-field sensor, a distance $r_z$ from the centre of the gun ports, is outside the bubble. At this stage in the bubble's development the pressure at the sensor is given by

$$p(r_z,\tau) = \frac{\rho}{r_z} f'(\tau - \frac{r_z}{c}) - \frac{\rho v^2(r_z,\tau)}{2}. \tag{6.15}$$

At such times that the zero-field sensor is inside the bubble, the pressure is given by

$$p(r_z,\tau) = P_B(\tau) = p_\infty + \frac{\rho}{R(\tau)} f'(\tau) - \frac{\rho \dot{R}^2(\tau)}{2}. \tag{6.16}$$

Figure 6.9 shows the pressure calculated at the zero-field sensor, after convolution with the estimated instrument response of Figure 6.3. The agreement between the actual measurement and that predicted using this scheme is good, showing that the the non-linear nature of the particle motion and acoustic wave propagation are well described in the zero field.

For completeness, the pressure in the far field is predicted using equation (6.1), including the reflection from the lake surface. This is shown in Figure 6.10 compared with the actual measurement made by the far-field hydrophone. Again, the agreement is good, although the measurement suffers from reflections from the sea bottom and objects in the lake.

This section demonstrates a recursive scheme capable of correctly predicting the non-linear acoustic radiation experienced when pressure measurements are made very close to an airgun. The extension of the theory to arrays of airguns is presented in Ziolkowski (1998). Using measurements made in the zero field to predict the pressure elsewhere has yet to be demonstrated on experimental or field data.

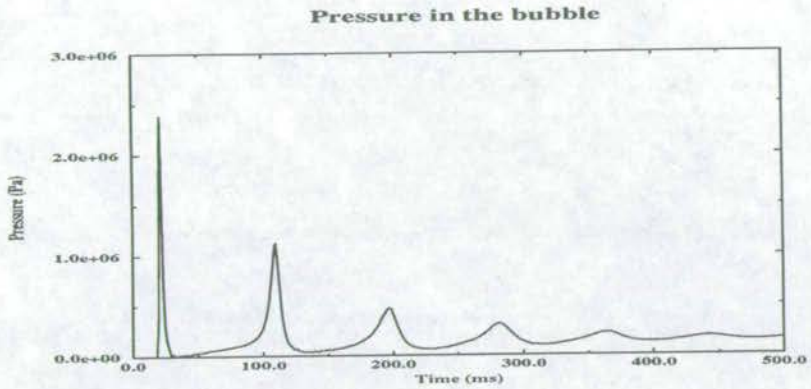


(a) The pressure in the bubble.

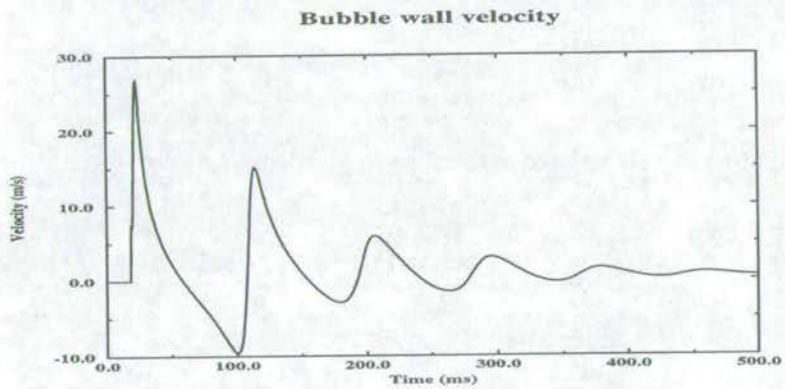


(b) The radius of the bubble wall.

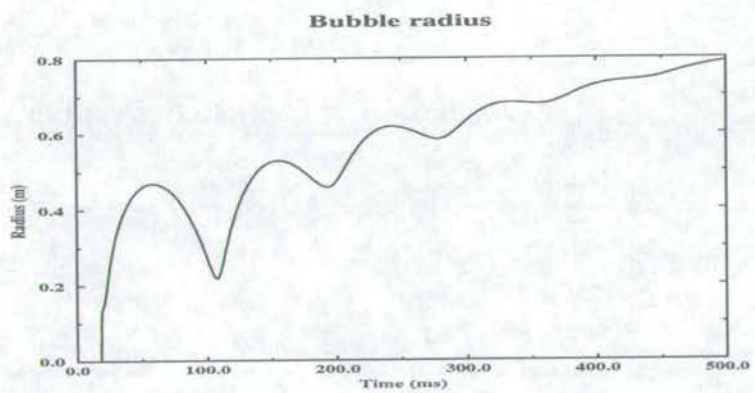


(c) The volume of the bubble.

Figure 6.8: The dynamic quantities associated with the oscillating bubble.

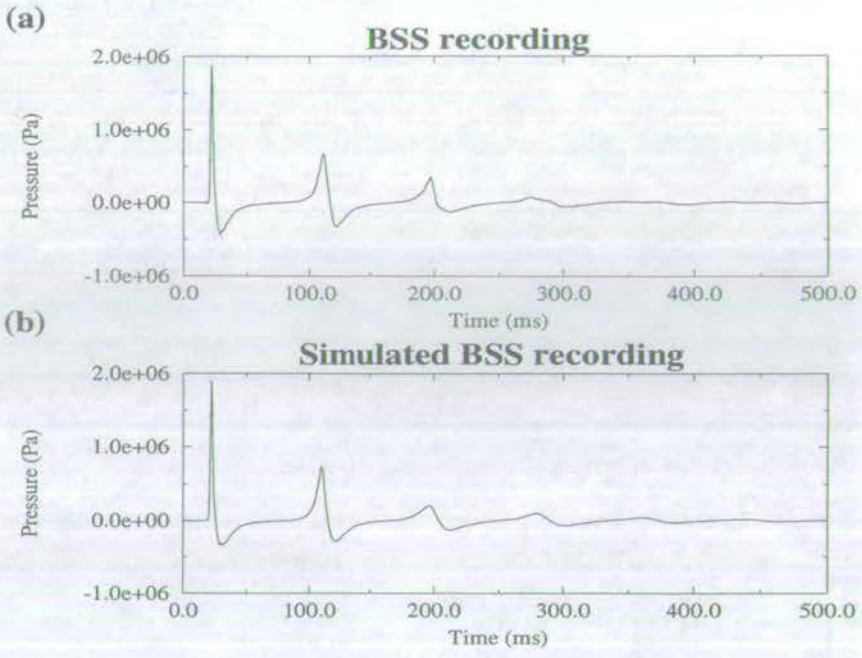


Figure 6.9: The voltage at the zero-field sensor: (a) measured; (b) simulated.

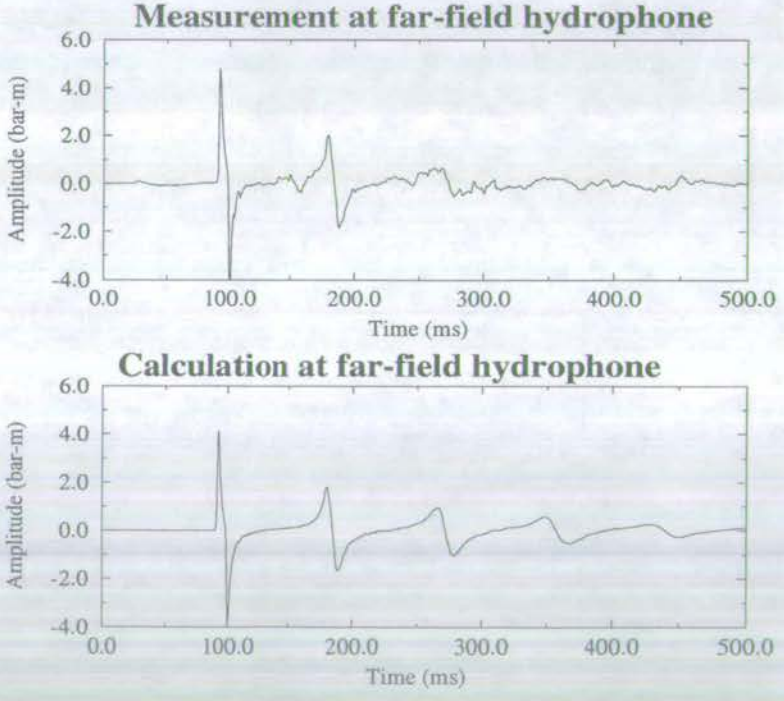


Figure 6.10: The measured pressure (above) and simulated pressure (below) at the far-field hydrophone.

## 6.3 Measurement of the wavefield in the near field

A method for measuring the wavefield of an airgun array using pressure sensors in the (near-field) linear zone of wave propagation has existed for many years (Ziolkowski *et al.*, 1982, Parkes *et al.*, 1984). Historically, the patent to the method (Ziolkowski *et al.*, 1984) is owned by Schlumberger Geco-Prakla and BP Amoco, the former of whom developed a product for source signature estimation (SSE) called Trisor (Lunde *et al.*, 1995). This is the only commercially available system for seismic source measurement using near-field hydrophones. The data in this section result from a study performed for Enterprise Oil plc., to validate the measurements and calculations of the Trisor system using production seismic data. The data were shot in the North Sea in August 1995.

The theory of source signature measurement using near-field hydrophones is well documented (Ziolkowski *et al.*, 1982; Parkes *et al.*, 1984), and a means of quality controlling the measurements and the wavefield calculation is discussed in Ziolkowski and Johnston (1997). What follows here is a summary of the theory presented in these papers.

In the near field, the pressure recorded by a single hydrophone at $(x,y,z)$ in response to a single airgun at $(x_s,y_s,z_s)$ is given by

$$p(x,y,z,t) = \frac{1}{r}s(t-\frac{r}{c}) - \frac{1}{r^g}s(t-\frac{r^g}{c}), \tag{6.17}$$

where $s(t) = \rho f'(t)$, $\rho$ and $c$ are as before, and

$$r = \sqrt{(x-x_s)^2+(y-y_s)^2+(z-z_s)^2},$$

and

$$r^g = \sqrt{(x-x_s)^2+(y-y_s)^2+(z+z_s)^2}.$$

The first term is due to the direct pressure wave from the source while the second term is its reflection in the sea surface; the sea surface reflection coefficient is $-1$. Note that the non-linear "afterflow" term is not present. The important point of the method (Ziolkowski *et al.*, 1984) is that the hydrophones are positioned in the linear near-field, so that the afterflow is negligible. The $s(t)$ is known as the "notional source" (Ziolkowski *et al.*, 1982), and is the monopole pressure output of the gun taking the effect of interaction with the free surface into account. The oscillation of a bubble in isolation is different from its oscillation in the presence of another bubble. Interaction describes the change in behaviour of the bubble. Suppose there are $n$ guns of varying sizes, as in an array, each displaced $(x_k,y_k,z_k)$ from the nominal source

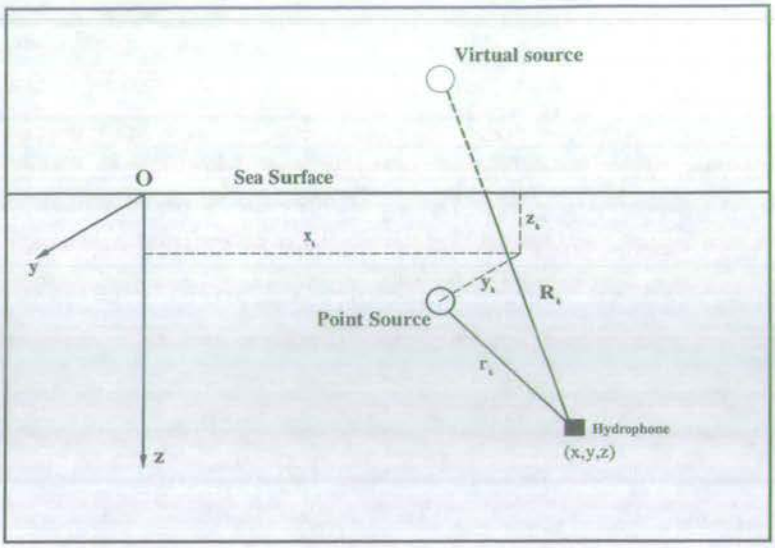


Figure 6.11: Geometry of a point source, its virtual image in the sea surface and a hydrophone.

location $(x_s, y_s, z_s)$, then the pressure recorded by a single hydrophone is

$$p(x,y,z,t) = \sum_{k=1}^{n} \left[ \frac{1}{r_k} s_k(t - \frac{r_k}{c}) - \frac{1}{r_k^g} s_k(t - \frac{r_k^g}{c}) \right], \tag{6.18}$$

where

$$r_k = \sqrt{(x - x_s - x_k)^2 + (y - y_s - y_k)^2 + (z - z_s - z_k)^2}, \tag{6.19}$$
$$r_k^g = \sqrt{(x - x_s - x_k)^2 + (y - y_s - y_k)^2 + (z + z_s + z_k)^2}.$$

This represents one equation in $n$ unknowns which is insoluble. In order to find the $s_k(t), k = 1, \ldots, n$, $n$ hydrophone measurements are required. Let the source positions be denoted simply by the subscript $k$ and the hydrophone locations by $i$ then

$$p_i(t) = \sum_{k=1}^{n} \left[ \frac{1}{r} s_k(t - \frac{r_{ik}}{c}) - \frac{1}{r^g} s_k(t - \frac{r_{ik}^g}{c}) \right], \; i = 1, \ldots, n \tag{6.20}$$

where

$$r_{ik} = \sqrt{(x_i - x_k)^2 + (y_i - y_k)^2 + (z_i - z_k)^2},$$

and

$$r_{ik}^g = \sqrt{(x_i - x_k)^2 + (y_i - y_k)^2 + (z_i + z_k)^2}.$$

These equations represent the ideal situation of static bubbles and stationary hydrophones

recording pressure. In practice, each airgun or cluster is suspended from a frame which houses a hydrophone. The frames are hung from a float which is towed behind the ship moving forward. When a gun fires, the bubble it emits is dragged backwards relative to the ship (and all the hydrophones) with velocity $v_x$, and since the bubbles are buoyant they float towards the surface with velocity $-v_z$ (see Figure 6.12). The hydrophones respond to changes in pressure but record voltages with (often unknown) sensitivies to convert these readings to pressure. The relative motion between bubbles and hydrophones introduces time-dependent distances $r_{ik}(t)$ and $r^g_{ik}(t)$:

$$m_i(t) = h_i \sum_{k=1}^{n} \left[ \frac{1}{r_{ik}(t)} s_k(t - \frac{r_{ik}(t)}{c}) - \frac{1}{r^g_{ik}(t)} s_k(t - \frac{r^g_{ik}(t)}{c}) \right], \; i = 1, \ldots, n, \tag{6.21}$$

where

$$r_{ik}(t) = \sqrt{(x_i - [x_k + v_x t])^2 + (y_i - y_k)^2 + (z_i - [z_k - v_z t])^2},$$

$$r^g_{ik}(t) = \sqrt{(x_i - [x_k + v_x t])^2 + (y_i - y_k)^2 + (z_i + [z_k - v_z t])^2},$$

$m_i(t)$ are the measurements at each hydrophone, and $h_i$ are the hydrophone sensitivities. Solution of these equations involves: precise knowledge of the distances between the guns and the hydrophones; calculation of the hydrophone sensitivities; and determination of the $v_x$ and $v_z$, to find the notional sources $s_k(t), k = 1, \ldots, n$.

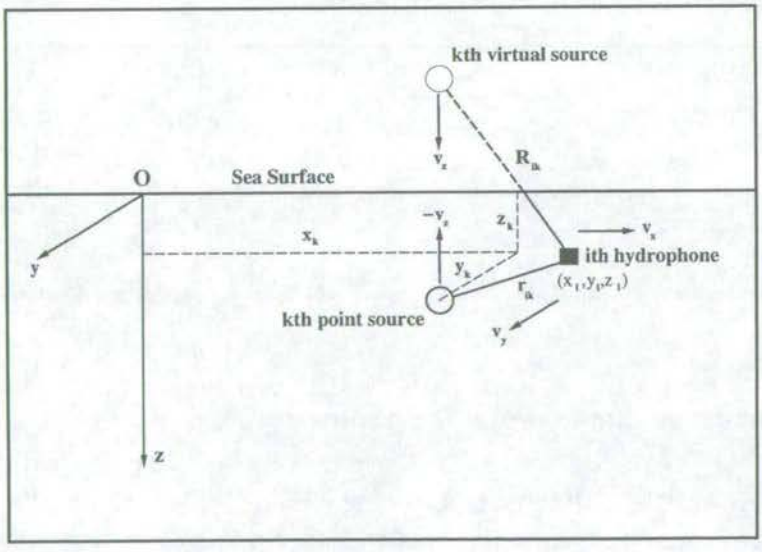


Figure 6.12: Geometry of the $k$th point source, its virtual image in the sea surface and the $i$th hydrophone, showing relative motion effects.

### The Enterprise array

The symmetrical array used by Enterprise Oil was composed of two identical sub-arrays, port and starboard. A schematic of the array is drawn in Figure 6.13. Each sub-array is made up of two strings of airguns. The six firing elements of each string increase in gun volume from the back to the front, where there is a three-gun cluster. The cross-line dimension of the array is much larger than the in-line dimension. The array was designed in this way to prevent bubble interactions occurring between the airgun strings. In the calculation of the notional sources each string may then be treated separately. If this is not the case, the cross-line geometry must be known accurately. Current technology does not yet allow this (Sabel *et al.*, 1998).

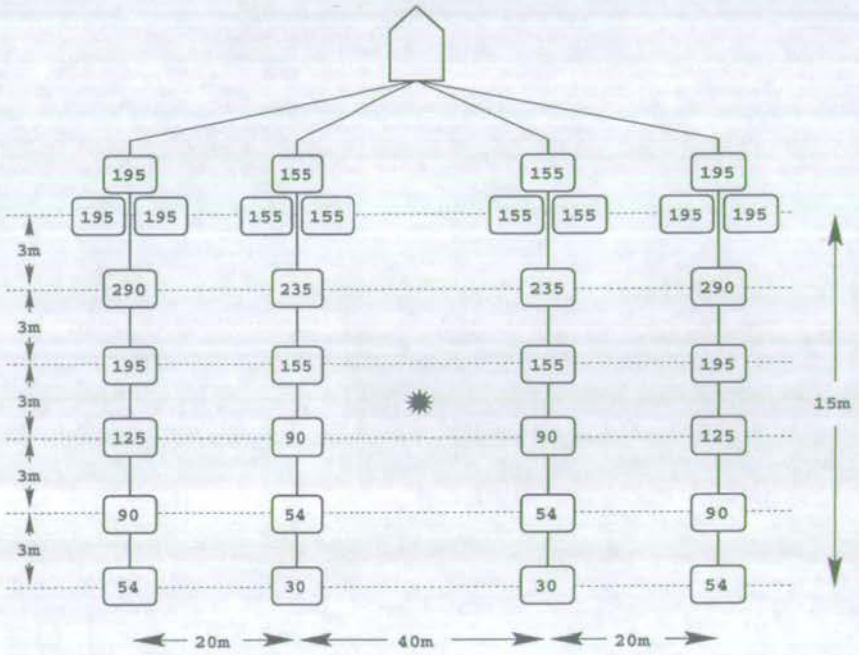


Figure 6.13: The configuration of the Enterprise airgun array equipped with near-field hydrophones (Note: not to scale). The star denotes the centre of the array. The total volume of the array is 2 x 2368 (4736) cu. in..

### Measurement of the gun-hydrophone geometry

In the Trisor system, each hydrophone is fixed to a frame, from which each firing element is hung, and all the frames are hung at fixed intervals from a float. Hence, the distances between the guns and the hydrophones in a single string is known accurately. The distances may be measured on the back deck of the boat, prior to any survey. The coordinates of the guns and hydrophones for the Enterprise survey are listed in Table 6.2.

| | | | | | | | | |
|---|---|---|---|---|---|---|---|---|
| | | x | 0.00 | 2.92 | 5.96 | 9.01 | 12.05 | 15.14 |
| | Gun | y | -30.00 | -30.00 | -30.00 | -30.00 | -30.00 | -30.00 |
| Starboard | | z | 5.00 | 5.00 | 5.00 | 5.00 | 5.00 | 5.00 |
| Outer | | x | 0.00 | 2.93 | 5.96 | 9.01 | 12.05 | 15.14 |
| | Phone | y | -30.00 | -30.00 | -30.00 | -30.00 | -30.00 | -30.00 |
| | | z | 4.06 | 4.20 | 4.21 | 4.31 | 4.30 | 4.30 |
| | | x | 0.00 | 2.85 | 5.91 | 8.96 | 12.06 | 15.15 |
| | Gun | y | -20.00 | -20.00 | -20.00 | -20.00 | -20.00 | -20.00 |
| Starboard | | z | 5.00 | 5.00 | 5.00 | 5.00 | 5.00 | 5.00 |
| Inner | | x | 0.00 | 3.00 | 6.03 | 9.08 | 12.13 | 15.19 |
| | Phone | y | -20.00 | -20.00 | -20.00 | -20.00 | -20.00 | -20.00 |
| | | z | 4.04 | 4.20 | 4.20 | 4.31 | 4.29 | 4.32 |
| | | x | 0.00 | 2.89 | 5.96 | 8.96 | 12.06 | 15.08 |
| | Gun | y | 20.00 | 20.00 | 20.00 | 20.00 | 20.00 | 20.00 |
| Port | | z | 5.00 | 5.00 | 5.00 | 5.00 | 5.00 | 5.00 |
| Inner | | x | 0.00 | 3.06 | 6.10 | 9.13 | 12.17 | 15.21 |
| | Phone | y | 20.00 | 20.00 | 20.00 | 20.00 | 20.00 | 20.00 |
| | | z | 4.02 | 4.20 | 4.22 | 4.34 | 4.39 | 4.33 |
| | | x | 0.00 | 2.87 | 5.90 | 8.98 | 12.05 | 15.10 |
| | Gun | y | 20.00 | 20.00 | 20.00 | 20.00 | 20.00 | 20.00 |
| Port | | z | 5.00 | 5.00 | 5.00 | 5.00 | 5.00 | 5.00 |
| Outer | | x | 0.00 | 3.04 | 6.09 | 9.13 | 12.16 | 15.20 |
| | Phone | y | 20.00 | 20.00 | 20.00 | 20.00 | 20.00 | 20.00 |
| | | z | 4.08 | 4.22 | 4.23 | 4.33 | 4.33 | 4.37 |

Table 6.2: The gun and hydrophone geometries for the four strings (coordinates are in metres).

### Calculating the relative sensitivites

If the hydrophones are uncalibrated, their sensitivities can be found by firing each gun separately at the start of a line. When one gun only fires, the signal is recorded on every hydrophone. Due to spherical divergence, the amplitude of the signal from the gun which fires decays as $1/r$; hence, given the amplitude at one hydrophone, the amplitude at another hydrophone may be predicted knowing the geometry. Suppose the $k$th gun fires. Let the amplitude of the first peak of the pressure signal from this gun be $A_k$ bars at 1m. This is recorded at the $i$th and $j$th hydrophones as

$$m_{i,peak} = \frac{h_i A_k}{r_{ik}} \tag{6.22}$$

and

$$m_{j,peak} = \frac{h_j A_k}{r_{jk}}. \tag{6.23}$$

Taking the ratio of these numbers yields

$$\frac{m_{i,peak}}{m_{j,peak}} = \frac{h_i r_{jk}}{h_j r_{ik}}, \tag{6.24}$$

from which it follows

$$\frac{h_i}{h_j} = \frac{r_{ik} m_{i,peak}}{r_{jk} m_{j,peak}}. \tag{6.25}$$

Knowledge of the geometry of the guns and hydrophones allows the relative sensitivities to be found. The relative sensitivities may be converted to absolute sensitivities if one of the hydrophones is calibrated with a known sensitivity. Alternatively, using the technical specifications of any gun firing in isolation, the numbers recorded by the adjacent hydrophone may be converted to the quoted peak pressure if the operating conditions are the same (Ziolkowski and Johnston, 1997).

The single gun shots for the four strings are shown in Figures 6.14-6.17. The numbers below each gather indicate the volume of the gun or cluster which fires, as documented in the observer's logs. There is one mis-fire per string. Since the bubble period is proportional to the cube root of the gun volume (see chapter 3), it is clear that the observer's logs are wrong for the starboard outer string (Figure 6.17). Interpretation of the data allows the true story to be revealed, as shown in Figure 6.18.

All the hydrophones in the Trisor system are properly calibrated, such that the data recorded is in the units of millibars. The values of the $h_i$ in equation (6.21) are therefore 1.

### Calculating the relative velocities

The $v_x$ and $v_z$ can also be found by firing each gun separately. When a single gun fires there is one notional source only, and the calculated notional sources at the other guns should be zero. Once the sensitivities are known, equations (6.21) are solved for the $s_k(t)$ while minimising the energy of the notional sources at the guns which do not fire (all but the firing gun). A velocity scan is performed to find the correct combination of $v_x$ and $v_z$ that yields minimum energy (a least-squares solution). Figure 6.19 shows the search for the velocities using a gun in the starboard outer string. The procedure is repeated for all the guns in each string to get representative velocities for the string. Table 6.3 gives the relative velocities used in the calculation for the notional sources for each of the four strings.

The Trisor system uses the relative velocities published in Parkes *et al.* (1984): for $v_x$, the speed of the ship through the water, 5 knots $\equiv -2.5\text{ms}^{-1}$, which may not necessarily be the speed of the bubbles through the water (as noted by Parkes *et al.* (1984)); for $v_z$, $-1.0\text{ms}^{-1}$, which is a velocity optimised for the data in Parkes *et al.* (1984).

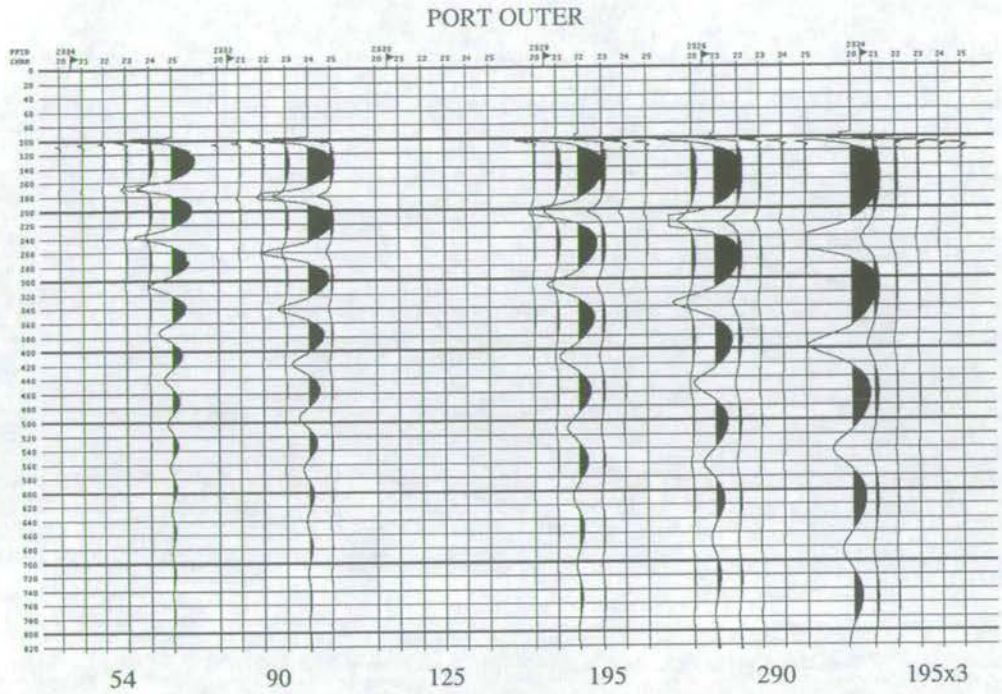


Figure 6.14: Single airgun shots for the port outer string. The numbers beneath each gather indicate the volume of the gun or cluster which fires in isolation.

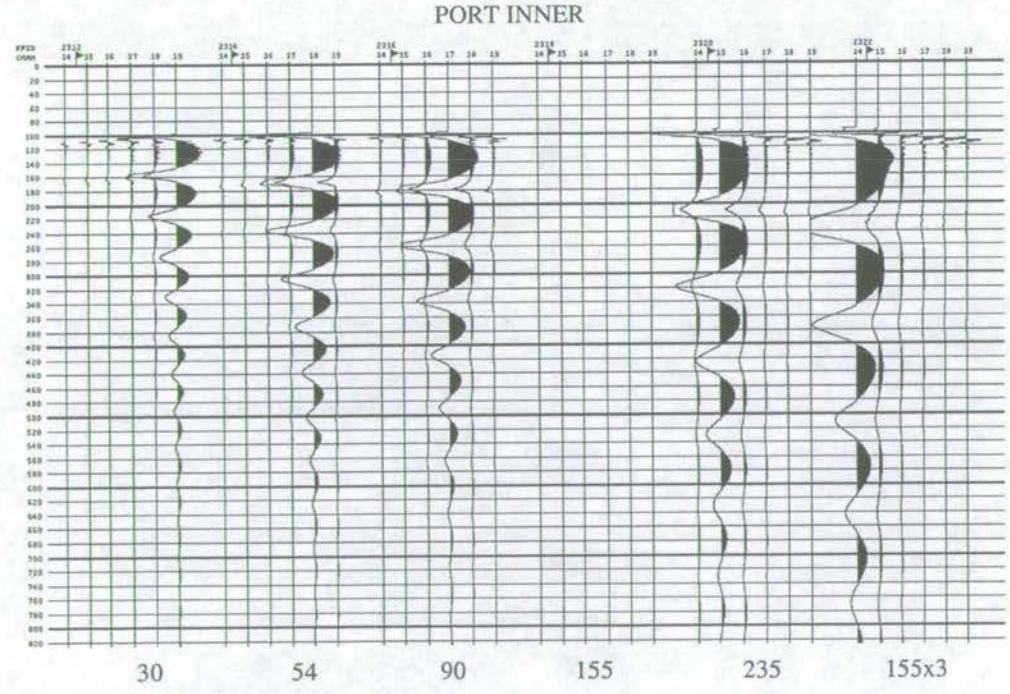


Figure 6.15: Single airgun shots for the port inner string. The numbers beneath each gather indicate the volume of the gun or cluster which fires in isolation.

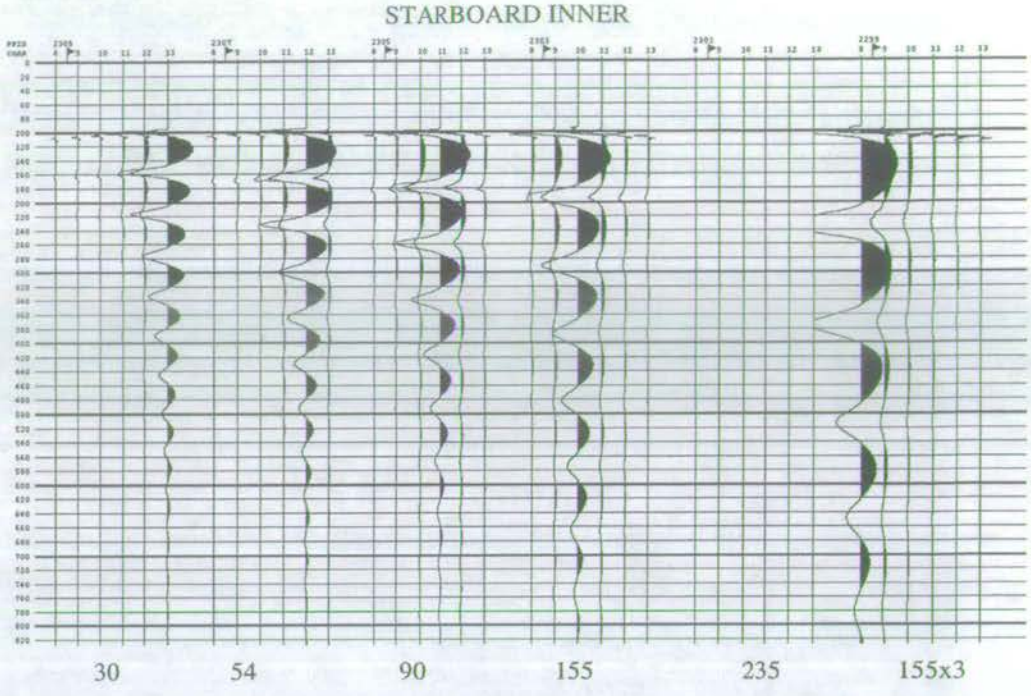


Figure 6.16: Single airgun shots for the starboard inner string. The numbers beneath each gather indicate the volume of the gun or cluster which fires in isolation.

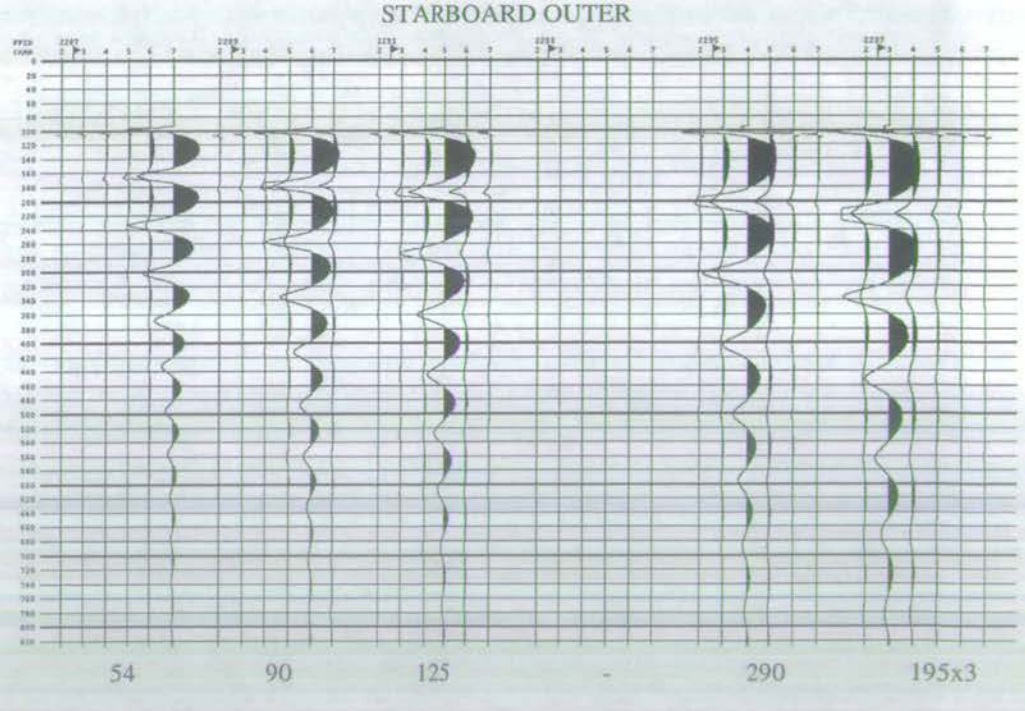


Figure 6.17: Single airgun shots for the starboard outer string. The numbers beneath each gather indicate the volume of the gun or cluster which is documentated as firing in isolation.

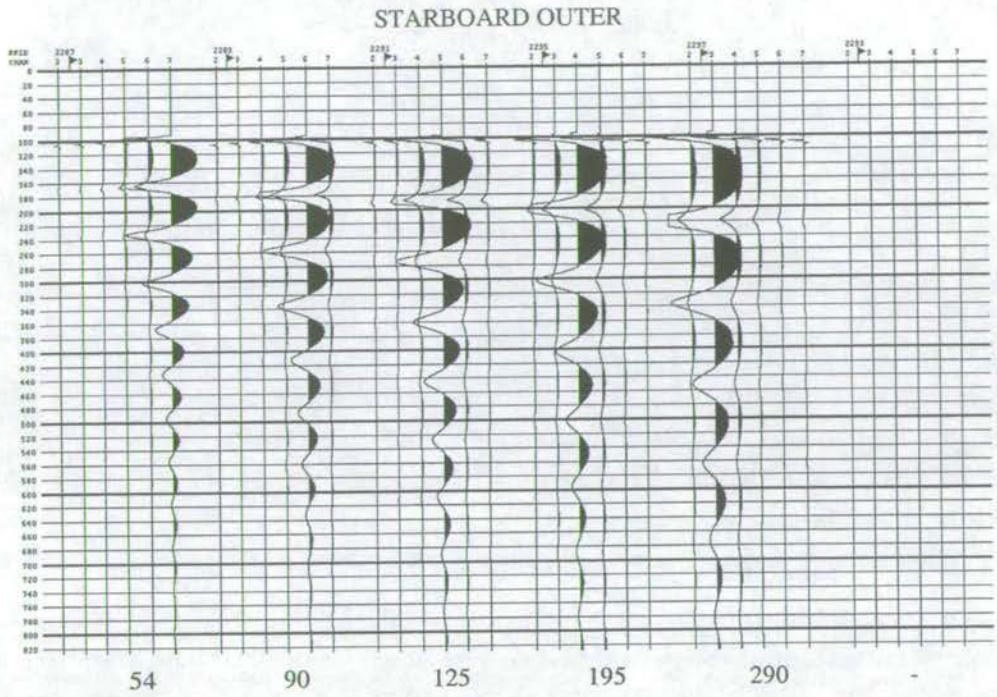


Figure 6.18: Single airgun shots for the starboard outer string. The numbers beneath each gather indicate the volume of the gun or cluster which actually fires in isolation.

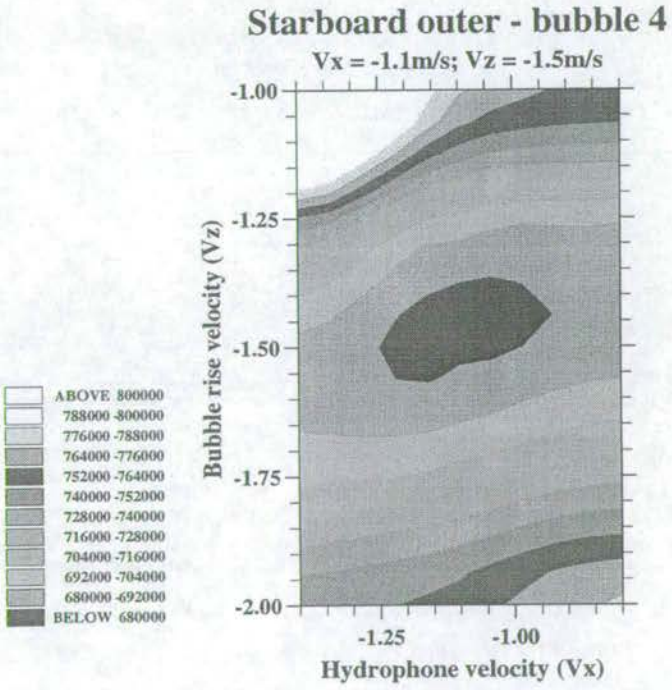


Figure 6.19: Velocity scan for bubble rise velocity and hydrophone velocity.

| | $v_x$ | $v_z$ |
|---|---|---|
| starboard outer | −1.1 | −1.5 |
| starboard inner | −1.1 | −1.5 |
| port outer | −1.5 | −1.5 |
| port inner | −1.5 | −1.5 |

Table 6.3: The relative velocities of bubble and hydrophone for the four strings. (values are in $ms^{-1}$).

### Calculating the notional source signatures

Using the known gun-hydrophone geometry, the known sensitivities, and the known relative velocities, equations (6.21) are solved on a shot-by-shot basis when all the guns fire simultaneously, yielding the notional sources, $s_k(t), k = 1, \ldots, n$.

The actual situation in the water consists of bubbles of varying sizes, filled with air supplied at a constant initial pressure, oscillating in water of varying background pressure. This is replaced with a fictitious situation consisting of bubbles of different sizes whose internal pressure is varying, oscillating in water of constant background pressure. Thus, the pressure modulation due to the presence of other sources is moved from the outside of the bubble to the inside. This is explained fully in chapter 3. In the fictitious situation, the oscillating bubbles are the notional sources, for which superposition applies because they exist in a constant background pressure (Ziolkowski *et al.*, 1982).

Following Parkes *et al.* (1984), the equations are solved by successive approximations. Rewriting equations (6.21) explicitly for the notional source at the $k$th gun

$$s_k(t) = r_{ik}\left[\frac{m_i}{h_i} - \sum_{\substack{k=1 \\ k\neq i}}^{n} \frac{1}{r_{ik}(t)} s_k(t - \frac{r_{ik}(t)}{c}) + \sum_{k=1}^{n} \frac{1}{r^g_{ik}(t)} s_k(t - \frac{r^g_{ik}(t)}{c})\right], i = 1, \ldots, n, \tag{6.26}$$

an iterative solution is obvious. The signal at any one hydrophone (the $i$th, say) is dominated by the pressure coming from the adjacent gun (the $k$th, say, where $k = i$). The measurement at the $i$th hydrophone is therefore a good first approximation to the notional source for the $k$th gun ($k = i$). The addition of the summation terms on the right-hand side of (6.26) refine the $k$th notional source with each iteration. Each airgun string may be treated independently because they are sufficiently separated that there is no interaction between strings.

The notional sources for the port outer and port inner strings are plotted in Figure 6.20 and 6.21 for shot number 2268: The first 6 traces are the near-field measurements; the second 6 traces are the notional sources derived from equations (6.26). The notional sources are quite different from the near-field measurements. In general, they decay more rapidly, but there are important amplitude and phase differences as well. For shot number 2269, the notional

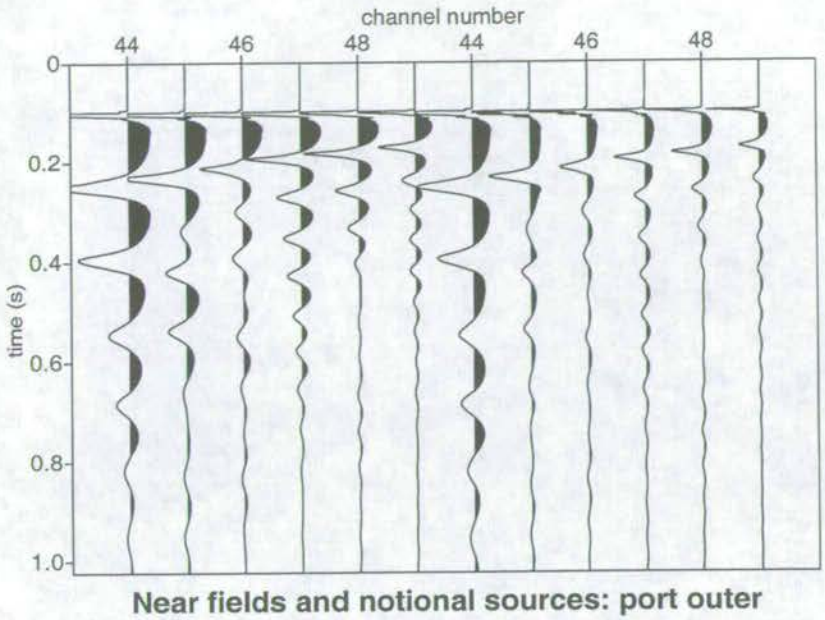


Figure 6.20: Notional sources for the port outer string on the last 6 channels. The near-field measurements are on the first 6 channels.

sources for the starboard inner and starboard outer strings are plotted in Figures 6.22 and 6.23, respectively. Note that in Figure 6.23 the near-field hydrophone signal on channel 31 is very weak. The corresponding gun experienced a mis-fire on this shot, and thus the notional source was set to zero, as observed on channel 31 (right).

### Constructing a far-field wavelet

Once equations (6.21) are solved, the wavefield may be calculated anywhere in the water, by linear superposition of the non-interacting notional sources, as in equation (6.20). To calculate a far-field wavelet, the location is typically chosen to be vertically below the array, at say 5000m distance. The calculation includes the reflection from the sea surface, or source ghost.

The far-field wavelets calculated from the near-field measurements are shown in Figures 6.24 and 6.25, for the port and starboard sub-arrays, respectively. In the absence of any other quality control check on the validity of the notional source signatures, and hence the far-field wavelet, a comparison was made with the calculations of the Trisor System performed during production. In Figures 6.24 and 6.25, the wavelets calculated on-line by Trisor are on the left, and those calculated in Edinburgh (UoE) are on the right. The Trisor calculations terminate at 500ms. The RMS difference between the two sets of calculations is 5.9% for the port sub-array, and 5.2% for the starboard sub-array. The two sub-arrays were supposed to be

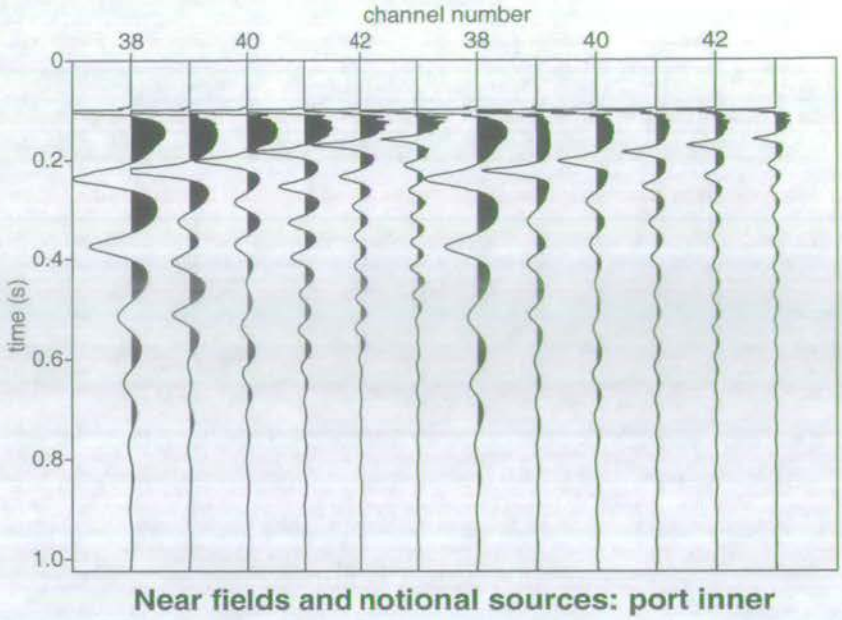


Figure 6.21: Notional sources for the port inner string on the last 6 channels. The near-field measurements are on the first 6 channels.

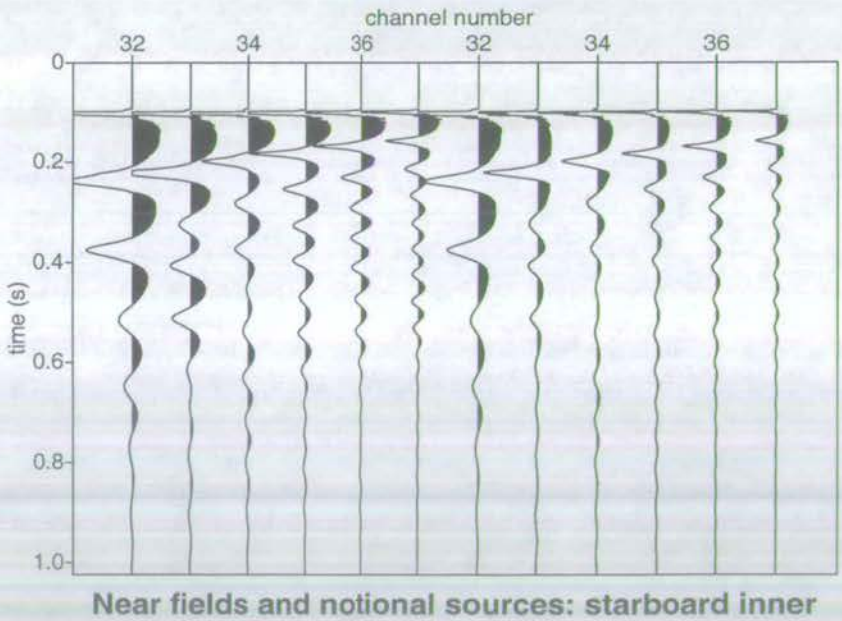


Figure 6.22: Notional sources for the starboard inner string on the last 6 channels. The near-field measurements are on the first 6 channels.

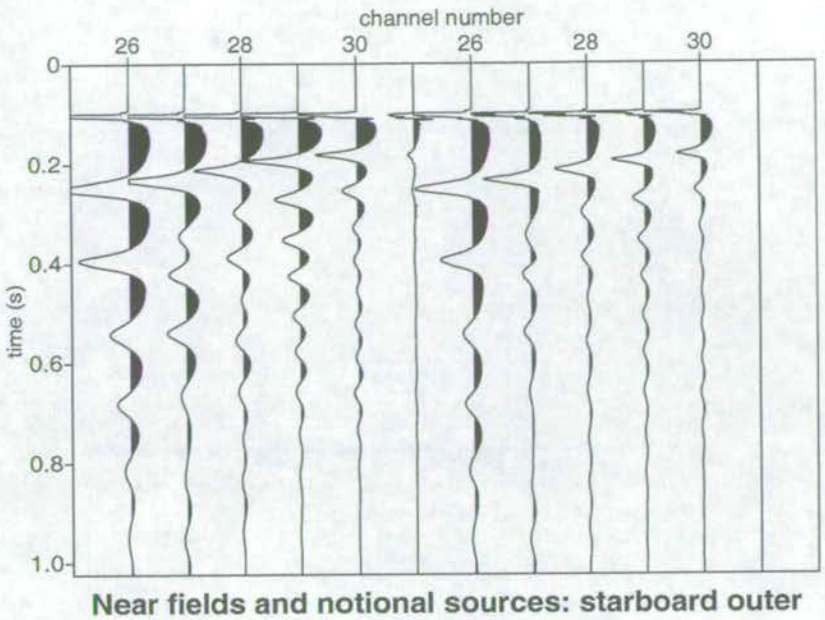


Figure 6.23: Notional sources for the starboard outer string on the last 6 channels. The near-field measurements are on the first 6 channels.

identical, and indeed the RMS difference between the port and starboard sub-arrays is 1%.

The agreement with the independent calculations of Trisor suggests that the far-field wavelet is valid, and hence the notional sources correctly describe the pressure output of the array. However, it is more desirable to have a continuous check on the validity and quality of the notional source calculations, independent of the measurements which give the solution. This is provided by extra hydrophones on the airgun array which are supplementary to the requirement of $n$ measurements for $n$ airguns, as discussed in Ziolkowski and Johnston (1997).

In signature deconvolution, a filter is found which shapes the far-field wavelet into something more desirable for subsequent processing, such as its minimum-phase equivalent (Dragoset *et al.*, 1987), or a much shorter smoother wavelet altogether (Ziolkowski, 1984 and 1987; Ziolkowski, Underhill & Johnston, 1998; Ziolkowski, Johnston & Underhill, 1999).

### Constructing the source signature

The signature which is required for the multiple removal scheme is not the far-field wavelet. It is the signature of the source array at the source location—this is where the convolution of the source with the earth occurs. The notional sources and their spatial disposition completely

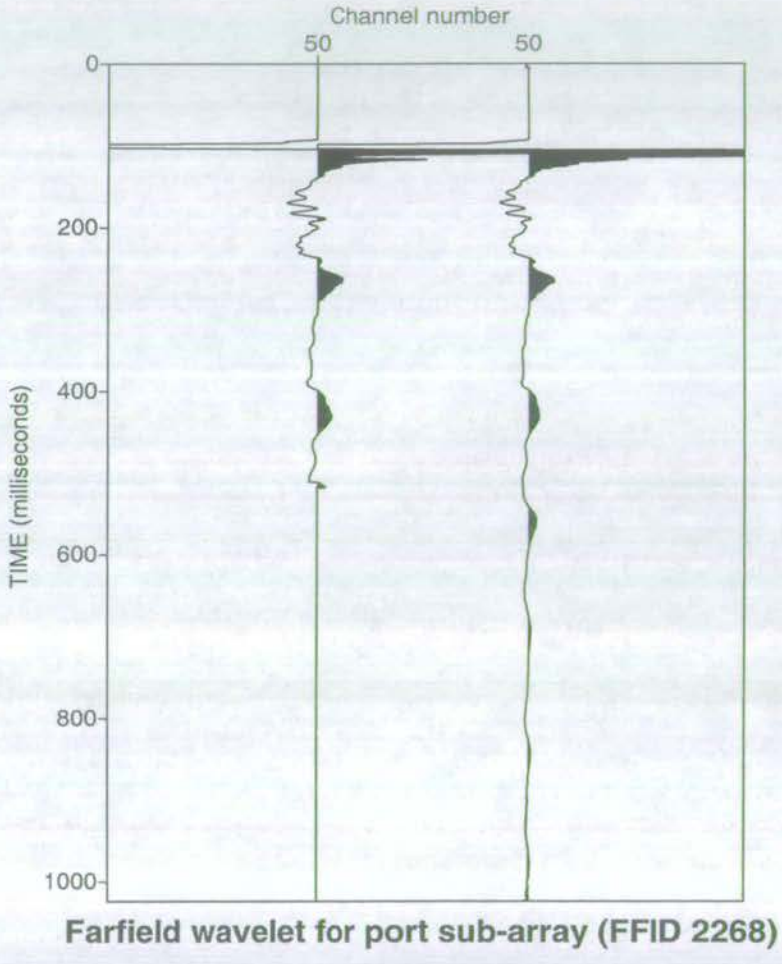


Figure 6.24: The far-field wavelet for the port sub-array. Trisor left, UoE right.

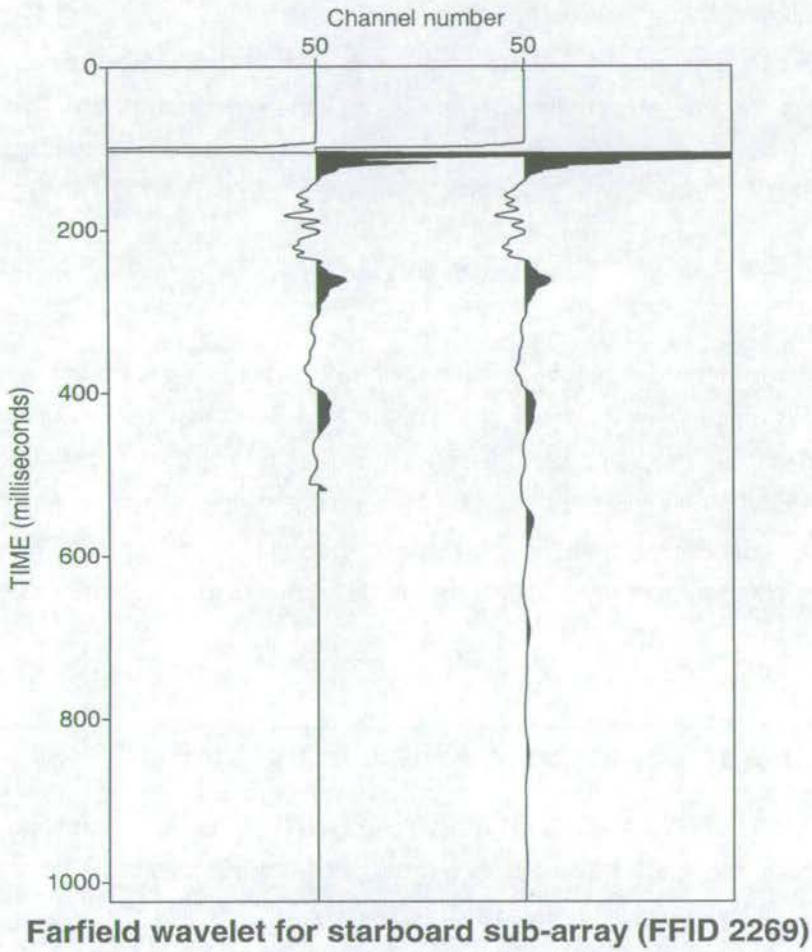


Figure 6.25: The far-field wavelet for the starboard sub-array. Trisor left, UoE right.

describe the signature of the airgun array, including any anisotropic radiation pattern:

$$s_A(x,y,z,t) = \sum_{k=1}^{n} s_k(t)\delta(x-[x_s+x_k])\delta(y-[y_s+y_k])\delta(z-[z_s+z_k]), \tag{6.27}$$

where $s_A$ is the distributed areal source. It is $s_A(x,y,z,t)$ which should be used in the construction of the incident field (see chapter 5), incorporating each of the notional sources with appropriate amplitude scaling and time delays, to account for the propagation from source array element position to receiver location.

If it may be argued that the array is compact enough in space to be treated approximately as a point source; then it can characterised by a single source signature. The point source signature is formed by superposing the notional sources, with suitable scaling and delays, at a point in the centre of the array:

$$s_E(x,y,z,t) = \sum_{k=1}^{n} \frac{1}{r_k} s_k(t-\frac{r_k}{c}), \tag{6.28}$$

where $s_E$ is the effective source signature of the array, and $r_k$ is given by equations (6.19). Any error which is incurred by assuming the array to be a point increases with frequency. (The wavelengths of sound radiated are 300-15m for 5-100Hz. Thus at 100Hz, a 15m wide array is comparable with one wavelength, and may not be considered to radiate seismic energy as a monopole.) The effective source signature may be calculated for any particular angle of incidence by choosing a point, at which to sum the notional sources, which is offset from the centre of the array.

## 6.4 Measurement of the wavefield in the far field

The measurement of the wavefield of an airgun array using a single hydrophone in the far-field region has been possible for many years (e.g. Lugg, 1979; Frick *et al.*, 1985). A hydrophone placed further than a distance $r_f$ from an airgun array, where

$$r_f = \frac{D^2}{\lambda}, \tag{6.29}$$

$D$ is the length of the array, and $\lambda$ is the wavelength of interest, is said to be in the far field (chapter 3).

In the far field, the array behaves like a point source in that the shape of the signature propagating from the array does not change with distance; the signature's amplitude decreases according to spherical divergence. However, because the point source is not a monopole (it comprises an array of airguns) it has a different far-field signature in every direction. Thus a number of hydrophones are needed to measure the signature as a function of direction.

While it is relatively simple to define the distance from an array at which a single pressure measurement fully characterises the wavefield of the array in that direction, it not so easy to make the measurement. Airgun arrays are usually tuned to optimise the wavefield travelling vertically downwards into the earth, and therefore the signature is generally required vertically below the airgun array. For an array which is 22m long, and considering an upper frequency of interest of 125 Hz, a hydrophone would have to be placed at least 40m below the array. Assuming the majority of the signature passes in 0.5s, there must be at least 375m of water below the hydrophone to allow it to be recorded in isolation. On the continental shelf, the water is usually too shallow to permit either the deployment of a hydrophone in the far field (because the sea floor intervenes), or the recording of far-field signatures uncontaminated by reflections from the sea floor.

The data in this section result from a survey conducted by the British Institutions Reflection Profiling Syndicate (BIRPS), across the Rockall Trough, West of Ireland, UK. The depth of the water in this area (200-3000m) allowed a far-field hydrophone to be deployed in a deep-tow "fish", to monitor and record the vertical far-field signature of the array on a shot-by-shot basis. The data were shot in August 1993 by Digicon Geophysical Corporation (now Veritas DGC).

The pressure recorded by a single hydrophone at $(x,y,z)$ in the far field of an airgun array with centre coordinates $(x_s,y_s,z_s)$ is given by

$$p(r_f,t) = \frac{1}{r_f} s_E(t-\frac{r_f}{c}) - \frac{1}{R_f} s_E(t-\frac{R_f}{c}) \tag{6.30}$$

where $s_E$ is the effective source-time function of the array, and, for the vertical direction, $r_f \approx z - z_s$ and $R_f \approx z + z_s$. Equation (6.30) may be written as a convolution,

$$p(r_f,t) = s_E(t) \star \left[ \frac{1}{r_f} \delta(t-\frac{r_f}{c}) - \frac{1}{R_f} \delta(t-\frac{R_f}{c}) \right], \tag{6.31}$$

where $\star$ denotes convolution, and the $\delta$-functions represent the time delays required to propagate the effective source-time function $s_E(t)$ from its origin to the far-field hydrophone, for the direct arrival from $(x_s,y_s,z_s)$, and for the ghost arrival from $(x_s,y_s,-z_s)$. Transformation of equation (6.31) to the frequency domain gives

$$P(r_f,\omega) = S_E(\omega) \cdot \left[ \frac{1}{r_f} \exp(i\omega\frac{r_f}{c}) - \frac{1}{R_f} \exp(i\omega\frac{R_f}{c}) \right], \tag{6.32}$$

where the convolution has been replaced by a multiplication, and the time delays, by complex phase shifts. The source-time function may be extracted through a complex division for the

geometrical factors related to source and receiver positions

$$S_E(\omega) = \frac{P(r_f, \omega)}{\left[\frac{1}{r_f}\exp(i\omega\frac{r_f}{c}) - \frac{1}{R_f}\exp(i\omega\frac{R_f}{c})\right]}. \tag{6.33}$$

The denominator is never zero because it is the difference of two quantities which cannot be zero simultaneously, since $r_f < R_f$. Thus, the division is stable. Moreover, the result is causal. Equation (6.33) represents a frequency-domain deconvolution of the measured pressure by the impulse response of the medium. This response is the Green's function for propagation in a homogeneous half-space bounded by a free surface. $S_E(\omega)$ is the (frequency-domain) effective source signature for the array, at the centre of the source location.

### The WESTLINE airgun array

The Western Extension across Slyne Trough (WESTLINE) profile was shot across the 250km wide Rockall Trough basin to provide controls on its age and development, with respect to the understanding of continental rifting and margin development. Because the basin is very deep (water depths up to 3km in places, and lower crustal reflectors at 10km), the airgun array was designed to maximise the signal output by deploying as many guns as possible. Thus, the conventional desired characteristic of a high primary-to-bubble ratio is sacrificed in exchange for deeper penetration of the low frequencies. The radiated energy at low frequencies is governed by the bubble oscillations, and not by the initial shock wave which carries the high-frequency energy.

A schematic of the airgun array is shown in Figure 6.26. The non-symmetrical array comprises two sub-arrays, port and starboard. Each of the sub-arrays comprises two strings of ten air guns, with the volume of the guns generally increasing from the back of the array to the front. The numbers indicate the chamber volume of the gun in cubic inches[1]. Note that the cross-line dimension of the array of 50m is much larger than the in-line dimension of 22m. Since the array is two-dimensional, it is always the larger of the two dimensions which should be considered in the deployment of a hydrophone in the far field. For frequencies of 125-30 Hz the far-field region of the array's radiation pattern is greater than 208-50m. Figure 6.27 is a cartoon illustrating the idea behind the deployment of a hydrophone in the far field of an airgun array to record the vertically-travelling signature. Note that the signature arriving at the streamer, travelling almost horizontally from the extended source array, is very different from the signature propagating vertically towards the far-field hydrophone.

The WESTLINE airgun array was modelled using the Modgun marine seismic source signature modelling software of PGS[2] Seres. This was done to assess the variation of hy-

[1] 1 cu. in. $\equiv$ 0.0164 l

[2] Petroleum Geo Services

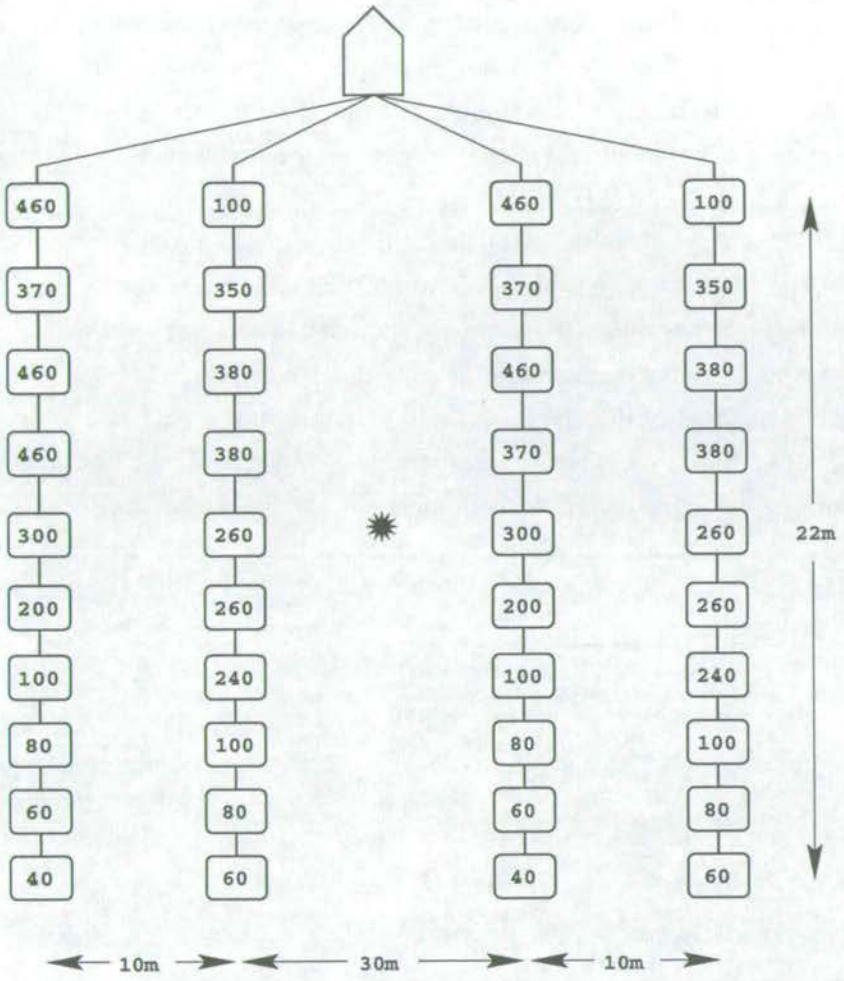


Figure 6.26: The configuration of the WESTLINE survey airgun array (Note: not to scale). The star denotes the centre of the array. The total volume of the array is 9390 cu. in..

drophone depth on the far-field signature, and to obtain an idea of what the signature from the WESTLINE array might look like. Modgun allows the pressure output of arrays of single guns and clusters to be modelled, taking the effects of interaction between the guns into account. The kernel of the modelling is based on the theory of Ziolkowski (1970; 1982). Figures 6.28 & 6.29 show the far-field signature for two positions, 45m and 75m vertically below the array. The signatures are calculated with a sampling interval of 0.5ms, without any recording filters. The difference between the two signatures is in their high frequency content, as indicated by the peak-to-peak amplitude and the primary-to-bubble (P/B) ratio indicated on the right of the plots. (The peak-to-peak amplitude is measured from the peak to the trough of the primary pulse, marked by the first two circles on the left of the plots. A similar measure may be made for the secondary (bubbble) pulse, marked by the second two circles. The P/B ratio is the ratio of the distance between the first two circles over the distance between the

second two.) The period of bubble oscillation is approximately the same, indicating that the low frequency content of the two signatures is similar. At 45m the high frequencies travelling from the different guns in the array arrive out of phase to reduce the amplitude of the primary. 45m is therefore not in the far field of the array for all the frequencies in this modelled result (up to a Nyquist frequency of 1000 Hz).

Figures 6.30 & 6.31 show the same far-field signatures filtered with a recording instrument filter which attenuates frequencies above 80 Hz. Note that, with the reduced bandwidth imposed by the recording filter, the array is now much less directional, and the signature at 45m is very similar to the signature at 75m. At this bandwidth, 45m and 75m are both effectively in the far field of the array. At the low frequencies ($< 35$ Hz) returning from the target this is even more true. Thus, a measured far-field signature will be of practical use in the processing of reflection data if the hydrophone is at least 45m deep.

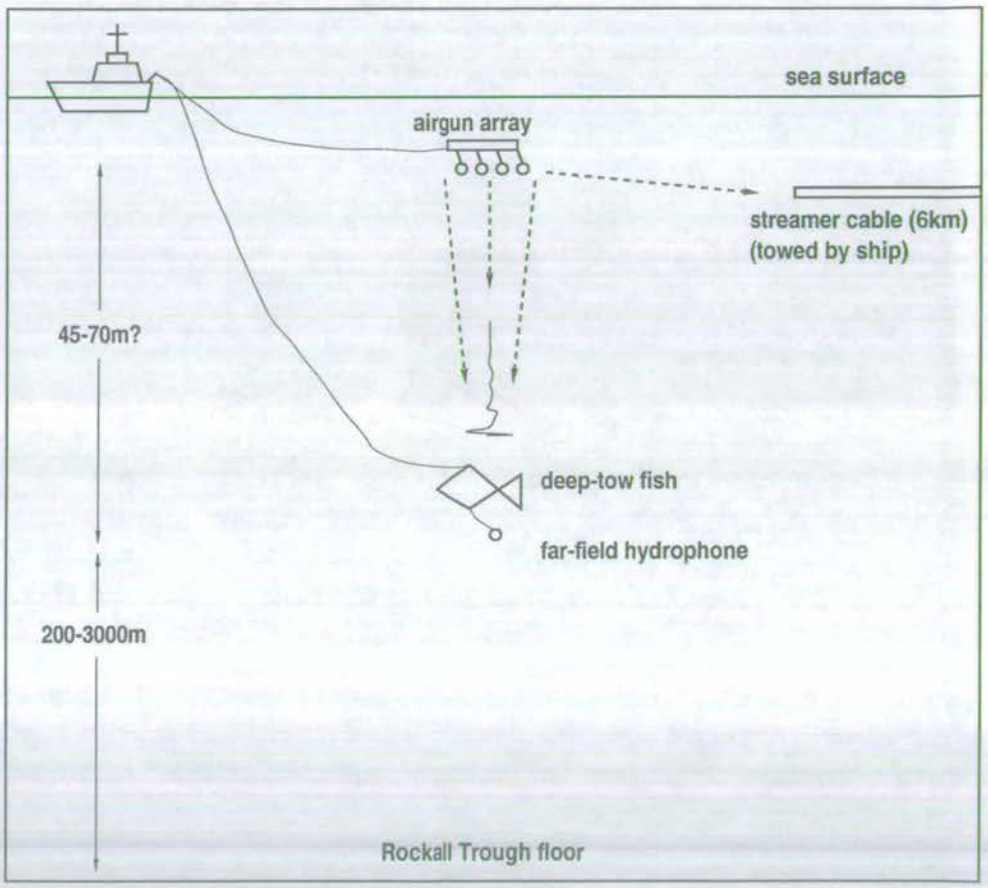


Figure 6.27: Cartoon illustrating the principal elements in the acquisition of the far-field signature of the airgun array as the boat steams to the left. The broken arrows indicate possible travel paths for the energy from the source to the receivers.

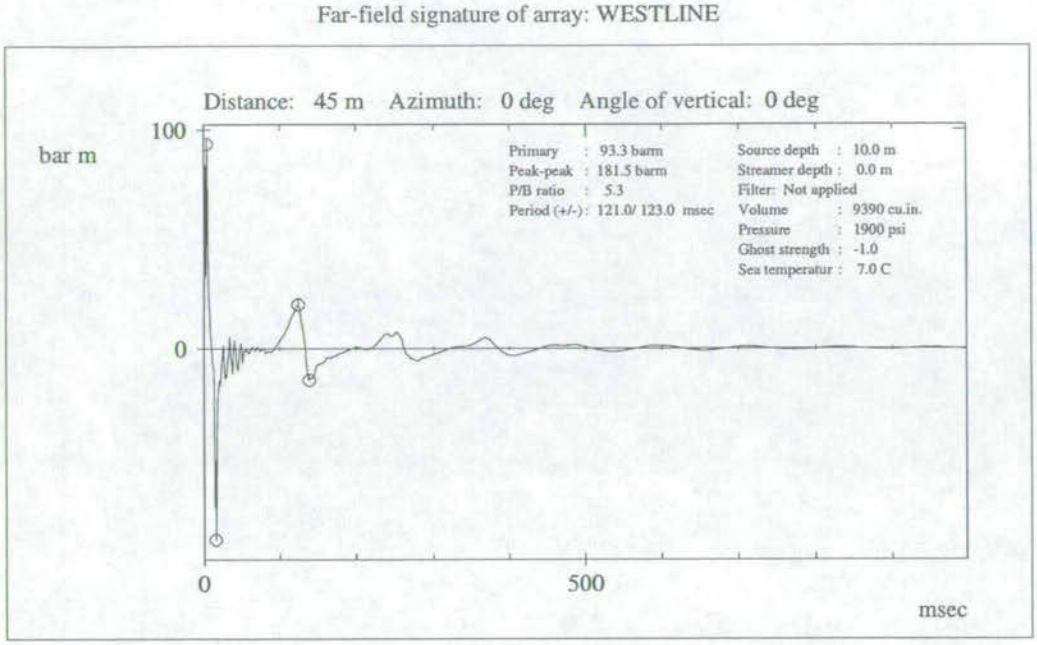


Figure 6.28: Unfiltered synthetic Modgun far-field signature 45m vertically below the WEST-LINE airgun array.

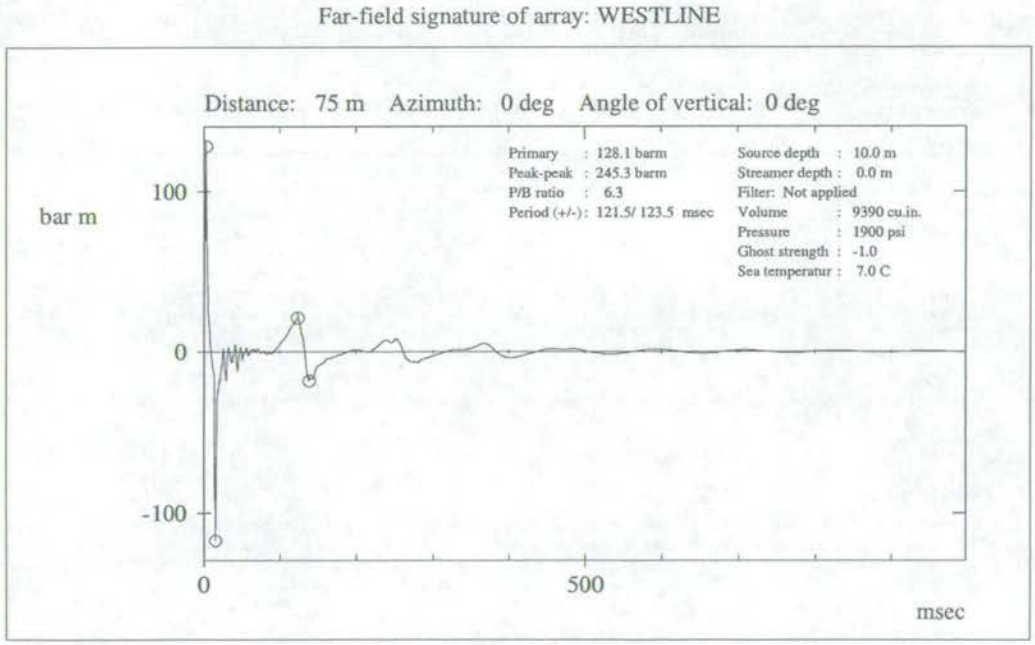


Figure 6.29: Unfiltered synthetic Modgun far-field signature 75m vertically below the WEST-LINE airgun array.

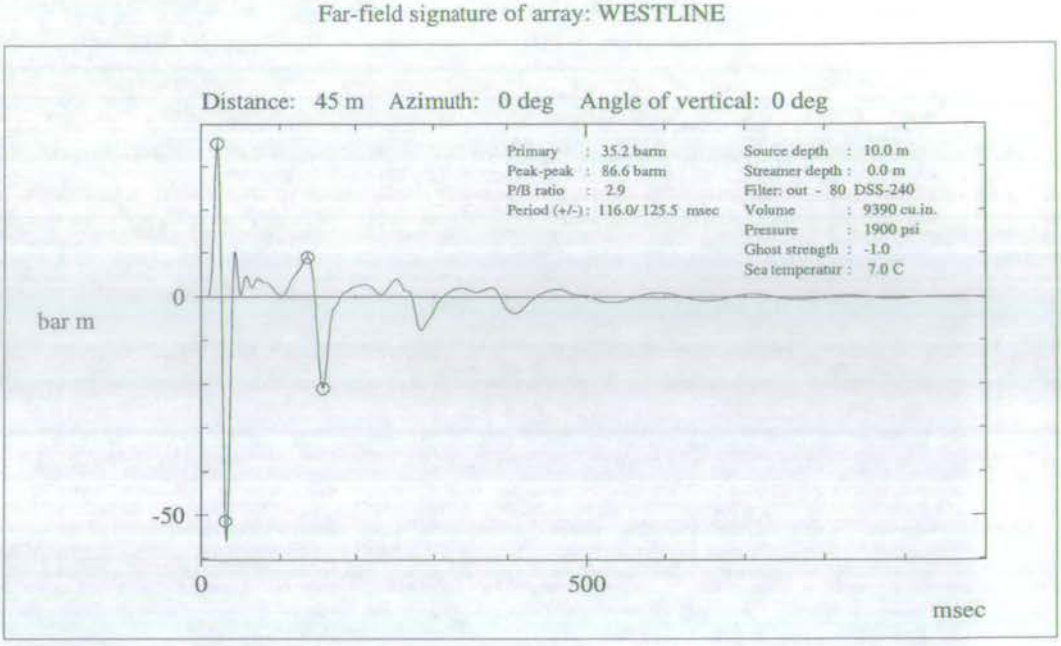


Figure 6.30: Modgun far-field signature 45m vertically below the WESTLINE airgun array, filtered with a DSS-240 instrument filter.

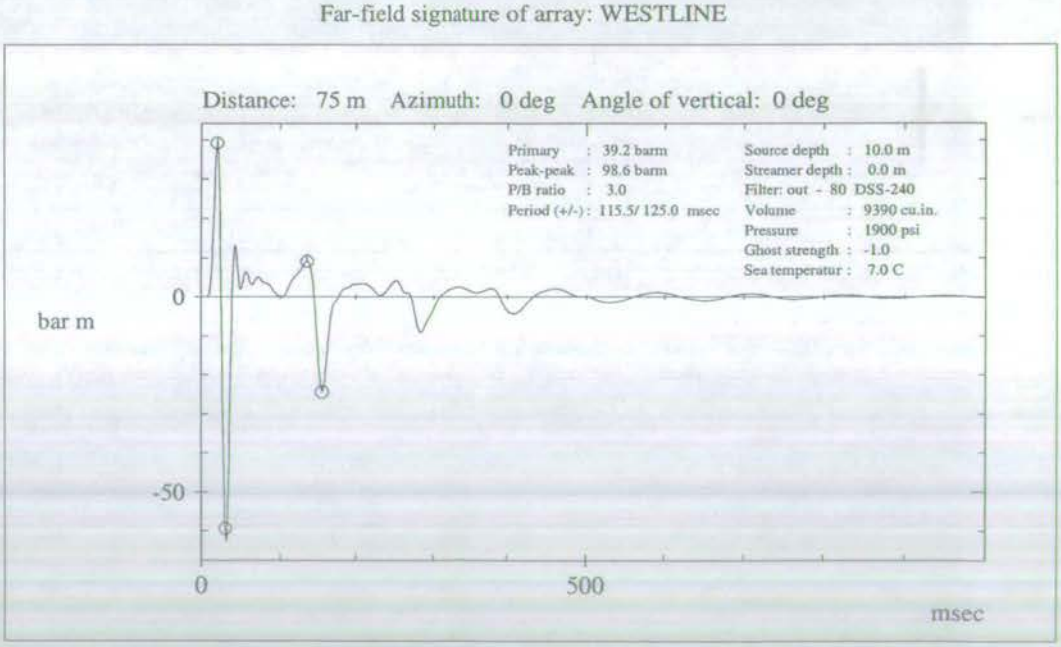


Figure 6.31: Modgun far-field signature 75m vertically below the WESTLINE airgun array, filtered with a DSS-240 instrument filter.

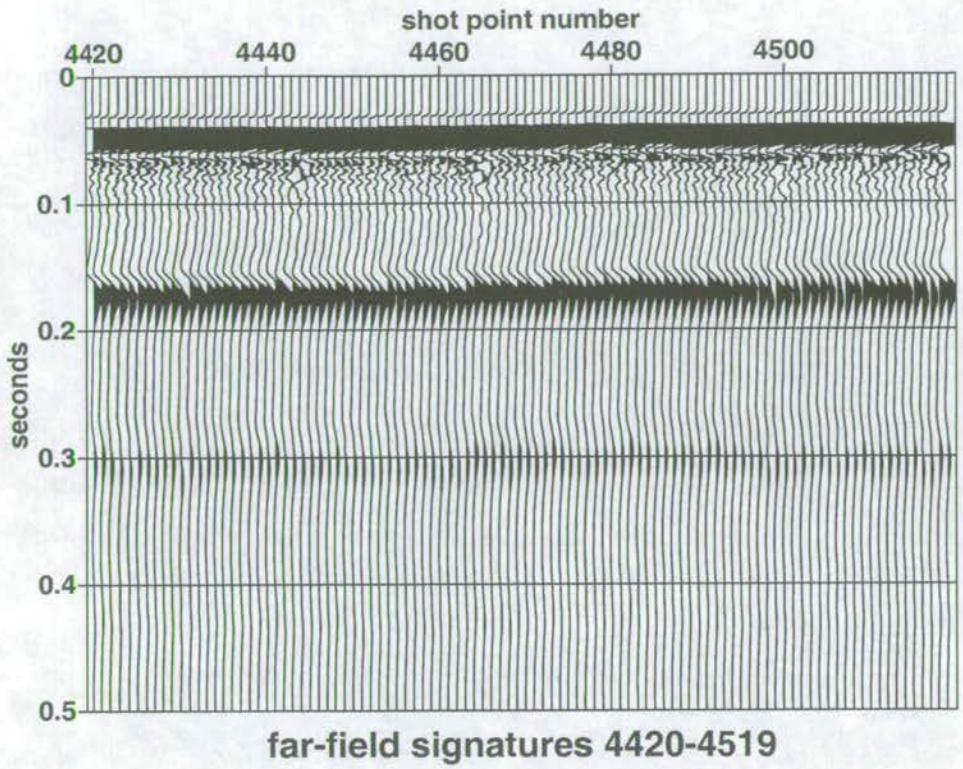


Figure 6.32: Far-field signatures from the central (deepest) part of the Rockall Trough, uncontaminated by any sea floor reflections.

### The recording system

The Digicon far-field recording system (DFFRS) was a PC-based system comprising several elements. At one end, the far-field hydrophone is housed in an Endeco deep-tow depressor 703 hydrodynamic tow fish, which, in theory, is capable of reaching depths of 100s of metres. However, due to a combination of prevailing weather conditions and ship speed, the far-field hydrophone in the WESTLINE survey was rarely at depths greater than 60-70m. The hydrophone itself is an Engineering Acoustics LS-93 which, through the use of a high impedance charge-coupled amplifier (with variable sensitivities), has an accuracy which is unaffected by the tow cable length. A Hewlett Packard HP 35665A signal analyser provides real-time displays of the far-field signature in the time and frequency domains, permitting positioning of the hydrophone during deployment. Finally, the signal is digitised with a Keithley metrabyte DAS-102 A/D card which permits sampling rates up to 100 kHz.

Two seconds of the far-field data were recorded to PC at a sampling rate of 5000 Hz (0.2 ms sampling interval). No recording filters were applied due to the high sampling rate. However, the data from the streamer were recorded through a DSS-240 out-80 Hz high-cut filter.

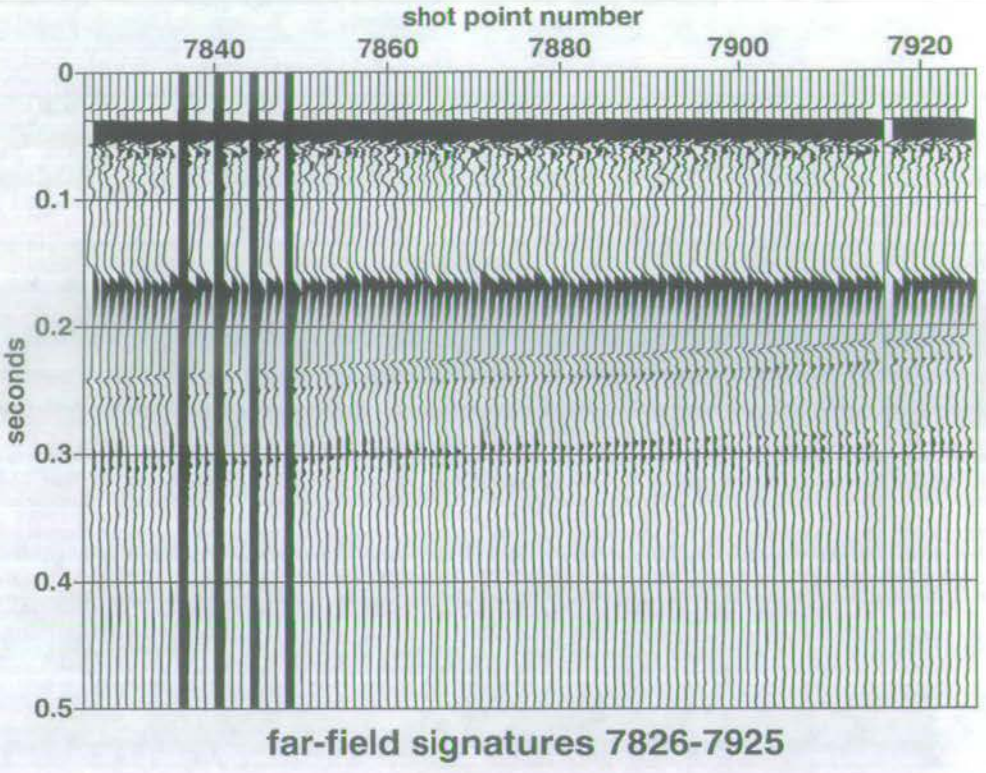


Figure 6.33: Far-field signatures from the south-easterly flank of the Rockall Trough, where the signal is contaminated by sea floor reflections.

Thus, before any combined processing of streamer and far-field data is possible, the latter must be convolved with the DSS-240 out-80 Hz high-cut filter. During the initial deployment and testing of the far-field acquisition system the hydrophone signal was contaminated by both a capacitive discharge and 60 Hz noise (Sacks, 1993). Removing the HP 35665A signal analyser from the recording circuit remedied the problem. It was assumed that the signal analyser was faulty (Sacks, 1993).

Examples of some of the far-field signatures recorded with the system are given in Figures 6.32 & 6.33. The first 500ms only are plotted. The signatures are displayed with SEG normal recording polarity, such that positive pressures are recorded as negative numbers on tape. The initial compressional pulse from the airgun array therefore plots as a negative excursion (trough). Figure 6.32 is from the central area of the trough where the water depth is around 3km. In this case, the sea floor is far enough below the far-field hydrophone that the vertically-travelling signature may be measured without contamination by reflections from the earth. Figure 6.33 is from the Rockall slope where the profile approaches the continental shelf. At this point, the water depth is at most 180m deep and too shallow to get an effective

measure of the far-field signature. This is illustrated by the reflections from the sea floor and the layers below cutting across the far-field signatures, beginning around 0.25s at shot point (SP) 7826, and continuing to almost 0.2s at SP 7925.

There is some additional information in Figure 6.33 which unfortunately does not fulfil its intended potential. A problem in the use of deep-tow systems is the lack of precise information on the location of the hydrodynamic fish, and hence the recorded data. Every hour during production shooting, the guns at the four corners of the array were fired individually to establish the far-field hydrophone position by triangulation. These positioning shots were recorded through the HP 35665A signal analyser, resulting in SPs 7836, 7840, 7844, 7848 in Figure 6.33, which are dominated by a strong DC signal, which is possibly the capacitative discharge mentioned in Sacks (1993). (SP 7916 in Figure 6.33 is a noise file where no guns fire.) Almost without fail, the shot points listed in the observer's logs (Bulat, 1993), which correspond to the single guns firing, record this DC signal. Often, the adjacent shots are contaminated as well, as illustrated in Figure 6.34. SP 4994 is the positioning shot where one gun only fires. These contaminated traces are presumably caused by the faulty HP 35665A signal analyser being switched in and out of the recording circuit.

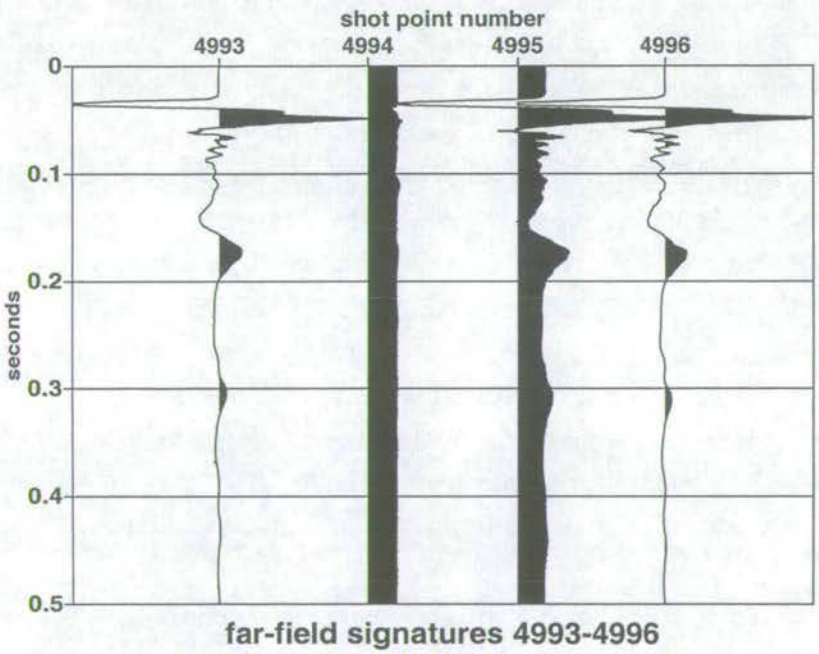


Figure 6.34: Far-field positioning signatures from the Rockall Trough, where the signal is dominated by a strong DC component.

In the absence of any other positioning information, the range to the hydrophone may be determined from the first-break time, knowing the velocity of sound in water. On-board

monitoring of the hydrophone position suggests the hydrophone was, at most, 4° astern of the array centre (P. Sacks, pers. comm.). Modelling with Modgun shows there to be little difference in the signatures obtained with the WESTLINE array for 0° and 4° to the vertical.

### Constructing the source signature

The purpose of far-field recording is to monitor the array behaviour, and to extract the effective source signature. The steps required to do this are illustrated below, using a typical far-field signature from the deep part of the WESTLINE profile at SP 3540. The hydrophone is approximately 62m below the source array. The first step is the removal of any so-called DC signal in the data by calculating the mean value and removing it. DC signal corresponds to energy at zero frequency, which clearly should not exist, but often is introduced by recording circuits. At this point the data are converted to meaningful units of pressure, if possible, and the polarity is reversed from the SEG's recording convention, so that positive pressure corresponds to positive numbers. After these manipulations, the quasi-raw data are shown in Figure 6.35 with its amplitude spectrum.

It is clear from Figure 6.35(b) that there is practically no energy above 500 Hz, so the data are resampled from a sampling interval of 0.0002s to 0.001s. To ensure that no energy above 500 Hz is aliased, the data are convolved with a minimum-phase Gaussian filter. The filter is defined in the frequency domain, by requiring that its amplitude spectrum falls to a value of $\frac{1}{e}$ at 350 Hz. The resampled data are shown in Figure 6.36. The source ghost is clear at approximately 62 Hz. This frequency corresponds with a source depth of 12m, which differs from the nominal source depth reported in the observer's logs. Transformation of the data to the frequency domain allows the source signature to be calculated by deconvolution using equation (6.33). On transformation back to the time domain, the data in Figure 6.37 result. This is the vertically-travelling effective source signature of the array. Note that there is no time delay on the signal. It represents the source time function which appears in equation (6.31) as a convolution, at the origin, of the seismic energy with the impulse response of the medium. In the absence of the source ghost, Figure 6.37(b) now shows the ghost notch filled at a fundamental frequency of 62 Hz, with smaller (raised) amplitudes at harmonics of 124, 186 and 248 Hz.

To relate the source signature of Figure 6.37 to the signature in the reflection data requires knowledge of the streamer recording system. The reflection data were sampled every 0.004s through a DSS-240 recording filter. The DSS-240 is an out-80 Hz high-cut filter, with a 72dB/octave roll-off at the high end, as shown in Figure 6.38, sampled every 0.001s. This filter was convolved with the source signature to give the data in Figure 6.39. The high-cut filter attenuates the amplitudes in the data above 80 Hz to permit sampling every 0.004s, as in the reflection data recording. Decimation to 0.004s of the DSS-240-filtered source signature gives the data in Figure 6.40. These are essentially the same data as in Figure 6.39, but with

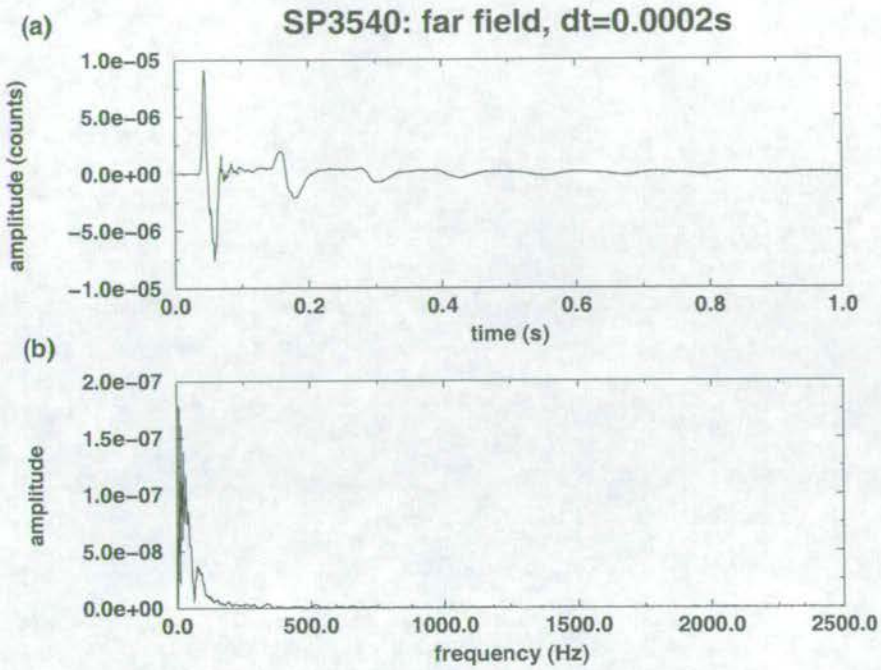


Figure 6.35: Far-field signature for SP 3540 after flipping the polarity and removing DC. (a) wavelet; (b) amplitude spectrum.

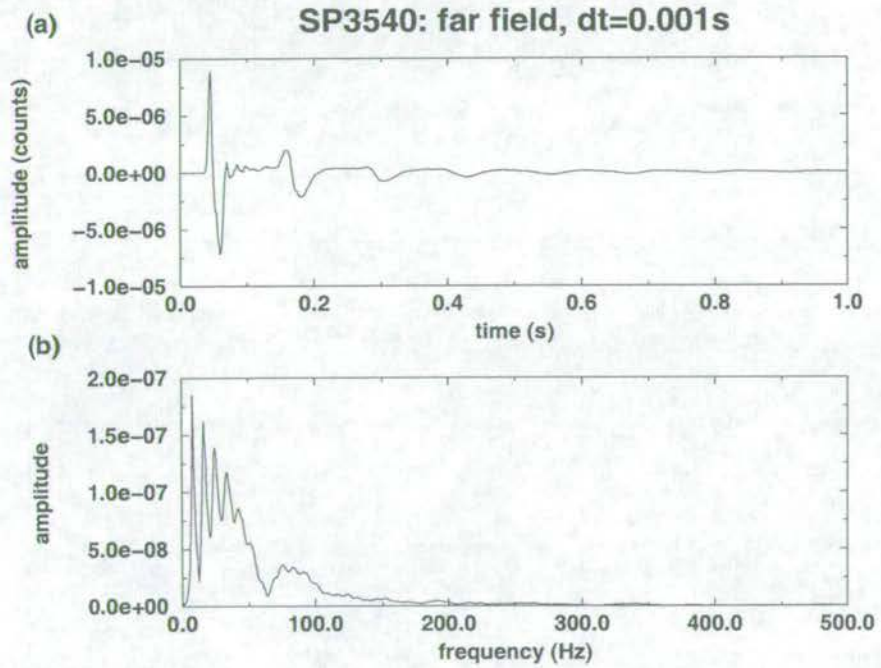


Figure 6.36: Far-field signature for SP 3540 after preliminary processing and resampling from 0.0002s to 0.001s. (a) wavelet; (b) amplitude spectrum.

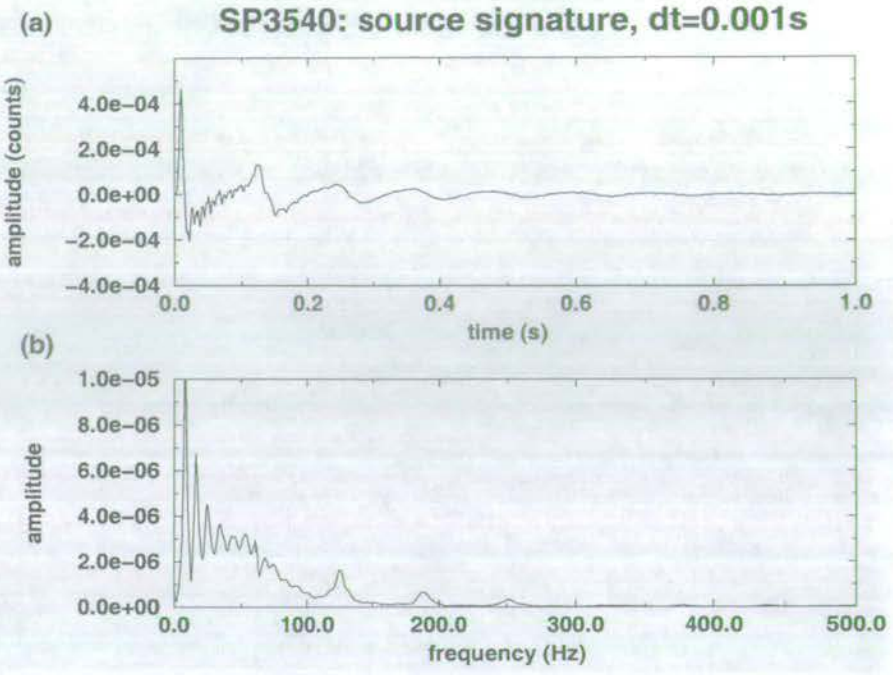


Figure 6.37: Effective source signature for SP 3540 by frequency-domain deconvolution of the far-field signature. (a) wavelet; (b) amplitude spectrum.

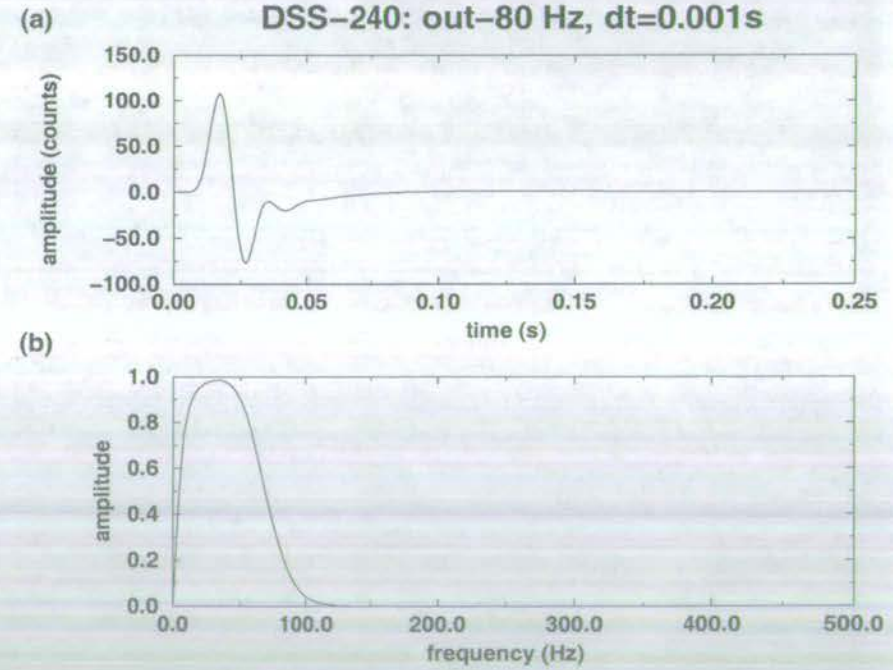


Figure 6.38: Digicon's DSS-240 instrument response: An out-80 Hz high cut filter with a 72 dB/octave roll-off slope. (a) wavelet; (b) amplitude spectrum.

a larger sampling interval. This now is the source signature which is present in the recorded reflection data.

If the data are to be processed at a larger sampling interval than the one used during recording, such as 0.008s, the source signature must be anti-alias filtered with the same filter as the reflection data and resampled to 0.008s. The result of applying a minimum-phase Gaussian filter with a high-cut of 35 Hz at the $1/e$ point to the DSS-240-filtered source signature, and resampling to 0.008s is shown in Figure 6.42. The signature is long and ringy. If the free surface is removed from reflection data acquired with the WESTLINE airgun array, the signature in Figure 6.40 or 6.42 will remain. Clearly some kind of signature shaping is desirable so that the reflections are not obscured by the source signature.

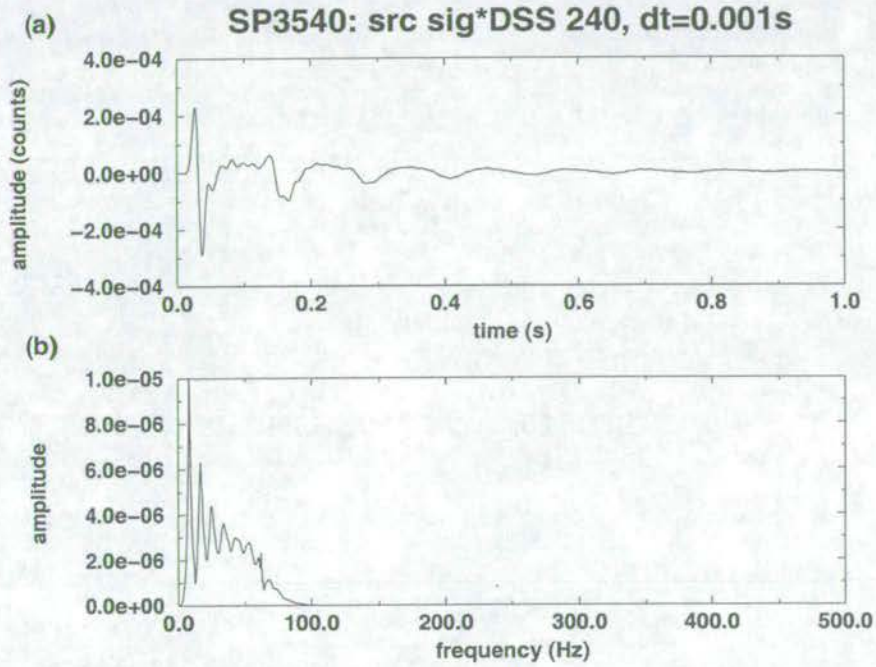


Figure 6.39: Effective source signature for SP 3540 convolved with DSS-240 instrument response ($\Delta t = 0.001$s). (a) wavelet; (b) amplitude spectrum.

## 6.5 Conclusions

It is always possible to make measurements of the wavefield of a single airgun or an array of airguns. The key to making useful measurements is to know which measurements to make, and how to manipulate them. Three different methods of measuring the wavefield of airgun sound sources are presented based on published theories. The analysis which is required to extract the source signature from these measurements is demonstrated using real data. If properly-sampled reflection data are acquired concurrently with source measurements, then

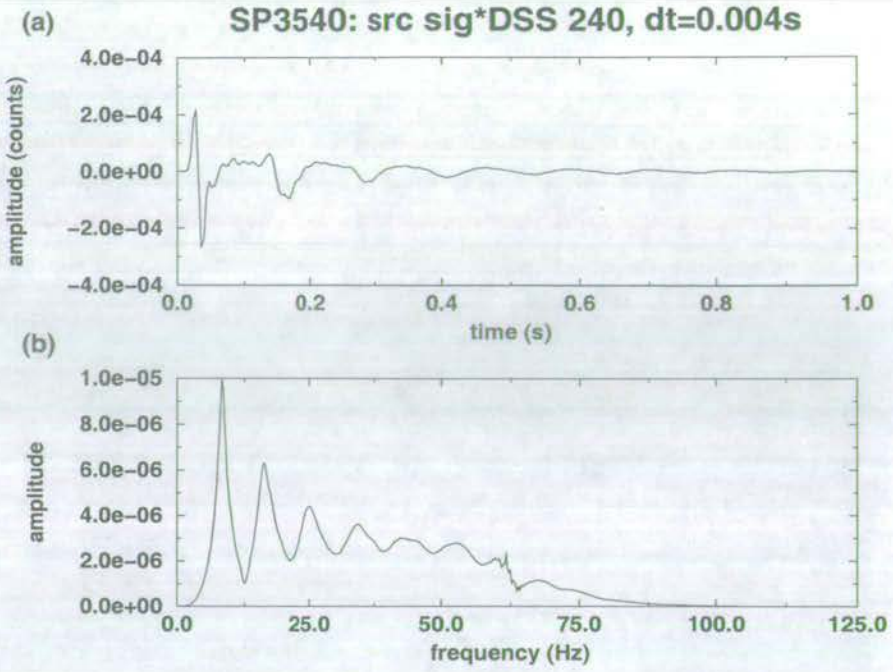


Figure 6.40: Effective source signature for SP 3540 convolved with DSS-240 instrument response ($\Delta t = 0.004$s). (a) wavelet; (b) amplitude spectrum.

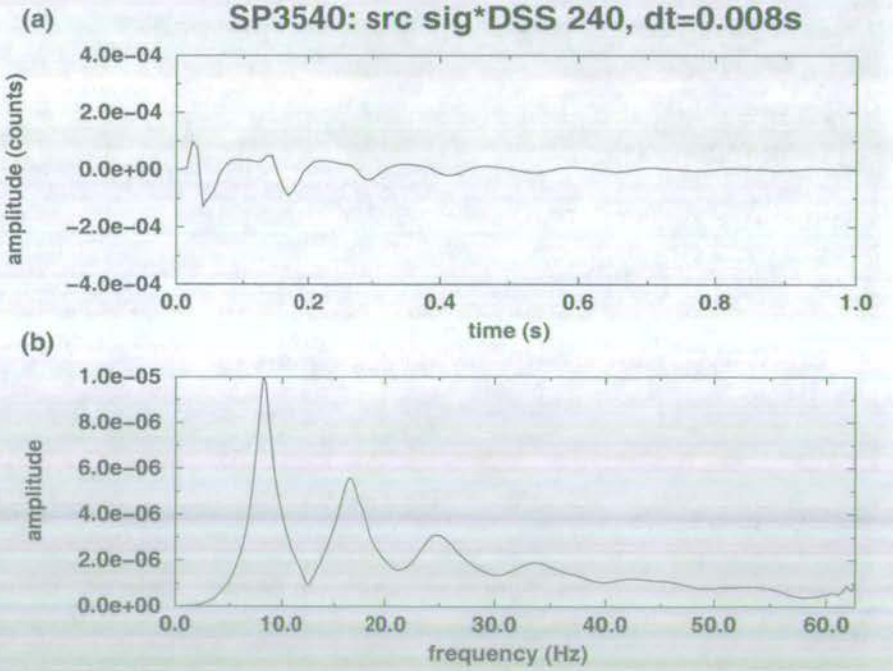


Figure 6.41: Effective source signature for SP 3540 convolved with DSS-240 instrument response ($\Delta t = 0.008$s). (a) wavelet; (b) amplitude spectrum.

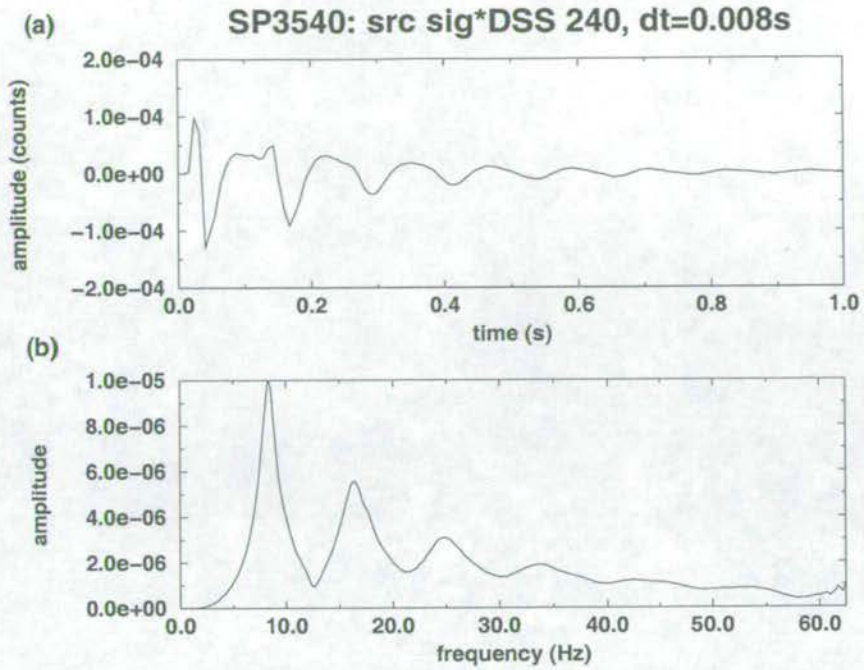


Figure 6.42: Effective source signature for SP 3540 convolved with DSS-240 instrument response ($\Delta t = 0.008$s). (a) wavelet; (b) amplitude spectrum.

the source signatures can be extracted as outlined above. These signatures are the key element in the implementation of the multiple removal scheme presented in chapter 5.

# MULTIPLE ELIMINATION IN ONE DIMENSION

*Chapter 7*

## 7.1 Introduction

Many approaches have been developed to the problem of eliminating sea surface multiples in a one-dimensional earth, as discussed in chapter 4.

Evaluation of the earth's reflection response, presented in chapter 5, removes all multiples related to the sea surface. In one dimension, the reflection response is simply the ratio of the upgoing to the downgoing plane waves. Unlike other methods, which are designed specifically for the one-dimensional case, the up/down ratio is valid for non-vertical incidence, and produces multiple-free seismograms which preserve the amplitude of the primary reflections.

Synthetic seismograms calculated over a plane layered elastic model illustrate the success of the technique for streamer and OBC data. Both line source and point source examples are given. In the latter case, to analyse the data in plane wave components, an extra spatial Fourier transform is applied, instead of the Hankel transform which involves asymptotic Bessel functions. A sensitivity analysis reveals how the method performs in the presence of random noise, and errors in the input parameters. Finally, in the OBC case, the effect of working with the total field is examined before drawing some conclusions. Some of the material shown here is in a paper (Johnston, Ziolkowski and Taylor, 1999), requested by the Petroleum Exploration Society of Great Britain, after a presentation at their 1998 technical exhibition. The paper is included as appendix C.

## 7.2 A synthetic example with line source streamer data

The synthetic data used to illustrate the multiple removal scheme are computed in a water layer overlying an elastic earth with the reflectivity method (Fuchs and Müller, 1971). The modelling code used is OSIRIS of Ødegaard A/S. A simple layered earth model is used where $P$- and $S$-wave velocities increase with depth, as tabulated in Table 7.1. Because the complexity of the earth model is contained within the upgoing and the downgoing wavefields, it does not affect the recovery of the earth's reflection response, as described in chapter 5.

Figure 7.1 shows a schematic of the acquisition set-up. The line source time function is a two-loop Ricker wavelet with a central frequency of 25 Hz (see Figure 7.2). 128 hydrophone receivers are arranged in a line below the sea surface 6.25m apart (Figure 7.1). The offset between the source and the first receiver is zero. Figure 7.3 shows seismograms for the scat-

| Depth(m) | P-wave (m/s) | S-wave (m/s) | density (kg/m$^3$) |
|---|---|---|---|
| 75 | 1500 | 0 | 1000 |
| 575 | 2000 | 1155 | 2200 |
| 1075 | 2500 | 1443 | 2150 |
| 1775 | 3000 | 1732 | 2200 |
| 2775 | 3500 | 2021 | 2200 |
| $\infty$ | 4000 | 2309 | 2400 |

Table 7.1: Earth parameters used for the simple layered earth model.

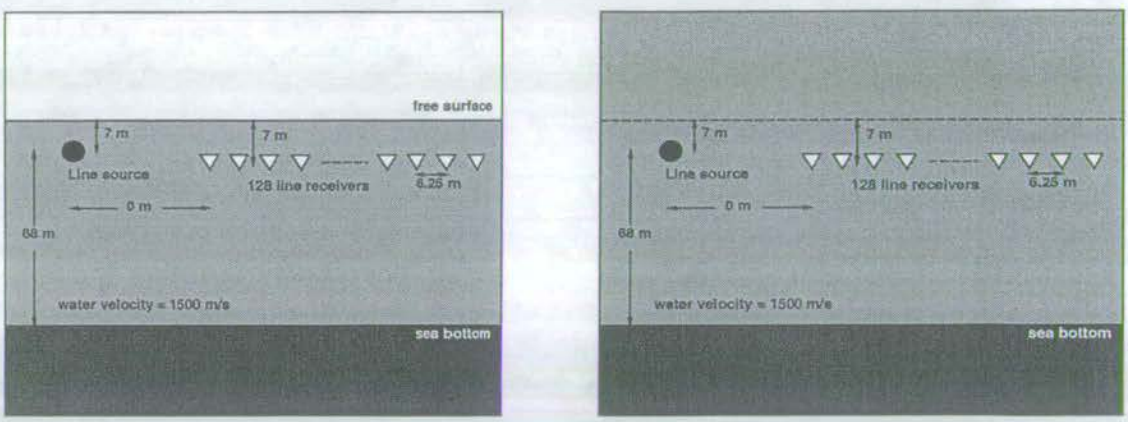


(a) With the free surface

(b) Without the free surface

Figure 7.1: Model acquisition geometry for 1D line source streamer synthetics.

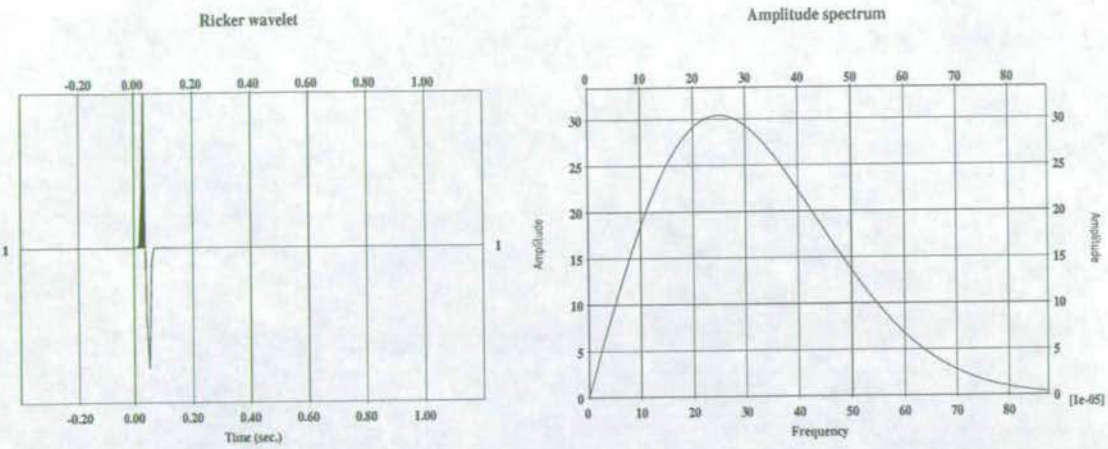


Figure 7.2: Ricker wavelet used as the source time function.

tered pressure field in the presence and absence of the sea surface: the left panel corresponds to Figure 7.1(a); the right panel corresponds to Figure 7.1(b). Most of the events on the left of Figure 7.3 are therefore free-surface multiples. The goal of multiple removal is to convert the data in the left panel of Figure 7.3 to those in the right panel.

### Data preparation

Because the data are synthetic, it is possible to model what the receivers would measure directly, or to model parts of the wavefield separately. The first step of the multiple removal scheme requires the scattered field to be isolated from the total field, by calculating the incident field and subtracting it from the total field. This step is performed implicitly, by modelling the scattered field only. The incident field is discussed later, and is plotted in Figure 7.6 beside the scattered field.

In this simple 1D model, the earth properties change in one direction only, the $z$-direction, which is vertical. Wave propagation from the line source is in two dimensions (the $x$- and $z$-directions, say), with invariance in the third dimension (the $y$-direction, say). To get the data $p^{scat}(x_r, z_r, t, z_s)$, recorded at depth $z_r$ in response to a line source at depth $z_s$, into the frequency-wavenumber domain it is sufficient to apply a Fourier transform over time $t$, and over distance $x$:

$$\tilde{P}^{scat}(k_x, z_r, \omega, z_s) = \int\int_{-\infty}^{\infty} p^{scat}(x_r, z_r, t, z_s) \exp\Big(+i[\omega t - k_x x]\Big)\, dt\, dx. \tag{7.1}$$

To accommodate the operations applied in the frequency-wavenumber domain, the data are padded with zeros, in time and offset, prior to the transforms, as illustrated in Figure 7.4. An exponential taper is applied to the time axis prior to the transform to frequency. This makes the frequency complex (see appendix A.1) which stabilises computations involving

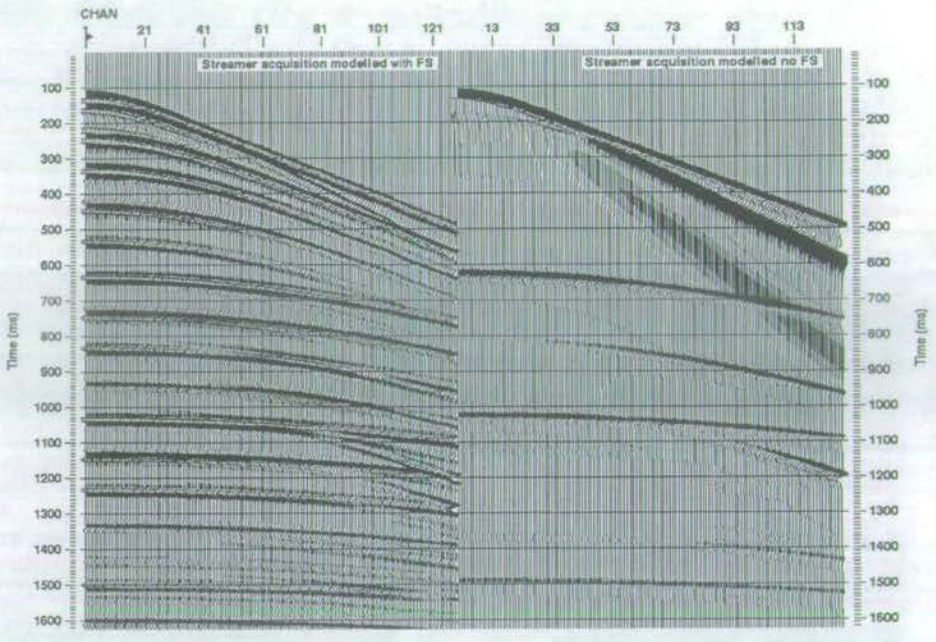


Figure 7.3: A line source over a 1D elastic earth with no incident field. The gather on the left is the pressure in the presence of the sea surface; the gather on the right is the pressure in the absence of the sea surface.

the vertical wavenumber $k_z$ (see appendix A.2). Because the data are real-valued and do not exist before $t = 0$, data for $-\omega$ are the complex conjugates of the data for $+\omega$, so only the positive frequencies are processed. The data for negative offsets are simulated from the positive offsets, making the data split-spread. The data at $-k_x$ and $+k_x$ are then identical so that only the positive wavenumbers are processed.

### Separating Upgoing and Downgoing Waves

When the acquisition geometry is towed streamers, it is possible to separate the upgoing and downgoing waves by deconvolving the receiver ghost. In the frequency-wavenumber domain the receiver ghost is

$$1 - \exp\Big(ik_z[2z_r]\Big), \tag{7.2}$$

where $k_z = \sqrt{\frac{\omega^2}{c^2} - {k_x}^2}$. This factor becomes zero whenever $\exp\Big(ik_z[2z_s]\Big)$ equals $+1$. Therefore, to remove the receiver ghost, the deconvolution is performed by a stabilised complex

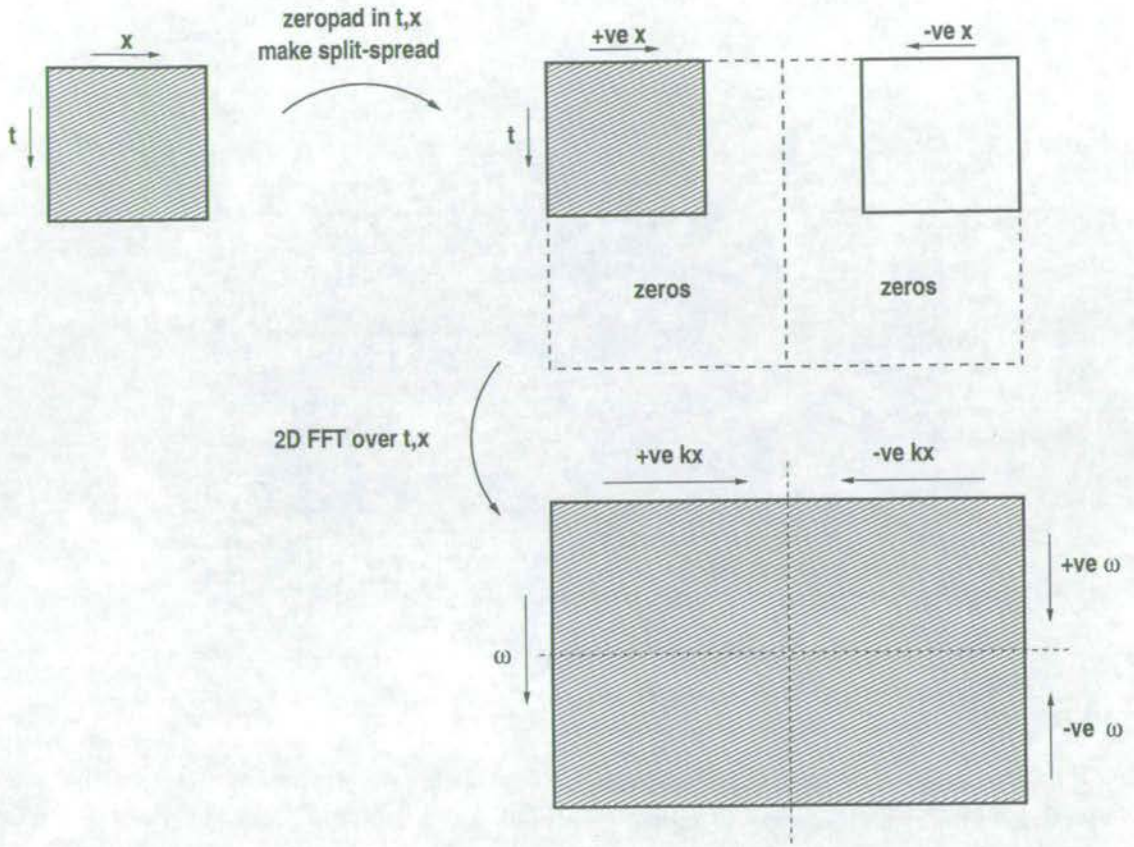


Figure 7.4: The data preparation required to transform from the time-space domain to the frequency-wavenumber domain, using line source data over a 1D earth.

division (Deregowski, 1971 and 1978)

$$\tilde{U}^{scat}(k_x, z_r, \omega, z_s) = \frac{\tilde{P}^{scat}(k_x, z_r, \omega, z_s)\left[1 - \exp\left(ik_z[2z_r]\right)\right]^*}{\left|1 - \exp\left(ik_z[2z_r]\right)\right|^2 + \varepsilon}, \tag{7.3}$$

where $\varepsilon$ is a small real constant, ensuring that the denominator is never zero. The downgoing wave is obtained from the scattered field by subtracting the upgoing wave:

$$\tilde{D}^{scat}(k_x, z_r, \omega, z_s) = \tilde{P}^{scat}(k_x, z_r, \omega, z_s) - \tilde{U}^{scat}(k_x, z_r, \omega, z_s) \tag{7.4}$$

The upgoing and downgoing waves, which together from the scattered field on the left of Figure 7.3, have been extracted following these equations, and are shown in Figure 7.5. Note that the multiples are contained in *both* the upgoing *and* the downgoing waves.

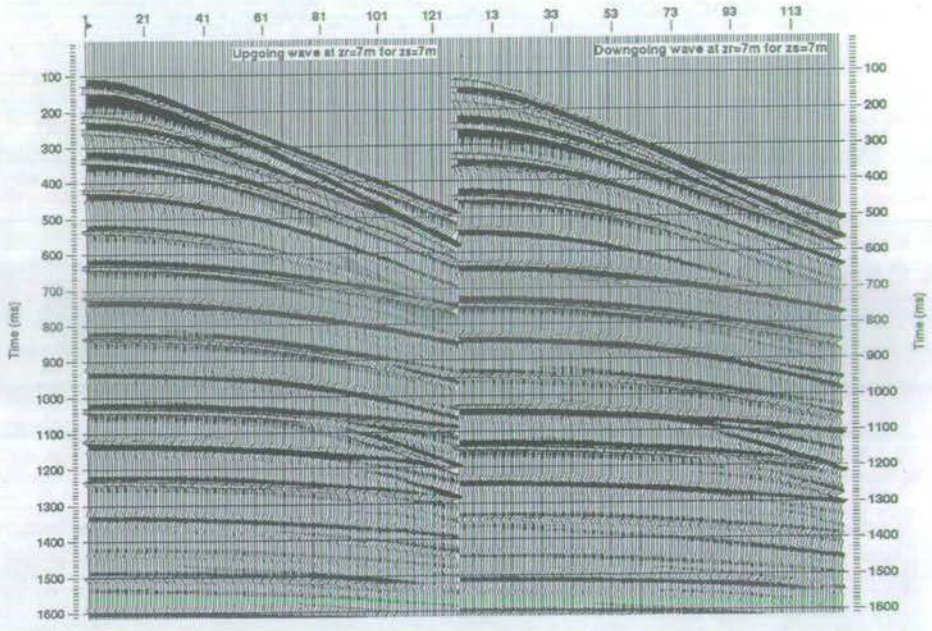


Figure 7.5: Separating upgoing and downgoing wavefields with pressure only: Upgoing wavefield at $z = z_r$ on the left; downgoing wavefield at $z = z_r$ on the right.

### Calculating the Incident Field

In addition to the upgoing and downgoing scattered wavefields, separated in the frequency-wavenumber domain, the downgoing incident field must be calculated.

Defining the incident field as that part of the total field which exists in the absence of the sea floor and the layers beneath it, as in chapter 5, each component of this field is defined in the frequency-wavenumber domain as

$$\tilde{I}(k_x, z_r, \omega, z_s) = \frac{i}{2k_z} S(\omega) \Big( \exp(ik_z|z_s - z_r|) - \exp(ik_z[z_s + z_r]) \Big). \tag{7.5}$$

where $S(\omega)$ is the spectrum of the single source signature used to produce the synthetic seismograms (see section 5.6 for details). The two phase factors in brackets propagate the source signature to the correct location in space for the direct arrival and its ghost. Transformation to time and space gives the recording of the incident field that would be made if the water were a half-space.

The incident pressure field calculated for the acquisition geometry given in Figure 7.1(a) is plotted in Figure 7.6 together with the scattered pressure field. A towed hydrophone would record the sum total of these two wavefields.

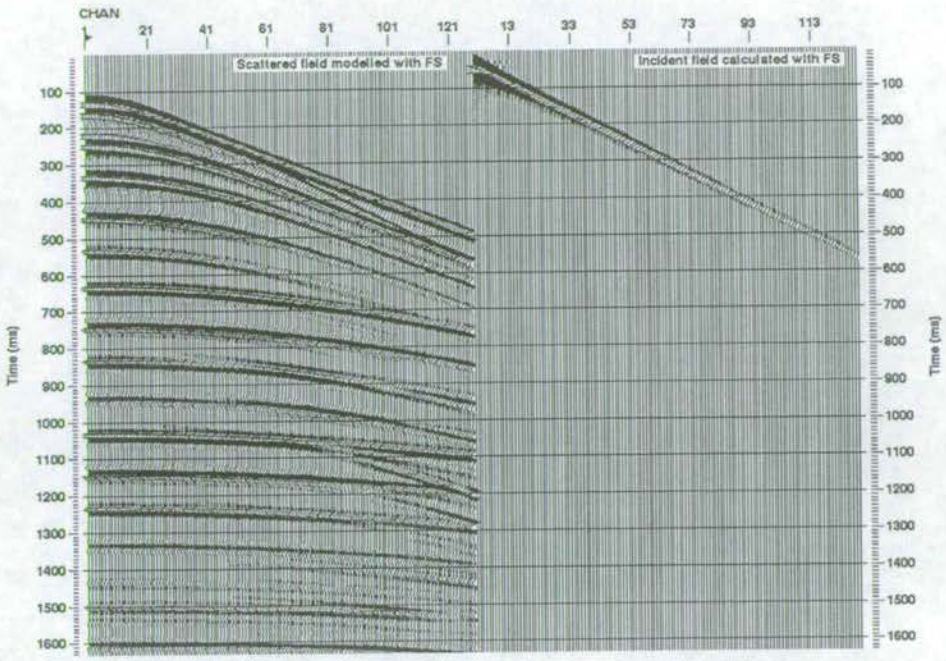


Figure 7.6: The scattered and incident fields for line source streamer data over a 1D elastic earth. The gather on the left is the pressure modelled in the presence of the free surface; the gather on the right is the calculated incident field (by definition direct and ghost arrivals).

### The reflection response

In the case of a horizontally-stratified earth, the situation is simplified considerably compared with the general 3D case. In the frequency-wavenumber domain, each upgoing scattered plane wave is simply the product of a downgoing incident plane wave with the reflection response plus the product of a downgoing scattered plane wave with the reflection response:

$$\begin{aligned}\tilde{U}^{scat}(k_x, z_r, \omega, z_s) = \tilde{I}(k_x, z_r, \omega, z_s)\tilde{R}(k_x, z_r, \omega, z_s) \\ + \tilde{D}^{scat}(k_x, z_r, \omega, z_s)\tilde{R}(k_x, z_r, \omega, z_s).\end{aligned} \tag{7.6}$$

(In the 3D case, the second term on the right is replaced by a summation over all possible downgoing scattered plane wave components.) Or, in other words, the reflection response of the whole earth (by definition in absence of the free surface) is equal to the ratio of the upgoing wave to the downgoing wave:

$$\tilde{R}(k_x, z_r, \omega, z_s) = \frac{\tilde{U}^{scat}(k_x, z_r, \omega, z_s)}{\tilde{I}(k_x, z_r, \omega, z_s) + \tilde{D}^{scat}(k_x, z_r, \omega, z_s)}. \tag{7.7}$$

This spectral division is evaluated in a stabilised way.

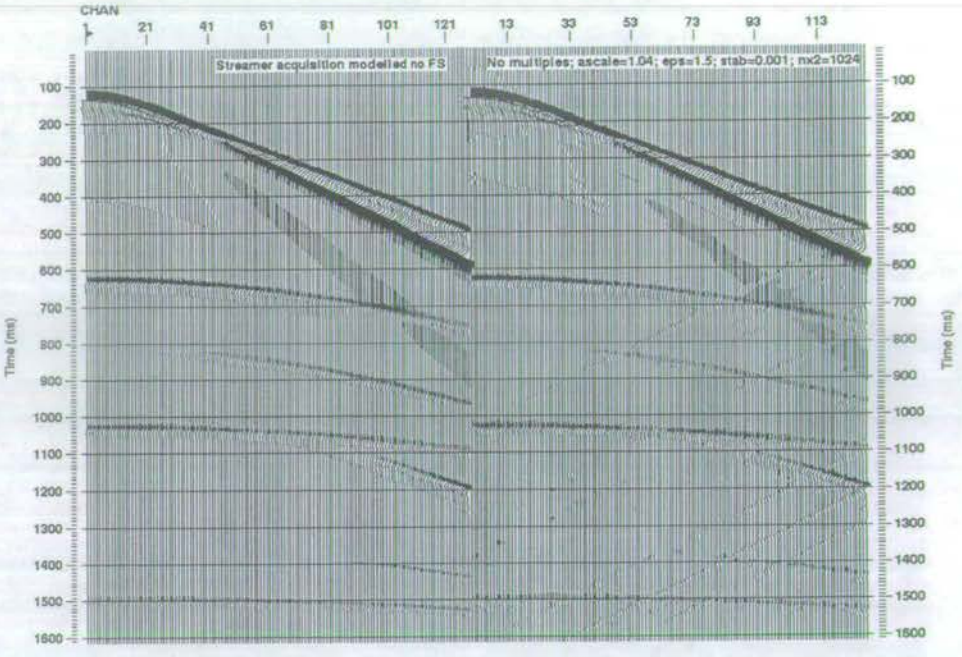


Figure 7.7: Multiple removal with line source streamer data over a 1D elastic earth. The gather on the left is pressure modelled with no free surface; the gather on the right is the result of processing the seismogram with multiples to remove them.

### Re-introducing an incident field

Carrying out the division in equation (7.7) results in the reflection response of the earth which is broad-band, where deconvolution for the source signature $S(\omega)$ is carried out implicitly by the division. In order to view the reflection response in the time-space domain it is necessary to band-limit it: an idealised incident field is propagated to the boundary where the reflection response is defined, multiplied by the response, and then propagated up to the receivers. In this case the reflection response is defined at the receiver level, so only propagation from the source to the receivers is required. The idealised incident field $\tilde{I}^z$ is defined thus,

$$\tilde{P}^0(k_x, z_r, \omega, z_s) = \tilde{I}^z(k_x, z_r, \omega, z_s)\tilde{R}(k_x, z_r, \omega, z_s), \tag{7.8}$$

where

$$\tilde{I}^z(k_x, z_r, \omega, z_s) = \frac{i}{2k_z} S^z(\omega)\Big(\exp(ik_z|z_s - z_r|)\Big), \tag{7.9}$$

and $S^z(\omega)$ has some smooth desired wavelet spectrum. In practice, the original signal $S(\omega)$ represents a long and oscillatory air gun array signature; however, in this synthetic case, the

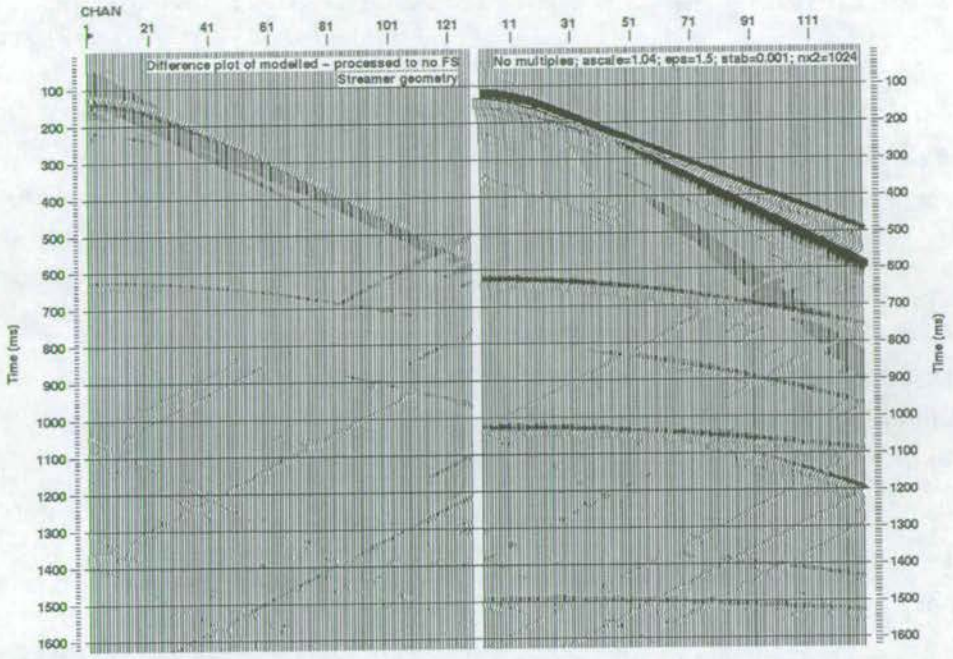


Figure 7.8: Multiple removal with line source streamer data over a 1D elastic earth. The gather on the left is the difference between the modelled with no free surface case and the processed to no free surface case; the gather on the right has been processed to no free surface.

$S(\omega)$ is a Ricker wavelet which already has the desired spectral characteristics, so $S^z(\omega) = S(\omega)$.

### Multiple-free seismograms

Transformation of $\tilde{P}^0(k_x, z_r, \omega, z_s)$ back to the time-space domain ,

$$p^0(x_r, z_r, t, z_s) = \left(\frac{1}{2\pi}\right)^2 \int\int_{-\infty}^{\infty} \tilde{P}_0(k_x, z_r, \omega, z_s) \exp\Big(-i[\omega t - k_x x]\Big) \mathrm{d}\omega \mathrm{d}k_x, \tag{7.10}$$

allows interpretation to follow. The result of sea surface multiple removal following these steps is plotted in Figure 7.7. The seismogram modelled without the free surface is on the left; the seismogram modelled with the free surface, then processsed to remove the multiples is on the right. The difference between these is small, as shown in Figure 7.8. The plot on the right of Figures 7.7 and 7.8 is comparable with the pressure data (with multiples) in Figures 7.3 and 7.6 (left panel). The multiples have clearly been eliminated, while the amplitudes of the primaries are intact.

## 7.3 A sensitivity analysis with line source streamer data

To calculate the reflection response of the earth as a ratio, as shown in the previous section, the data ($P^{scat}(k_x, z_r, \omega, z_s)$ and $S(\omega)$) must have the correct amplitudes in units of pressure. This means that the data cannot be tapered in offset to try to reduce any undesirable edge effects, otherwise incorrect amplitudes result in the frequency-wavenumber domain, giving incomplete multiple elimination. In addition, any recorded dataset must be internally consistent so that measurements at the source array can be related to the data recorded by the streamer. Both of these recordings should be converted to pressure.

What follows below is a discussion of some possible sources of error which might influence the performance of the multiple-removal scheme. It is given in the context of the simple case of a line source over a 1D earth. However, the results are generally valid for more complicated examples which appear later in the thesis (chapter 8).

### Random noise

Uncorrelated, normally distributed, random noise can be simulated using a portable random number generator. Processing synthetic data with additive noise gives an indication of the algorithm's robustness and stability. This is important when considering the application of a multiple removal scheme to real data which always contains noise of some kind, uncorrelated and/or correlated.

Figure 7.9 shows the data of Figure 7.3, with increasing amounts of random noise added. The noise is specified with respect to the maximum value in the gather: 0.1%, 0.3%, 1.0% and 3.0%, clockwise from the top left. Figure 7.10 shows the application of the multiple removal scheme to the data in Figure 7.9.

The scheme performs well in all of the four cases given here. The primary information is recovered, and the multiples are supressed. As the noise level increases, the weaker primaries, which are obscured by the multiples in the noise-free case (left panel of Figure 7.6), are obscured by the noise in the processed result. Note, however, in the worst case given here of 3.0% additive noise, that the primary reflection (Figure 7.10) between 0.5 and 0.8s is recovered from a zone where there is very little amplitude information in the original data (Figure 7.9). The stability of the multiple-free result is ensured through careful handling of the complex division for the reflection response in equation (7.7).

### Input parameter selection

The recovery of the reflection response, and hence multiple removal, is performed in the frequency-wavenumber domain. Small errors in the required input parameters have a complicated effect which is felt for all times and all offsets. Because the method presented in this thesis is deterministic, and as such requires all the input data to be defined as precisely as

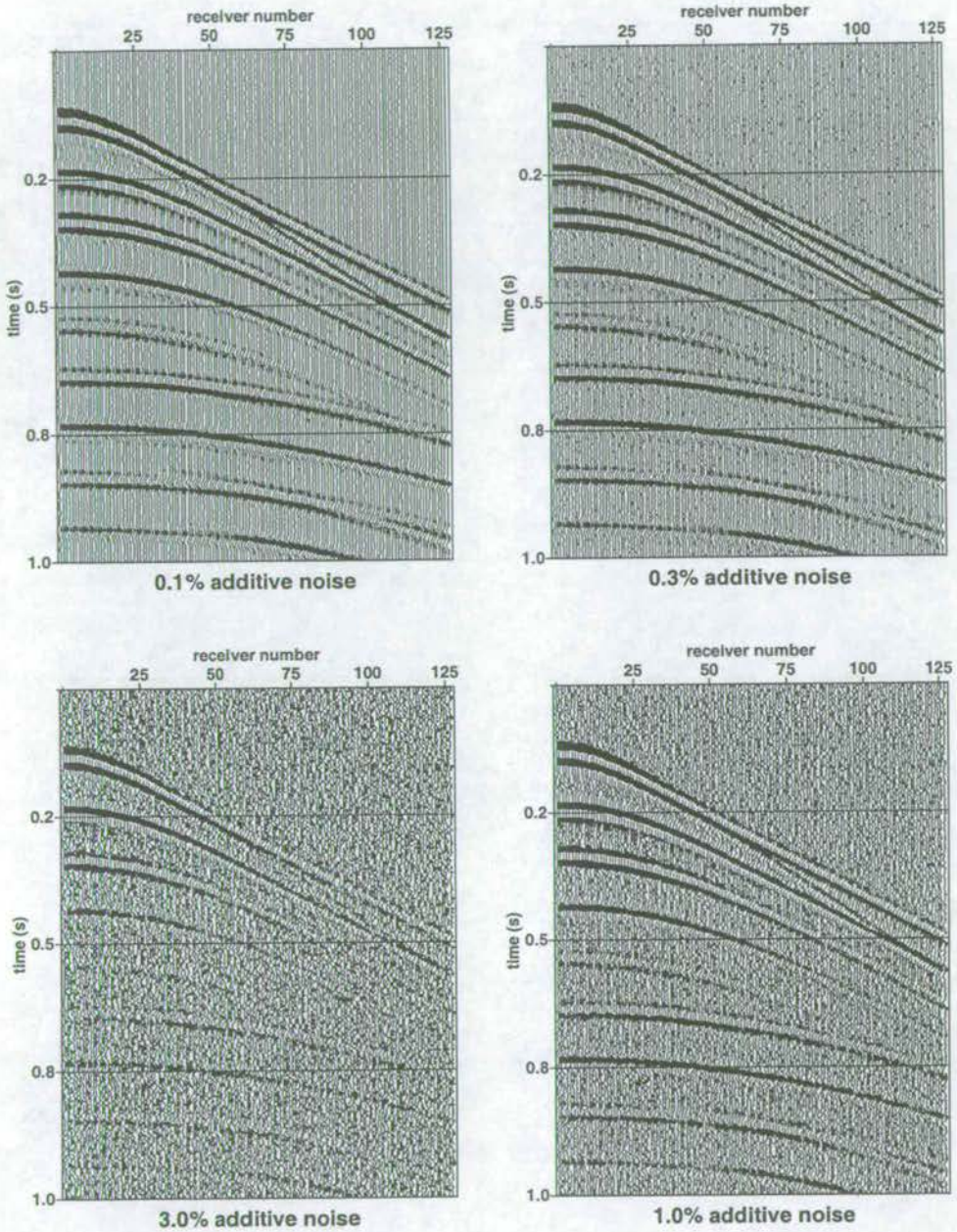


Figure 7.9: The scattered pressure wavefield for line source streamer data in the presence of random noise. The noise is calculated as a percentage of the maximum value in the data: 0.1%, 0.3%, 1.0% and 3.0%, clockwise from the top left.

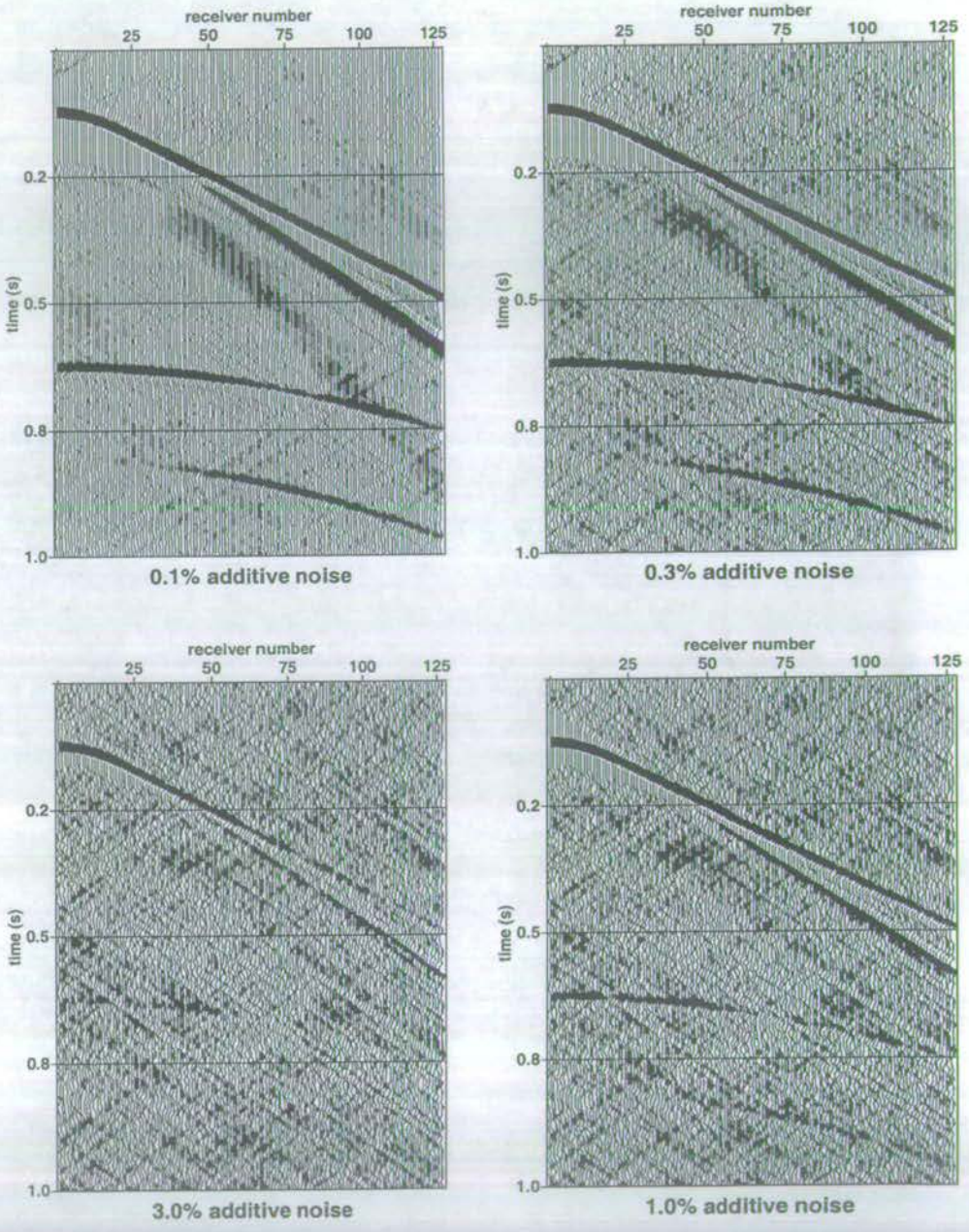


Figure 7.10: The processed multiple-free wavefield for line source streamer data in the presence of random noise. The noise is calculated as a percentage of the maximum value in the (multiple-contaminated) data: 0.1%, 0.3%, 1.0% and 3.0%, clockwise from the top left.

possible, insight can be gained into the stability of the multiple-free solution by varying some of the possible parameters.

The reflection response is described as a ratio involving three quantities, $\tilde{U}^{scat}$, $\tilde{D}^{scat}$ and $\tilde{I}$. Writing these quantities out in terms of the data, which are invariant, and parameters, their variation with respect to a particular input value can be assessed in isolation:

$$\tilde{U}^{scat}(k_x, z_r, \omega, z_s) = \tilde{P}^{scat}(k_x, z_r, \omega, z_s)\,\tilde{U}_f \tag{7.11}$$

$$\text{where} \quad \tilde{U}_f = \left[1 - \exp\left(ik_z[2z_r]\right)\right]^{-1}, \tag{7.12}$$

$$\tilde{D}^{scat}(k_x, z_r, \omega, z_s) = \tilde{P}^{scat}(k_x, z_r, \omega, z_s)\,\tilde{D}_f \tag{7.13}$$

$$\text{where} \quad \tilde{D}_f = -\left[1 - \exp\left(ik_z[2z_r]\right)\right]^{-1} \exp\left(ik_z[2z_r]\right), \tag{7.14}$$

$$\tilde{I}(k_x, z_r, \omega, z_s) = \frac{i}{2} S(\omega)\,\tilde{I}_f \tag{7.15}$$

$$\text{where} \quad \tilde{I}_f = \left[\exp\left(ik_z|z_s - z_r|\right) - \exp\left(ik_z[z_s + z_r]\right)\right]\frac{1}{k_z}. \tag{7.16}$$

The two factors $\tilde{U}_f$ and $\tilde{D}_f$ depend on the water velocity $c$ (via $k_z$), and the receiver depth $z_r$, whereas $\tilde{I}_f$ depends on the source depth $z_s$, as well as $c$ and $z_r$. By calculating the amplitude and phase of each of these quantities for a fixed frequency $\omega$ and horizontal wavenumber $k_x$, the effect of varying each of $z_s$, $z_r$ and $c$ can be monitored independently of the data. The associated effect on the reflection response is given by the amplitude and phase of $\tilde{R}_f$:

$$\tilde{R}_f = \frac{\tilde{U}_f}{\tilde{I}_f + \tilde{D}_f}. \tag{7.17}$$

Figure 7.11 shows, for a dominant $\omega$ and $k_x$, the amplitude and phase of $\tilde{U}_f$, $\tilde{D}_f$, $\tilde{I}_f$ and $\tilde{R}_f$ for fixed $c$ and $z_s$, and varying $z_r$ from 4m to 10m in 1m steps. The correct receiver depth is 7m. The 1m steps correspond to a 14% change. $\tilde{I}_f$ undergoes a phase change about the correct value of $z_r$; this is accompanied by gradual changes in both $\tilde{U}_f$ and $\tilde{D}_f$. The change in $\tilde{I}_f$ acts essentially as a scale factor, since the incident field does not affect the upgoing and downgoing waves, only their ratio. The changes in $\tilde{U}_f$ and $\tilde{D}_f$ are more subtle, but their effect on the upgoing and downgoing waves is biggest when the receivers are too shallow. The combined effect of these errors on the reflection response in the time-space domain is a failure to remove all the multiples when the receivers are too deep, and a complete breakdown in the scheme when the receivers are too shallow (Figures 7.12 and 7.13).

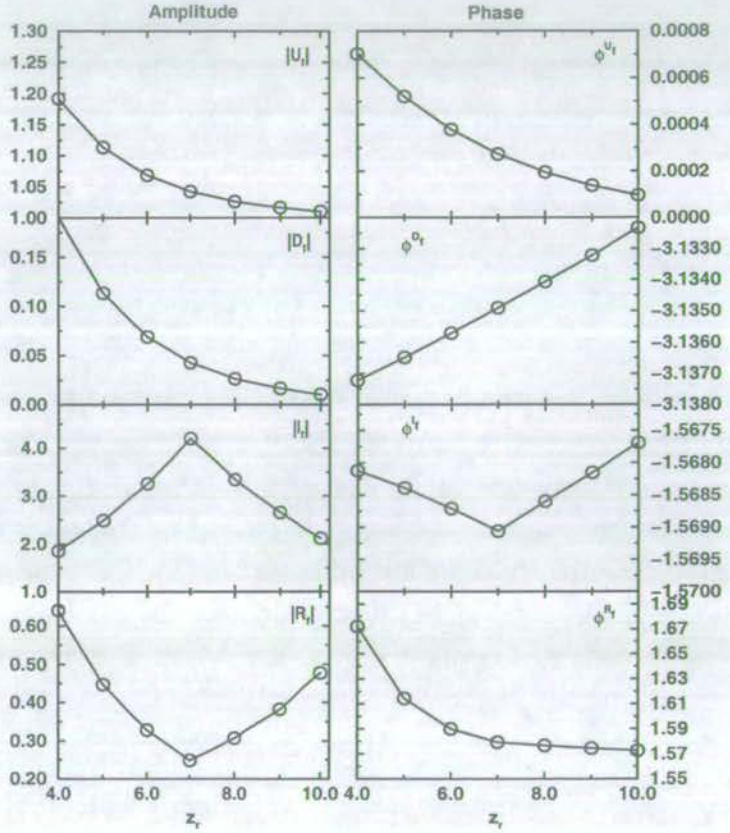


Figure 7.11: Amplitude and phase factors for the upgoing, downgoing, incident and reflection frequency-wavenumber domain responses, for varying $z_r$.

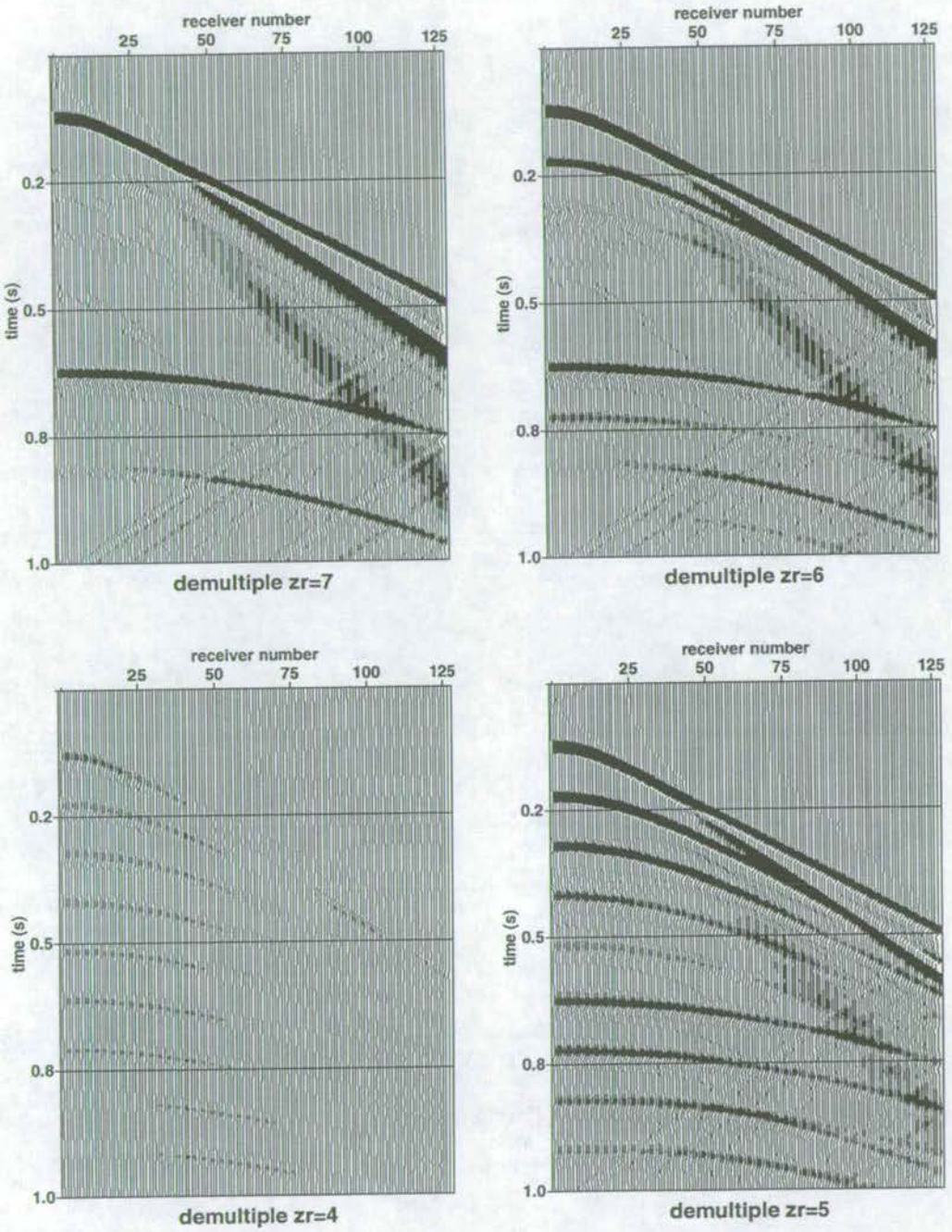


Figure 7.12: The multiple-free wavefield calculated from line source streamer data. The receiver depth is in error by −0m (0%), −1m (14%), −2m (28%), −3m (42%), clockwise from the top left.

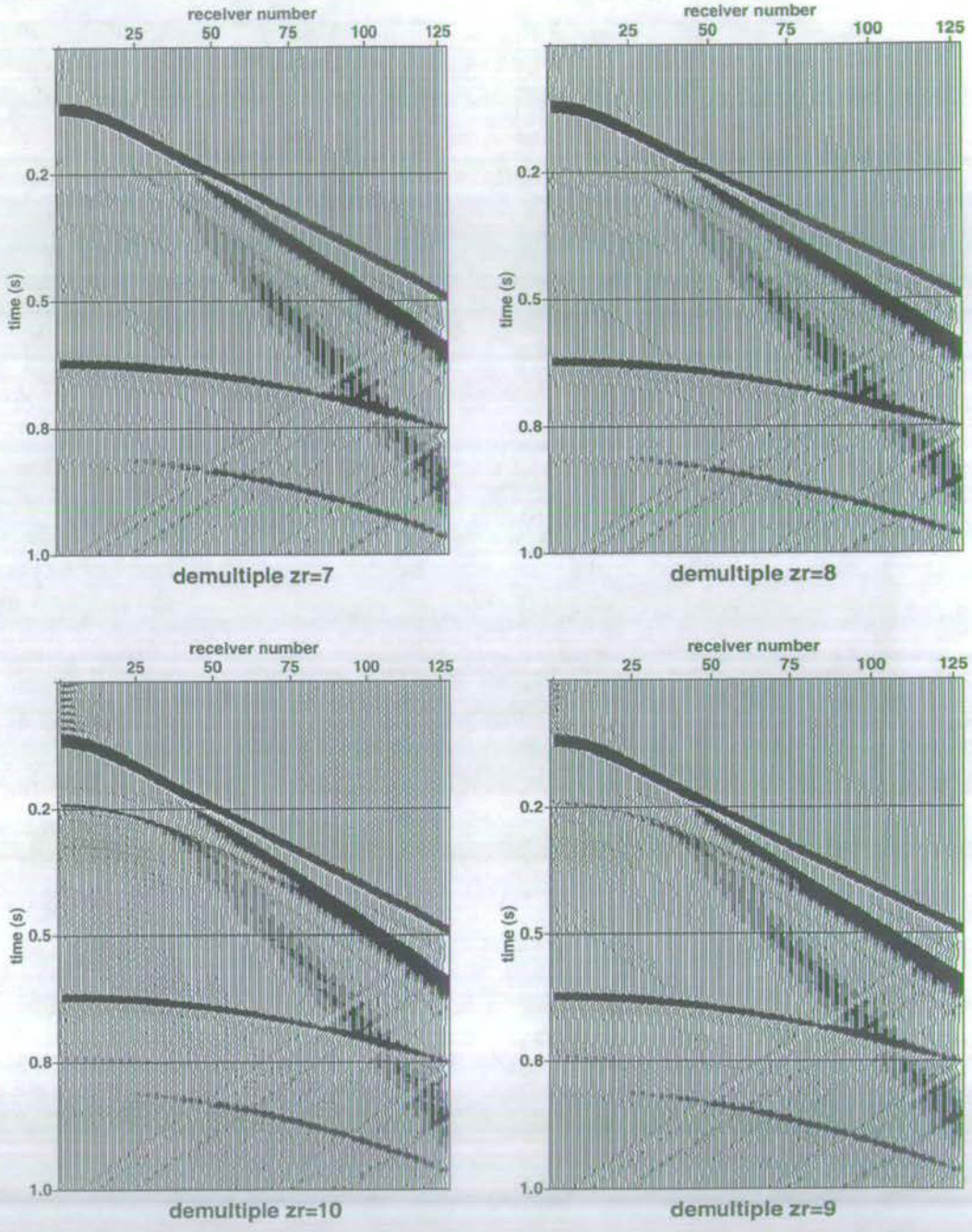


Figure 7.13: The multiple-free wavefield calculated from line source streamer data. The receiver depth is in error by +0m (0%), +1m (14%), +2m (28%), +3m (42%), clockwise from the top left.

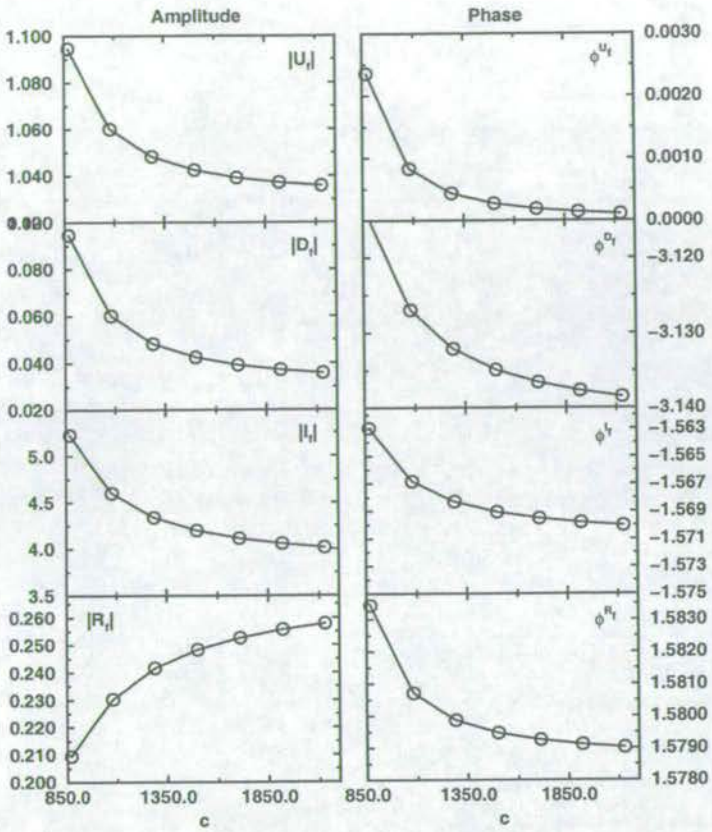


Figure 7.14: Amplitude and phase factors for the upgoing, downgoing, incident and reflection frequency-wavenumber domain responses, for varying $c$.

Figure 7.14 shows, for a dominant $\omega$ and $k_x$, the amplitude and phase of $\tilde{U}_f$, $\tilde{D}_f$, $\tilde{I}_f$ and $\tilde{R}_f$ for fixed $z_r$ and $z_s$, and varying $c$ from 870ms$^{-1}$ to 2130ms$^{-1}$ in 210ms$^{-1}$ steps. The correct water velocity is 1500ms$^{-1}$. The 210ms$^{-1}$ steps correspond to the same 14% (1m) change in $z_r$ above. It is unlikely that the water velocity would vary as much in practice, but keeping the percentage change in parameters the same allows for a better comparison. All of $\tilde{U}_f$, $\tilde{D}_f$ and $\tilde{I}_f$ undergo gradual changes as $c$ is varied about the correct value. The error in $c$ means that an incorrect dispersion relation is being used to propagate the data in the water layer. For the incident field this essentially means scaling. For the upgoing and downgoing fields extracted from the scattered field, this means a complex distortion through treating the propagating and evanescent parts of the data incorrectly. The combined effect on the reflection response in the time-space doman causes the scheme to become unstable when $c$ is too low by amplifying horizontally travelling waves, and causes the scheme to break down when $c$ is too high (Figures 7.15 and 7.16). In Figure 7.16, the lower two plots show coherent noise when displayed with a gain which is higher than the other displays in this section.

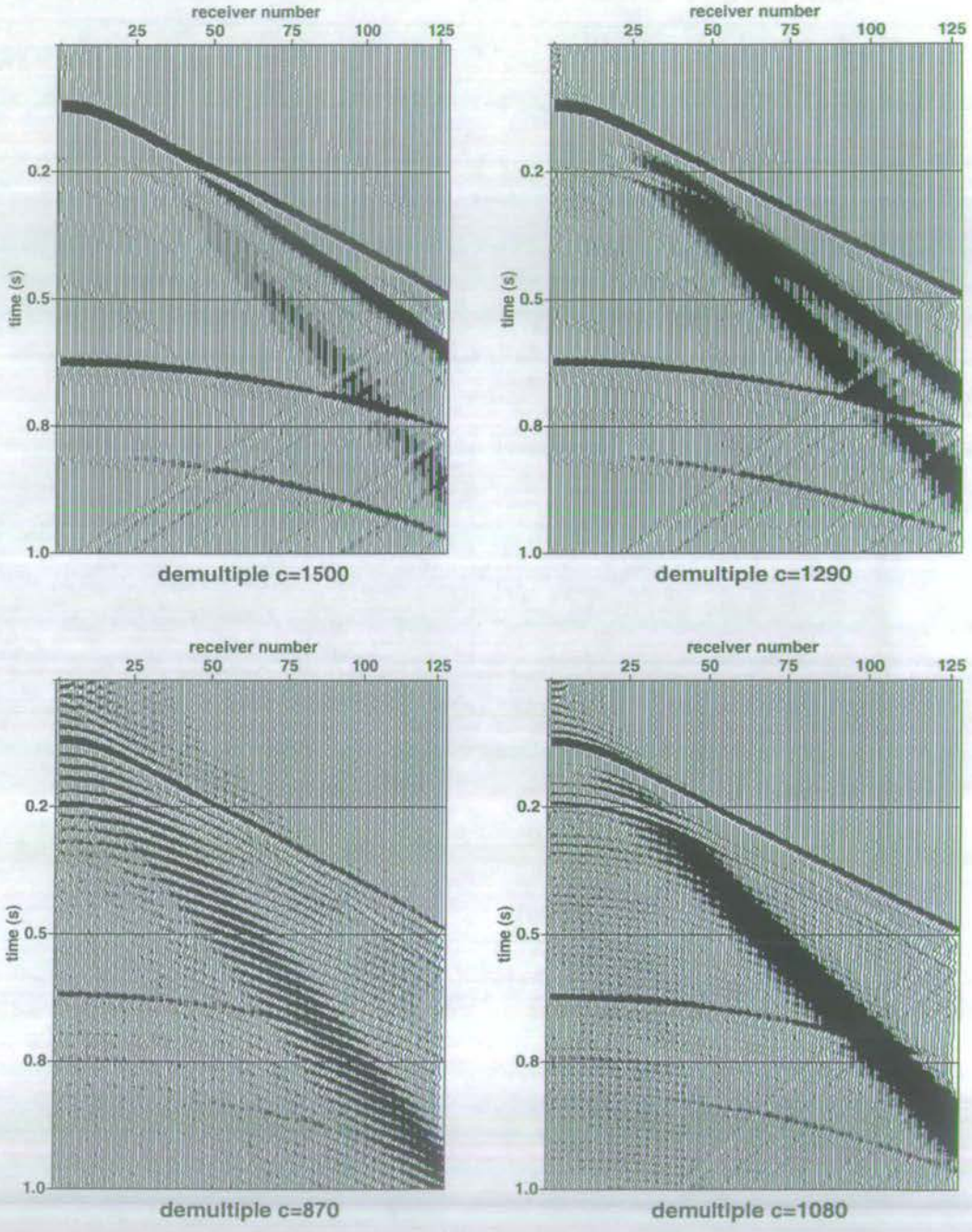


Figure 7.15: The multiple-free wavefield calculated from line source streamer data. The acoustic velocity is in error by $-0\text{ms}^{-1}$ (0%), $-210\text{ms}^{-1}$ (14%), $-420\text{ms}^{-1}$ (28%), $-630\text{ms}^{-1}$ (42%), clockwise from the top left.

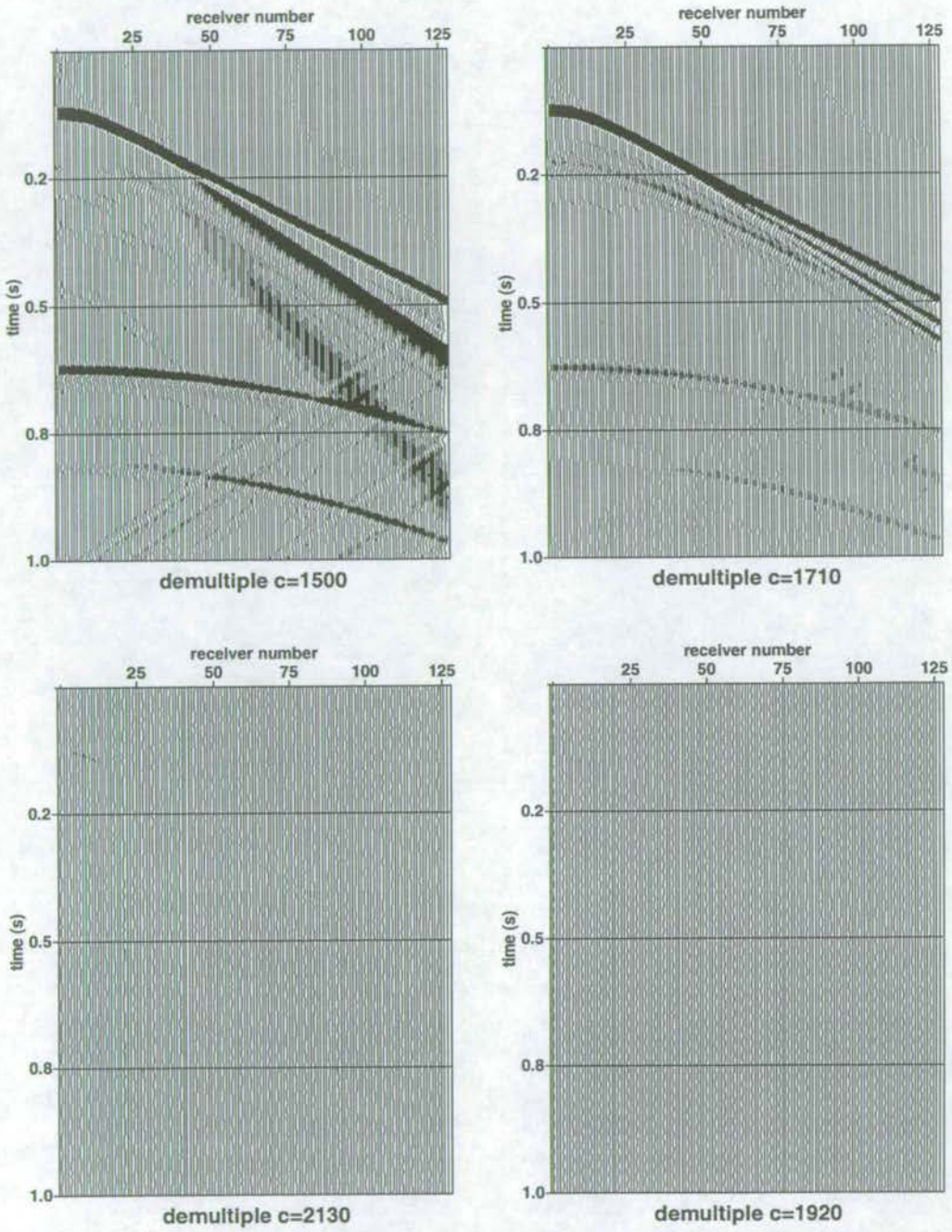


Figure 7.16: The multiple-free wavefield calculated from line source streamer data. The acoustic velocity is in error by $+0\text{ms}^{-1}$ (0%), $+210\text{ms}^{-1}$ (14%), $+420\text{ms}^{-1}$ (28%), $+630\text{ms}^{-1}$ (42%), clockwise from the top left.

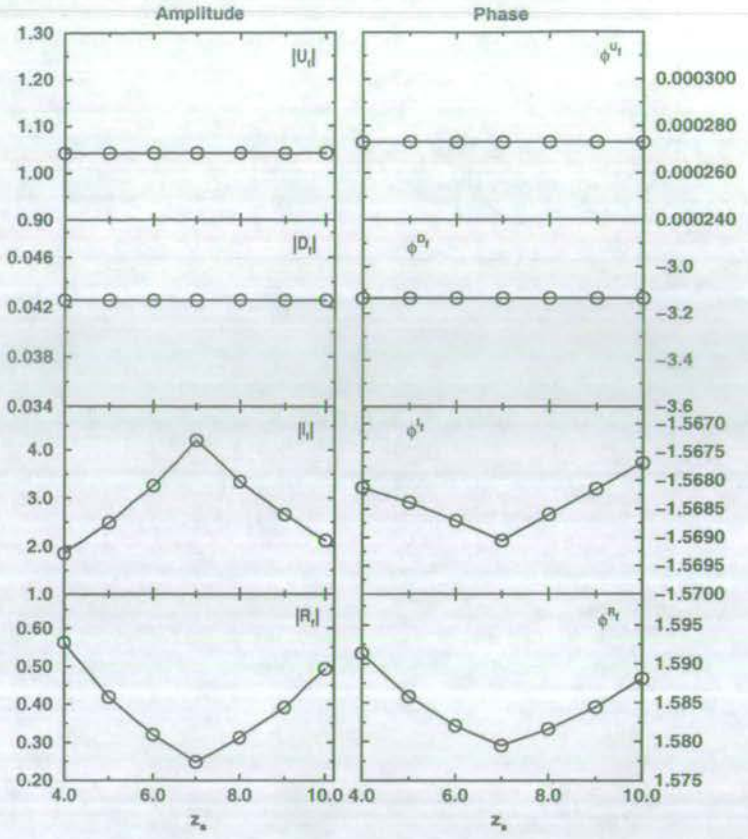


Figure 7.17: Amplitude and phase factors for the upgoing, downgoing, incident and reflection frequency-wavenumber domain responses, for varying $z_s$.

Figure 7.17 shows, for a dominant $\omega$ and $k_x$, the amplitude and phase of $\tilde{U}_f$, $\tilde{D}_f$, $\tilde{I}_f$ and $\tilde{R}_f$ for fixed $z_r$ and $c$, and varying $z_s$ from 4m to 10m in 1m steps. The correct source depth is 7m. The 1m steps correspond to a 14% change. To measure the source signature correctly requires the source depth to be known accurately (to within 10%: Ziolkowski and Johnston, 1997). $\tilde{U}_f$ and $\tilde{D}_f$ are unaffected by an error in the source depth. $\tilde{I}_f$ undergoes a phase change about the correct value of $z_s$, as observed when $z_r$ changes. If the the upgoing and downgoing waves are extracted from the scattered field correctly, $\tilde{R}_f$ is only affected by the change in $\tilde{I}_f$ as observed in Figure 7.17. The implications of this are clear: as $z_s$ passes from too low to too high, the reflection response passes through the correct value, where the ratio of upgoing to downgoing waves is properly balanced by the incident field. On either side of the correct value of $\tilde{R}_f$, the ratio is not correct and either too much or too little multiple energy is removed so that in the time-space domain we observe the phase change in the multiples caused by the error in $z_s$ (Figures 7.18 and 7.19). Only at the correct value of $z_s$ are the multiples completely cancelled.

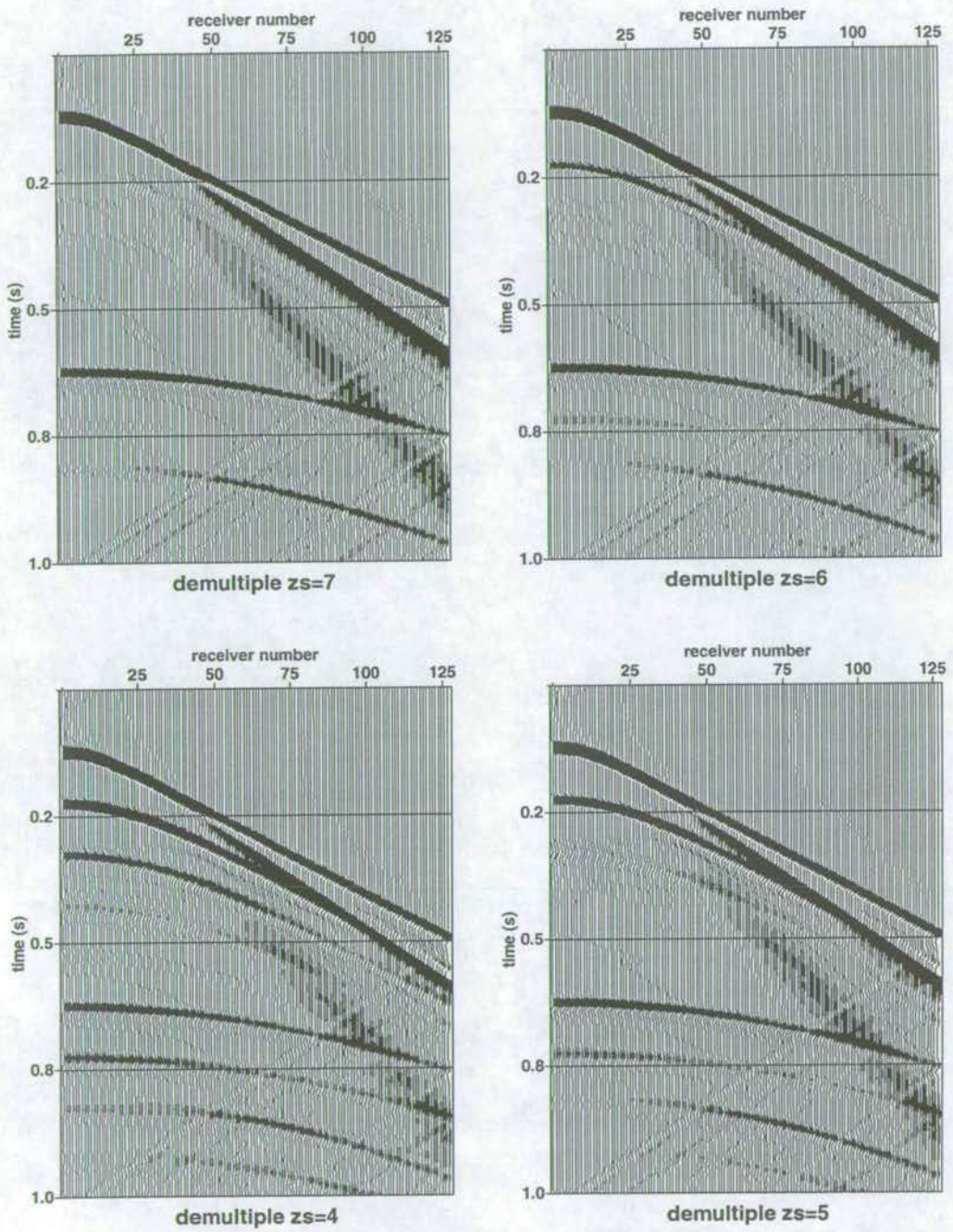


Figure 7.18: The multiple-free wavefield calculated from line source streamer data. The source depth is in error by −0m (0%), −1m (14%), −2m (28%), −3m (42%), clockwise from the top left.

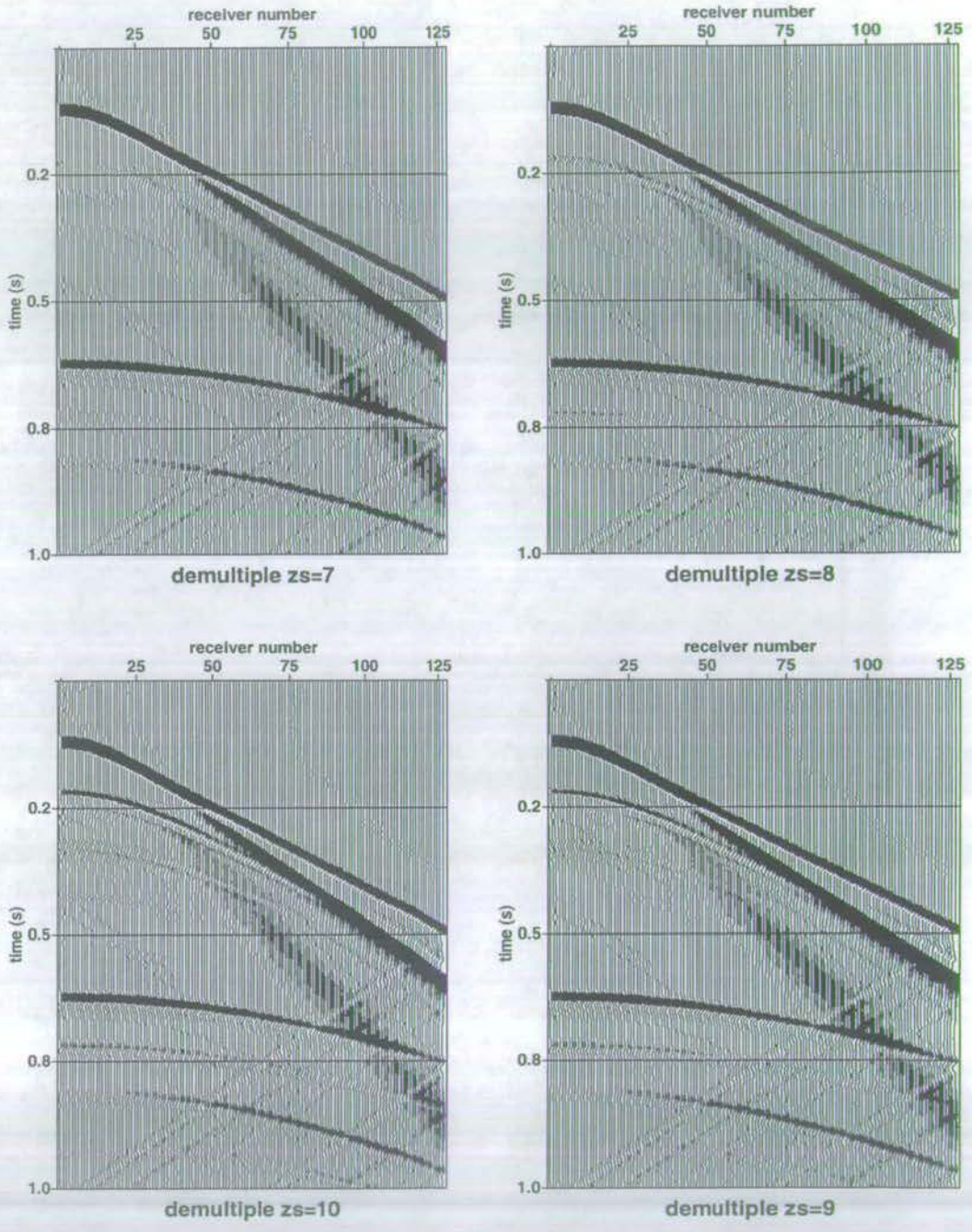


Figure 7.19: The multiple-free wavefield calculated from line source streamer data. The source depth is in error by +0m (0%), +1m (14%), +2m (28%), +3m (42%), clockwise from the top left.

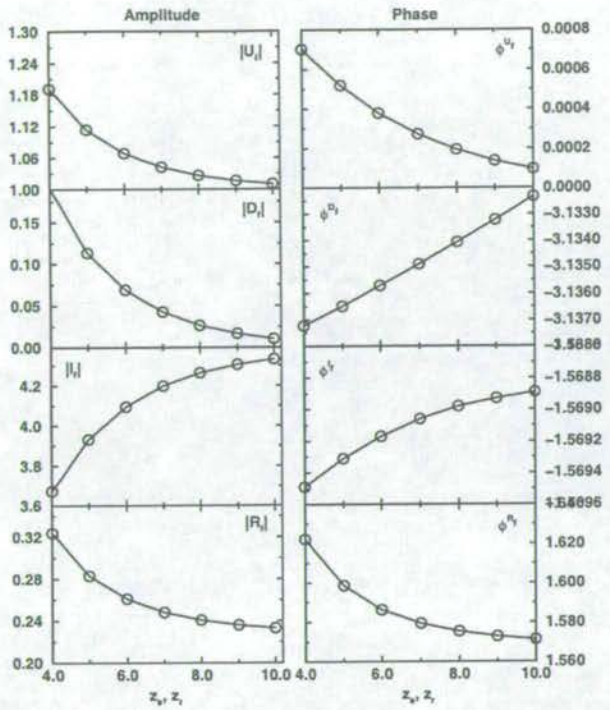


Figure 7.20: Amplitude and phase factors for the upgoing, downgoing, incident and reflection frequency-wavenumber domain responses, for varying $z_s$ and $z_r$.

Figure 7.20 shows, for a dominant $\omega$ and $k_x$, the amplitude and phase of $\tilde{U}_f$, $\tilde{D}_f$, $\tilde{I}_f$ and $\tilde{R}_f$ for fixed $c$, and varying $z_s$ and $z_r$ concurrently from 4m to 10m in 1m steps. The correct source depth and the correct receiver depth is 7m. The effect of changing both $z_s$ and $z_r$ at the same time causes a gradual change in the incident field, and gradual changes in the upgoing and downgoing fields, as for changing $z_r$ alone. The net effect on the multiple-free seismograms (Figures 7.21 and 7.22) is dominated by the change in $z_r$, seen already in Figures 7.12 and 7.13.

In summary, errors in $z_r$ and $c$ have a complicated effect on the upgoing, downgoing and incident wavefields, hence the reflection response, and the multiple-free seismograms. Errors of up to $\pm 14\%$ in $c$ are tolerable, and the result is still useful (that is to say, the majority of the multiples are eliminated at the expense of some wavefield distortion). Errors of up to $+35\%$ in $z_r$ are tolerable, whereas having the receivers too shallow is not, and the scheme breaks down. Errors in $z_r$ are more damaging to the multiple-free result than errors in $z_s$. Errors in the source depth, are tolerable up to $\pm 20\%$. However, the passage either side of the correct $z_s$ value results in the multiples undergoing a phase change, at which point they are completely eliminated. This is a characteristic of the incident field effectively scaling the ratio of the upgoing and downgoing scattered fields. The tolerated errors are larger than the precision with which the measurements are currently available, and therefore well within

normal acquisition specifications.

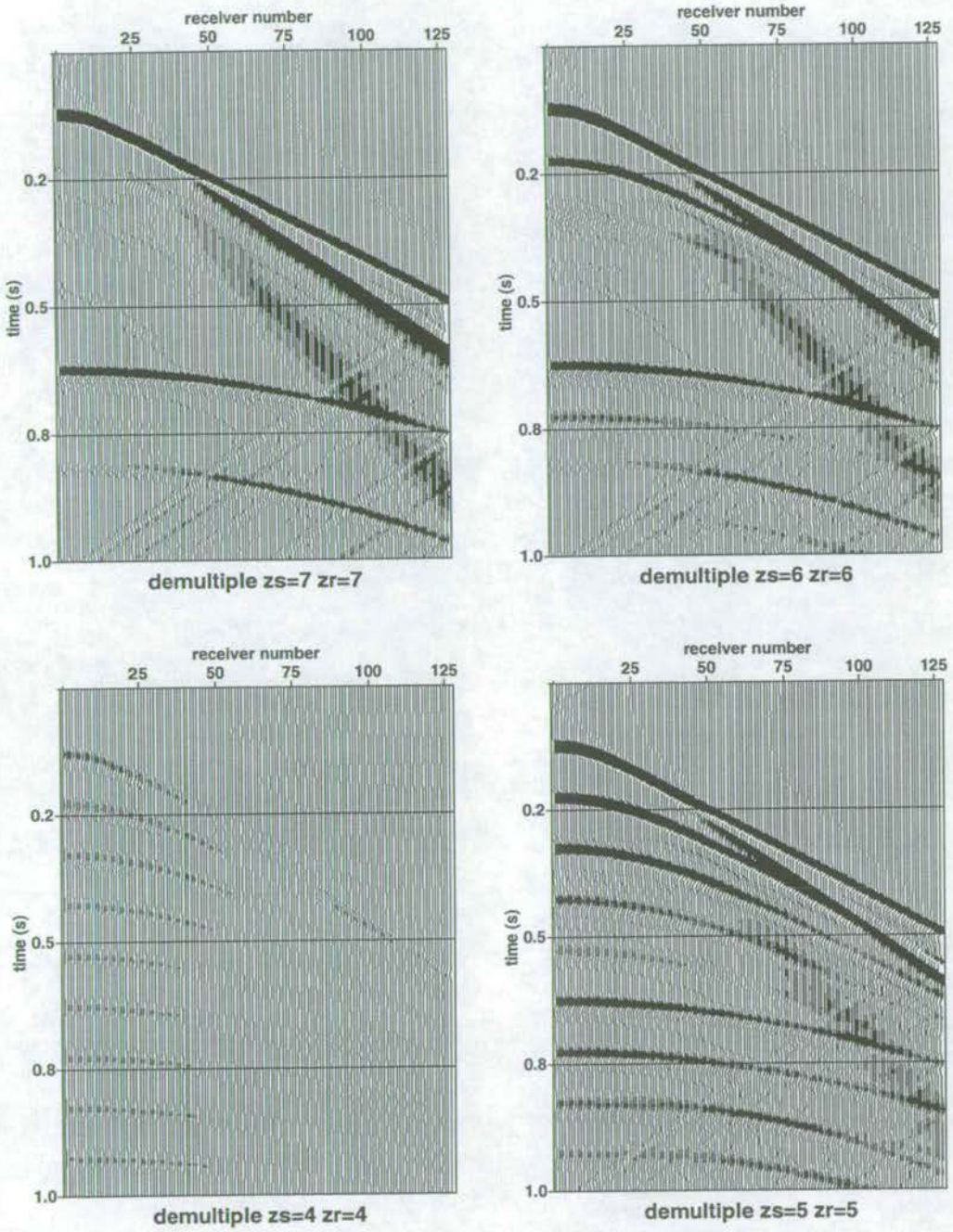


Figure 7.21: The multiple-free wavefield calculated from line source streamer data. The source and receiver depths are in error by −0m (0%), −1m (14%), −2m (28%), −3m (42%), clockwise from the top left.

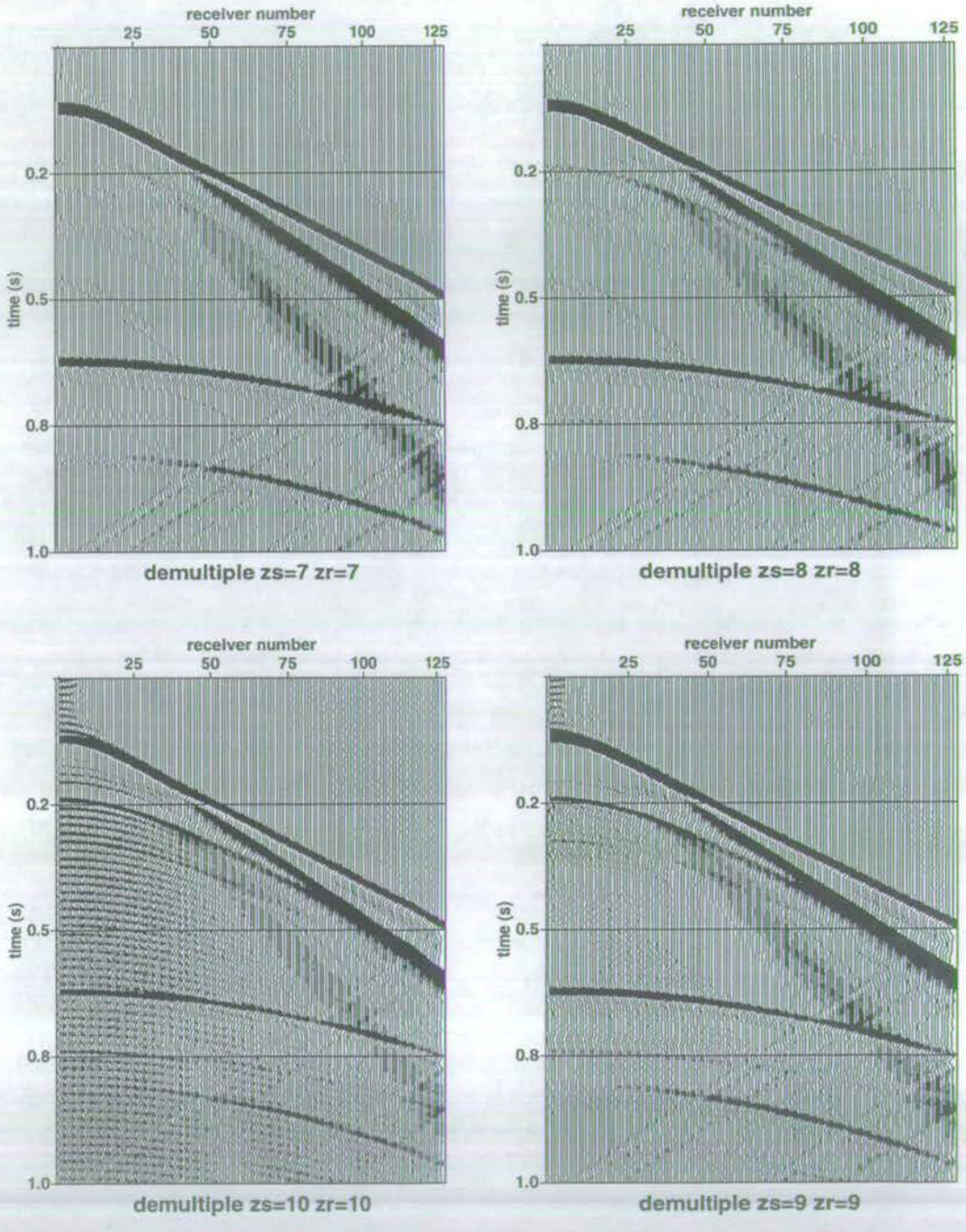


Figure 7.22: The multiple-free wavefield calculated from line source streamer data. The source and receiver depths are in error by +0m (0%), +1m (14%), +2m (28%), +3m (42%), clockwise from the top left.

## 7.4 A synthetic example with OBC data

The synthetic data used to illustrate the multiple removal scheme are computed at the interface between a water layer and an elastic earth with the reflectivity method (Fuchs and Müller, 1971). The modelling code used is OSIRIS of Ødegaard A/S. The layered earth model is detailed in Table 7.1.

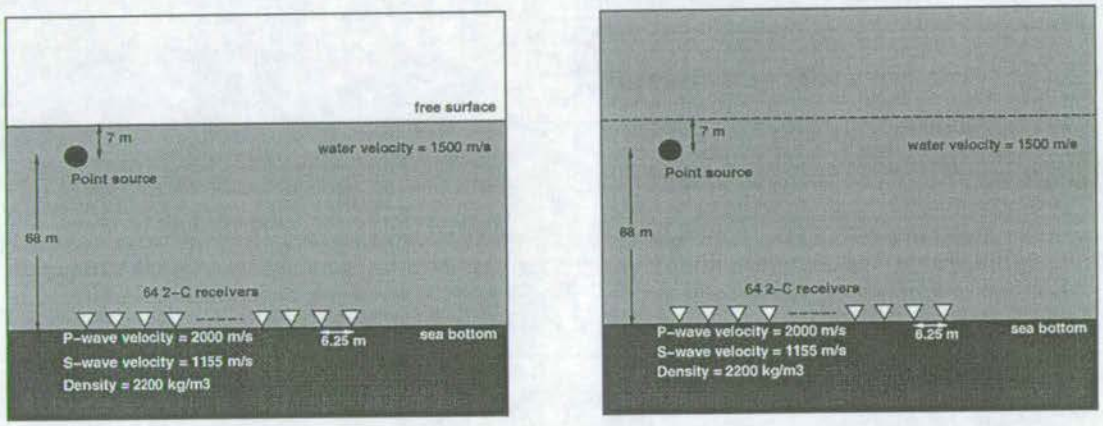


(a) With the free surface

(b) Without the free surface

Figure 7.23: Model acquisition geometry for 1D point source OBC synthetics.

Figure 7.23 shows a schematic of the acquisition set-up. The point source time function is a two-loop Ricker wavelet with a central frequency of 25 Hz (see Figure 7.2). 64 two-component receivers (pressure and the vertical component of particle velocity) are arranged in a line on the sea floor 6.25m apart (Figure 7.23). There is zero offset between the source and the 1st receiver. Figure 7.24 shows seismograms for the scattered pressure field in the presence of the sea surface, corresponding to Figure 7.23(a): the left panel is pressure; the right panel is the vertical component of particle velocity at the sea floor which is assumed to be continuous across the interface. Figure 7.25 shows seismograms for the scattered pressure field in the absence of the sea surface, corresponding to Figure 7.23(b): the left panel is pressure; the right panel is the vertical component of particle velocity. Most of the events on Figure 7.24 are therefore free-surface multiples which obscure the primary reflections and mode-conversions clearly observed in Figure 7.25. The goal of multiple removal in the water layer using OBC data is to convert the data in Figure 7.24 to the data in the left panel of Figure 7.25.

### Data preparation

As in section 7.2, the scattered field only is modelled so that the incident field need not be subtracted from the total field. It is shown later that for OBC data over a 1D earth this step is

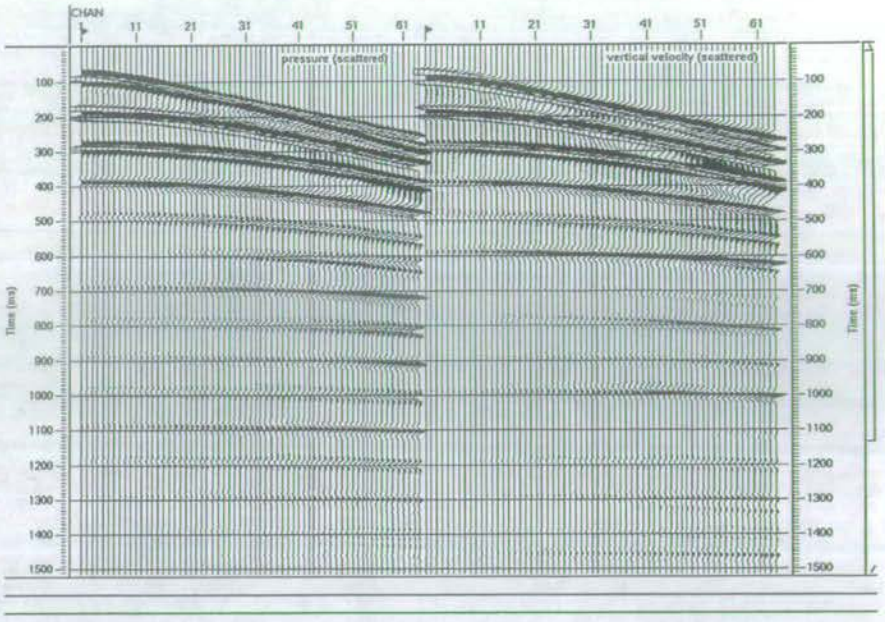


Figure 7.24: A point source over a layered earth with no incident field, in the presence of the free surface. The gather on the left is the pressure; the gather on the right is the vertical component of particle velocity.

not necessary.

In this simple 1D model, the earth properties change in one direction only, the $z$-direction which is vertical. Wave propagation from the point source is in three dimensions (the $x$-, $y$- and $z$-directions). To get the data $p^{scat}(x_r, y_r, z_r, t, z_s)$, recorded at depth $z_r$, in response to a point source at depth $z_s$, into the frequency-wavenumber domain, the data are Fourier transformed over time $t$, and over distance $x$ and $y$:

$$\tilde{P}^{scat}(k_x, k_y, z_r, \omega, z_s) = \iiint_{-\infty}^{\infty} p^{scat}(x_r, y_r, z_r, t, z_s) \exp\Big(+i[\omega t - k_x x - k_y y]\Big) \mathrm{d}t \mathrm{d}x \mathrm{d}y, \tag{7.18}$$

where the change from lowercase to uppercase $P$ indicates transformation from time to frequency, and the $\sim$, transformation from distance to wavenumber.

The propagation of spherical waves in a horizontally-layered medium is cylindrically symmetric about an axis pointing vertically downwards. The wavefield along a single line may therefore be expressed in the frequency-wavenumber domain by an expansion into cylindrical waves, as expressed by the Sommerfeld integal in equation (2.59). However, this integral (a Hankel transform) requires the calculation of asymptotic Bessel functions which is difficult to do with precision. Instead, (orthogonal) Fourier transforms are applied in two

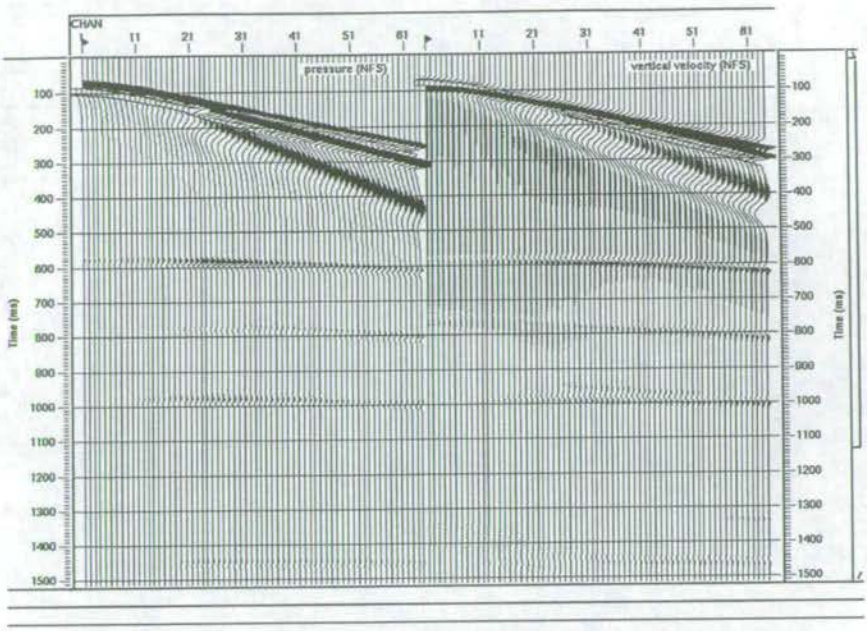


Figure 7.25: A point source over a layered earth with no incident field, in the absence of the free surface. The gather on the left is the pressure; the gather on the right is the vertical component of particle velocity.

spatial directions.

The transform to frequency is applied first. To stabilise computations in the frequency-wavenumber domain involving the vertical wavenumber $k_z$ (see appendix A.2), an exponential taper is applied to to each trace in the the time domain which makes the frequency complex (see appendix A.1). Zeros are added to the time axis to accommodate the operations applied in the frequency-wavenumber domain. This is shown schematically in Figure 7.26. Because the data are real-valued and do not exist before $t = 0$, data for $-\omega$ are the complex conjugates of the data for $+\omega$, so only the positive frequencies are processed.

Each frequency slice is a function of the $x$-direction, but the transform (equation (7.18)) requires data in both the $x$- and $y$-directions. Consider a point source of energy radiating in a one-dimensional earth. Spherical waves spread out in all directions away from the source location. Because the earth is 1D and the radiation pattern of a point source is spherically-symmetrical, the measurements along a horizontal line will be invariant with the position of the line. In other words, using the symmetry of the wavefield and the invariance of the earth model in the $x$- and $y$-directions, data on an $(x,y)$ grid can be interpolated from data along a line in $x$. Every point on a desired $(x,y)$ grid is mapped back onto the $x$-axis, and its value is found by cubic spline interpolation of the existing data. With $N$ receivers along the $x$-axis, the largest square $(x,y)$ grid is of side $2\frac{N}{\sqrt{2}}$ (as indicated on the extreme left of Figure 7.27).

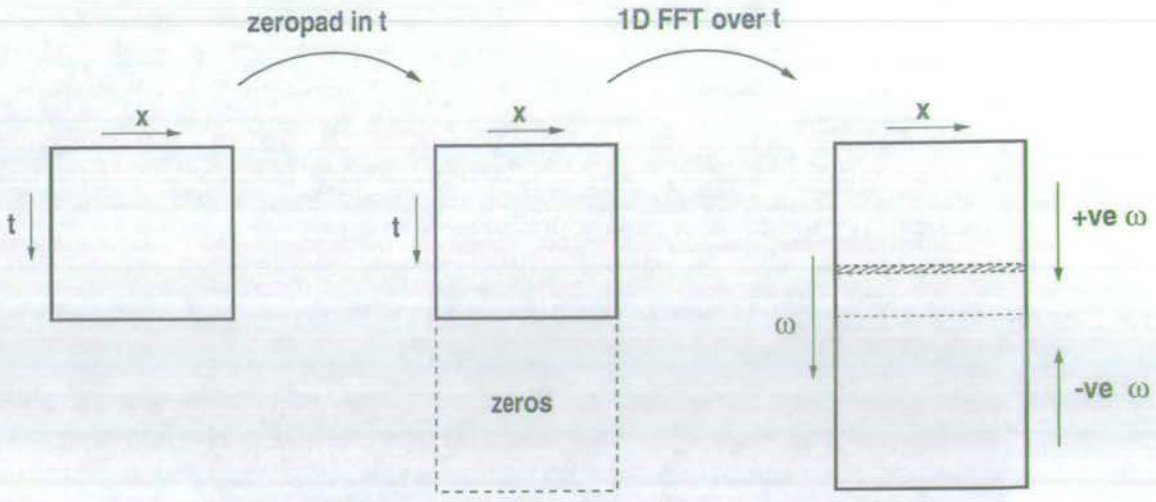


Figure 7.26: The data preparation required to transform from the time-space domain to the frequency-space domain, using point source data over a 1D earth.

Figure 7.27 shows schematically how each 1D frequency slice is interpolated onto a 2D grid. The data for negative $x$ and $y$ are simulated from the positive values making the data split-spread. Zeros are added in the $x$- and $y$-directions to accommodate operations in the frequency-wavenumber domain, and therefore prevent wraparound in the time-space domain. The data at negative and positive wavenumbers are then identical, so only the positive wavenumbers are processed.

This process is illustrated on the data shown in Figure 7.24. The data in the time-space domain are transformed to the frequency-space domain where they are interpolated on a per-frequency basis. Figure 7.28 shows a frequency slice through the data to illustrate the interpolation from a line (in the this case the ordinate $x$) to a grid in $(x,y)$. The amplitudes decay away radially from the source location in the bottom left-hand corner. The concentric arcs reflect the cylindrical symmetry exploited. Figure 7.28 shows positive offsets only. Figure 7.29 shows the non-unique offsets mirrored in the $x$- and $y$-directions and spatial data padding.

### Separating Upgoing and Downgoing Waves

When the acquisition geometry is OBC it is possible to separate the upgoing and downgoing waves by scaled sums and differences of the pressure and the vertical component of particle velocity:

$$2\tilde{U}^{scat}(k_x,k_y,z_r,\omega,z_s) = \tilde{P}^{scat}(k_x,k_y,z_r,\omega,z_s) - \frac{\rho\omega}{k_z}\tilde{V}_z^{scat}(k_x,k_y,z_r,\omega,z_s), \tag{7.19}$$

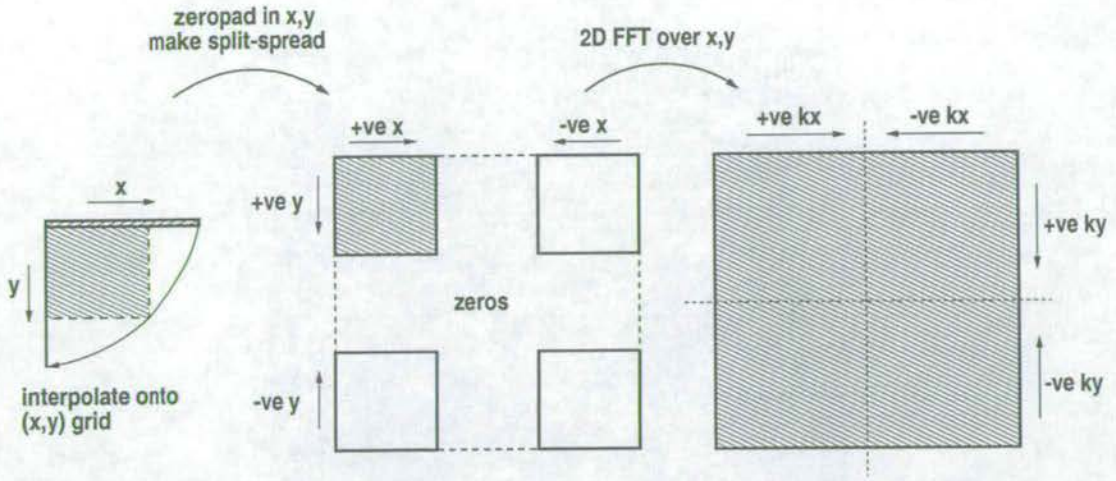


Figure 7.27: The data preparation required to transform from the frequency-space domain to the frequency-wavenumber domain, using a line of point source data over a 1D earth.

and

$$2\tilde{D}^{scat}(k_x,k_y,z_r,\omega,z_s) = \tilde{P}^{scat}(k_x,k_y,z_r,\omega,z_s) + \frac{\rho\omega}{k_z}\tilde{V}_z^{scat}(k_x,k_y,z_r,\omega,z_s), \tag{7.20}$$

where $k_z = \sqrt{\frac{\omega^2}{c^2} - k_x^2 - k_y^2}$ is the vertical wavenumber, and $\rho$ and $c$ are, respectively, the density and compressional wave velocity in the water. Application of equations (7.19) and (7.20) to the data of Figure 7.24 is shown in Figure 7.30.

### Calculating the Incident Field

In addition to the upgoing and downgoing scattered fields, the downgoing incident field from the source array to the receivers is required. Defining the incident field, as before, as that part of the total field which exists in the absence of the sea floor and the layers beneath it, each component of this field is defined in the frequency-wavenumber domain as

$$\tilde{I}(k_x,k_y,z_r,\omega,z_s) = \frac{i}{2k_z}S(\omega)\Big(\exp(ik_z|z_s - z_r|) - \exp(ik_z[z_s + z_r])\Big), \tag{7.21}$$

where all terms are as described previously. Figure 7.31 shows the incident field calculated for the acquisition geometry of Figure 7.23(a), with the scattered pressure field of Figure 7.24.

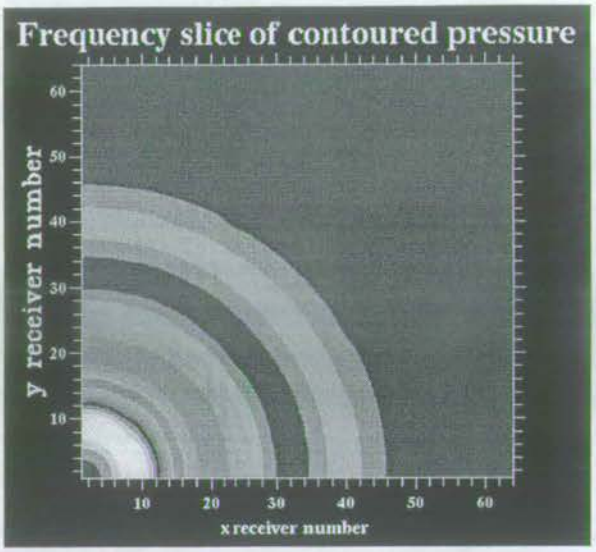


Figure 7.28: Data interpolation from a line of receivers along the $x$-axis to fill an $(x,y)$ grid of receivers, per frequency slice. The amplitudes decay away radially from the source position in the bottom left-hand corner.

### The reflection response

In the frequency-wavenumber domain the reflection response is defined as:

$$\tilde{R}(k_x,k_y,z_r,\omega,z_s)=\frac{\tilde{U}^{scat}(k_x,k_y,z_r,\omega,z_s)}{\tilde{I}(k_x,k_y,z_r,\omega,z_s)+\tilde{D}^{scat}(k_x,k_y,z_r,\omega,z_s)}. \tag{7.22}$$

This spectral division is evaluated in a stabilised way.

### Re-introducing an incident field

To view the reflection response in the time-space domain requires band-limiting with an idealised incident field $\tilde{I}^z$:

$$\tilde{P}^0(k_x,k_y,z_r,\omega,z_s)=\tilde{I}^z(k_x,k_y,z_r,\omega,z_s)\tilde{R}(k_x,k_y,z_r,\omega,z_s), \tag{7.23}$$

where

$$\tilde{I}^z(k_x,k_y,z_r,\omega,z_s)=\frac{i}{2k_z}S^z(\omega)\Big(\exp\left(ik_z|z_s-z_r|\right)\Big) \tag{7.24}$$

also propagates the plane waves to the receiver level. The frequency is complex to stabilise divisions by $k_z$, such as in the obliquity factor in equation (7.24). However, increased stability

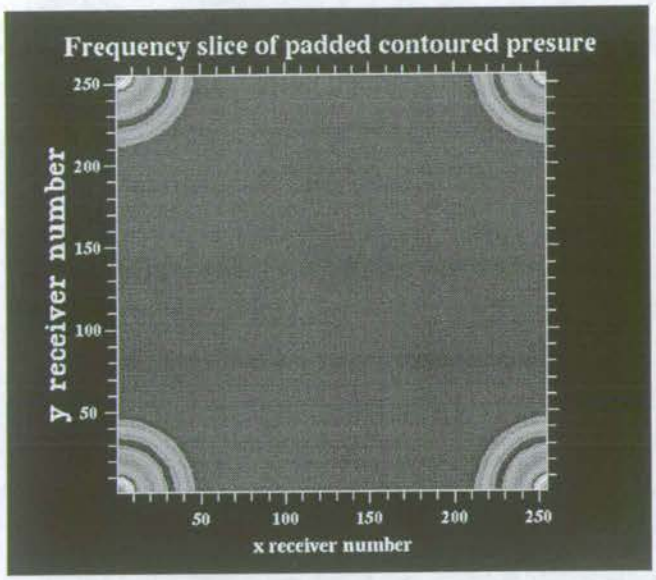


Figure 7.29: Using the data for positive offsets over a 1D earth to simulate a split-spread geometry to give data at negative offsets in the $x$- and $y$-directions, per frequency slice.

may be achieved by not dividing by $k_z$ at all. The partial derivative with respect to depth ($\frac{\partial}{\partial z}$) is equal to $-ik_z$ in the frequency-wavenumber domain. Therefore the factor $\frac{i}{k_z} = -\frac{1}{ik_z}$ in equation (7.24) effectively integrates the source pulse. Including the sea surface ghost reflection effectively differentiates the source pulse and cancels the effect of the $\frac{i}{k_z}$ factor. Therefore, a more desirable incident field which results in multiple-free seismograms with less numerical noise is

$$\tilde{I}^z(k_x,k_y,z_r,\omega,z_s) = \frac{i}{2k_z}S^z(\omega)\Big(\exp(ik_z|z_s-z_r|) - \exp(ik_z[z_s+z_r])\Big). \qquad (7.25)$$

### Multiple-free seismograms

Fourier transformation of $\tilde{P}^0(k_x,k_y,z_r,\omega,z_s)$ over frequency $\omega$, and over horizontal wavenumbers $k_x$ and $k_y$,

$$p^0(x_r,y_r,z_r,t,z_s) = \left(\frac{1}{2\pi}\right)^3 \int\int\int_{-\infty}^{\infty} \tilde{P}^0(k_x,k_y,z_r,\omega,z_s)\cdot \exp\Big(-i[\omega t - k_x x - k_y y]\Big)\,d\omega dk_x dk_y, \qquad (7.26)$$

allows interpretation to follow. The multiple-free seismograms calculated using this wavefield division approach are plotted in Figure 7.32. Figure 7.33 shows the multiple-free seimograms using (7.25). In both cases the gather modelled with no free surface is on the left, and the gather modelled with the free surface, then processsed to remove the multiples is on the right.

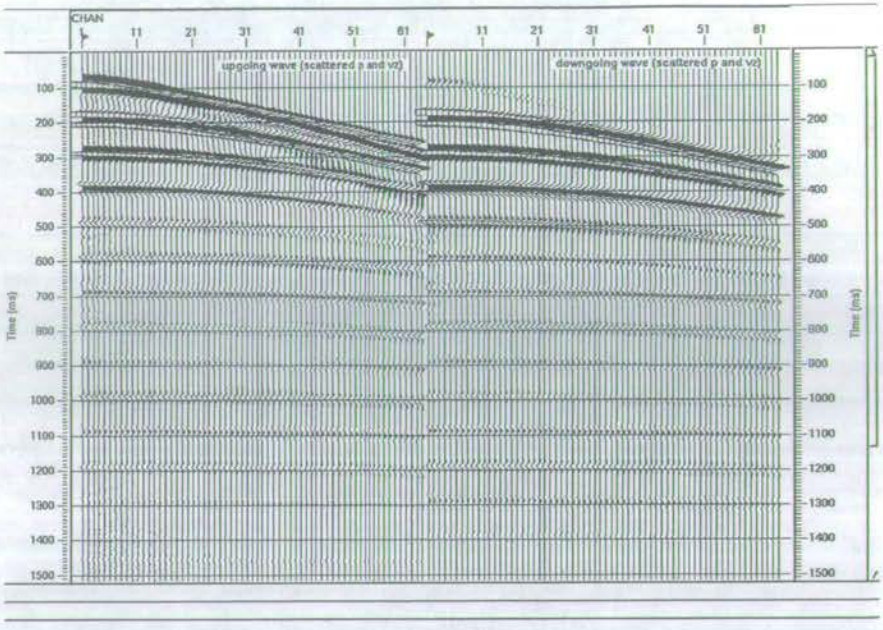


Figure 7.30: Separating upgoing and downgoing waves with the scattered fields of pressure and the vertical component of particle velocity for point source data over a 1D earth: Upgoing pressure wave on the left; downgoing pressure wave on the right.

The multiples have clearly been eliminated in both cases, although including the source ghost in the forward modelling step reduces numerical noise considerably.

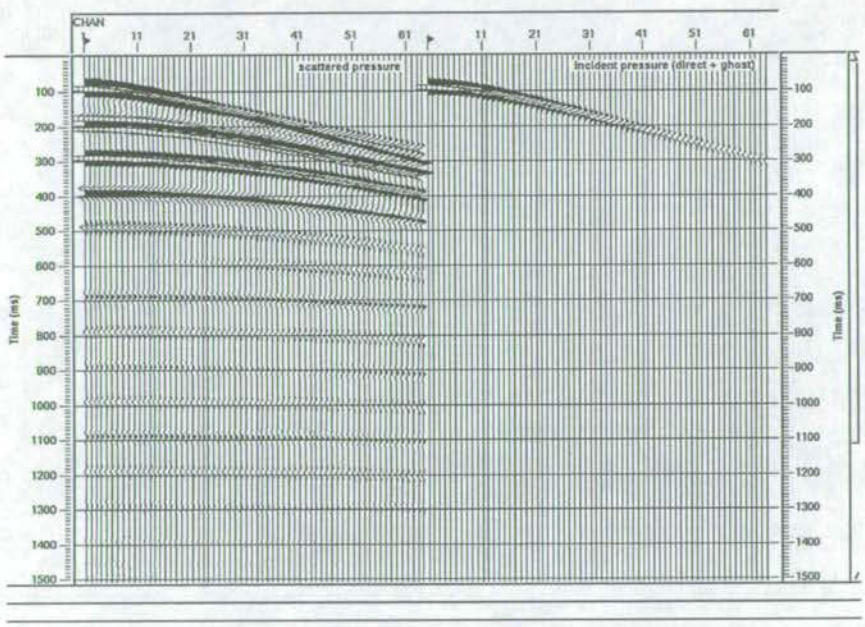


Figure 7.31: The scattered and incident fields for point source OBC data over a 1D elastic earth. The gather on the left is the pressure modelled in the presence of the free surface; the gather on the right is the calculated incident field (by definition direct and ghost arrivals).

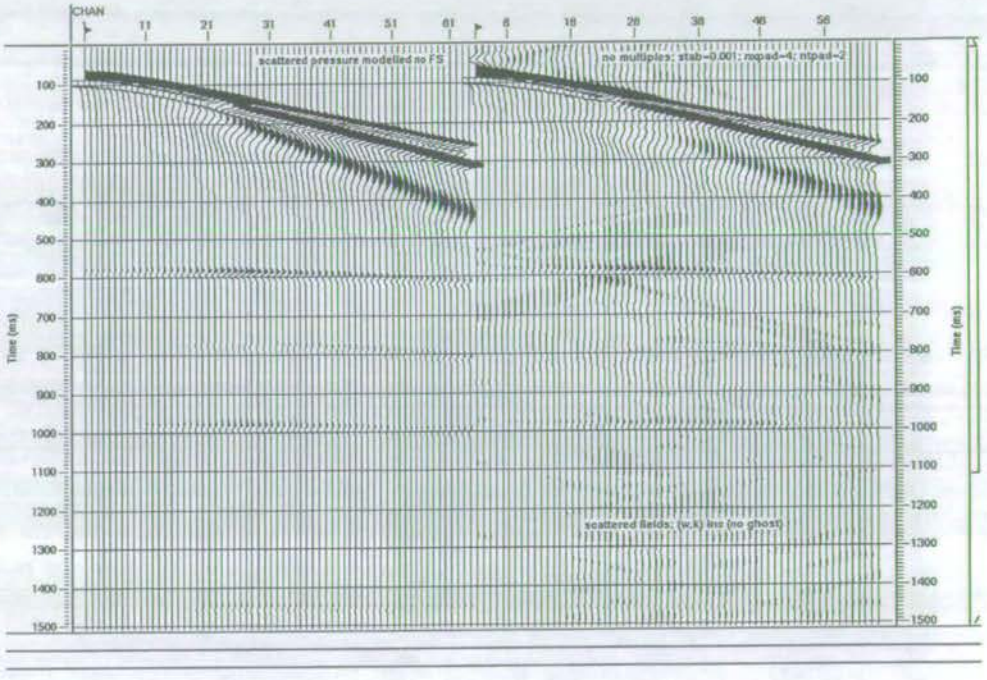


Figure 7.32: Multiple removal with point source OBC data over a 1D earth. The gather on the left is pressure modelled with no free surface; the gather on the right is the result of processing the scattered field seismograms with multiples to remove them. The incident field band-limiting the reflection response excludes the source ghost.

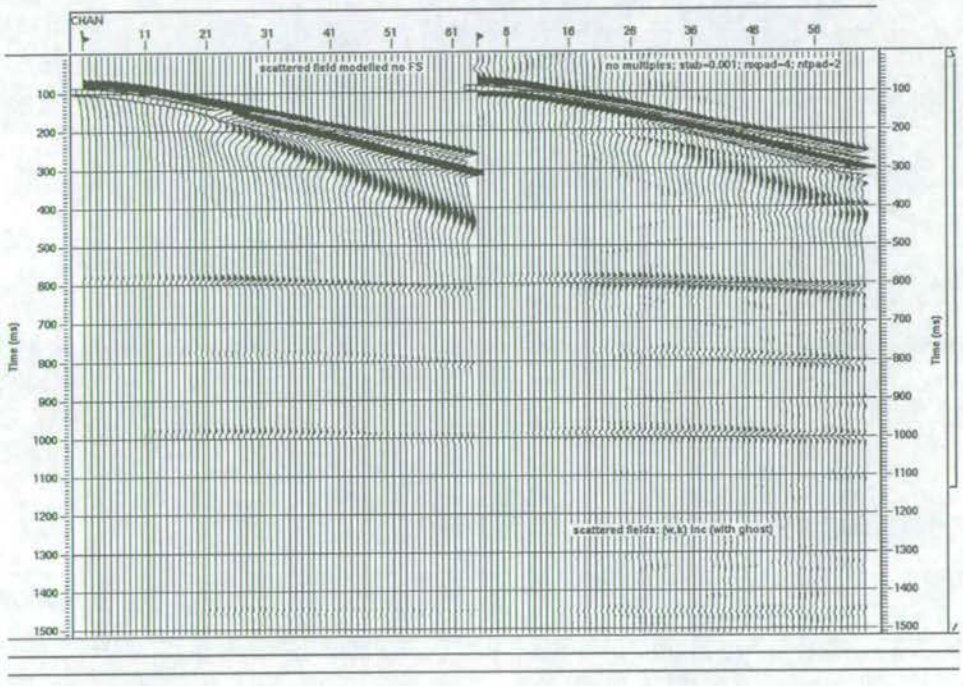


Figure 7.33: Multiple removal with point source OBC data over a 1D earth. The gather on the left is pressure modelled with no free surface; the gather on the right is the result of processing the scattered field seismograms with multiples to remove them. The incident field band-limiting the reflection response includes the source ghost.

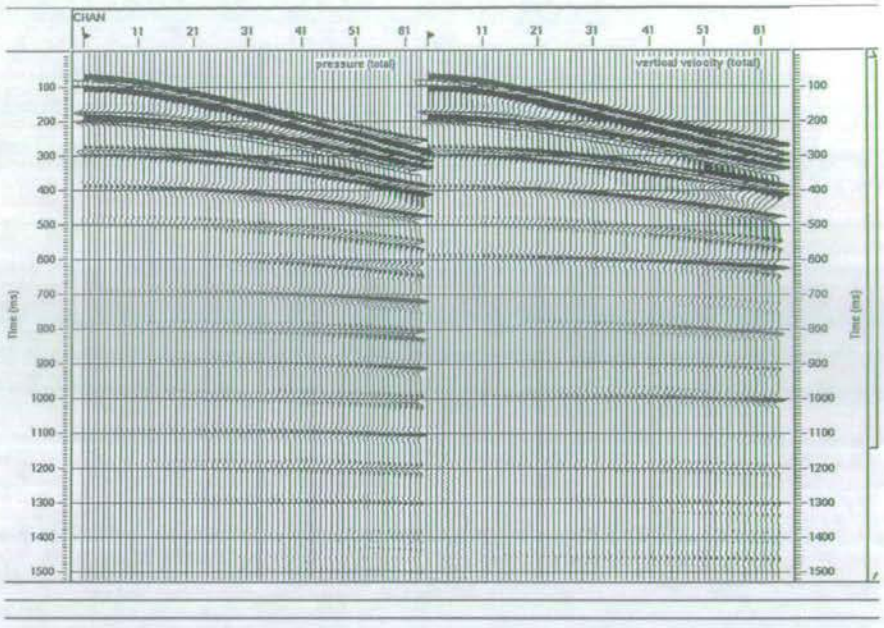


Figure 7.34: A point source over a layered elastic earth including the incident field. The gather on the left is the pressure; the gather on the right is the normal component of particle velocity.

## 7.5 The incident field in OBC data

The first step in the multiple-removal scheme is the subtraction of the incident field from the total measured field to yield the scattered field. In the special case of a 1D earth, any single downgoing plane wave component gives rise to a single upgoing plane wave component (they propagate with the same angle). Therefore, to calculate the plane wave reflection response of the earth requires spatial transformation of the data with respect to the source or the receiver coordinate. Because of this, in the OBC recording geometry over a 1D earth, the incident field need not be subtracted from the total field before separation into upgoing and downgoing waves. For wave propagation in a 1D earth, to separate all the plane waves, spatial transforms are required over source *or* over receiver coordinates, but not over both. In 2D or 3D this is not the case, and the incident and scattered fields need to be treated separately to achieve a stable multiple-free solution (see chapter 8). The equations for wave separation in the frequency-wavenumber domain ((7.19) and (7.20)) follow from solution of the homogenous wave equation for pressure and the vertical component of particle velocity. Solution of the inhomogeneous wave equation, which includes a source term, gives rise to equations for the upgoing and downgoing wave which include the incident field implicitly in the downgoing wave, providing $z_s < z_r$ as in OBC recording.

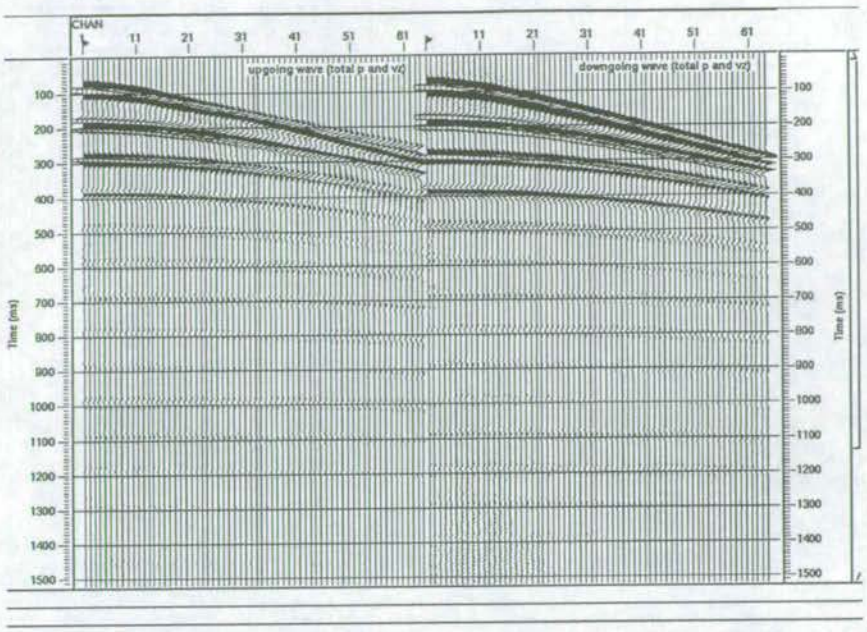


Figure 7.35: Separating upgoing and downgoing waves with the total fields of pressure and the vertical component of particle velocity, for point source data over a 1D earth: Upgoing pressure wave on the left; downgoing pressure wave on the right.

If the total field is expressed as the sum of a scattered and an incident field,

$$\tilde{P}^{tot}(k_x, k_y, z_r, \omega, z_s) = \tilde{P}^{inc}(k_x, k_y, z_r, \omega, z_s) + \tilde{P}^{scat}(k_x, k_y, z_r, \omega, z_s), \tag{7.27}$$

and

$$\tilde{V}_z^{tot}(k_x, k_y, z_r, \omega, z_s) = \tilde{V}_z^{inc}(k_x, k_y, z_r, \omega, z_s) + \tilde{V}_z^{scat}(k_x, k_y, z_r, \omega, z_s), \tag{7.28}$$

then the upgoing pressure wave is given by

$$\begin{aligned} 2\tilde{U}^{tot}(k_x, k_y, z_r, \omega, z_s) &= \tilde{P}^{inc}(k_x, k_y, z_r, \omega, z_s) + \tilde{P}^{scat}(k_x, k_y, z_r, \omega, z_s) \\ &\quad - \frac{\rho\omega}{k_z}\Big(\tilde{V}_z^{inc}(k_x, k_y, z_r, \omega, z_s) + \tilde{V}_z^{scat}(k_x, k_y, z_r, \omega, z_s)\Big), \end{aligned} \tag{7.29}$$

while the downgoing pressure wave is

$$\begin{aligned} 2\tilde{D}^{tot}(k_x, k_y, z_r, \omega, z_s) &= \tilde{P}^{inc}(k_x, k_y, z_r, \omega, z_s) + \tilde{P}^{scat}(k_x, k_y, z_r, \omega, z_s) \\ &\quad + \frac{\rho\omega}{k_z}\Big(\tilde{V}_z^{inc}(k_x, k_y, z_r, \omega, z_s) + \tilde{V}_z^{scat}(k_x, k_y, z_r, \omega, z_s)\Big). \end{aligned} \tag{7.30}$$

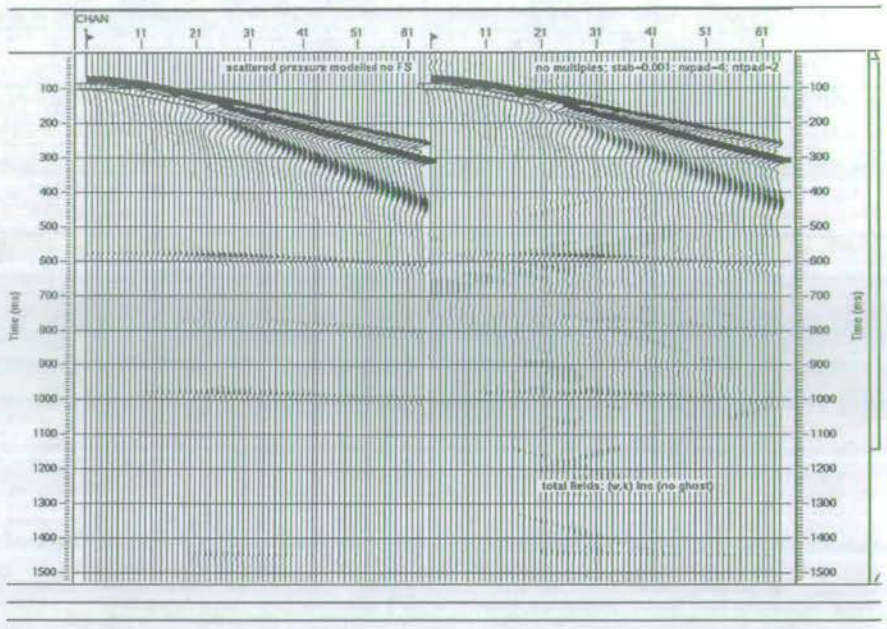


Figure 7.36: Multiple removal with point source OBC data over a 1D earth. The gather on the left is pressure modelled with no free surface; the gather on the right is the result of processing the total field seismograms with multiples to remove them. The incident field band-limiting the reflection response excludes the source ghost.

When $z_s < z_r$, as is the case in OBC recording,

$$\tilde{P}^{inc}(k_x, k_y, z_r, \omega, z_s) - \frac{\rho\omega}{k_z}\tilde{V}_z^{\,inc}(k_x, k_y, z_r, \omega, z_s) = 0, \tag{7.31}$$

and

$$\tilde{P}^{inc}(k_x, k_y, z_r, \omega, z_s) + \frac{\rho\omega}{k_z}\tilde{V}_z^{\,inc}(k_x, k_y, z_r, \omega, z_s) = 2\tilde{P}^{inc}(k_x, k_y, z_r, \omega, z_s), \tag{7.32}$$

and $\tilde{U}^{tot}$ contains only the upgoing scattered pressure,

$$2\tilde{U}^{tot}(k_x, k_y, z_r, \omega, z_s) = \tilde{P}^{scat}(k_x, k_y, z_r, \omega, z_s) - \frac{\rho\omega}{k_z}\tilde{V}_z^{\,scat}(k_x, k_y, z_r, \omega, z_s), \tag{7.33}$$

whereas $\tilde{D}^{tot}$ contains the downgoing scattered pressure plus the incident pressure,

$$\begin{aligned} 2\tilde{D}^{tot}(k_x, k_y, z_r, \omega, z_s) = \tilde{P}^{scat}(k_x, k_y, z_r, \omega, z_s) + \frac{\rho\omega}{k_z}\tilde{V}_z^{\,scat}(k_x, k_y, z_r, \omega, z_s) \\ + 2\tilde{P}^{inc}(k_x, k_y, z_r, \omega, z_s). \end{aligned} \tag{7.34}$$

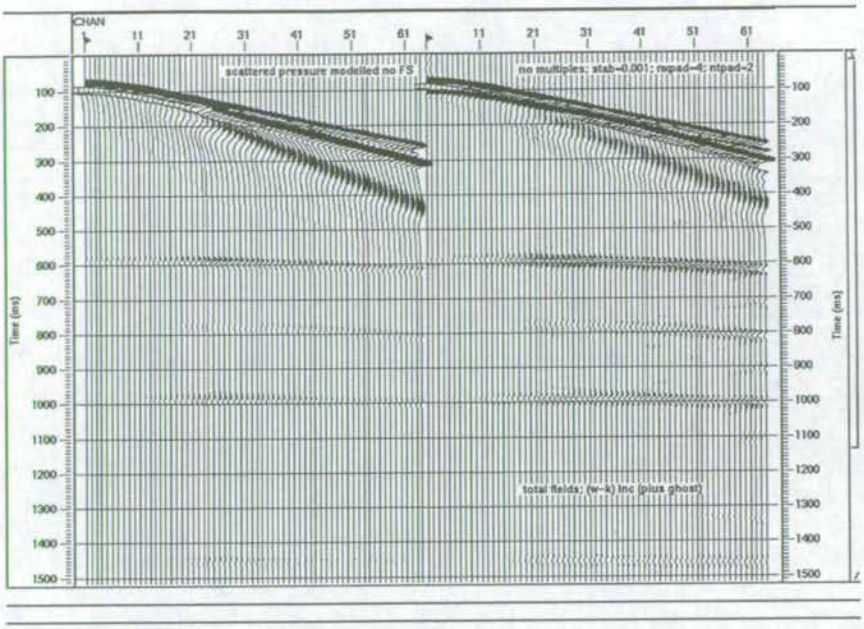


Figure 7.37: Multiple removal with point source OBC data over a 1D earth. The gather on the left is pressure modelled with no free surface; the gather on the right is the result of processing the total field seismograms with multiples to remove them. The incident field band-limiting the reflection response includes the source ghost.

This shows that for a 1D earth the total field data may be used directly to separate the upgoing and downgoing waves, without first removing the incident field. This is illustrated in Figure 7.35 where the total field data of Figure 7.34 have been separated into upgoing and downgoing waves using equations (7.33) and (7.34). Figure 7.35 should be compared with Figure 7.30 where the inclusion of the incident field on the downgoing wave is obvious in the total field data. A comparison of Figures 7.24 and 7.34 reveals the incident field recorded on the particle velocity (right panel) as a positive pulse on first arrival, where on the scattered field a negative pulse is recorded. The difference is more difficult to detect on the pressure (left panel) since the first arrivals of the incident and scattered fields have the same polarity.

Figure 7.36 shows the result of calculating the reflection response as the ratio of upgoing to downgoing plane wave components. The incident field band-limiting the reflection response includes the direct wave from the source only. There is some noise in the result. Figure 7.37 shows the multiple-free seismograms when the incident field band-limiting the reflection response includes the direct wave plus the source ghost. There is less numerical noise and the results are better than those of Figures 7.32 and 7.33, where the scattered fields only were modelled.

## 7.6 Conclusions

The earth's reflection response has been successfully recovered from 1D synthetic seismograms contaminated by sea surface multiples. After band-limiting the reflection response with a suitable incident field to propagate a source wavefield through the response to the receivers, multiple-free seismograms result.

The scheme works successfully with line source and point source data, with both streamers and OBC dual sensors recording geometries. In the special case of OBC acquisition over a 1D earth, the total field data recorded on the sensors may be used directly. Addition of random noise shows the scheme to be robust to moderate levels of noise where the signal is still identifiable. Errors in input parameters which are within the measurement error of current acquisition technology do not adversely degrade the multiple elimination.

# MULTIPLE ELIMINATION IN TWO DIMENSIONS

## *Chapter 8*

### 8.1 Introduction

The sea surface multiple problem is conceptually more complicated in 2D and 3D than in 1D. When the earth departs from a horizontally-stratified model, recovering the reflection response, and hence multiple removal, becomes more difficult: the earth reflects a single incident plane wave into many plane wave components, each of which is reflected at the sea surface.

Undoing the effect of the sea surface in 2D requires more data than in 1D. Although the data manipulation required to yield the reflection response is more involved than in 1D, all orders of sea surface multiples can successfully be removed with properly sampled data.

This chapter begins with the data requirements for a 2D test of the method described in chapter 5, and the synthetic data which are suitable for this purpose. The next section discusses a direct method of solution of equations (5.17) for the reflection reponse, followed by an explanation of the data preparation necessary before transforming the data to the frequency-double wavenumber domain. Synthetic data examples for streamer and OBC configurations illustrate the separation into the different plane wave components, and solution of the equations to allow recomposition of the data into multiple-free seismograms. Some of the material shown here is published in conference proceedings as Johnston and Ziolkowski (1999), and in internal reports as Johnston and Taylor (1999) and Johnston, Taylor and Ziolkowski (1999).

### 8.2 The data required for a two-dimensional test

The 2D problem is one in which the earth properties vary in two directions ($x$ and $z$, say), and are invariant in the third ($y$, say). The source is of infinite extent in the $y$-direction so that wave propagation is confined to the other two directions. Because both the earth and the wave propagation are constant in the $y$-direction, receivers are required at different positions along a line in the $x$-direction only. Movement of the source location along the $x$-axis, with respect to the line of receivers, provides all the information about the 2D structure below the surface. As long as the spatial sampling in the source and receiver directions is sufficient for the frequency content of the input signal, the data contain the predictive capabilities to remove

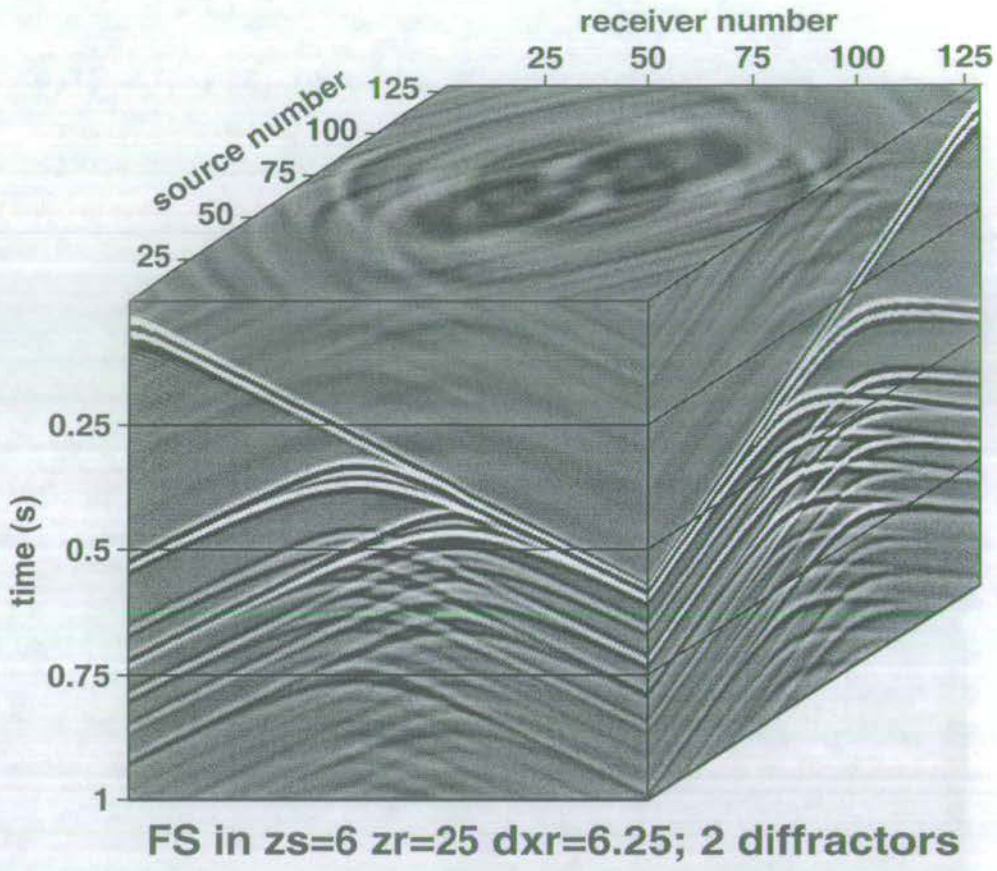


Figure 8.1: A cube of 2D synthetic data for varying source and receiver offsets. The total field is modelled in the presence of the free surface for 128 receivers and 128 shots with 2 line diffractors at 100m depth.

the effect of the free surface completely.

Two-dimensional data are impossible to collect in practice because line sources do not exist. An earth structure may be dominantly two dimensional, but the wave propagation from the source is three dimensional. To test a wave-theoretical technique for sea surface multiple removal requires data, both with the sea surface present and with the sea surface absent. The "answer" is then known in advance of trying to remove the multiples. The only way to do this is to synthesise the reflection experiment, either numerically, or in a physical modelling experiment. The former of these options is discussed here. Kelly and Marfurt (1990) provide a comprehensive review on the subject of numerical modelling of seismic wave propagation.

It is common practice in the testing of wave-theoretical multiple removal schemes (e.g. Verschuur, 1991; Carvalho *et al.*, 1991) to use the finite-difference method (Alterman and Karal, 1968) to produce synthetic seismograms. A gridded velocity model is designed in the

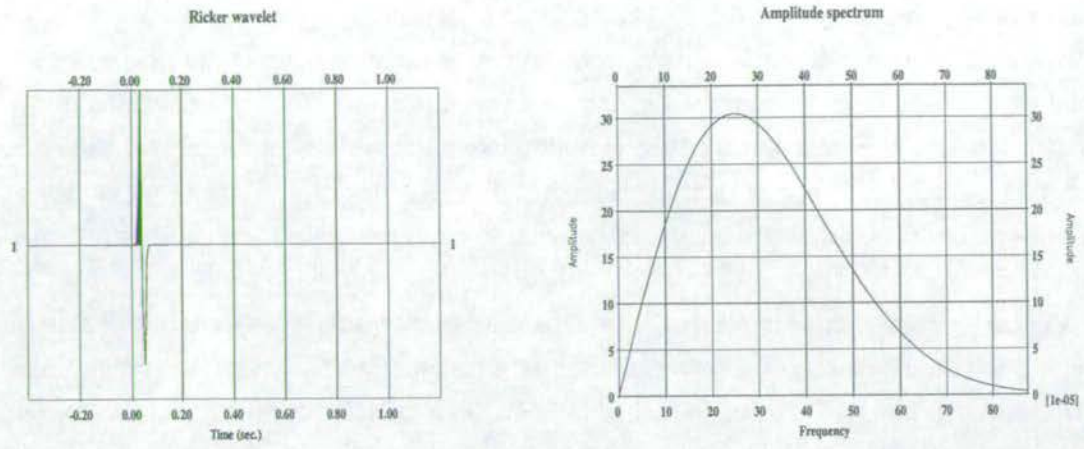


Figure 8.2: Ricker wavelet used as the source time function.

$x$- and $z$-directions, and then waves are propagated through the model in time steps, using finite differences to approximate the wave equation. The process is both time-consuming and inexact. Artefacts may result due to the artificial boundary conditions which are imposed at the edges of the (finite) computation. These boundary conditions try to mimic real life, where, at the free surface, the energy is reflected, but, in all other directions, it dissipates with distance from the source. However, realisitic earth models can be constructed so that complicated seismograms can be produced which resemble real data.

The inaccuracy of the finite-difference method is its main weakness as an aid to testing a multiple removal scheme. Artefacts related to the modelled data are indistinguishable from artefacts related to the multiple removal algorithm applied to the synthetic data with multiples. What is required is synthetic data that is accurate to machine precision, and is cheap and quick to produce. Since the data themselves contain the information required to remove the multiples, a wave-theoretical solution to remove the sea surface multiples is, in theory, independent of the complexity of the earth. With this in mind, Taylor (1999) developed a theory and computer program to model line diffractors in a constant acoustic background medium. Exact seismograms are constructed in the frequency-space domain from combinations of monopole line source solutions to the acoustic wave equation. For further details see appendix B. The seismograms are not necessarily very complicated, and do not look like field seismograms. However, they are very fast to produce, and they have all the characteristics required for testing multiple removal algorithms (Taylor and Johnston, 1999). In fact, because diffractors radiate energy in all directions, removing multiple diffractions is a severe test of any multiple removal scheme.

The synthetic data used here are a suite of seismograms calculated in the frequency domain for a number of source and receiver positions: the receivers are fixed in space and the source position is moved along the $x$-direction. The earth model can be a combination of

line diffractors at depth in an acoustic half-space. One feature of the modelling is that the diffractors are designed to radiate energy equally in all directions when stimulated by an external source, regardless of its location in relation to the diffractor. The synthetic seismograms are calculated for the ideal world where sampling requirements are completely satisfied and money is no object. It is important to understand how the theory performs with as few of the assumptions compromised as possible, before introducing sources of possible error due to incomplete data.

Figure 8.1 shows an example of a data cube calculated with Taylor's modelling code in terms of source and receiver number, and time. In this model the free surface is present; two diffractors are positioned at (-50,100)m and (100,100)m in a half-space of water, with respect to the midpoint of the receiver spread and the $z = 0$ surface. The sources are positioned at 6m depth, and the receivers, at 25m depth. There are 128 receivers spaced 6.25m apart. In the first common source gather (the front face of the cube in Figure 8.1), the source location is $x$-coincident with the first receiver. In common shot gather $n$, the source location is $x$-coincident with receiver number $n$. The spatial extent of the cube is therefore 0.63 $km^2$ for 128 sources and 128 receivers. The source time function is a two-loop Ricker wavelet with a central frequency of 25 Hz (see Figure 8.2).

Figures 8.3 and 8.4 show source and receiver gathers, respectively, which cut through the cube shown in Figure 8.1, and do not appear already on the faces of the cube. Note that, because source and receiver depths are not equal, interchanging source and receiver number does not result in the same seismograms. The incident field is easily identified as the mainly linear event arriving at earlier times, whereas the scattered field is composed of all the interfering hyperbolas.

Figures 8.5-8.7 show data collected over the same model except that the free surface is replaced by a half-space of water. Source and receiver positions are as before. This is the goal of the multiple removal scheme, except that in the processed result the incident field is removed in the first step. Note that the seismograms show all orders of free-surface multiples (Figures 8.1, 8.3 & 8.4), and all orders of internal multiples, as seen in Figures 8.5-8.7. The magnitude of the internal multiples is controlled by the diffractors' stimulation factors $E_i(\omega)$ (see appendix B), which correspond to reflection coefficients in the case of specular reflectors.

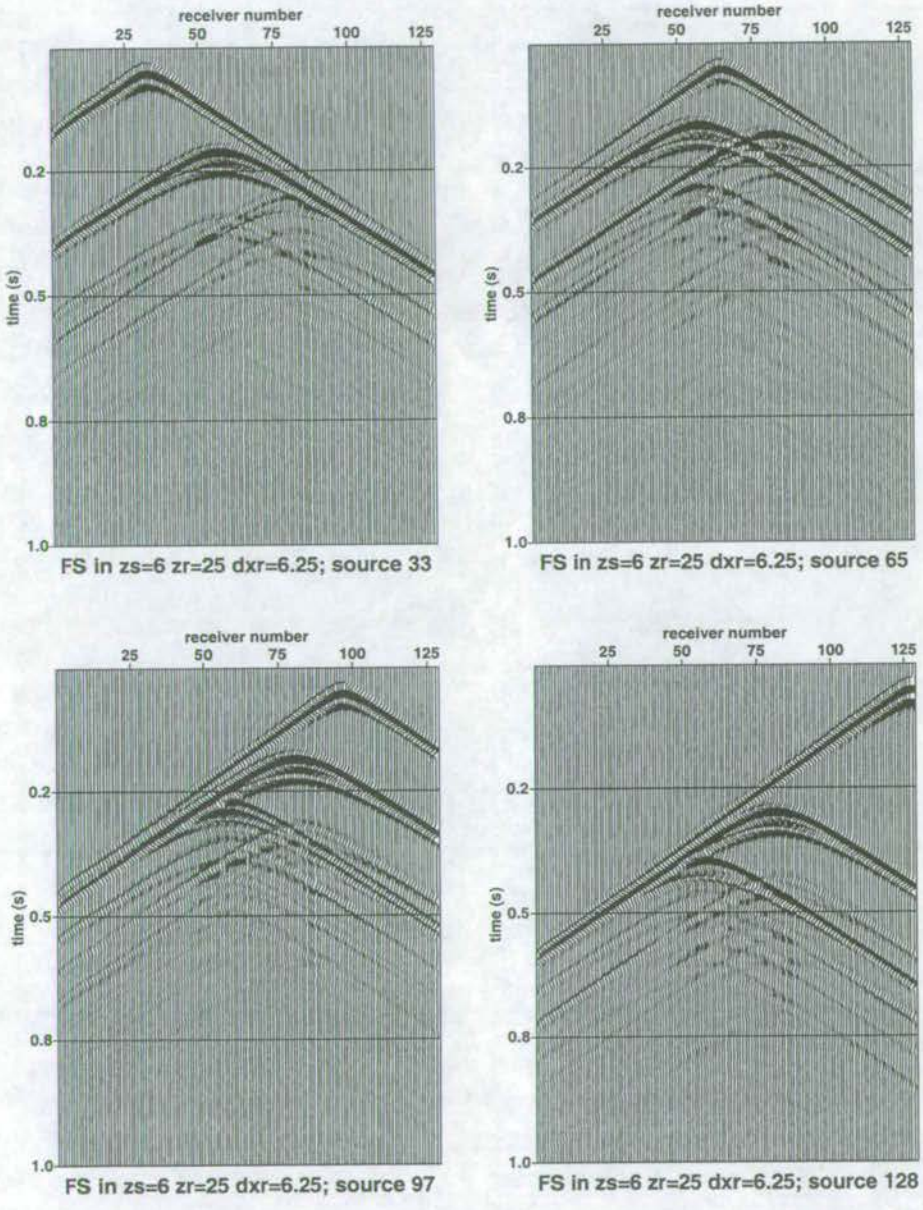


Figure 8.3: Slices along different source numbers of the 2D cube shown in Figure 8.1.

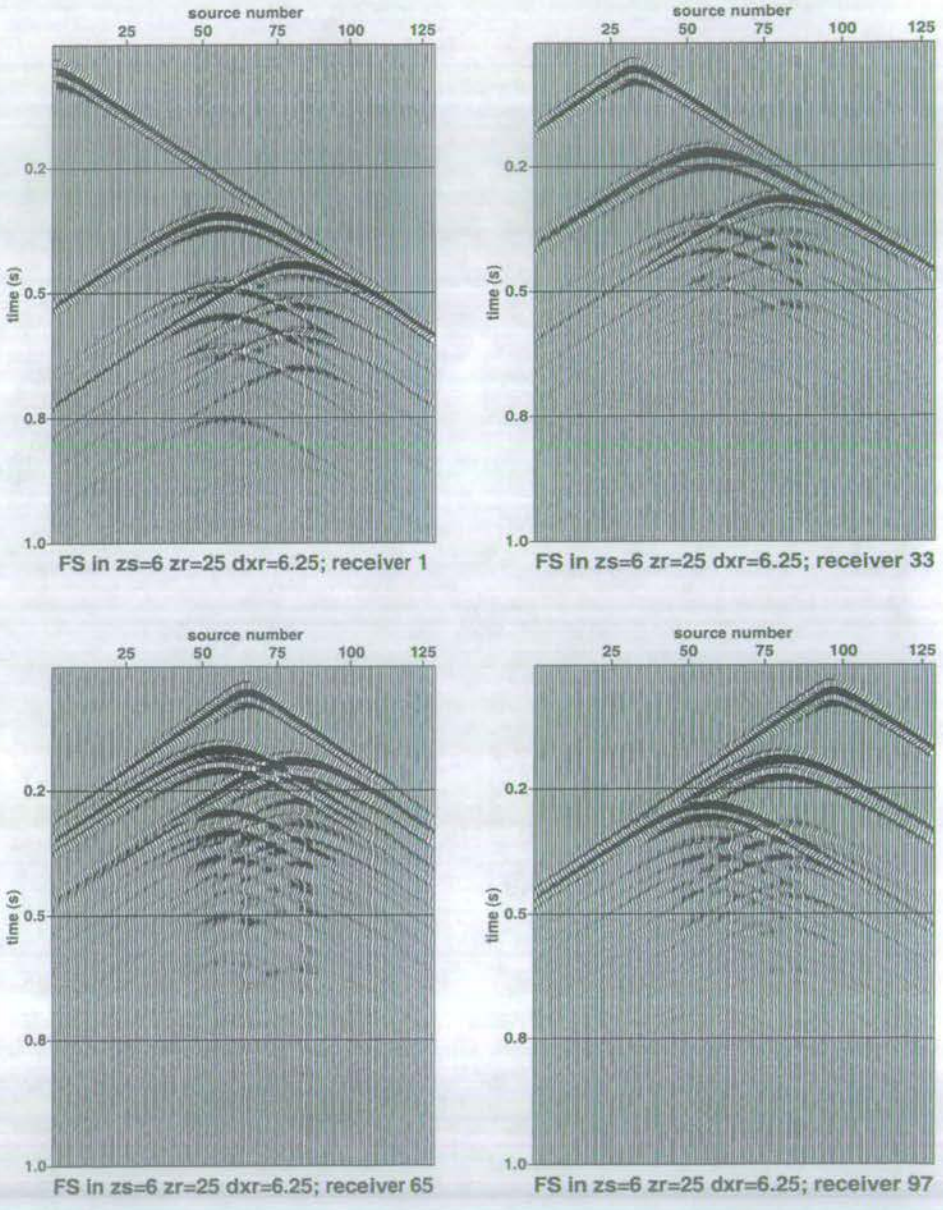


Figure 8.4: Slices along different receiver numbers of the 2D cube shown in Figure 8.1.

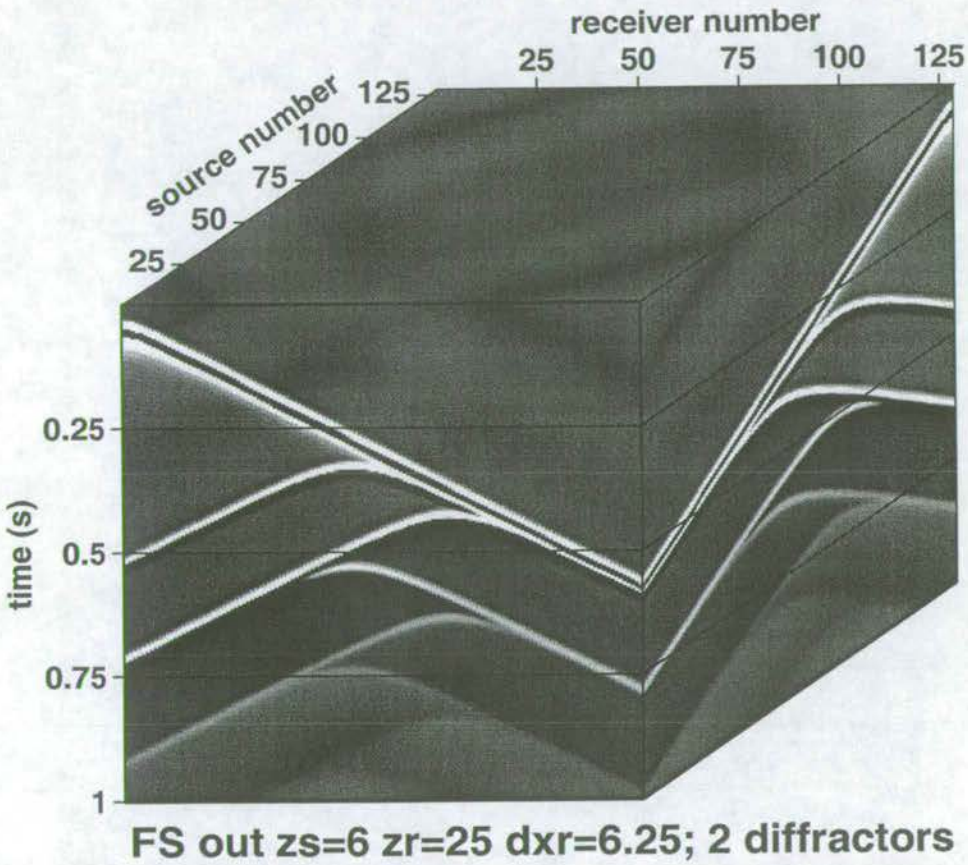


Figure 8.5: A cube of 2D synthetic data for varying source and receiver offsets. The total field is modelled in the absence of the free surface for 128 receivers and 128 shots with 2 line diffractors at 100m depth.

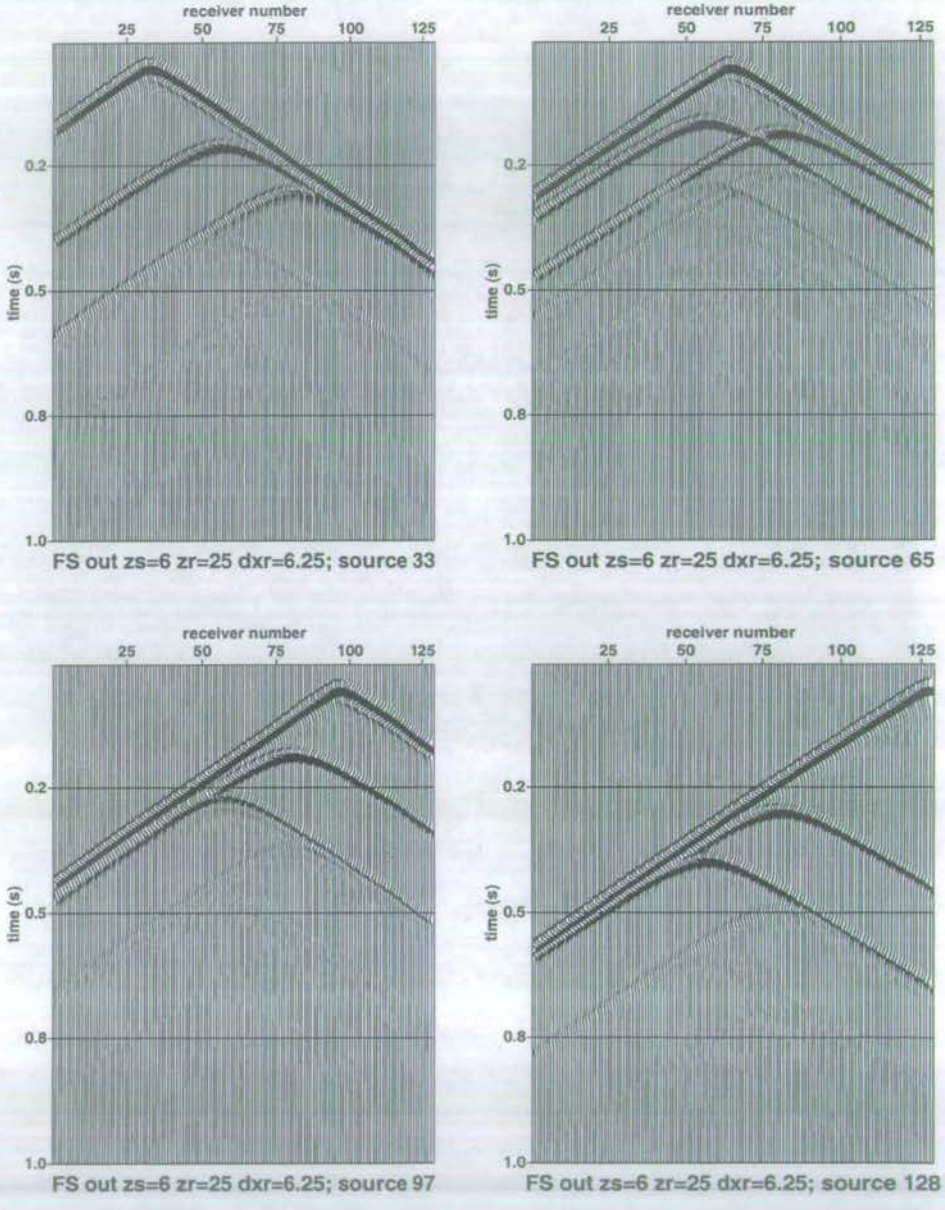


Figure 8.6: Slices along different source numbers of the 2D cube shown in Figure 8.5.

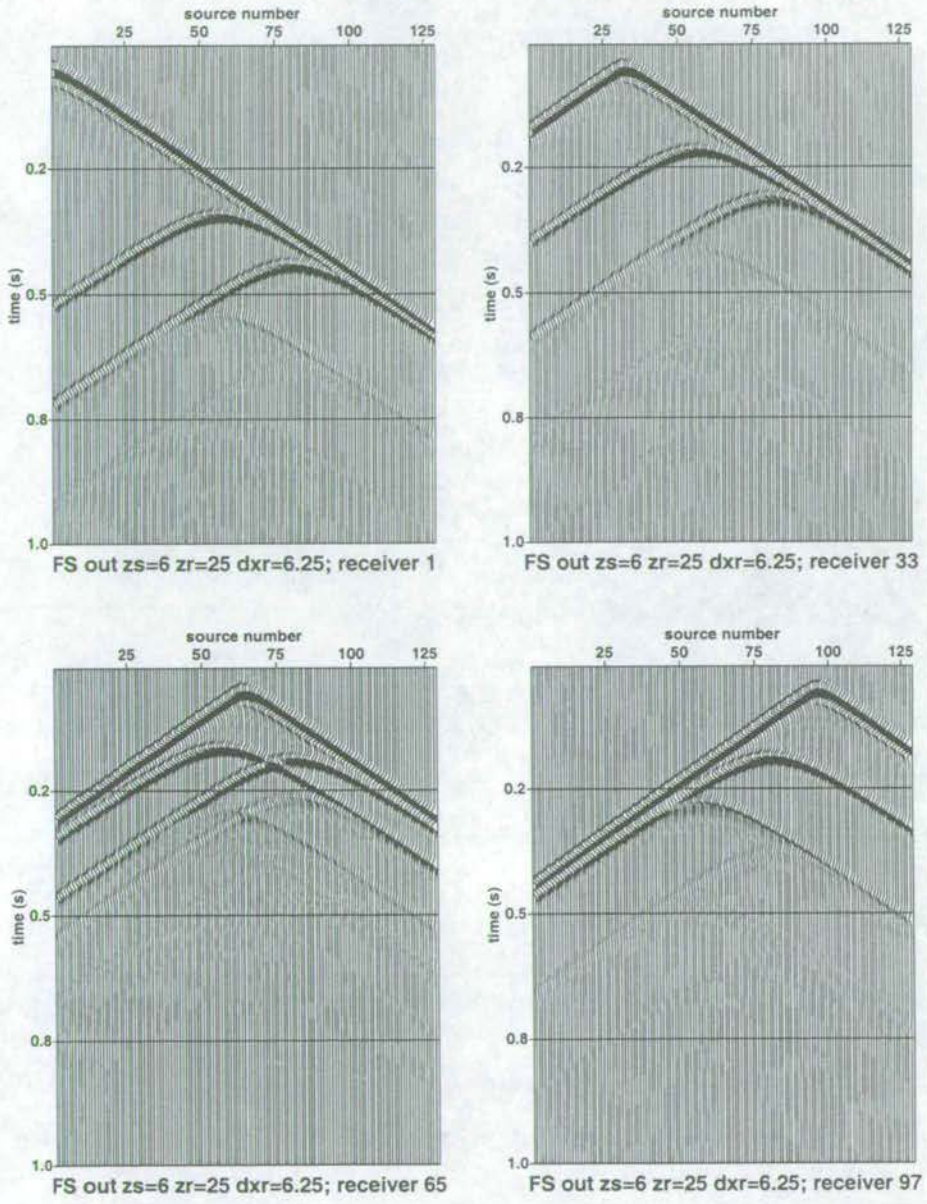


Figure 8.7: Slices along different receiver numbers of the 2D cube shown in Figure 8.5.

## 8.3 Solution to a large set of simultaneous equations

The equations to be solved are (5.19) in chapter 5. They are written again here for convenience:

$$\begin{pmatrix} \hat{\hat{U}}_{j1} \\ \hat{\hat{U}}_{j2} \\ \vdots \\ \hat{\hat{U}}_{jN} \end{pmatrix} = \begin{pmatrix} \hat{\hat{I}}_1 + \hat{\hat{D}}'_{11} & \hat{\hat{D}}'_{21} & \cdots & \hat{\hat{D}}'_{N1} \\ \hat{\hat{D}}'_{12} & \hat{\hat{I}}_2 + \hat{\hat{D}}'_{22} & \cdots & \hat{\hat{D}}'_{N2} \\ \vdots & \vdots & \vdots & \vdots \\ \hat{\hat{D}}'_{1N} & \hat{\hat{D}}'_{2N} & \cdots & \hat{\hat{I}}_N + \hat{\hat{D}}'_{NN} \end{pmatrix} \begin{pmatrix} \hat{\hat{R}}_{j1} \\ \hat{\hat{R}}_{j2} \\ \vdots \\ \hat{\hat{R}}_{jN} \end{pmatrix}, \tag{8.1}$$

where

$$\hat{\hat{D}}'_{ki} = \frac{\Delta k_x^s}{2\pi} \hat{\hat{D}}_{ki}. \tag{8.2}$$

They can be rewritten in traditional matrix notation as

$$AX = B \tag{8.3}$$

where $A$ is non-singular and $n$-by-$n$, $B$ is $n$-by-$p$, and the desired $X$ is $n$-by-$p$. Equations (8.3) represent the classic *multiple right-hand side problem* in matrix algebra (Golub and Van Loan, 1996). One way to solve these equations directly is to write

$$X = A^{-1}B \tag{8.4}$$

which involves calculating a matrix inverse. Instead, a more effecient algorithm results from factoring $A$ into lower and upper triangular matrices (Cholesky's $LU$ decomposition) such that

$$A = LU, \tag{8.5}$$

to enable the solution of

$$LY = B \qquad \text{then} \qquad UX = Y, \tag{8.6}$$

by block forward, and then block reverse, substitution. The $LU$ factorisation is a form of Gaussian elimination, and allows the solution $X$ to be found without explicitly calculating the inverse of $A$, unless of course $B$ is $\mathbf{I}$ the identity matrix. The matrix $A$ need be factored only once.

In terms of the seismic data, frequency slices of the upgoing & downgoing scattered and incident plane wave components are required in the source/receiver wavenumber domain. The total downgoing wavefield ($\hat{\hat{I}} + \hat{\hat{D}}'$) is factored once per frequency.

## 8.4 Data preparation

The equations of section 8.3 are formulated in the frequency-double wavenumber domain in terms of upgoing and downgoing plane wave components. Data preparation is required to produce these elements from the collected data (measurements of the total field of pressure, and possibly the vertical component of particle velocity as well).

The first step is the separation of the incident field from the total field, to isolate the scattered field. This step is performed implicitly in modelling by calculating the scattered and incident fields separately. A single cube of data in terms of $(x_r, t, x_s)$ is now referred to as "a dataset", whether it is an incident field, $p^{inc}(x_r, z_r, t, x_s, z_s)$, or a scattered field, $p^{scat}(x_r, z_r, t, x_s, z_s)$.

### Transformation to frequency

Each dataset has zeros added to the time axis to prevent temporal wraparound (after data processing and transformation back to the time domain). This is illustrated schematically in Figure 8.8. When complex frequencies are used (see appendix A.1) an exponential taper is applied to each trace prior to the Fourier transform over time, to stabilise computations involving $k_z$ (see appendix A.2). The transform is

$$P^{scat}(x_r, z_r, \omega, x_s, z_s) = \int_{-\infty}^{\infty} p^{scat}(x_r, z_r, t, x_s, z_s) \exp\Big(+i[\omega t]\Big) \mathrm{d}t. \tag{8.7}$$

The data consist of frequency slices as a function of receiver and source wavenumber, for positive and negative frequencies. Because the data are real-valued and causal in the time domain, upon transformation to the frequency domain, the values of the data at negative frequencies are the complex conjugates of those at positive frequencies. Consequently, the data for positve frequencies are processed only.

### Transformation to wavenumber

Each frequency slice is a function of source and receiver offset, as shown in Figure 8.9. To accommodate the operations in the frequency-wavenumber domain (and thereby prevent spatial wraparound), the data are padded with zeros in both source and receiver directions. This process is illustrated schematically in Figure 8.9. In common shot gathers, the data are transformed to the horizontal receiver wavenumber domain:

$$\tilde{P}^{scat}(k_x^r, z_r, \omega, x_s, z_s) = \int_{-\infty}^{\infty} P^{scat}(x_r, z_r, \omega, x_s, z_s) \exp\Big(-i[k_x x_r]\Big) \mathrm{d}x_r. \tag{8.8}$$

This decomposes the earth's response at the receivers into plane wave components. Transform 8.8 can be considered as discretising the downgoing incident wavenumbers, as illustrated in Figure 8.10.

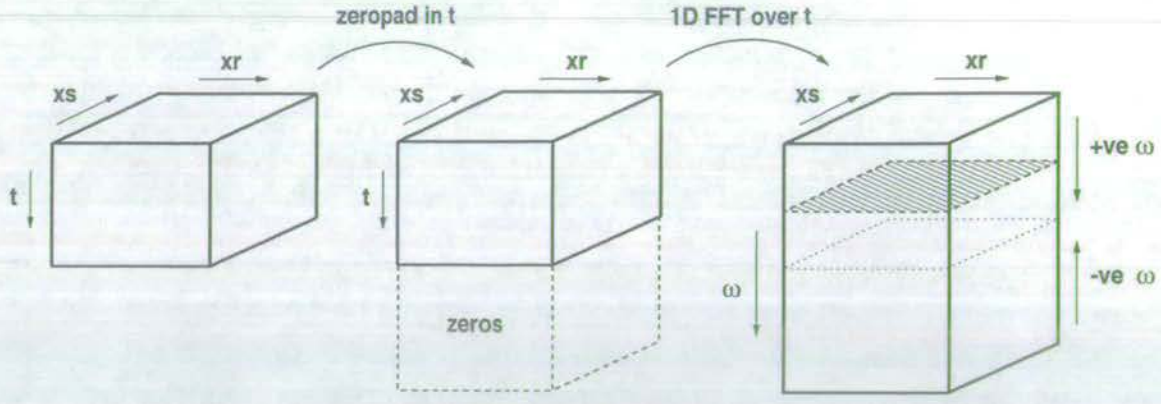


Figure 8.8: The data preparation required to transform from the time-space domain to the frequency-space domain.

Next, the data are reordered into common receiver gathers, and transformed over source coordinate:

$$\hat{\tilde{P}}^{scat}(k_x^r, z_r, \omega, k_x^s, z_s) = \int_{-\infty}^{\infty} \tilde{P}^{scat}(k_x^r, z_r, \omega, x_s, z_s) \exp\Big(+i[k_x x_s]\Big) \mathrm{d}x_s. \tag{8.9}$$

Transform (8.8) sums up all the plane wave contributions from each source to simulate the response at the receivers due to plane waves. This can be thought of as discretising a chosen upgoing wavenumber, as illustrated in Figure 8.11. Because the spatial transforms decompose waves moving away from or towards the transform variable, the sign convention in (8.8) is opposite to that in (8.9).

The positive and negative wavenumbers are, in general, unique and thus must all be processed. The only exception to this arises when there is symmetry in the underlying earth structure.

### Separating upgoing and downgoing plane wave components

The elements required to solve the equations of section 8.3 are upgoing and downgoing scattered plane wave components. These are derived in two ways: from the scattered pressure, and from the scattered pressure and the scattered vertical component of particle velocity. The two methods are discussed separately, in the following two sections, in the context of the line diffractor synthetic data.

## 8.5 A synthetic example with streamer data

A model with one diffractor situated at (0,100)m, and a free surface at $z = 0$m is used to demonstrate the steps involved in the processing. The acquisition has 128 source and receiver $x$ positions, spaced 6.25m apart, beginning at 0m. The corresponding depths of sources

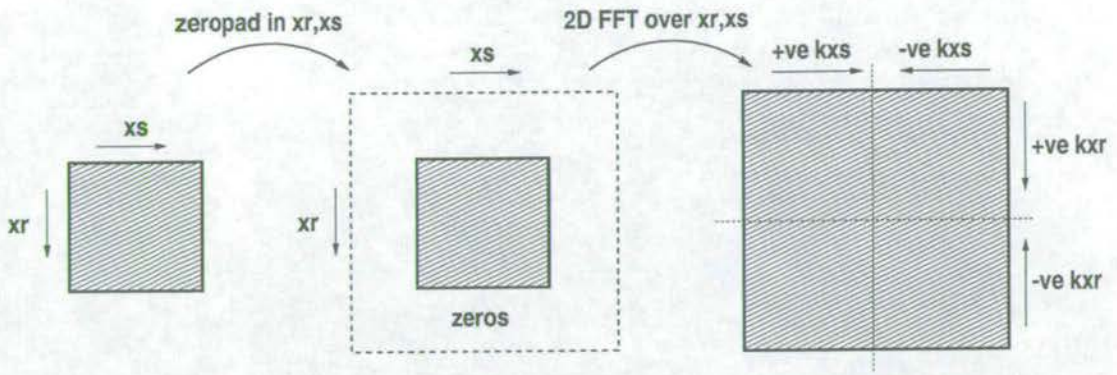


Figure 8.9: The data preparation required to transform a single frequency slice from the receiver-source space domain to the receiver-source wavenumber domain, for data processing on a per-frequency basis.

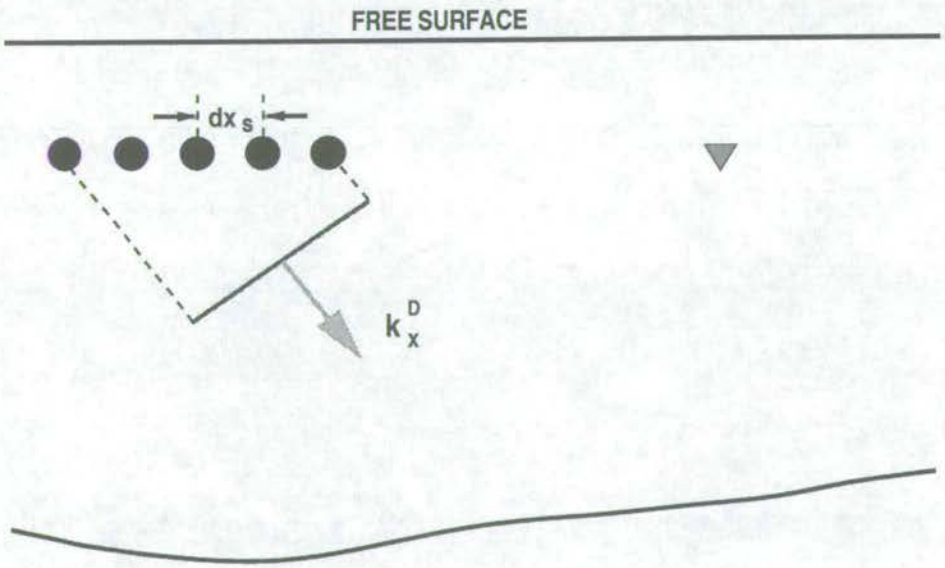


Figure 8.10: Transforming over sources analyses downgoing wavenumbers.

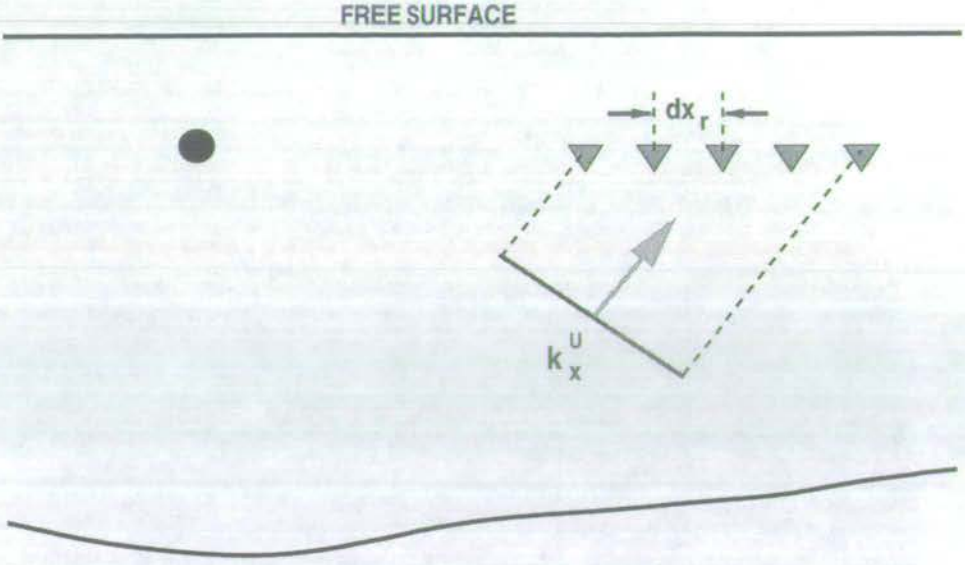


Figure 8.11: Transforming over receivers analyses upgoing wavenumbers.

and receivers are 6m and 25m, respectively. The source time function is shown in Figure 8.2. The scattered and incident fields for the whole dataset are shown in Figures 8.12 and 8.13. Examples of frequency slices for the scattered and incident pressures are shown in Figures 8.14 and 8.15, where zeros have been added to enlarge the dataspace.

### Separating upgoing and downgoing plane wave components: Pressure only

With pressure alone, the upgoing and downgoing waves may be separated by dividing out the receiver ghost,

$$1-\exp\left(ik_z^U[2z_r]\right), \tag{8.10}$$

where

$$k_z^U=\sqrt{\frac{\omega^2}{c^2}-k_x^{r2}}. \tag{8.11}$$

This factor becomes zero whenever $\exp\left(ik_z^U[2z_r]\right)$ equals $+1$. The division is stabilised as in chapter 7:

$$\tilde{U}^{scat}(k_x^r,z_r,\omega,x_s,z_s)=\frac{\tilde{P}^{scat}(k_x^r,z_r,\omega,x_s,z_r)\left[1-\exp\left(ik_z^U[2z_r]\right)\right]^*}{\left|1-\exp\left(ik_z^U[2z_r]\right)\right|^2+\varepsilon}, \tag{8.12}$$

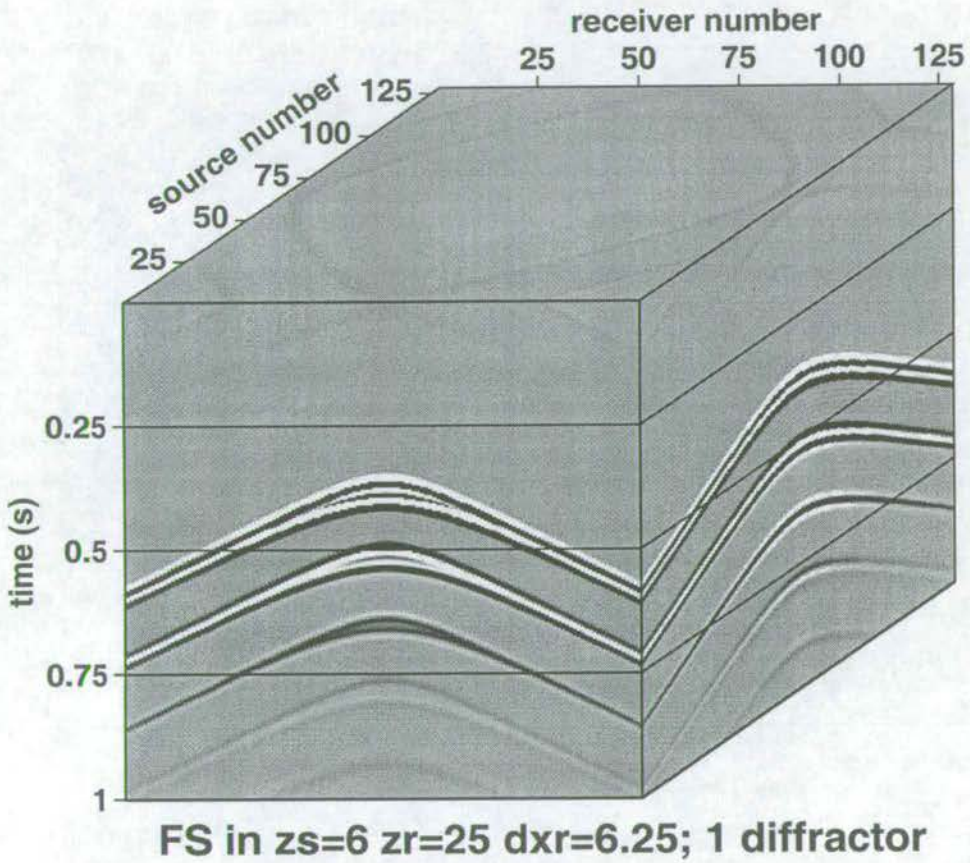


Figure 8.12: A cube of 2D synthetic data for varying source and receiver offsets. The scattered field is modelled in the presence of the free surface for 128 receivers and 128 shots, with 1 line diffractor in the middle of the receiver spread at 100m depth.

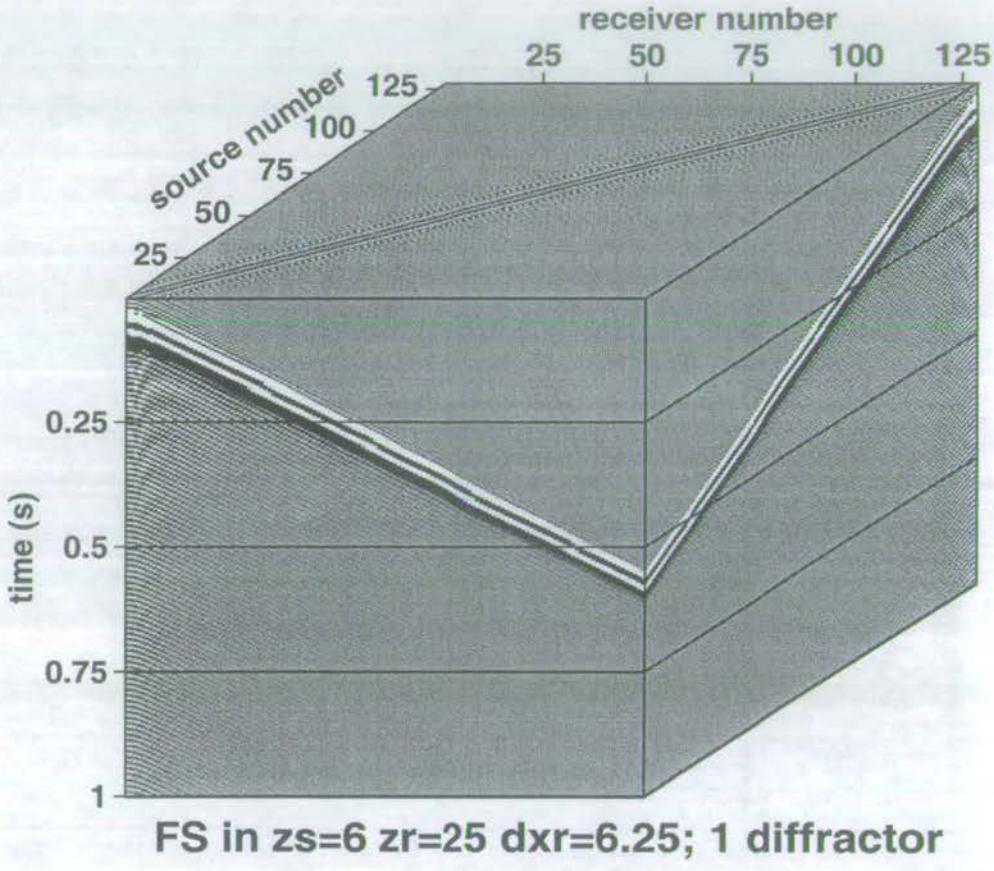


Figure 8.13: A cube of 2D synthetic data for varying source and receiver offsets. The incident field is modelled in the presence of the free surface for 128 receivers and 128 shots, with 1 line diffractor in the middle of the receiver spread at 100m depth.

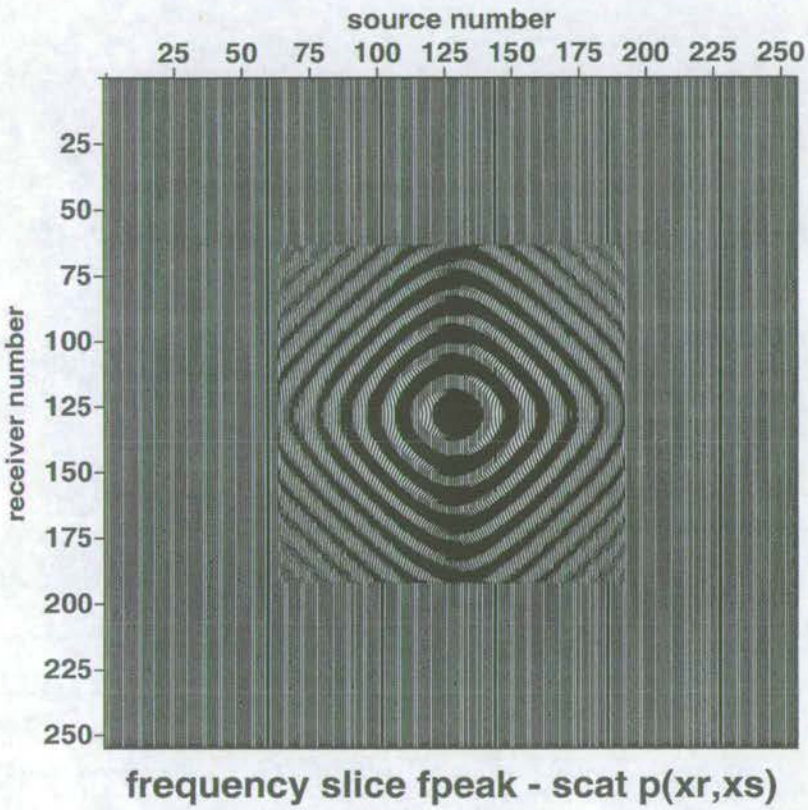


Figure 8.14: A frequency slice of the scattered field in terms of source and receiver number. (The real part only is shown.) The scattered field is transformed to the frequency domain, and then data for a single frequency is selected and surrounded with zeros.

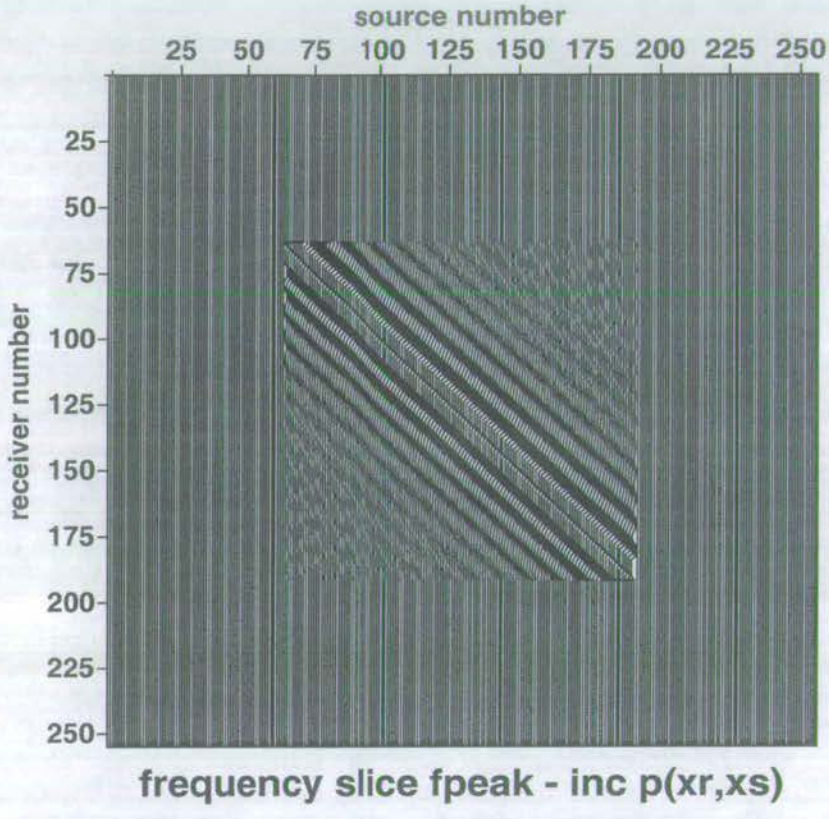


Figure 8.15: A frequency slice of the incident field in terms of source and receiver number. (The real part only is shown.) The incident field is transformed to the frequency domain, and then the data for a single frequency is selected and surrounded with zeros.

where $\varepsilon$ is a small real constant which ensures that the denominator is never zero. The downgoing wave is obtained from the scattered field by subtracting the upgoing wave

$$\tilde{D}^{scat}(k_x^r, z_r, \omega, x_s, z_s) = \tilde{P}^{scat}(k_x^r, z_r, \omega, x_s, z_s) - \tilde{U}^{scat}(k_x^r, z_r, \omega, x_s, z_s). \tag{8.13}$$

Figures 8.16 and 8.17 show these fields after transformation back to the frequency-space domain, for one (dominant) frequency slice. They should be compared with Figures 8.18 and 8.19 which show the result of modelling the upgoing and downgoing fields separately. Note that the deghosting operator in equation (8.10) is dependent on the receiver wavenumber only. Thus, Figures 8.16 and 8.17 show smearing over receiver numbers but not over source numbers. However, it is more convenient to perform the deghosting operation in the double wavenumber domain.

Figures 8.20 and 8.21 show the upgoing and downgoing wavefields, respectively, for the whole datacube after transformation back to the time-space domain. The smearing along receiver number, discussed above, produces undesirable artefacts at low and high receiver numbers (compare with Figures 8.34 and 8.35 on pages 226 and 227).

### Solving the equations

Frequency slices as a function of source and receiver wavenumbers for the three plane wave components of upgoing and downgoing scattered, and downgoing incident are plotted in Figures 8.22–8.24. Note that the incident field appears principally along the leading diagonal in the source/receiver wavenumber domain.

Equations (8.1) state that for a fixed $j$, that is upgoing wavenumber, the rows of the equation vary over $i$, that is downgoing wavenumber. The equations may be expressed in terms of the frequency slices of Figures 8.22-8.24 ordered by $(k_x^U, k_x^D)$: one row of the upgoing field (Figure 8.22), expressed as a column vector, is equal to the transpose of the matrix composed of the downgoing field plus the diagonal of the incident field (Figures 8.23 and 8.24), multiplied by one row of the reflection response, expressed as a column vector.

Solving (8.1) for each different upgoing plane wave component $j$ builds up the matrix of the reflection response in terms of the upgoing and downgoing wavenumbers. The matrix of downgoing plane wave components is independent of the upgoing plane wave component, $j$. It is simply all of the downgoing plane wave data.

Once equations (8.1) are solved, incident plane waves must be propagated to the reflection response and multiplied by each of its components:

$$\hat{\hat{P}}^0_{ji} = \hat{\hat{R}}_{ji}\hat{\hat{I}}_i. \tag{8.14}$$

Equation (8.14) defines the multiple-free pressure in the source/receiver wavenumber domain for any upgoing plane wave $j$ in response to an incident downgoing plane wave $i$. It is equal

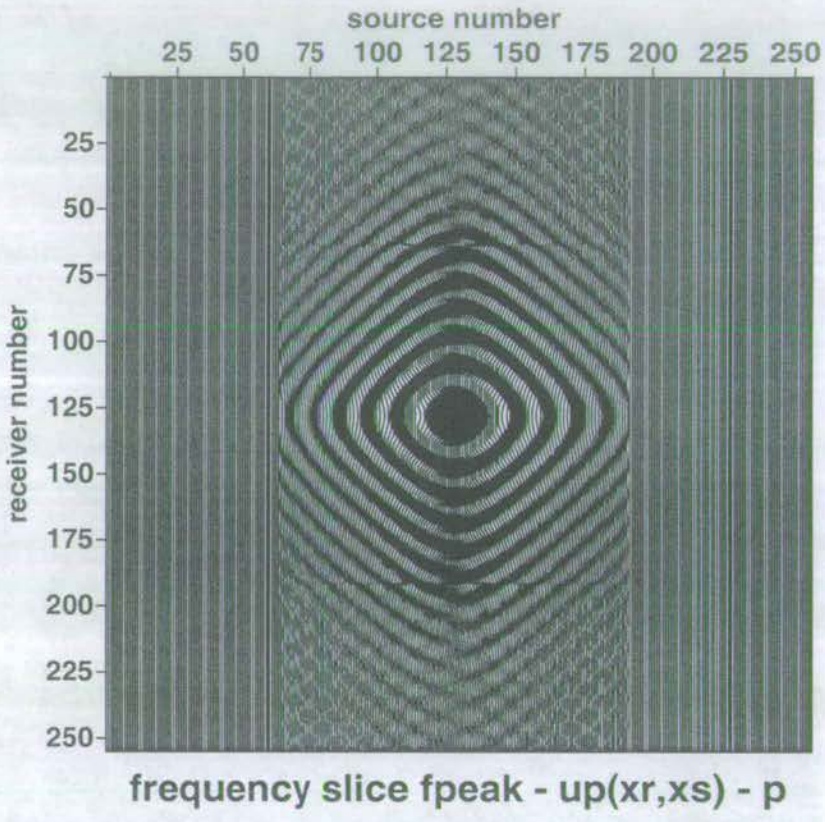


Figure 8.16: A frequency slice of the upgoing scattered field in terms of source and receiver number. (The real part only is shown.) A frequency slice of the scattered pressure field is transformed to the wavenumber domain where the receiver ghost is divided out, and then transformed back to the space domain. The smearing over receiver number arises because the deghosting operator is a function of receiver wavenumber and involves data for all receiver offsets, including where the wavefield is zero.

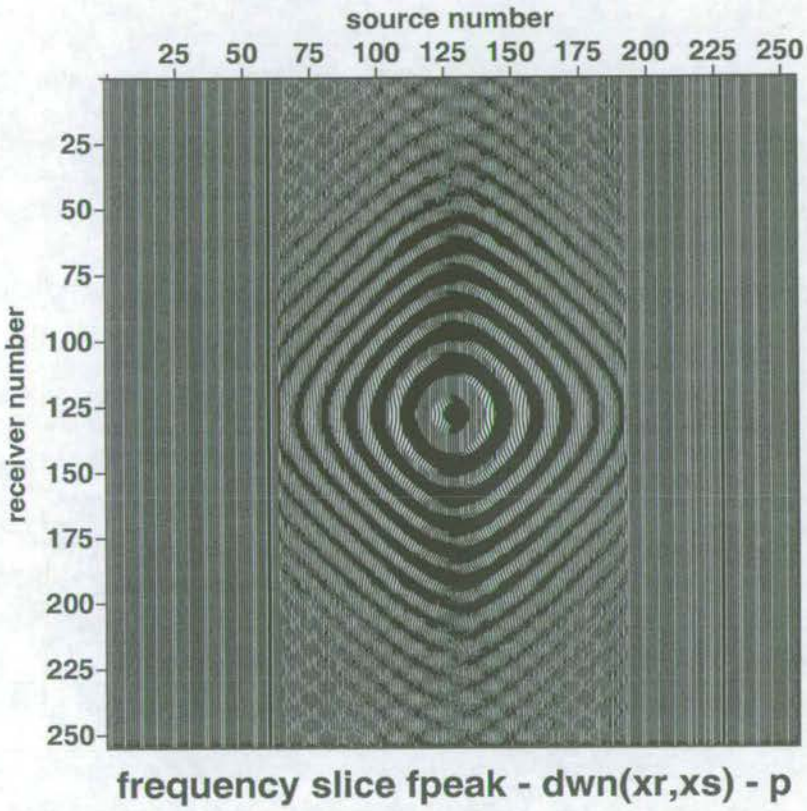


Figure 8.17: A frequency slice of the downgoing scattered field in terms of source and receiver number. (The real part only is shown.) A frequency slice of the scattered pressure field is transformed to the wavenumber domain where the receiver ghost is divided out. The result is subtracted from the pressure and then transformed back to the space domain. The smearing over receiver number arises because the deghosting operator is a function of receiver wavenumber and involves data for all receiver offsets, including where the wavefield is zero.

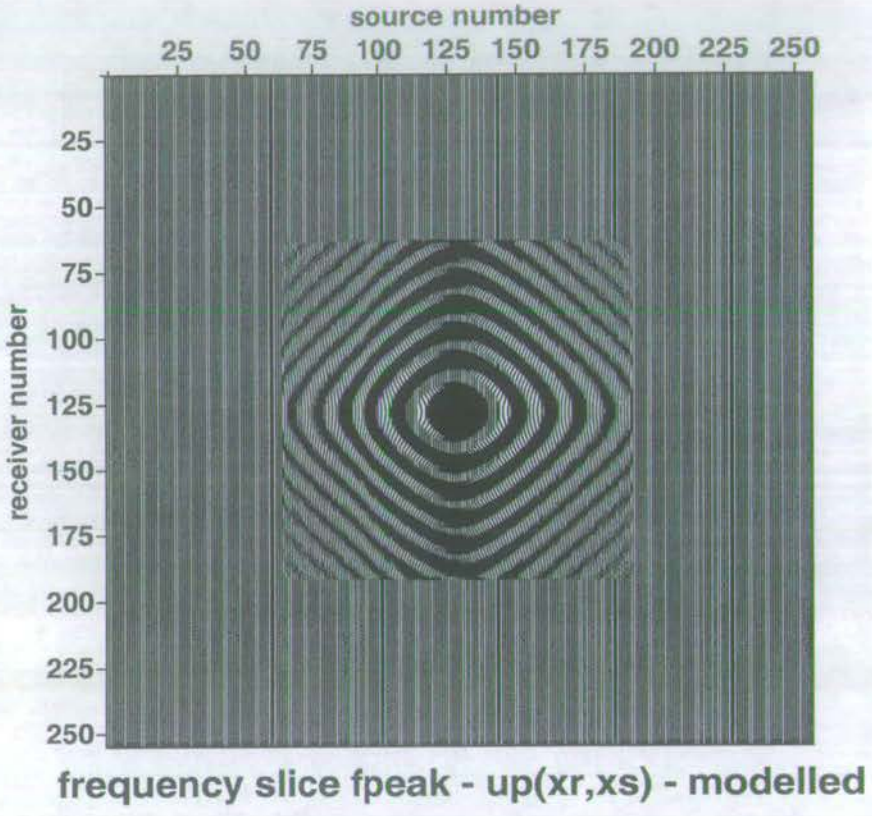


Figure 8.18: A frequency slice of the upgoing scattered field in terms of source and receiver number. (The real part only is shown.) The upgoing field is modelled directly and transformed to the frequency domain. The data for a single frequency is selected and surrounded with zeros.

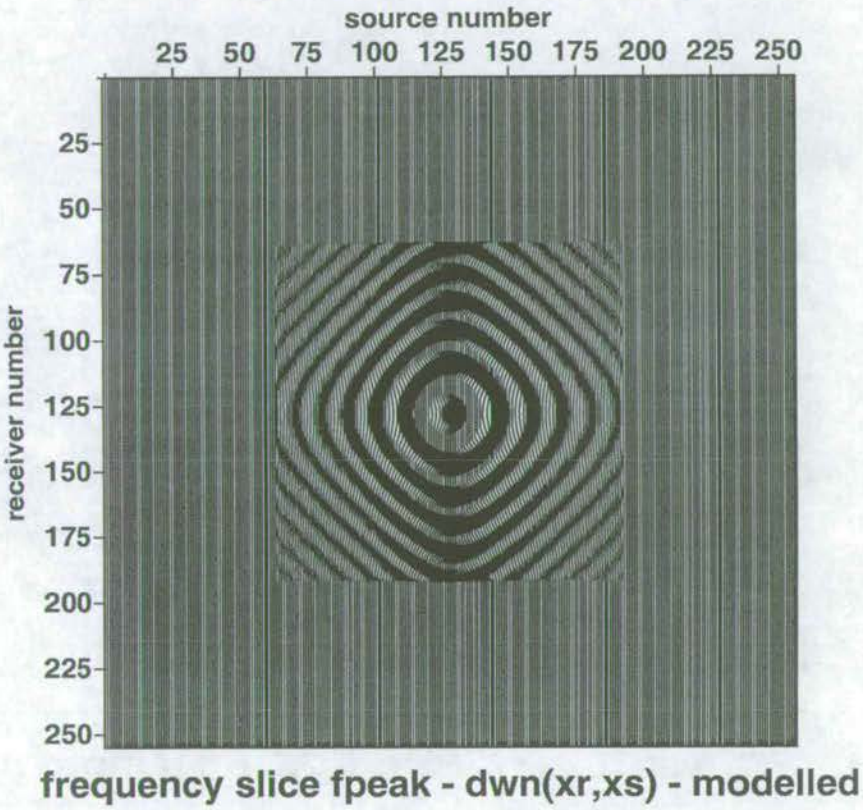


Figure 8.19: A frequency slice of the downgoing scattered field in terms of source and receiver number. (The real part only is shown.) The downgoing field is modelled directly and transformed to the frequency domain. The data for a single frequency is selected and surrounded with zeros.

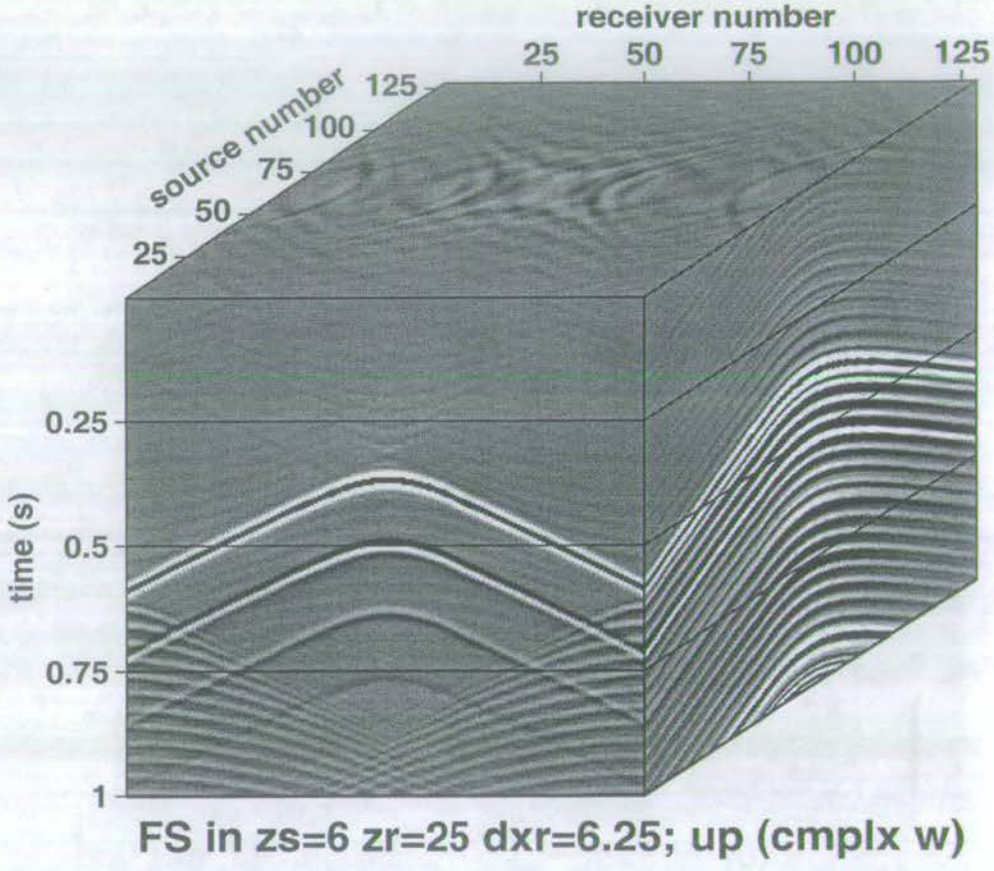


Figure 8.20: A cube of processed 2D data showing the upgoing field for varying source and receiver offsets. The pressure data only are processed in the frequency-wavenumber domain to separate the upgoing field from the scattered field, then transformed back to the space-time domain. The hyperbolic artefacts occur during the wave propagation step required to deghost the data. They are caused by the abrupt transition to zero at the edges of the data, and their magnitude is proportional to the depth of the receivers.

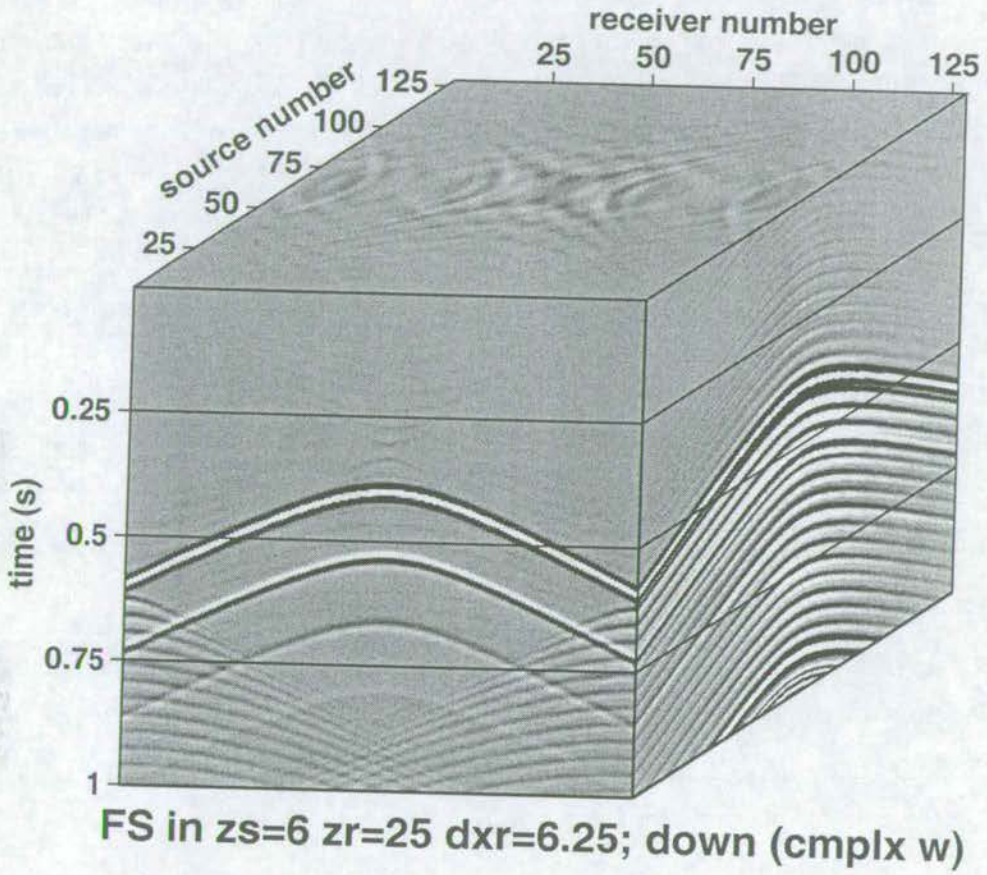


Figure 8.21: A cube of processed 2D data showing the downgoing field for varying source and receiver offsets. The pressure data only are processed in the frequency-wavenumber domain to separate the downgoing field from the scattered field, then transformed back to the space-time domain. The hyperbolic artefacts occur during the wave propagation step required to deghost the data. They are caused by the abrupt transition to zero at the edges of the data, and their magnitude is proportional to the depth of the receivers.

to the reflection response for that $j-i$ combination, $\hat{\hat{R}}_{ji}$, multiplied by the incident field $\hat{\hat{I}}_i$.

Note the correspondance between equation (8.14) and the first term on the right-hand side of equations (5.18). The last step in the multiple-removal scheme propagates an incident field through the reflection response of the earth and on to the receivers, and stops before reaching the free surface.

The incident field re-introduced to the reflection response in these results is the one used to create the synthetic seismograms. It is the Ricker line source plus its virtual image propagated from the source to the receiver locations. The Ricker wavelet already has the desired characteristics. Section 7.4 explains the possible gains in stability provided by using the ghost as well as the direct wave in the final incident field.

After solving the equations at each (real) frequency, the results for the whole data cube are shown in Figure 8.25. Note that the edge effects at low and high receiver number, produced by the up/down separation, are present in the multiple-free result. Significant reductions in the noise level are possible through using complex frequency as shown in Figure 8.26. Figures 8.27 and 8.28 show source and receiver gathers through the cube which don't already appear on the faces of Figure 8.26. The aperture effects related to the wavefield separation into upgoing and downgoing waves are obvious at low and high receiver numbers. The artefacts are smallest at the centre of the cube.

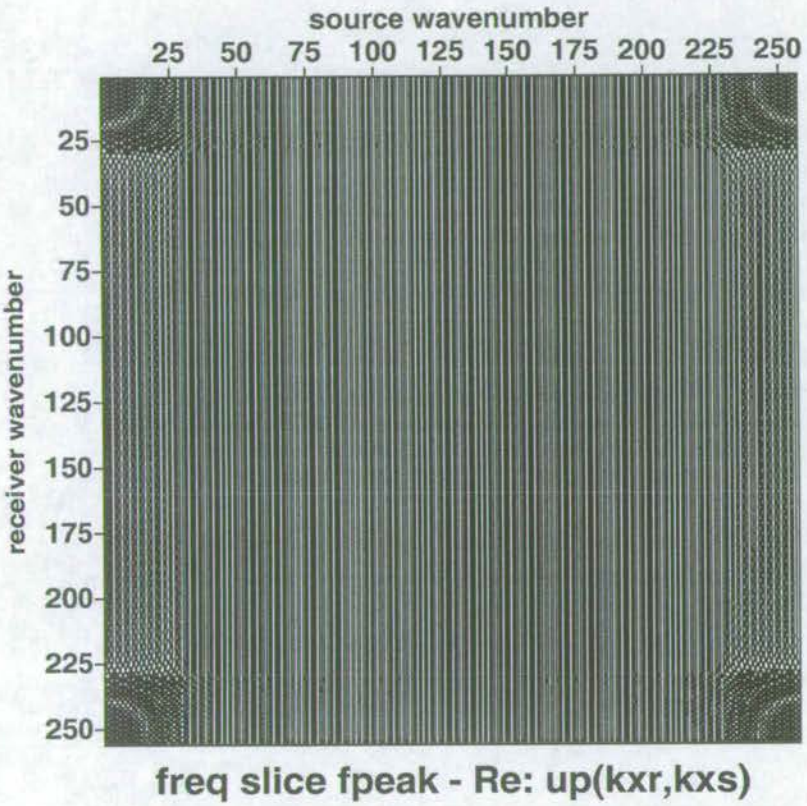


Figure 8.22: A frequency slice of the upgoing scattered field in terms of source and receiver wavenumber. (The real part only is shown.) A frequency slice of the scattered pressure field is transformed to the wavenumber domain where the receiver ghost is divided out. The data are displayed as they are stored for the Fourier transform: (from left to right, and from top to bottom) the positive wavenumbers increasing from zero up to the Nyquist, followed by the data for decreasing negative wavenumbers.

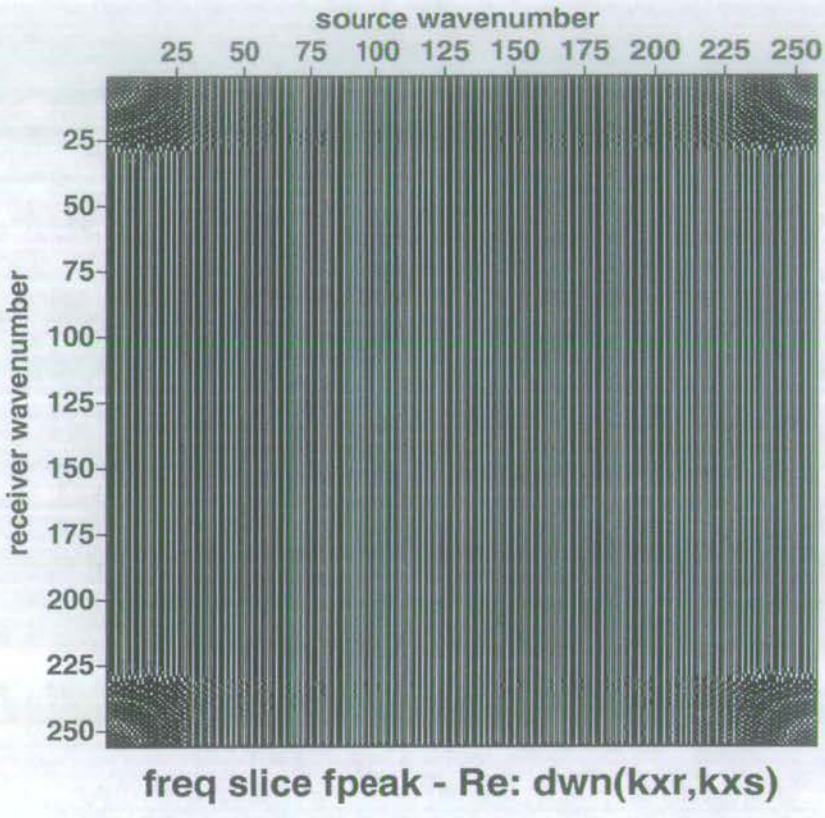


Figure 8.23: A frequency slice of the downgoing scattered field in terms of source and receiver wavenumber. (The real part only is shown.) A frequency slice of the scattered pressure field is transformed to the wavenumber domain where the receiver ghost is divided out. The result is subtracted from the pressure. The data are displayed as they are stored for the Fourier transform: (from left to right, and from top to bottom) the positive wavenumbers increasing from zero up to the Nyquist, followed by the data for decreasing negative wavenumbers.

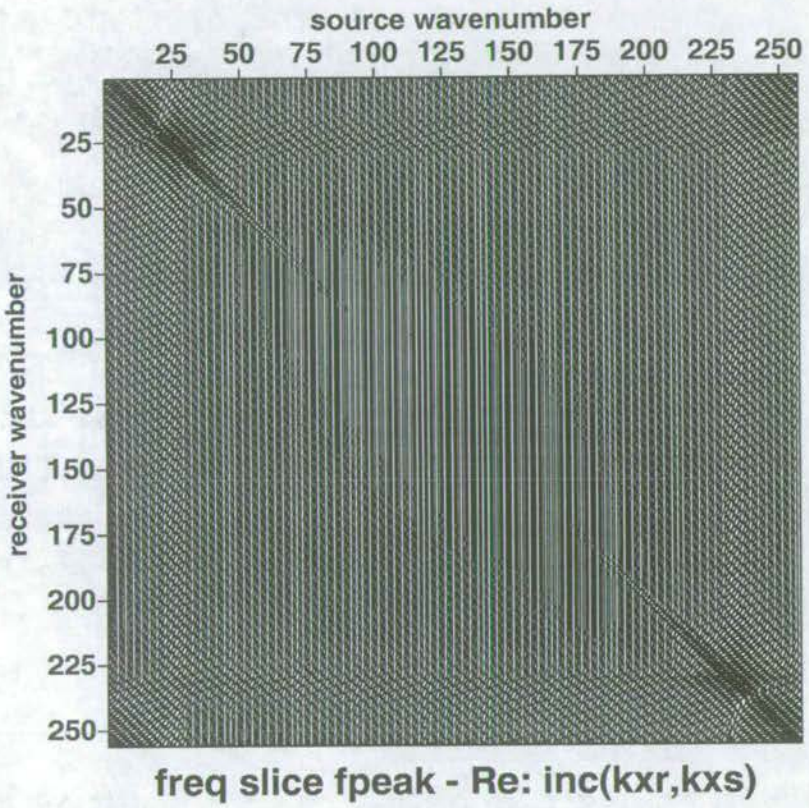


Figure 8.24: A frequency slice of the incident field in terms of source and receiver wavenumber. (The real part only is shown.) A frequency slice of the incident field is transformed to the wavenumber domain. The data are displayed as they are stored for the Fourier transform: (from left to right, and from top to bottom) the positive wavenumbers increasing from zero up to the Nyquist, followed by the data for decreasing negative wavenumbers.

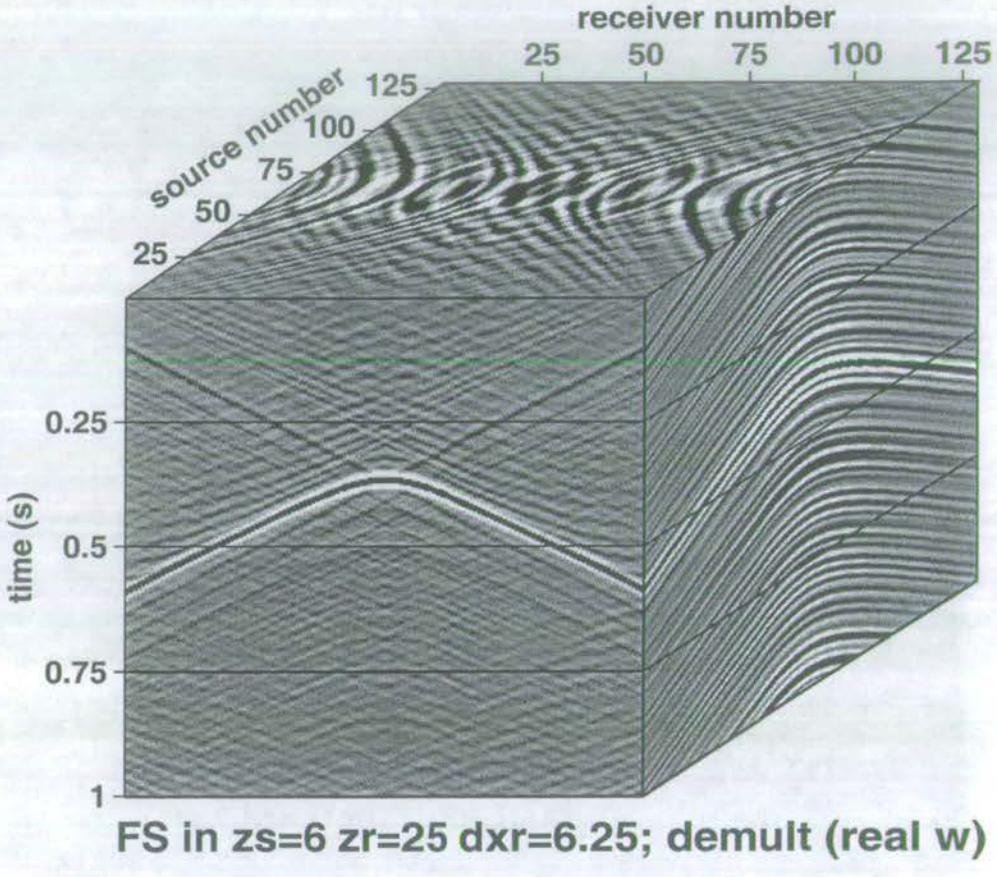


Figure 8.25: A cube of processed 2D data showing the multiple-free field for varying source and receiver offsets. The pressure data only are processed in the frequency-wavenumber domain to remove the multiples from the scattered field, then transformed back to the space-time domain. The numerical noise is a result of performing all the calculations with real frequencies.

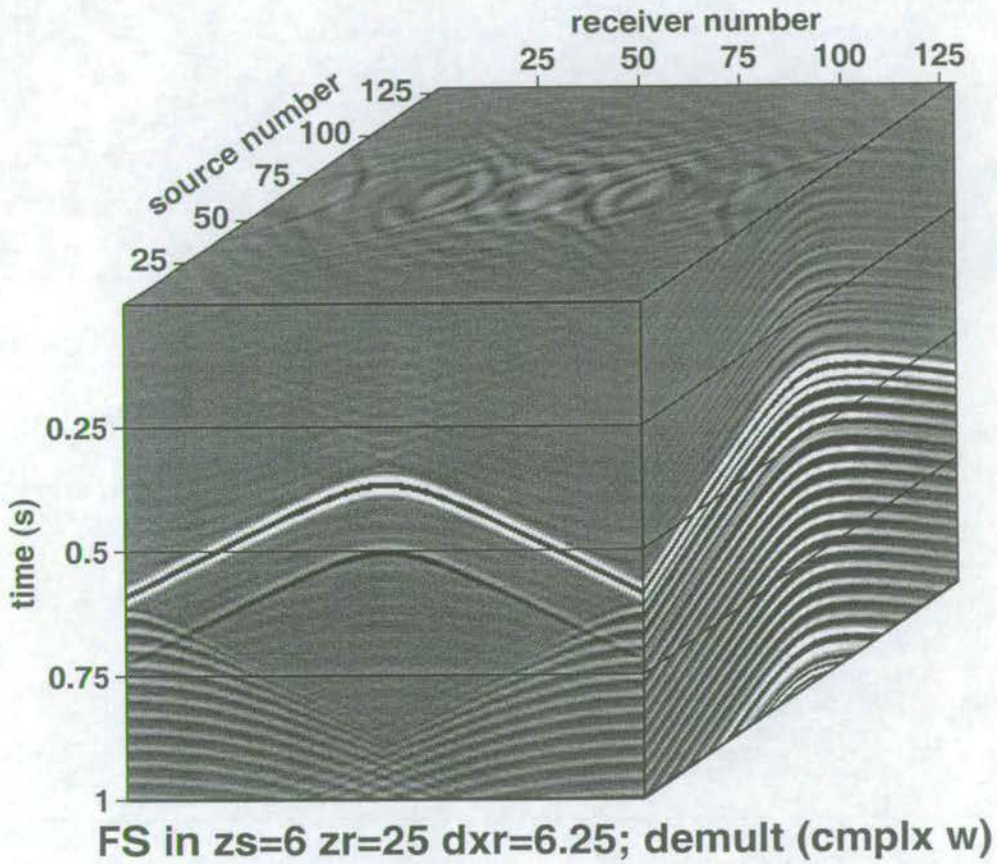


Figure 8.26: A cube of processed 2D data showing the multiple-free field for varying source and receiver offsets. The pressure data only are processed in the frequency-wavenumber domain to remove the multiples from the scattered field, then transformed back to the space-time domain. The calculation was performed with complex frequencies, and padding the time axis with zeros to double its original length before transforming to frequency. The hyperbolic artefacts occur during the wave propagation step required to deghost the data. They are caused by the abrupt transition to zero at the edges of the data, and their magnitude is proportional to the depth of the receivers.

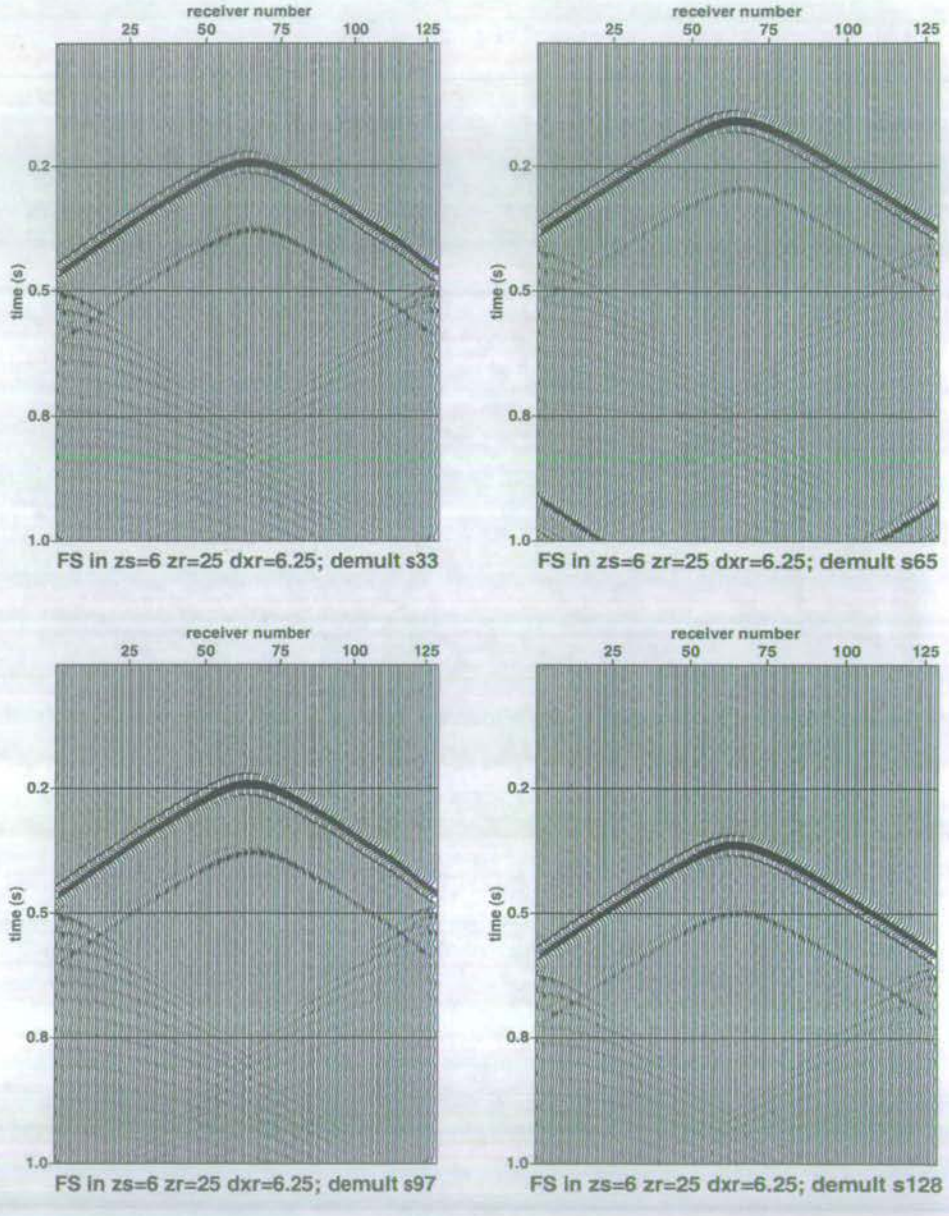


Figure 8.27: Slices along different source numbers of the 2D cube shown in Figure 8.26. These are shot gathers processed to remove the sea surface using pressure only.

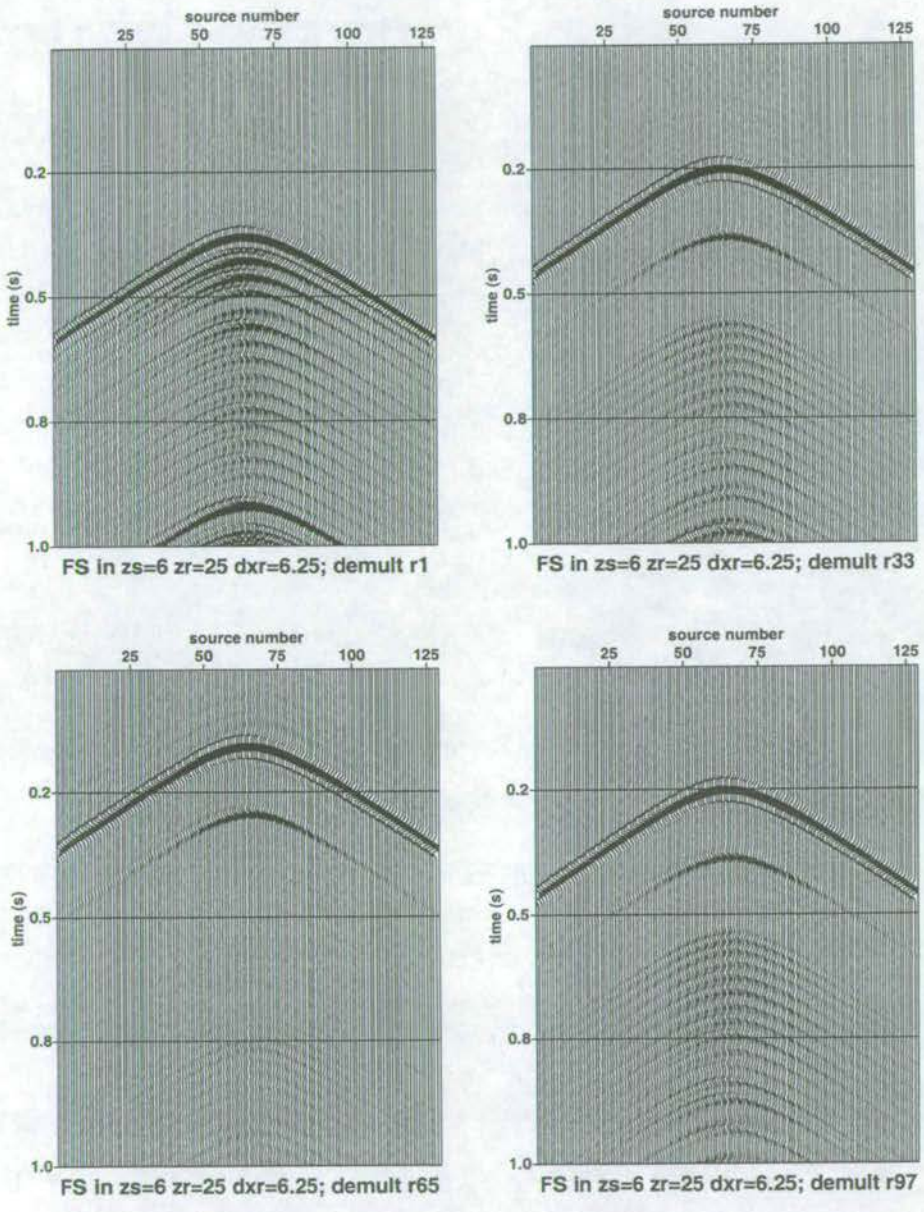


Figure 8.28: Slices along different receiver numbers of the 2D cube shown in Figure 8.26. These are receiver gathers processed to remove the sea surface using pressure only.

## 8.6 A synthetic example with OBC data

Using the same model as in section 8.5, a suite of seismograms are calculated for the vertical component of particle velocity (Figure 8.29). The source time function is shown in Figure 8.2. The vertical particle velocity is distinct from the pressure because it results from a scaled difference of the downgoing and upgoing waves, whereas the pressure is the sum of the downgoing and upgoing waves (compare Figure 8.29 with Figure 8.12).

The vertical particle velocity seismograms shown in Figure 8.29 are processed with the pressure data of Figures 8.12 and 8.13. As before, the scattered pressure and the scattered vertical particle velocity are modelled separately from the incident field.

The scattered fields of pressure and of the vertical component of particle velocity, and the incident pressure field are transformed to the frequency-wavenumber domain. With dual sensor data the wave separation step is different.

### Separating upgoing and downgoing plane wave components: Pressure and the vertical component of particle velocity

The pressure and particle velocity are separated by the following differences and sums:

$$2\tilde{D}^{scat}(k_x^r, z_r, \omega, x_s, z_s) = \tilde{P}^{scat}(k_x^r, z_r, \omega, x_s, z_s) + \frac{\rho\omega}{k_z^U}\tilde{V}_z^{scat}(k_x^r, z_r, \omega, x_s, z_s) \tag{8.15}$$

$$2\tilde{U}^{scat}(k_x^r, z_r, \omega, x_s, z_s) = \tilde{P}^{scat}(k_x^r, z_r, \omega, x_s, z_s) - \frac{\rho\omega}{k_z^U}\tilde{V}_z^{scat}(k_x^r, z_r, \omega, x_s, z_s). \tag{8.16}$$

Note that, as in the separation with pressure alone (equation (8.11), the expressions for upgoing and downgoing pressure are independent of the source number, so the separation may be applied as a function of source number or source wavenumber. Any artefacts caused by the separation appear as a function of receiver number, but are independent of source number. The separation is actually applied in the double wavenumber domain.

Figures 8.30 and 8.31 show these fields after transformation back to the frequency-space domain, for one frequency slice, for comparison with Figures 8.18 and 8.19 on pages 208 and 209. Figures 8.32 and 8.33 show the upgoing and downgoing wavefields, respectively, for the whole datacube after transforming back to the time domain. Compare these cubes with modelling the upgoing and downgoing fields separately, shown in Figures 8.34 and 8.35.

There is much less noise present on these separated fields than the result using pressure alone: the introduction of the particle velocity avoids the receiver ghost deconvolution step. There is, however, an artefact at high and low receiver wavenumber which is due to the limited spatial aperture of the data, and the amount of zeros padded around the data prior to the transformation to the double wavenumber domain. This is discussed further later.

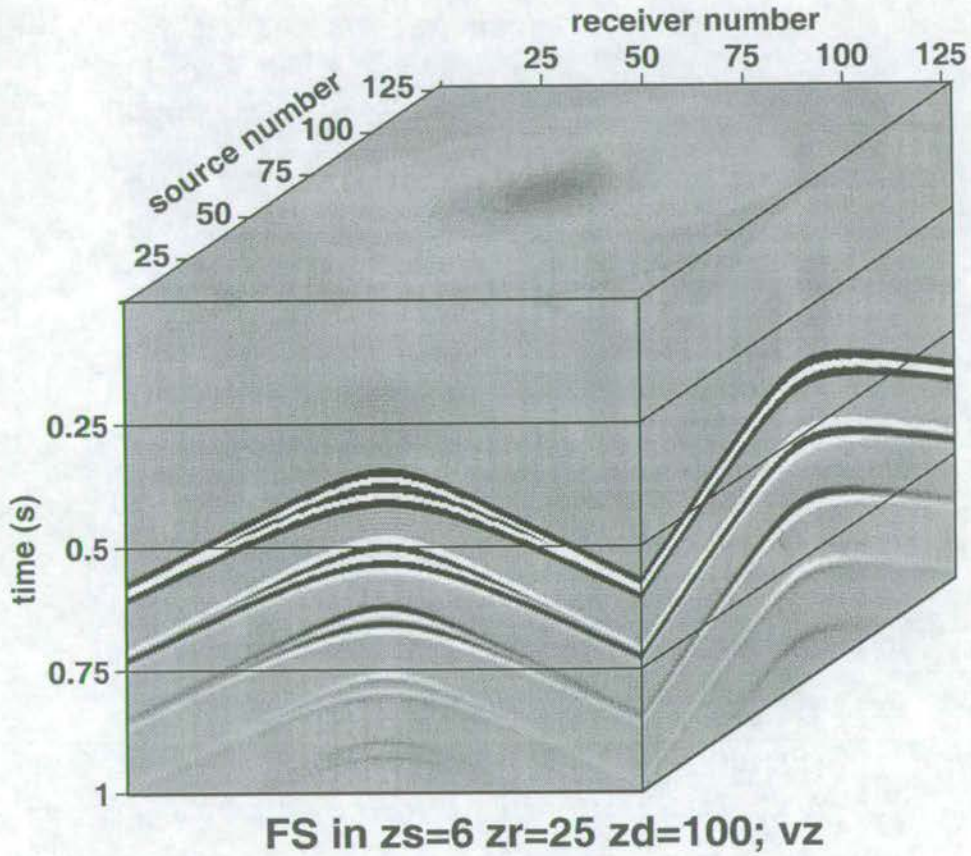


Figure 8.29: A cube of 2D synthetic data for varying source and receiver offsets. The scattered field for the vertical component of particle velocity is modelled in the presence of the free surface for 128 receivers and 128 shots, with 1 line diffractor in the middle of the receiver spread at 100m depth.

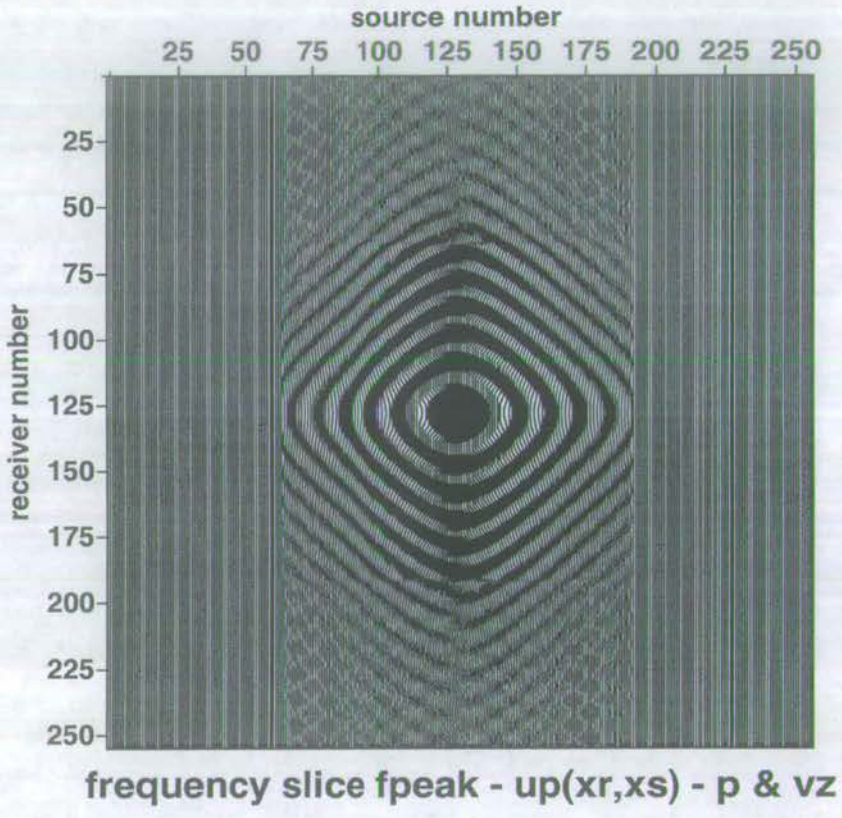


Figure 8.30: A frequency slice of the upgoing scattered field in terms of source and receiver number. (The real part only is shown.) Frequency slices of the scattered fields for pressure and the vertical component of particle velocity are transformed to the wavenumber domain where they are combined to give the upgoing field, and then transformed back to the space domain. The smearing over receiver number arises because the wavefield combination is a function of receiver wavenumber and involves data for all receiver offsets, including where the wavefield is zero.

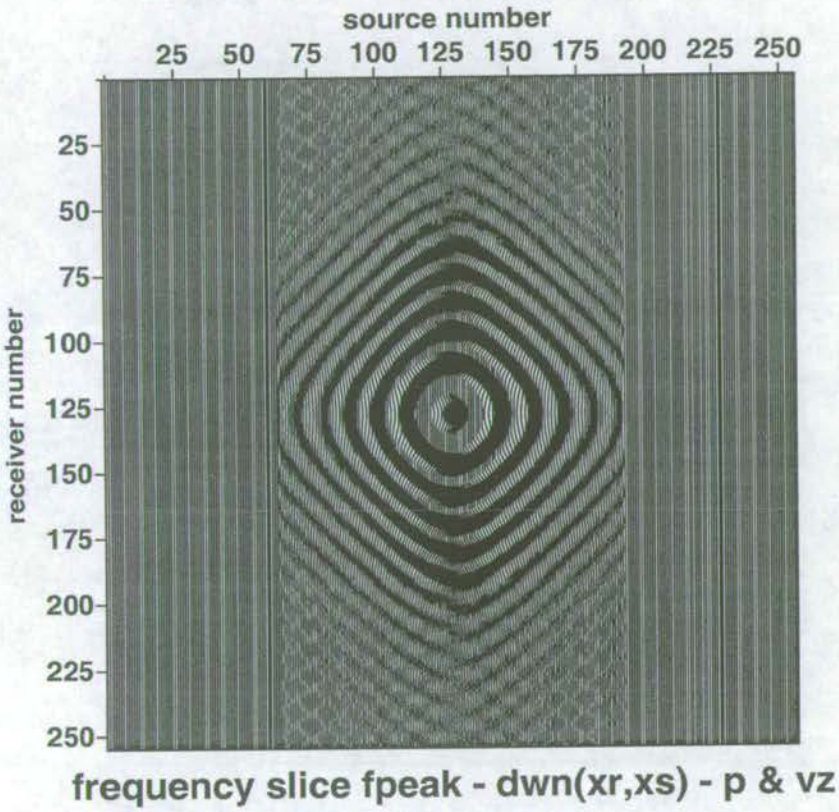


Figure 8.31: A frequency slice of the downgoing scattered field in terms of source and receiver number. (The real part only is shown.) Frequency slices of the scattered fields for pressure and the vertical component of particle velocity are transformed to the wavenumber domain where they are combined to give the downgoing field, and then transformed back to the space domain. The smearing over receiver number arises because the wavefield combination is a function of receiver wavenumber and involves data for all receiver offsets, including where the wavefield is zero.

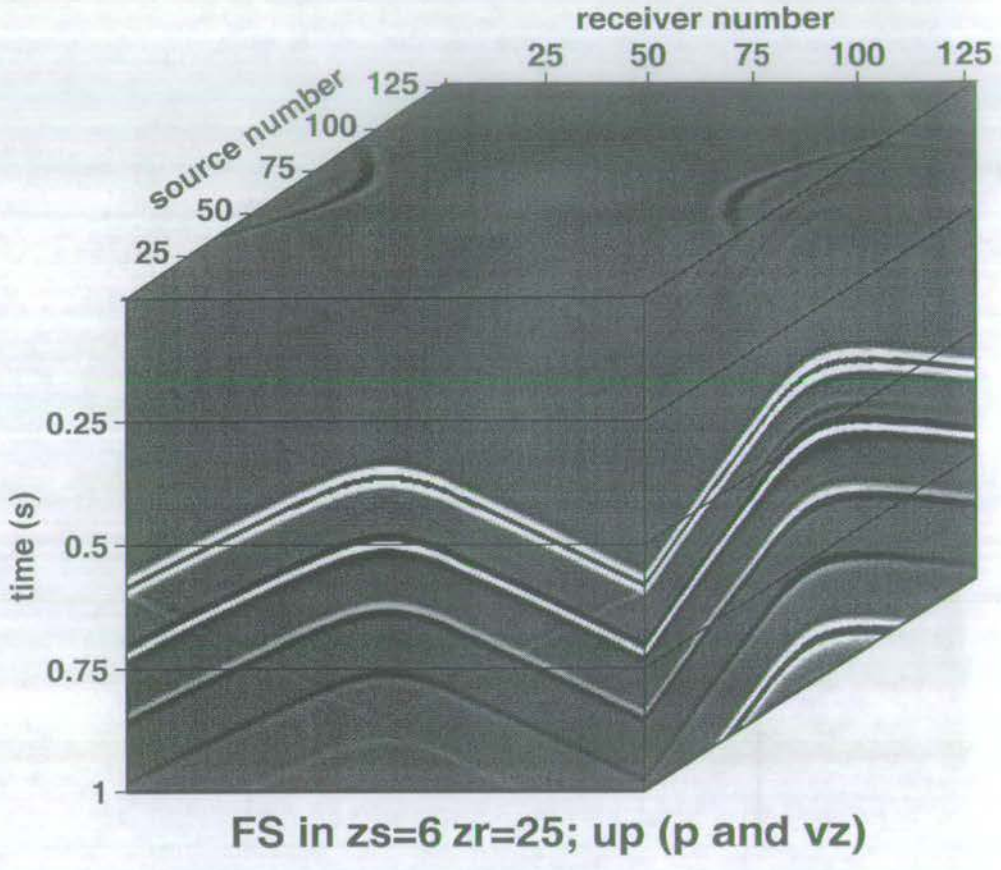


Figure 8.32: A cube of processed 2D data showing the upgoing field for varying source and receiver offsets. The pressure and particle velocity data are processed in the frequency-wavenumber domain to separate the upgoing field from the scattered fields, then transformed back to the space-time domain. Note that there are no hyperbolic artefacts as in the pressure only case. This is due to the additional information provided by the particle velocity, which removes the requirement for a wave propagation step in the separation.

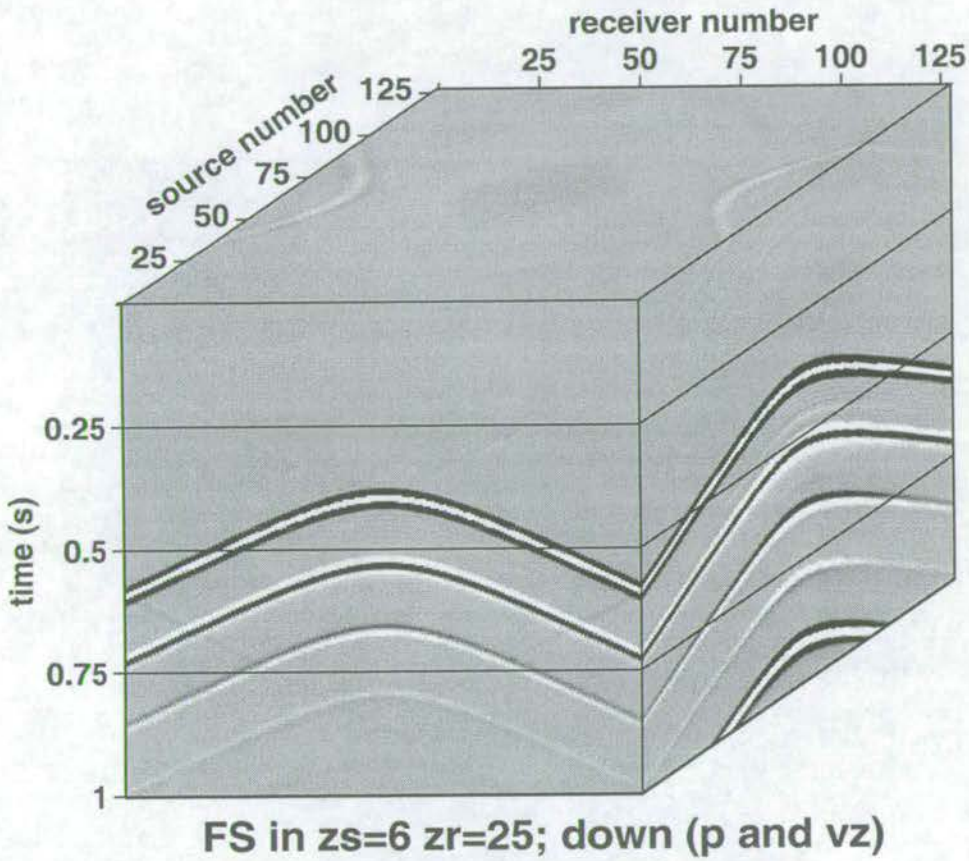


Figure 8.33: A cube of processed 2D data showing the downgoing field for varying source and receiver offsets. The pressure and particle velocity data are processed in the frequency-wavenumber domain to separate the downgoing field from the scattered fields, then transformed back to the space-time domain. Note that there are no hyperbolic artefacts as in the pressure only case. This is due to the additional information provided by the particle velocity, which removes the requirement for a wave propagation step in the separation.

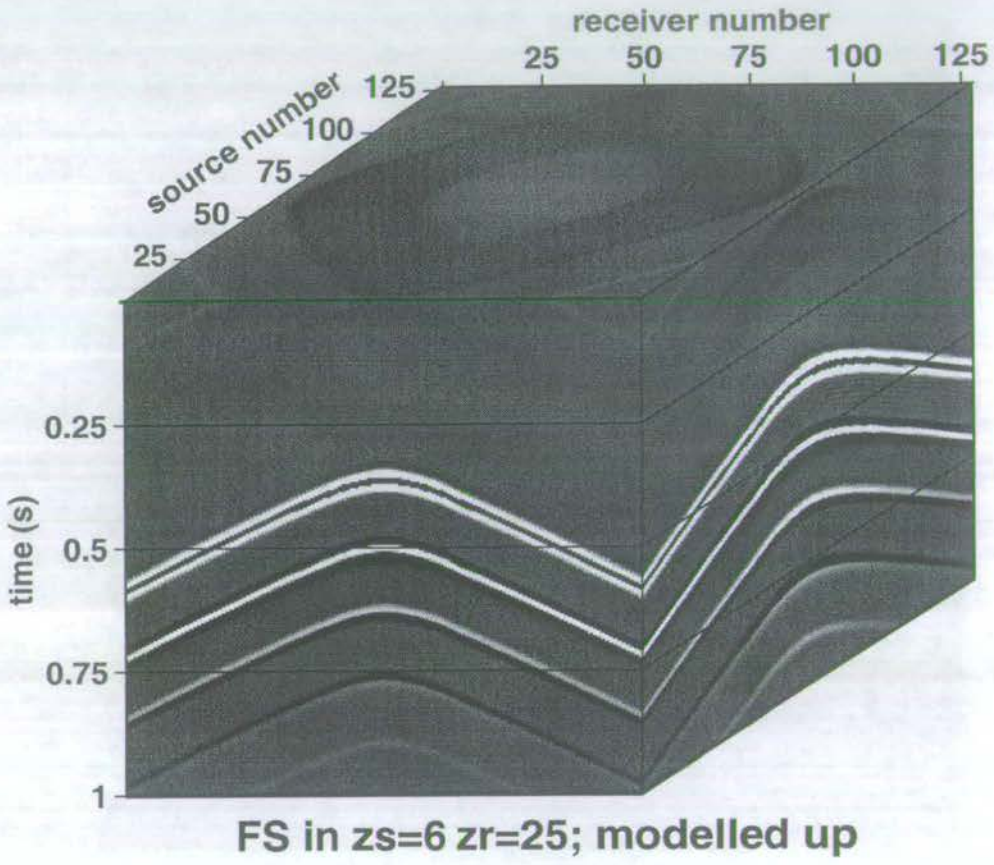


Figure 8.34: A cube of 2D synthetic data showing the upgoing field for varying source and receiver offsets. The upgoing field is modelled directly.

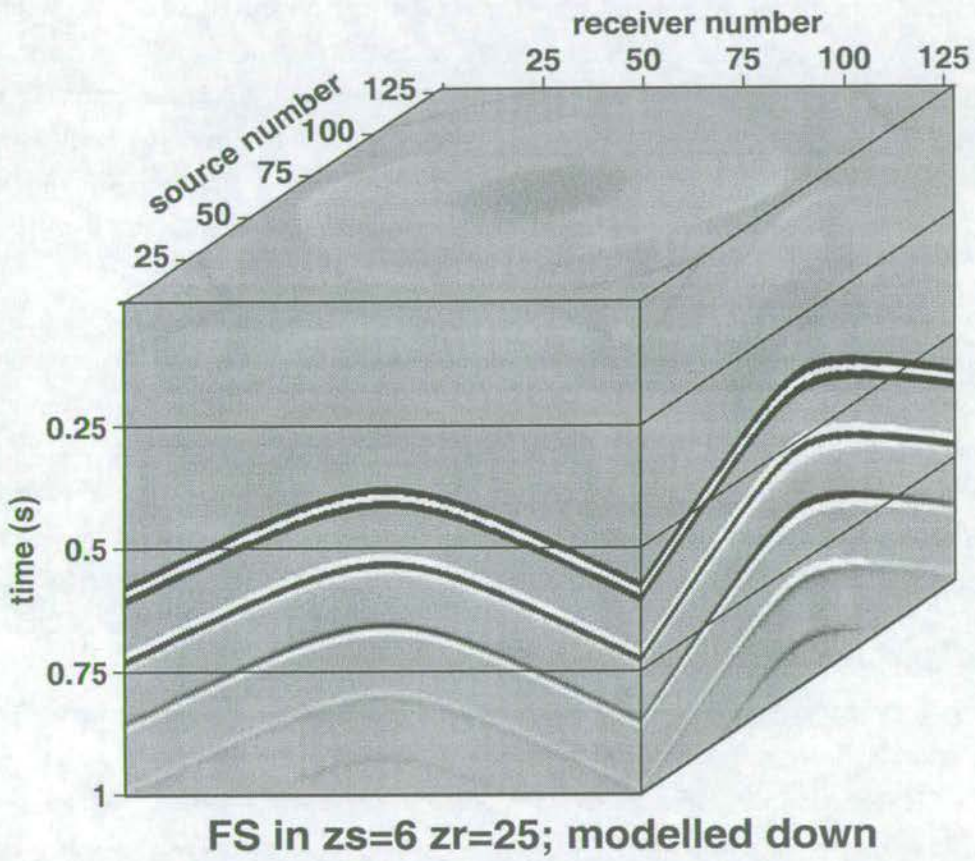


Figure 8.35: A cube of 2D synthetic data showing the downgoing field for varying source and receiver offsets. The downgoing field is modelled directly.

### Solving the equations

After solving the equations using the direct solve method of section 8.3, described in detail in section 8.5, the results for the whole datacube are shown in Figure 8.36. There are artefacts in the result which are related to the finite data aperture. Figures 8.37 and 8.38 show source and receiver gathers through the cube which don't already appear on the faces of Figure 8.36. A first-order residual multiple is visible which is caused by the finite data aperture: the data do not sample the highest dips of the diffraction hyperbola. Because the diffractors are modelled in a constant velocity, the hyperbolas have the same shape regardless of depth. Reducing the number of shots and receivers, and hence the data sampling of the diffractor, results in residual multiples of higher order remaining in the multiple-free processed result. For the same configuration as above, but with only 64 receivers and 64 sources the result is much worse, as shown in Figure 8.39. In the bottom left is the scattered pressure (with multiples) for reference. Clockwise from the top left is the upgoing, downgoing, and multiple-free results. Note now that there are residual multiples of all orders due to the limited aperture of the data. The results are very noisy in general.

Figures 8.36-8.38 also exhibit spatial wraparound artefacts related to the finite data aperture. These artefacts at high and low source and receiver wavenumber are due to the spatial extent of the data, and the number of zeros added to accommodate the operations caried out in the frequency-wavenumber domain. The bottom of each record exhibits spatial wraparound of the primary hyperbola. The equations are evaluated for all source and all receiver wavenumbers, but data do not exist for the complete corresponding source and receiver range. Half of the data area is composed of zeros (as seen in Figure 8.14 and 8.15). The Fourier transform assumes the data to be periodic. The manifestation of this on transforming back to the time-space domain is that data which would appear at high source/receiver wavenumbers is folded back in at low source/receiver wavenumbers.

By adding more zeros before the transformation to wavenumber these effects still exist but arrive outside the time window of the data.

## 8.7 The incident field in OBC data

It was observed in section 7.5 that in the simple situation of one dimension it is possible to obtain multiple-free data without first subtracting the incident field. This is because in one dimension, a single spatial transform is required to decompose the data into plane wave components.

The incident energy which travels from the source to the receivers does so in a straight line. In two dimensions, because two spatial transforms are performed, the incident field is transformed into a delta function which lies principally along the diagonal between source wavenumber and receiver wavenumber (Figure 8.24). Note, however, that the energy is also

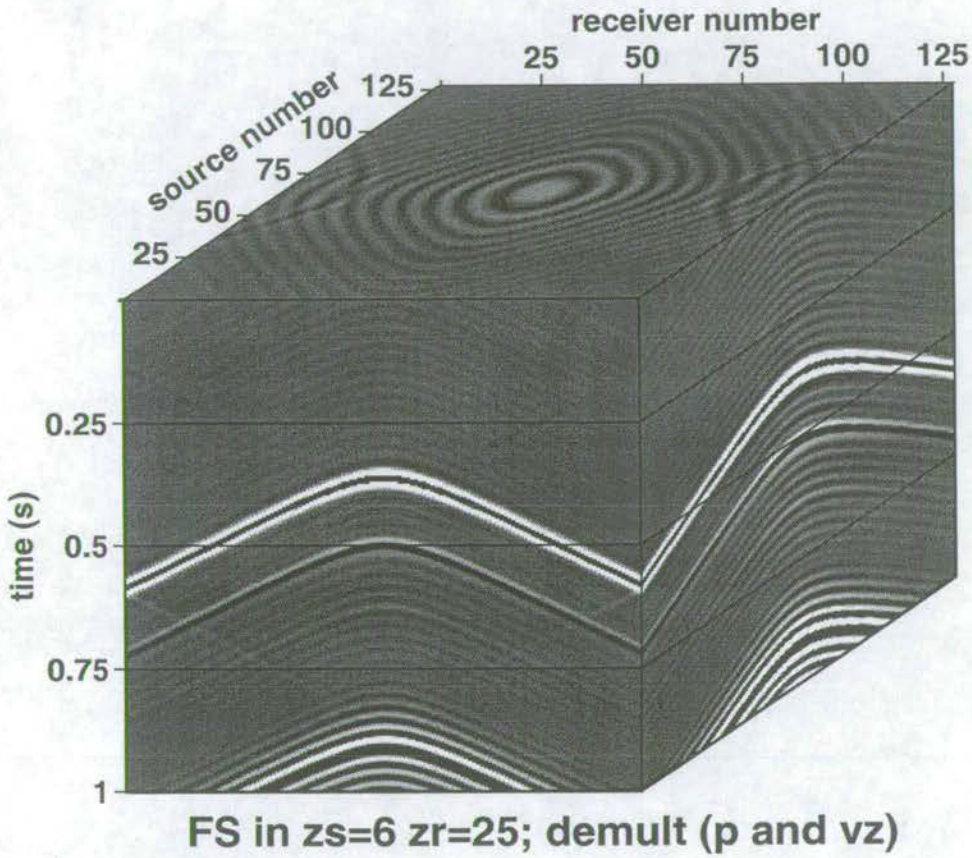


Figure 8.36: A cube of processed 2D data showing the multiple-free field for varying source and receiver offsets. The pressure and particle velocity data are processed in the frequency-wavenumber domain to remove the multiples from the scattered pressure field. The calculation was performed with complex frequencies, and padding the time axis with zeros to double its original length before transforming to frequency.

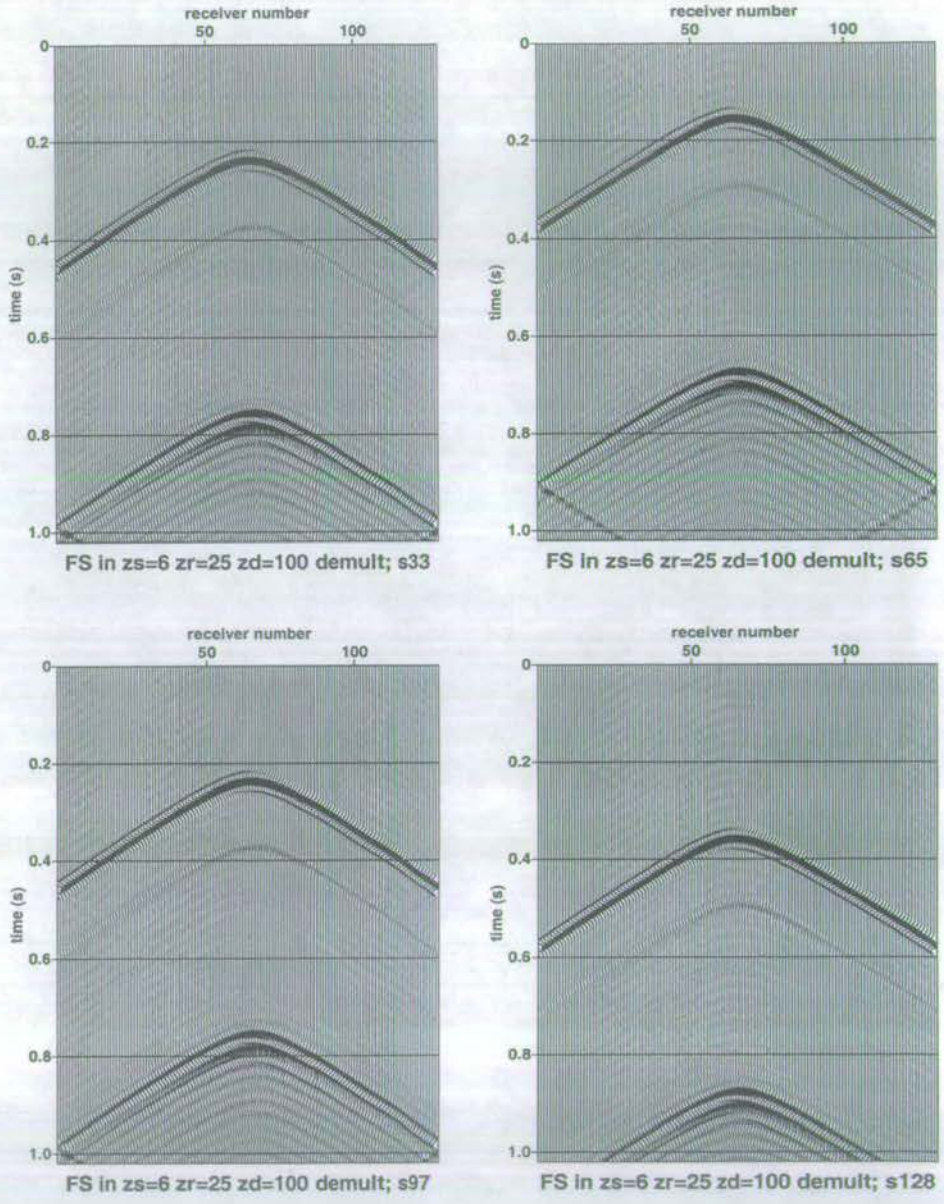


Figure 8.37: Slices along different source numbers of the 2D cube shown in Figure 8.36. These are shot gathers processed to remove the sea surface using pressure and the vertical component of particle velocity.

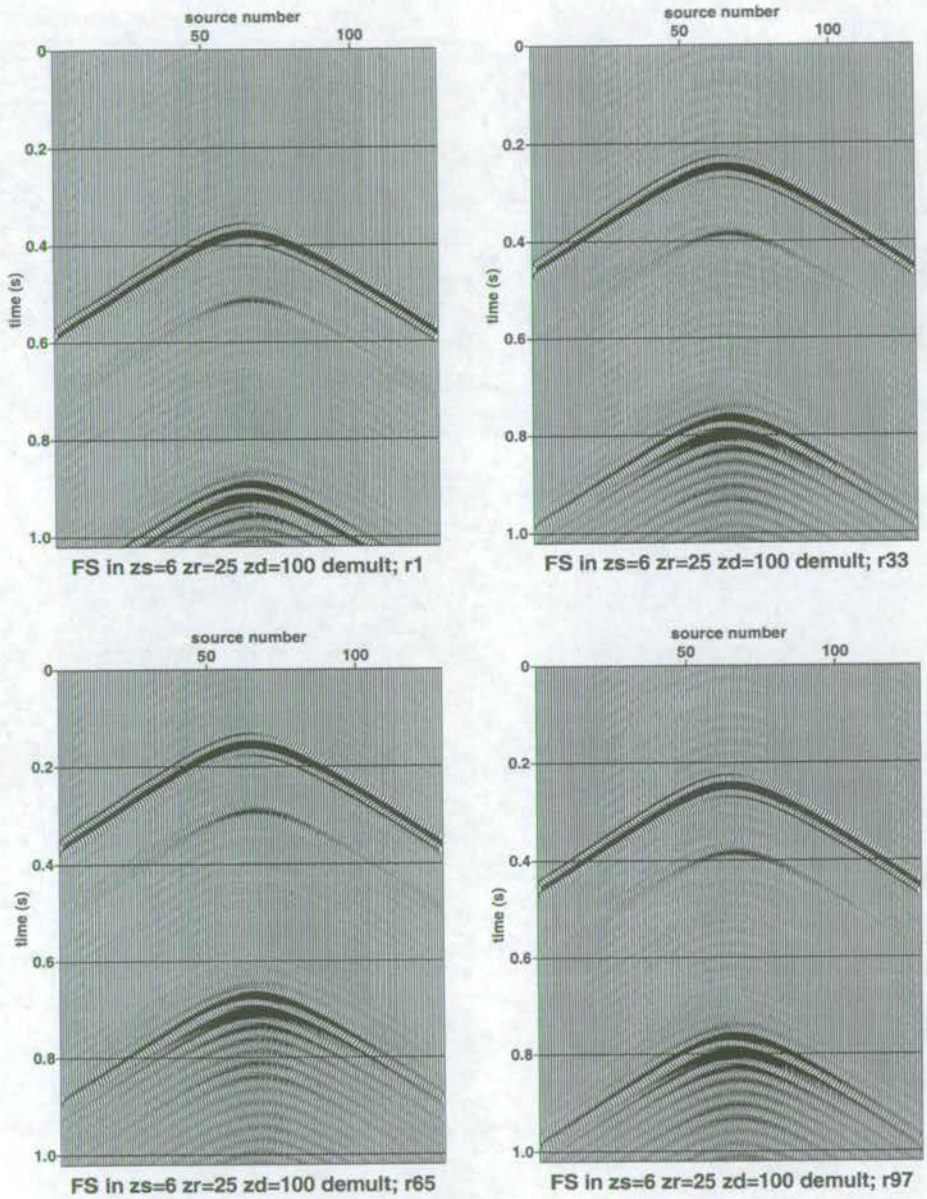


Figure 8.38: Slices along different receiver numbers of the 2D cube shown in Figure 8.36. These are receiver gathers processed to remove the sea surface using pressure and the vertical component of particle velocity.

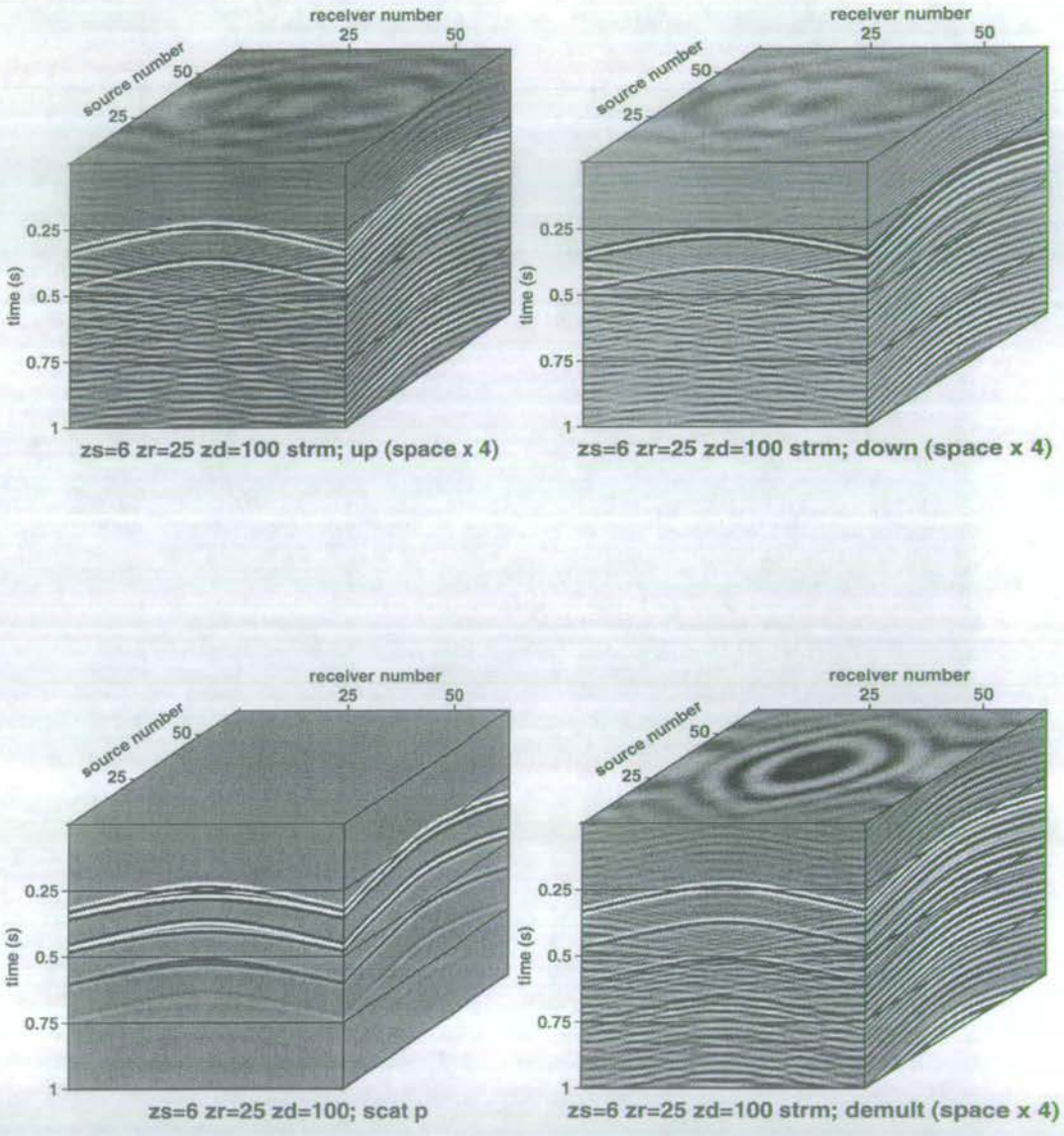


Figure 8.39: Reducing the data aperture severely degrades the multiple-free result. These plots show the result of using 64 receivers and shots instead of 128. The following data are plotted clockwise from the bottom left: scattered pressure with multiples, upgoing field, downgoing field, and multiple-free result.

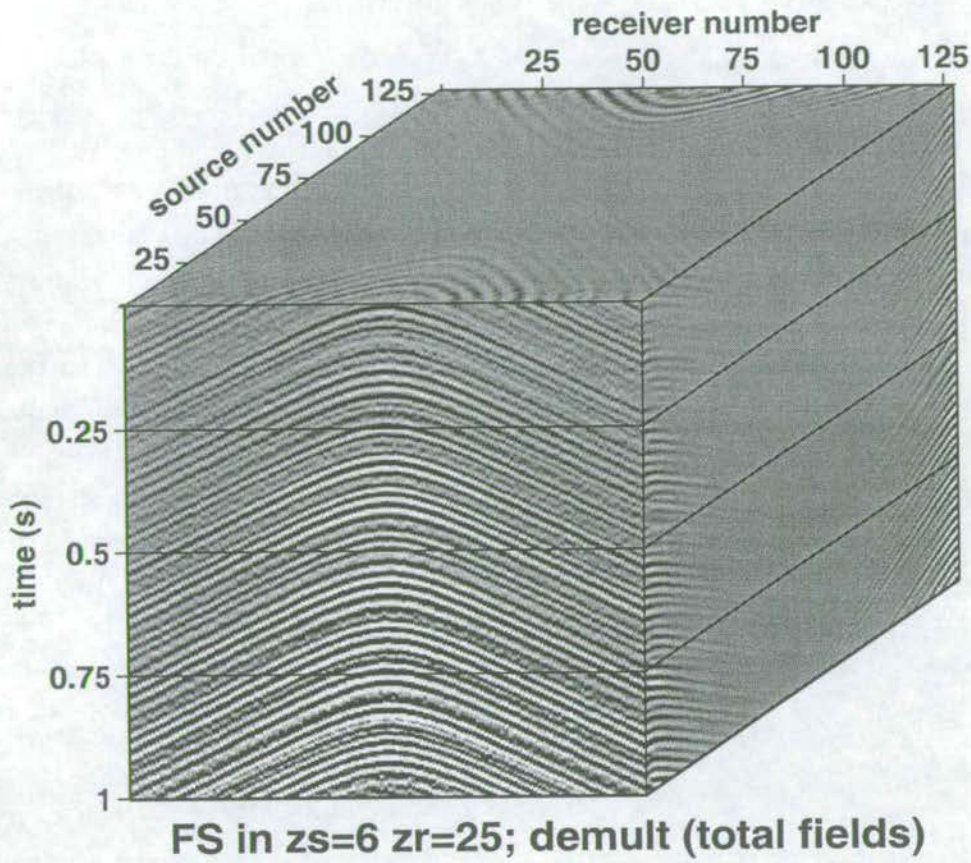


Figure 8.40: A cube of processed 2D data showing the multiple-free fields for varying source and receiver offsets. The pressure and particle velocity data are processed in the frequency-wavenumber domain to remove the multiples from the total fields. The inclusion of all of the incident field after transformation to the frequency-wavenumber domain (as is necessary when the incident field is an integral part of the total field) makes the result unstable.

spread out away from the diagonal. This is due to the finite extent of the incident field (which does not exist for infinite source and receiver numbers). If all of the incident field in Figure 8.24 is included in equations (8.1) for the reflection response (i.e. the off-diagonal elements as well) the result is unstable, as shown in Figure 8.40.

In order to obtain a stable solution in the frequency-wavenumber domain, as in the examples above, the incident field must be included in the equations only along the main diagonal, as in equations (8.1). This is not possible if the incident field is included in the total field.

## 8.8 Conclusions

It is possible to remove multiple diffractions in 2D by recovering the reflection respose of the earth. This is possible with streamer data or OBC data. The wavefield separation into upgoing and downgoing wavefields works better with dual sensor data.

The multiple-free results for both streamer and OBC data suffer from numerical artefacts which are related to the limited spatial extent of the data. The spatial wraparound seen at low and high receiver and source numbers is caused by the periodic nature of the Fourier transform essentially extrapolating the data where there is none. It is expected that zero padding would push these spatial wraparound artefacts out of the time window of interest. This is not possible in the present incarnation of the computer code due to memory limitations. It is necessary to switch from a serial algorithm to a parallel algorithm.

Residual multiple energy which remains results from the data not sampling all of the energy from the diffractor. To solve this problem, data from a wider aperture over the diffractor are needed. To do so requires a parallel implementatiion of the modelling code. However, the method clearly works.

# CONCLUSIONS

## *Chapter 9*

This thesis presents a new wave-theoretical method for multiple removal in a three-dimensional earth which calculates directly from the data the reflection response of the earth in the absence of the sea surface. The method is deterministic in nature because it uses information about the input source wavefield in its formulation and solution. This is a departure from other methods for two reasons: (1) conventional methods of multiple removal assume that the earth is one-dimensional and are not designed to succeed in complex earth structures; (2) state-of-the-art methods, which are wave-theoretical and three-dimensional in nature, assume a simplified source and predict the multiples then subtract them from the data iteratively. The prediction-and-subtraction step, which is common to some of the conventional methods, uses an energy minimisation citerion to estimate an effective wavelet which removes all the multiples in a statistical sense.

The source wavefield produced by a conventional airgun array can be analysed in several stages. First, a single oscillating bubble is considered which gives rise to the non-linear wave equation in terms of a particle velocity potential. Examination of various approximate solutions to this non-linear equation, each of which is valid at different distances from the bubble, allows a single approximation to be found which has the same level of accuracy at all distances from the bubble. Second, using the approximate particle velocity potential, expressions for the pressure and particle velocity at three key zones of wave propagation may be found: non-linear near field, linear near field, and far field. These expressions dictate the measurements required to characterise the wavefield of a single airgun. Third, considering the effect of forming an airgun array allows the three key zones just mentioned to be redefined for the array, as well as the requisite measurements to characterise the wavefield. The array may be interacting or non-interacting which alters the data processing of the measurements in the non-linear and linear near fields.

Appropriate measurements made in the non-linear field of a single gun, and in the linear near field and far field of an airgun array, provide the information required for the multiple removal scheme presented in this thesis. The data recorded in the non-linear near field are experimental only, but the technique can potentially provide the whole signature of the array in all directions. It is, however, computationally tricky due to the non-linear nature of the equations. The source measurements in the linear near field are robust, as are the computations required to manipulate the measurements. They characterise the wavefield of the array in all directions, and thus provide the elements required to construct the incident field for the

multiple removal scheme. To make a measurement in the far field is operationally difficult because it is not easy to keep a hydrophone at the required depth. The far-field measurement may be made in water depths of several hundred metres only; this reduces the geographic locations in which it may be used. If the water is not deep enough the measurement is contaminated by the reflections from the earth. Although a single measurement does not provide the wavefield of the array in all directions, when the target is deep, propagation from the array is almost vertically-incident. Thus, the single source signature which is extracted from the far-field measurement may be sufficient for the multiple removal scheme. This needs to be tested.

Sea surface multiples may be removed in the frequency-wavenumber domain by calculating plane wave reflection responses below the sea surface. A source signature with desired characteristics is used to propagate an incident field through the plane wave reflection response to receiver positions to produce multiple-free seismograms. Each plane wave response is a component of the three-dimensional response of the earth to an impulse as input. In constructing the responses, the data themselves contain the information required to eliminate the multiples. In order to do this, each receiver must record from a two-dimensional array of sources, and each source must shoot into a two-dimensional array of receivers. A complicated upgoing wave reflected by the earth, which contains primaries and multiples, may be decomposed into plane wave components. The primaries in the upgoing wave result from a multiplication of an incident downgoing plane wave component with a plane wave reflection response, unique for the particular upgoing and downgoing plane wave components. The multiples are a sum of products of scattered downgoing plane wave components with plane wave reflection responses, related to the chosen upgoing and downgoing plane wave components.

For a one-dimensional earth this results simply in a ratio of upgoing to downgoing plane wave components, where the downgoing component has an incident and scattered part. Results with synthetic 1D data show that the method works well for line source and point source data, either with towed streamers or OBC acquisition geometries. The method is amplitude-preserving, which means it removes the multiples without altering the primaries. A sensitivity analysis shows that the scheme is robust to moderate levels of noise, and to errors in the input parameters.

For a three-dimensional earth, expressing the upgoing wave in terms of the reflection response and the downgoing waves results in a set of simultaneous equations whose unknowns form the three-dimensional reflection response. The formulation is the same in 2D and 3D. Using accurate synthetic seismograms calculated for line diffractors in an acoustic background velocity (Taylor, 2000), the multiple removal scheme has been tested in two dimensions. The equations are solved in 2D by a direct solve $LU$ decomposition, for both towed streamer and OBC geometeries. The solution is very fast because it proceeds in the

frequency-wavenumber domain (of the order of hours for the examples given), and it successfully removes the diffracted multiples. These multiples represent the most difficult multiple energy to remove because it travels in all directions at once. The method preserves the amplitude of primaries. A small residual first-order multiple exists in the multiple-free data which is due to the data being of limited spatial extent, and thus does not sample the diffracted energy completely. To be able to handle more data requires a parallel implementation of the multiple removal algorithm. The non-physical artefacts produced in the solution can also be examined more thoroughly with a parallel implementation.

For the future, there is much work still to be done. The first step is to be able to handle more data with bigger computers, hence parallelisation. Different methods of solution to the simultaneous equations should be examined for their relative stabilities, in the presence of non-ideal data, and in the presence of noise. Although the method is extremely fast in the frequency-wavenumber domain, it may be useful to examine other domains of solution. Once this has been achieved, and an algorithm capable of handling large quantities of data is available, then all the work related to the source measurements can be incorporated into the scheme. The examples here are only for 2D, but of course the world is 3D. Current acquisition technology is not capable of collecting the data with proper spatial sampling. However, with the move in the industry from receiver groups to single receiver recording, marine OBC data will be available in the near future which will solve the spatial sampling problems. Once suitably sampled real data are available, the difficult task of working with real data can be attempted.

# REFERENCES


Achenbach, J. D., 1973, Wave propagation in elastic solids: Elsevier Science Publishers B.V., Amsterdam, The Netherlands.

Aki, K., and Richards, P. G., 1980, Quantitative seismology, theory and methods: W. H. Freeman and company, New York NY, USA.

Alterman, Z. S., and Karal, F., 1968, Propagation of elastic waves in layered media by finite difference methods: Bull. seism. Soc. Am., **58**, 367–398.

Backus, M. M., 1959, Water reverberations—their nature and elimination: Geophysics, **24**, 233–261.

Barr, F. J., and Sanders, J. I., 1989, Attenuation of water-column reverberations using pressure and velocity detectors in a water-bottom cable: 59th Ann. Internat. Mtg., Soc. Expl. Geophys., Expanded abstracts, 653–656.

Båth, M., 1968, Mathematical aspects of seismology: Elsevier Publishing Company, Amsterdam, The Netherlands.

Berkhout, A. J., and Verschuur, D. J., 1997, Estimation of multiple scattering by iterative inversion, Part I: Theoretical considerations: Geophysics, **62**, 1586–1595.

Berkhout, A. J., 1982, Seismic Migration: Imaging of Acoustic Energy by Wavefield Extrapolation. A. Theoretical Aspects (2nd Edition): Elsevier Science Publishers B.V., Amsterdam, The Netherlands.

Beylkin, G., 1987, Discrete Radon transform: IEEE Trans. Acoust., Speech and Signal Proc., **ASSP-35**, no. 2, 162–172.

Brekhovskikh, L., and Goncharov, V., 1984, Mechanics of continua and wave dynamics: Springer-Verlag, Berlin, Germany.

Bulat, J., 1993, WESTLINE Deep Seismic Survey: Operations Report to BIRPS, Cambridge: British Geological Survey Technical Report WB/93/37C.

Bullen, K. E., 1963, Theory of seismology: Cambridge University Press, Cambridge, UK, 3rd edition.

Burg, K. E., Ewing, M., Press, F., and Stulken, E. J., 1951, A seismic wave guide phenomenon: Geophysics, **16**, 594–612.

Carvalho, P. M., and Weglein, A. B., 1994, Wavelet estimation for surface elimination using a simulated annealing algorithm: 64th Ann. Internat. Mtg., Soc. Expl. Geophys., Expanded abstracts, 1481–1484.

Carvalho, P. M., Weglein, A. B., and Stolt, R. H., 1991, Examples of a nonlinear inversion method based on the T matrix of scattering theory: Application to multiple suppression: 61st Ann. Internat. Mtg., Soc. Expl. Geophys., Expanded abstracts, 1319–1322.

Carvalho, P. M., Weglein, A. B., and Stolt, R. H., 1992, Nonlinear inverse scattering for multiple suppression: Application to real data. Part I: 62th Ann. Internat. Mtg., Soc. Expl. Geophys., Expanded abstracts, 1093–1095.

Claerbout, J. F., 1976, Fundamentals of geophysical data processing: McGraw-Hill, New York NY, USA.

Cole, R. H., 1948, Underwater explosions: Princeton University Press, Princeton NJ, USA.

De-La-Vallée-Poussin, C.-J., 1938, Cours d'analyse infinitésimale, 1: Gauthier-Villars, Paris, France.

Deregowksi, S. M., 1971, Optimal digital filtering and inverse filtering in the frequency domain: Geophysical Prospecting, **19**, 729–768.

Deregowksi, S. M., 1978, Self-matching deconvolution in the frequency domain: Geophysical Prospecting, **26**, 252–290.

Dragoset, W. H., and Jeričević, Ž., 1998, Some remarks on surface multiple attenuation: Geophysics, **63**, no. 2-supplement, 772–789.

Dragoset, B., and Mackay, S., 1993, Surface multiple attenuation and sub-salt imaging: Exploration Geophysics, **24**, 463–472.

Dragoset, B., Hargreaves, N., and Larner, K., 1987, Air-gun nsource instabilities: Geophysics, **52**, 1229–1251.

Dragoset, W. H., 1993, Surface multiple elimination—theory, practical issues, examples: 55th Conference and Exhibition, European Assoc. Expl. Geophys., Expanded abstracts, B027.

Dragoset, B., 1999, A practical approach to surface multiple attenuation: The Leading Edge, **18**, 104–108.

Ewing, J., and Zaunere, R., 1964, Seismic profiling with a pneumatic sound source: J. Geophys. Res., **69**, 4913–4915.

Ewing, W. M., Jardetzky, W. S., and Press, F., 1957, Elastic waves in layered media: McGraw-Hill, New York NY, USA.

Fokkema, J. T., and van den Berg, P. M., 1990, Removal of surface-related wave phenomena: The marine case: 60th Ann. Internat. Mtg., Soc. Expl. Geophys., Expanded abstracts, 1689–1692.

Fokkema, J. T., and van den Berg, P. M., 1993, Seismic applications of acoustic reciprocity: Elsevier Science Publishers B.V., Amsterdam, The Netherlands.

Fokkema, J. T., and Ziolkowski, A., 1987, The critical reflection theorem: Geophysics, **52**, 965–972.

Foster, D. J., and Mosher, C. C., 1992, Suppression of multiple reflections using the Radon transform: Geophysics, **57**, 386–395.

Fricke, J. R., Davis, J. M., and Reed, D. H., 1985, A standard quantitative calibration procedure for marine seismic data: Geophysics, **50**, 1525–1532.

Fuchs, K., and Müller, G., 1971, Computation of synthetic seismograms with the reflectivity method and comparison with observations: Geophys. J. R. astr. Soc., **23**, 417–433.

Gilbert, F., and Backus, G. E., 1966, Propagator matrices in elastic wave and vibrational problems: Geophysics, **31**, 326–332.

Giles, B. F., and Johnston, R. C., 1973, System approach to air-gun array design: Geophys. Prosp., **21**, 77–101.

Giles, B. F., 1968, Pneumatic acoustic energy source: Geophys. Prosp., **16**, 21–53.

Golub, G. H., and Loan, C. F. V., 1996, Matrix computations: John Hopkins University Press, Baltimore MY, USA.

Goupillaud, P. L., 1961, An approach to inverse filtering of near-surface layer effects from seismic records: Geophysics, **26**, 754–760.

Haggerty, P. E., 1954, Method and apparatus for cancelling reverberations in water layers: U. S. Patent 2 757 356.

Hampson, D., 1986, Inverse velocity stacking for multiple elimination: Journal of the Canadian Soc. Expl. Geophys., **22**, 44–55.

Hartley, B. M., Uren, N. F., and Lamont, M. G., 1998, 3-D multiple moveout wavefield transformation for pre-conditioning data for the removal of water bottom multiples: 68th Ann. Internat. Mtg., Soc. Expl. Geophys., Expanded abstracts, 1252–1255.

Haskell, N. A., 1950, The dispersion of surface waves on multilayered media: Bull. seism. Soc. Am., **43**, 17–34.

Ikelle, L. T., Roberts, G., and Weglein, A. B., 1997, Source signature estimation based on the removal of first-order multiples: Geophysics, **62**, 1904–1920.

Johnston, R., and Taylor, D., 1999, Results on synthetic data for a line source and a two-dimensional earth: Sea surface multiples consortium, Semi-Anuual report no. 3.

Johnston, R., and Ziolkowski, A., 1999, Benefits of source signature measurements for multiple removal in streamer and OBC data: 69th Ann. Internat. Mtg., Soc. Expl. Geophys., Expanded abstracts, 1346–1349.

Johnston, R., Taylor, D., and Ziolkowski, A., 1999, Results on synthetic data for a line source and a two-dimensional earth—Part 2: Sea surface multiples consortium, Semi-Anuual report no. 4.

Kelly, K. R., and Marfurt, K. J., 1990, Numerical modelling of seismic wave propagation: Society of Exploration Geophysicists, Tulsa OK, USA.

Kennett, B. L., 1979, The suppression of surface multiples on seismic records: Geophys. Prosp., **27**, 584–600.

Kennett, B. L. N., 1983, Seismic wave propagation in stratified media: Cambridge University Press, Cambridge, UK.

Klemperer, S., and Hobbs, R. W., 1991, The BIRPS atlas: deep seismic reflection profiles around the British Isles: Cambridge University Press, Cambridge, UK.

Knapp, R. T., Daily, J. W., and Hammitt, F. G., 1970, Cavitation: McGraw-Hill, New York NY, USA.

Koehler, K., Krey, T., and Wachholz, H., 1974, Cancelling multiple reflections by feedback: Geophys. Prosp., **22**, 652–666.

Kramer, F. S., Peterson, R. A., and Walter, W. C., 1968, Seismic Energy Sources 1968 Handbook: Bendix United Geophysical Corp., Pasadena CA, USA.

Kunetz, G., and d'Erceville, I., 1962, Sur certaines propriétés d'une onde acoustique plane de compression dans un milieu stratifié: Annales de Géophysique, **18**, 351–359.

Kunetz, G., and Fourman, J. M., 1968, Efficient deconvolution of marine seismic records: Geophysics, **33**, 412–423.

Lamb, H., 1923, The early stages of submarine explosion: Phil. Mag., **45**, 257–265.

Lamb, H., 1932, Hydrodynamics: Cambridge University Press, Cambridge, UK, 6th edition.

Lavergne, M., 1970, Emission by underwater explosions: Geophysics, **35**, 419–435.

Levin, F. A., and Shah, P. M., 1977, Peg-leg multiples and dipping reflectors: Geophysics, **42**, 957–981.

Levy, S., and Stinson, K., 1986, Separation of up and downgoing waves from pressure measurements on a single plane: 56th Ann. Internat. Mtg., Soc. Expl. Geophys., Expanded abstracts, 461–464.

Lokshtanov, D., 1995, Multiple suppression by single and multichannel deconvolution: 65th Ann. Internat. Mtg., Soc. Expl. Geophys., Expanded abstracts, 1482–1485.

Love, A. E. H., 1927, A treatise on the mathematical theory of elasticity: Cambridge University Press, Cambridge, UK, 4th edition.

Lugg, R., 1979, Marine Seismic Sources, *in* Fitch, A. A., Ed., Developments in Geophysical Exploration Methods—1: Applied Science Publishers, 143–203.

Lunde, N., Peebles, B., and Walker, L., 1995, On-line estimation of the seismic source signature on a shot-by-shot basis: 57th Ann. Internat. Mtg., European Assoc. Expl. Geophys., Expanded Abstracts, B028.

Matson, K., 2000, An overview of wavelet estimation using free-surface multiple removal: The Leading Edge, **19**, 50–55.

Mayne, W. H., 1950, Seismic surveying: U. S. Patent 2 732 906 (application 1950).

Mayne, W. H., 1962, Common reflection point horizontal data stacking techniques: Geophysics, **27**, 927–938.

Monk, D. J., 1990, Wavefield separation of twin streamer data: First Break, **8**, 96–104.

Moretun, R., 1995, Tales from early UK oil exploration, 1960-1970: Petroleum Exploration Society of Great Britain, London, UK.

Morley, L., and Claerbout, J., 1983, Predictive deconvolution in shot-receiver space: Geophysics, **48**, 515–531.

Moses, H. E., 1956, Calculation of scattering potential from reflection coefficients: Phys. Rev., **102**, 559–567.

Osen, A., Amundsen, L., and Reitan, A., 1999, Removal of water-layer multiples from multicomponent sea-bottom data: Geophysics, **64**, 838–851.

Parkes, G. E., Ziolkowski, A. M., Hatton, L., and Haugland, T.-A., 1984, The signature of an air gun array: computation from near field measurements including interactions—practical considerations: Geophysics, **49**, 105–111.

Peacock, K. L., and Treitel, S., 1969, Predictive deconvolution: theory and practice: Geophysics, **34**, 155–169.

Rayleigh, L., 1917, On the pressure developed in a liquid during the collapse of a spherical cavity: Phil. Mag., **34**, 94–99.

Riley, D. C., and Claerbout, J. F., 1976, 2-D multiple reflections: Geophysics, **41**, 592–620.

Robinson, E. A., 1957, Predictive deconvolution of seismic traces: Geophysics, **22**, 767–778.

Rosenbaum, J. H., 1974, Synthetic microseismograms: Logging in porous formations: Geophysics, **39**, 14–32.

Ross, W. S., and Shah, P. M., 1987, Vertical seismic profile reflectivity: Ups over downs: Geophysics, **52**, 1149–1154.

Ryu, J. V., 1982, Decomposition (DECOM) approach applied to wave-field analysis with seismic reflection records: Geophysics, **47**, 869–883.

Sabel, P., Brink, M., Eidsvig, S., and Jensen, L., 1998, The source signature estimator—system improvements and applications: NPF seminar—"Integrated geophysical techniques in seismic interpretation", Papers and summaries.

Sacks, P., 1993, BIRPS/BGS Rockall survey: Far-field acquisition report: Digicon technical report.

Schneider, W. A., Prince, E. R., and Giles, B. F., 1965, A new data-processing technique for multiple attenuation exploiting differential normal moveout: Geophysics, **30**, 348–362.

Silverman, D., and Sparks, N. R., 1965, Some experiments on multiple reflection cancellation: Geophysics, **30**, 1085–1093.

Sommerfeld, A., 1909, Über die Ausbreitung der Wellen in der drahtlosen Telegraphie: Ann. Physik, **28**, 665–736.

Sonneland, L., Berg, L. E., Eidsvig, P., Haugen, A., Fontland, B., and Vestby, J., 1986, 2D deghosting using vertical receiver array: 56th Ann. Internat. Mtg., Soc. Expl. Geophys., Expanded abstracts, 516–519.

Stoffa, P. L., and Ziolkowski, A., 1983, Seismic source decomposition: Geophysics, **48**, 1–11.

Taner, M. T., and Koehler, F., 1977, Direct and inverse problems relating reflection coefficients and reflection response for horizontally layered media: Geophysics, **42**, 1199–1206.

Taner, M. T., Doherty, R. F. O., and Koehler, F., 1995, Long period multiple suppression by predictive deconvolution in the *x-t* domain: Geophys. Prosp., **43**, 433–468.

Tatham, R. H., Noponen, I., and Keeney, J. W., 1983, Application of the tau-p transform (slant stack) in processing seismic reflection data: ASEG/PESA symposium on petroleum geophysics—Its roll in Australia's energy future, Australian Soc. Expl. Geophys., Papers and summaries, 163–172.

Tatham, R. H., 1989, Tau-p filtering, *in* Stoffa, P. L., Ed., Tau-p, a plane wave approach to the analysis of seismic data: Kluwer Academic Publishers, 386–395.

Taylor, D. B., and Johnston, R. G. K., 1999, Synthetic seismograms for testing multiple removal algorithms: 62nd Ann. Internat. Mtg., Soc. Expl. Geophys., Expanded abstracts, 1346–1349.

Taylor, D. B., 2000, Fast 2D synthetic seismograms for testing multiple-removal algorithms: Geophysical Prospecting, accepted for publication.

Thomson, W. T., 1950, Transmission of elastic waves through a stratified solid medium: J. App. Phys., **21**, 89–93.

Thorson, J. R., and Claerbout, J. F., 1985, Velocity-stack and slant-stack stochatic inversion: Geophysics, **50**, 2727–2741.

Treitel, S., and Robinson, E. A., 1966, Seismic wave propagation in layered media in terms of communication theory: Geophysics, **31**, 17–32.

Trilling, L., 1952, The collapse and rebound of a gas bubble: J. Appl. Phys., **23**, 14–17.

Ursin, B., 1983, Review of elastic and electromagnetic wave propagation in horizontally layered media: Geophysics, **48**, 1063–1081.

van Borselen, R. G., Fokkema, J. T., van den Berg, P. M., van der Weiden, R. M., and Tan, T. H., 1994, A modified conjugate gradient method for minimising the energy in the removal of free-surface-related wavefields: Journal of seismic exploration, **3**, 351–363.

van Borselen, R. G., Fokkema, J. T., and van den Berg, P. M., 1996, Removal of surface-related wave phenomena—The marine case: Geophysics, **61**, 202–210.

Verschuur, D. J., and Berkhout, A. J., 1997, Estimation of multiple scattering by iterative inversion, Part II: Practical aspects and examples: Geophysics, **62**, 1596–1611.

Verschuur, D. J., Hermann, P., Kinneging, K. A., Wapenaar, C. P. A., and Berkhout, A. J., 1988, Elimination of surface-related multiply reflected and converted waves: 58th Ann. Internat. Mtg., Soc. Expl. Geophys., Expanded abstracts, 1017.

Verschuur, D. J., Berkhout, A. J., and Wapenaar, C. P. A., 1989, Wavelet estimation by prestack multiple elimination: 59th Ann. Internat. Mtg., Soc. Expl. Geophys., Expanded abstracts, 1129–1132.

Verschuur, D. J., Berkhout, A. J., and Wapenaar, C. P. A., 1992, Adaptive surface-related multiple elimination: Geophysics, **57**, 1166–1177.

Verschuur, D. J., 1991, Surface-related multiple elimination, an inversion approach: Ph.D. thesis, Delft University of Technology.

Watson, R. J., 1965, Decomposition and supression of multiple reflections: Geophysics, **30**, 54–71.

Weglein, A. B., Gasparatto, F. A., Carvalho, P. M., and Stolt, R. H., 1997, An inverse scattering series method for attenuating multiples in seismic reflection data: Geophysics, **62**, 1975–1989.

Weyl, H., 1919, Ausbreitung elektromagnetischer Wellen über einen ebenen Leiter: Ann. Physik, **60**, 481–500.

Wiggins, J. W., 1988, Attenuation of complex water-bottom multiples by wave-equation-based prediction and subtraction: Geophysics, **53**, 1527–1539.

Willis, H. F., 1941, Underwater exposions, time interval between successive explosions: British Report, **WA-47-21**.

Ziolkowski, A. M., and Johnston, R. G. K., 1997, Marine seismic sources: QC of wavefield computation from near-field pressure measurements: Geophysical Prospecting, **45**, 611–639.

Ziolkowski, A., and Johnston, R., 1998, Measurement of air-gun bubble oscillations: experiment to test the method on real data: Geophysics, **63**, 2018–2024.

Ziolkowski, A. M., Parkes, G. A., Hatton, L., and Haugland, T.-A., 1982, The signature of an air gun array: computation from near field measurements including interactions: Geophysics, **47**, 1413–1421.

Ziolkowski, A. M., Parkes, G. A., Hatton, L., and Haugland, T.-A., 1984, U. S. Patent 4 476 553.

Ziolkowski, A., Underhill, J. R., and Johnston, R. G. K., 1998, Wavelets, well ties, and the search for subtle stratigraphic traps: Geophysics, **63**, 297–313.

Ziolkowski, A., Johnston, R. G. K., and Underhill, J. R., 1999, Reply to discussion on "Wavelets, well ties, and the search for subtle stratigraphic traps" by R. E. White and R. Simm: Geophysics, **64**, 640–649.

Ziolkowski, A. M., Taylor, D. B., and Johnston, R. G. K., 1999, Marine seismic wavefield measurement to remove sea surface multiples: Geophysical Prospecting, **47**, 841–870.

Ziolkowski, A., 1970, A method for calculating the output pressure waveform from an air gun: Geophys. J. R. astr. Soc., **21**, 137–161.

Ziolkowski, A., 1982, An airgun model which includes heat transfer and bubble interactions: 52nd Ann. Internat. Mtg., Soc. Expl. Geophys., Expanded Abstracts, 187–189.

Ziolkowski, A., 1984, Deconvolution: International Human Resources Development Corporation, Boston MA, USA.

Ziolkowski, A., 1987, The determination of the far-field signature of an interacting array of marine seismic sources from near-field measurements—results from the Delft Air Gun Experiment: First Break, **5**, 15–29.

Ziolkowski, A., 1998, Measurement of air-gun bubble oscillations: Geophysics, **63**, 2009–2018.

Ziolkowski, A., 1999, "Zero-field" air-gun measurements for improved efficiency in marine acquisition: 69th Ann. Internat. Mtg., Soc. Expl. Geophys., Expanded Abstracts, 601–604.

# IMPLEMENTATION ISSUES

## *Appendix A*

### A.1 Complex frequency

Defining the frequency as complex has two effects: (1) It attenuates temporal wraparound, caused by carrying out multiplications in the frequency domain which correspond to temporal convolutions; (2) Operations involving the vertical wavenumber $k_z$ are more stable, producing less noise in time and space.

This is a trick used in synthetic seismogram computation and is described by Rosenbaum (1974). It is a useful device when processing data in the frequency-domain, and is included here for completeness. Multiplying a trace by an exponential decay, $\exp(-\alpha t)$, results in a Fourier transform of the trace which is evaluated just off the real axis, with a complex frequency $\omega = \omega' + i\alpha$.

Consider the Z-transform of a causal discrete time series $a(t)$,

$$A(Z) = \sum_t^n a_t Z^t = a_0 + a_1 Z + a_2 Z^2 + a_3 Z^3 + \cdots + a_n Z^n, \tag{A.1}$$

where the $a_t$ are the filter coefficients, and $Z$ is the unit delay operator. Multiplying $a(t)$ by $e^{-\alpha t}$ gives

$$A(e^{-\alpha}.Z) = \sum_t^n e^{-\alpha t} a_t Z^t = a_0 + a_1 e^{-\alpha} Z + a_2 e^{-2\alpha} Z^2 + a_3 e^{-3\alpha} Z^3 + \cdots. \tag{A.2}$$

Substituting $Z = e^{i\omega'}$,

$$\begin{aligned} A(e^{-\alpha}.e^{i\omega'}) &= \sum_t^n a_t e^{-\alpha t} e^{i\omega' t} = a_0 + a_1 e^{-\alpha} e^{i\omega'} + a_2 e^{-2\alpha} e^{2i\omega'} + a_3 e^{-3\alpha} e^{3i\omega'} + \cdots \\ A(e^{i(\omega'+i\alpha)}) &= \sum_t^n a_t e^{i(\omega'+i\alpha)t} = a_0 + a_1 e^{i(\omega'+i\alpha)} + a_2 e^{2i(\omega'+i\alpha)} + a_3 e^{3i(\omega'+i\alpha)} + \cdots, \end{aligned} \tag{A.3}$$

which in continuous time is the Fourier transform of $a(t)$:

$$A(\omega) = \int_{-\infty}^{\infty} a(t) \exp(i\omega t) \mathrm{d}t, \tag{A.4}$$

where $\omega = \omega' + i\alpha$. The value of $\alpha$ is chosen such that ramp decays to 1% by the end of the

trace.

On transformation back to the time domain an exponential ramp must be applied to the trace to reverse the process.

## A.2 Complex wavefield extrapolator

Wavefield extrapolation may be performed by multiplying by the complex factor $\exp(\pm ik_z z)$ in the frequency-wavenumber domain. With real frequency, the vertical wavenumber is

$$k_z = \left( \frac{\omega^2}{c^2} - k_x^2 - k_y^2 \right)^{\frac{1}{2}}. \tag{A.5}$$

The behaviour of $k_z$ in the complex plane is shown in Figure A.1. The value of $k_z$ is either pure real or pure imaginary with an abrupt transition through zero between the two cases. The effect this has on the complex wavefield extrapolator for different parts of the frequency-wavenumber domain is described below.

For *positive* phase shifts, which with the sign convention used in this thesis corresponds with a time *delay*:

1. For $\frac{\omega^2}{c^2} > k_x^2 + k_y^2$ (propagating), $k_z$ is pure real and $\exp(+ik_z z)$ applies a simple phase shift.
2. For $\frac{\omega^2}{c^2} = k_x^2 + k_y^2$ (horizontally-travelling), $k_z$ is 0 and $\exp(+ik_z z)$ is 1. This is unstable when division by $k_z$ is required.
3. For $\frac{\omega^2}{c^2} < k_x^2 + k_y^2$ (evanescent), $k_z$ is pure imaginary and $\exp(+ik_z z) = \exp(-k_z z)$ applies an exponential decay, which is stable.

For *negative* phase shifts, which with the sign convention used in this thesis corresponds with a time *advance*:

1. For $\frac{\omega^2}{c^2} > k_x^2 + k_y^2$ (propagating), $k_z$ is pure real and $\exp(-ik_z z)$ applies a simple phase shift.
2. For $\frac{\omega^2}{c^2} = k_x^2 + k_y^2$ (horizontally-travelling), $k_z$ is 0 and $\exp(-ik_z z)$ is 1.
3. For $\frac{\omega^2}{c^2} < k_x^2 + k_y^2$ (evanescent), $k_z$ is pure imaginary and $\exp(-ik_z z) = \exp(+k_z z)$ applies an exponential gain, which is undesirable.

When complex frequency is introduced, by putting $\omega = \omega' + i\alpha$, the vertical wavenumber becomes

$$k_z = \left( \frac{(\omega' - \alpha)^2}{c^2} - k_x^2 - k_y^2 + i\frac{2\alpha\omega'}{c^2} \right)^{\frac{1}{2}}, \tag{A.6}$$

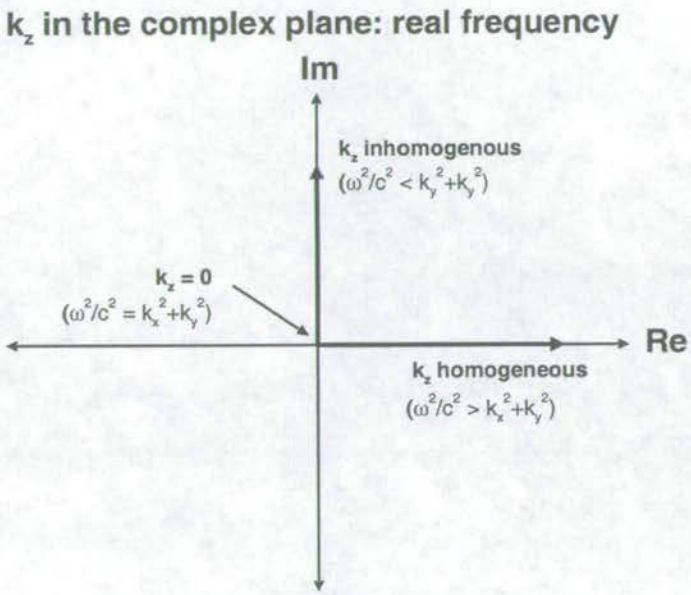


Figure A.1: $k_z$ in the complex plane for real frequencies.

which can be split up into the following real and imaginary parts

$$k_z = k_z^A + ik_z^B. \tag{A.7}$$

Factoring the complex $i$ out of the square root in equation (A.6) gives

$$k_z = i\left(k_x^2 + k_y^2 - \frac{(\omega' - \alpha)^2}{c^2} - i\frac{2\alpha\omega'}{c^2}\right)^{\frac{1}{2}}, \tag{A.8}$$

which can also be rewritten as a sum of real and imaginary parts

$$k_z = k_z^C + ik_z^D. \tag{A.9}$$

The behaviour of $k_z$ in the complex plane is shown schematically in Figure A.2 for three cases listed below. Note that the addition of a small imaginary part to the frequency moves $k_z$ off the real and imaginary axes and ensures that $k_z$ is never zero. This allows a smoother transition from propagating to evanescent waves. The effect on wavefield extrapolation is described below.

For *positive* phase shifts (time *delay*):

1. $\frac{(\omega'-\alpha)^2}{c^2} > k_x^2 + k_y^2$ (propagating), $k_z$ is complex and $\exp(+ik_z z) = \exp(+ik_z^A z)\exp(-k_z^B z)$

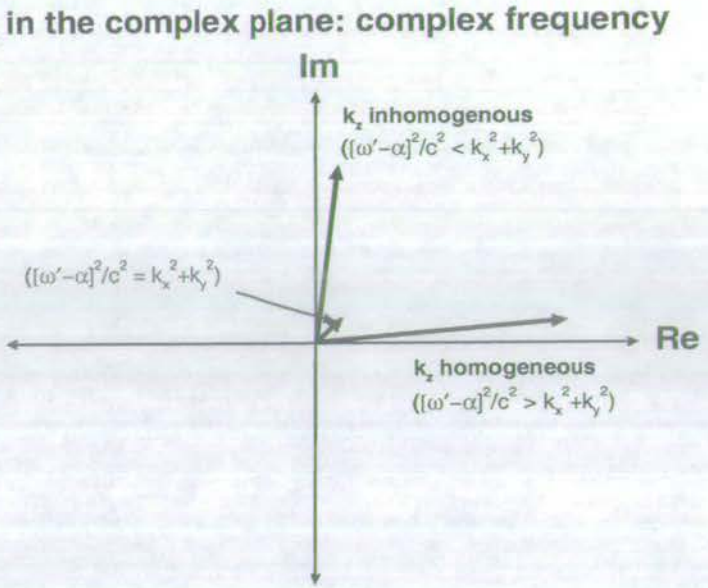


Figure A.2: $k_z$ in the complex plane for complex frequencies.

applies a phase shift and an exponential decay.

2. $\frac{(\omega'-\alpha)^2}{c^2} = k_x^2 + k_y^2$ (horizontally-travelling), $\exp(+ik_z z) = \exp(-k_z^B z)$ applies a small exponential decay.

3. $\frac{(\omega'-\alpha)^2}{c^2} < k_x^2 + k_y^2$ (evanescent), $k_z$ is complex and $\exp(+ik_z z) = \exp(+ik_z^C z)\exp(-k_z^D z)$ applies a phase shift and an exponential decay.

All of the three cases result in stable operators.

For *negative* phase shifts (time *advance*):

1. $\frac{(\omega'-\alpha)^2}{c^2} > k_x^2 + k_y^2$ (propagating), $\exp(-ik_z z) = \exp(-ik_z^A z)\exp(+k_z^B z)$ applies a phase shift and an exponential gain.

2. $\frac{(\omega'-\alpha)^2}{c^2} = k_x^2 + k_y^2$ (horizontally-travelling), $\exp(-ik_z z) = \exp(+k_z^D z)$ applies a small exponential gain.

3. $\frac{(\omega'-\alpha)^2}{c^2} < k_x^2 + k_y^2$ (evanescent), $\exp(-ik_z z) = \exp(-ik_z^C z)\exp(+k_z^D z)$ applies a phase shift and an exponential gain.

Negative phaseshifts apply an exponential gain to all the waves which is unstable.

# THEORY OF CONSTRUCTED ANALYTICAL MODELS, AFTER TAYLOR (2000)

*Appendix B*

A brief explanation follows on the theory of constructed analytical models (Taylor, 2000), derived for testing multiple removal algorithms and used in chapter 8. This theory allows fast exact 2D synthetic seismograms to be modelled in the frequency-space domain. Although the seismograms do not represent the real earth, they possess the important property of being constructed with 2D solutions of the linear acoustic wave equation. This makes them a suitable test for any multiple removal scheme which honours the same linear acoustic wave equation. Line diffractors in an acoustic background medium are represented as secondary sources, using scaled solutions of the primary monopole line source signature. Hence the term, constructed analytical models.

## B.1 The basic model

The general description of the constructed analytical models as a function of angular frequency ($\omega$) is

$$P(x,z,\omega) = P^{inc} + \sum_{i=1}^{N} C_i(\omega) P_i^{scat}, \tag{B.1}$$

where $P(x,z,\omega)$ is the pressure at a receiver in response to an incident pressure from the monopole line source $P^{inc}$ (the direct wave), plus the scattered pressures $P_i^{scat}$ derived from $N$ secondary sources at $(x_i, z_i)$. This description is the same whether the sea surface is present or not. In the former, the incident pressure includes the sea surface (ghost) reflection, and the $N$ secondary sources are divided between $D = N/2$ sources below the sea surface, and $D = N/2$ images of these, at points $i' = i + D$, above the sea surface.

The $C_i(\omega)$ linearly relate the pressures from the secondary sources to the incident pressure. They can be thought of as the strengths of the diffractors, in much the same way as a reflector is defined by a reflection coefficient. They are frequency-dependent because they need to account for the interference, or feedback, which occurs between diffractors (free surface and internal diffracted multiples). In the presence of the sea surface the zero pressure condition at

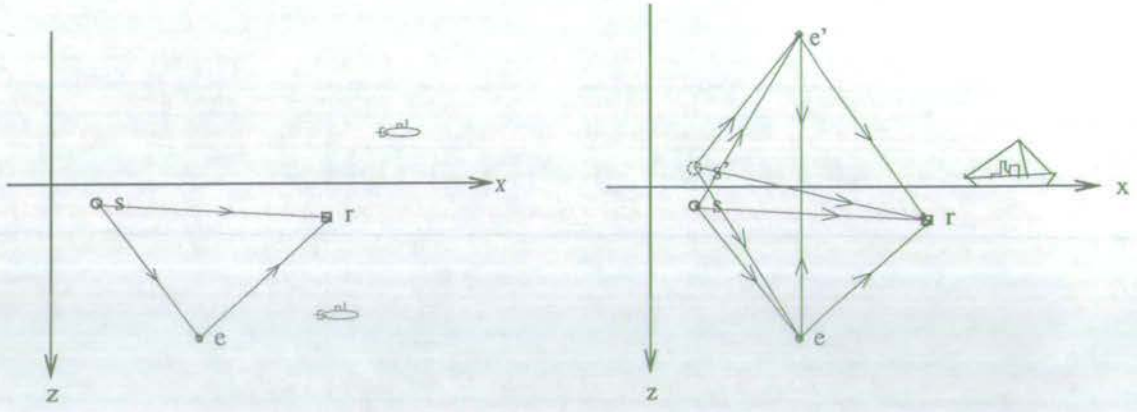


(a) A full-space of water

(b) A half-space of water

Figure B.1: Locations of the sources, diffractors and receivers. The arrows indicate the direction of propagation (After Taylor & Johnston (1999)).

the surface requires $C_{i'}(\omega) = -C_i(\omega)$.

The pressure at a distance $R$ from a monopole line source is defined in the frequency domain as

$$P(x,z,\omega) = -i\pi\omega^2\rho {H_0}^2\left(\frac{\omega R}{\alpha}\right), \tag{B.2}$$

where $\alpha$ is the velocity of the wave and $\rho$ is the density of the medium in which it propagates. This solution to the acoustic wave equation is used as the basic element to build up the constructed analytical models.

## B.2 A single line diffractor

Introducing a single line diffractor at a point $e(x_e, z_e)$, characterised by $\mathsf{e}(t)$ which is proportional to the incident pressure, and a delta-function monopole line source at $s(x_s, z_s)$ in a full-space of water, a hydrophone receiver at $r(x_r, z_r)$ records the following (as a function of frequency)

$$P(x_r, z_r, \omega) = P^{rs} + P^{re}EP^{es}, \tag{B.3}$$

where $P^{rs}$ is shorthand for $P(x_r - x_s, z_r - z_s)$ and indicates propagation from $s$ to $r$, all frequency dependence is assumed implicitly by the uppercase characters, and $E$ is the frequency-domain equivalent of $\mathsf{e}(t)$. This is illustrated by the cartoon in Figure B.1(a). A comparison of equation (B.3) with the general expression (B.1) shows that $C = EP^{es}$.

When a free surface is introduced at $z = 0$, there necessarily is now an image source at

$s'(x_s, -z_s)$ and an image diffractor at $e'(x_e, -z_e)$. To ensure that the pressure is zero at the surface, the signals at the images $s'$ and $e'$ must be equal in size and opposite in polarity to those at $s$ and $e$, respectively. Reasoning that both the diffractor and its image act as secondary sources whose strengths are related to the pressure which arrives at the diffractor position $e$, Taylor (1999) writes for the pressure at the diffractor

$$P^e = P^{es} - P^{es'} - P^{ee'} E P^e, \tag{B.4}$$

where the diffractor's own pressure has been omitted. The interference produced by the sea surface is represented by the appearance of the pressure at the diffractor $P^e$ on both sides of the equation. The first two terms on the right-hand side of equation (B.4) are the direct wave from the source to the diffractor plus the source ghost. Rearranging this expression, the multiple-generating factor due to the sea surface is obvious as the denominator

$$P^e = \frac{P^{es} - P^{es'}}{1 + E P^{ee'}}. \tag{B.5}$$

The pressure at the receiver is now constructed in the same way as the pressure at the diffractor in equation (B.4),

$$P(x_r, z_r, \omega) = P^{rs} - P^{rs'} + (P^{re} - P^{re'}) G (P^{es} - P^{es'}), \tag{B.6}$$

where $G = E[1 + E P^{ee'}]^{-1}$. This is illustrated by the cartoon in Figure B.1(b). By comparison with equation (B.3), the pressure arriving at the diffractor in the wholespace case $P^{es}$, has now been replaced in equation (B.6) by the more complicated expression $P^e$ given by equation (B.5).

Similar expressions may be derived for particle velocity at the receiver.

## B.3 Many line diffractors

A similar analysis has been carried out by Taylor (1999) for many line diffractors. The equations (B.3)-(B.6) have counterparts in the many diffractors-case with similar terms, but they are composed of vectors and matrices instead of scalars. In the case of no free surface, equation (B.3) becomes

$$P^r = P^{rs} + (\underline{P}^{re})^T \mathsf{F} \underline{P}^{es}, \tag{B.7}$$

where $\mathsf{F} = \mathsf{E}[\mathsf{I} - \mathsf{A}\mathsf{E}]^{-1}$, and $\mathsf{E}$ is a diagonal matrix describing the $E_i(\omega)$. The $D$ by $D$ matrix $\mathsf{A}$ is composed of the pressures arriving at each diffractor from every other diffractor, so that the diagonal $i = j$ is zero, and each $(j,i)$th element is $P^{ji}(\omega)$, for $i \neq j$.

When the free surface is present, equation (B.6) becomes

$$P^r = P^{rs} - P^{rs'} + (\underline{P}^{re} - \underline{P}^{re'})^T \mathsf{M}(P^{es} - P^{es'}), \tag{B.8}$$

where $\mathsf{M} = \mathsf{E}[\mathsf{I} - \mathsf{AE} + \mathsf{BE}]^{-1}$. Matrix B introduces the interactions with the image diffractors at the locations $e_{i'}$, and each $(j,i)$th element is $P^{ji'}(\omega)$.

PETEX98 PAPER

*Appendix C*

# Multiple wavefields: separating incident from scattered, up from down, and primaries from multiples.

Presented at PETEX98, "Scaling the peaks", 1-3 December 1998,
Business Design Centre, London

Paper requested by PESGB
for publication on CD-ROM of best papers.

# Multiple wavefields: separating incident from scattered, up from down, and primaries from multiples

Rodney Johnston, Anton Ziolkowski and David Taylor

Presented at PETEX98, "Scaling the peaks", 1-3 December 1998, Business Design Centre, London.

Selected in "Top 10 best presentations" for publication on CD-ROM by PESGB, 1999.


Centre for Reservoir Geoscience, The University of Edinburgh,
Department of Geology & Geophysics, The Grant Institute,
West Mains Road, Edinburgh EH9 3JW

e-mail: Rodney.Johnston@glg.ed.ac.uk

## Multiple wavefields: separating incident from scattered, up from down, and primaries from multiples

Rodney Johnston, Anton Ziolkowski and David Taylor,
Centre for Reservoir Geoscience, The University of Edinburgh

### Summary
We present examples of a multiple removal scheme which formulates the problem using the concept of the earth's reflection response, defined essentially as the ratio of the upgoing wave to the downgoing wave. We show synthetic examples for a one-dimensional earth which demonstrate that we can separate the upgoing waves from the downgoing waves, using either streamer or dual sensor synthetic data. Using these wavefields and the incident field, calculated from measurements of the source signature, we find the ratio of upgoing to downgoing waves in the frequency-wavenumber domain to yield multiple-free seismograms.

### Introduction
One of the most persistent problems today in marine seismic data analysis is the sea surface. The problem is illustrated schematically in Figure 1, where we show some ray paths travelling through a simplified earth, (a) in the presence of the sea surface, and (b) with the sea surface absent. Because the reflection coefficient at the sea surface is, for all practical purposes, -1, the interface between the air and water is a free surface where the pressure vanishes. All upgoing energy is reflected back down again, as sea surface multiple reflections, which interferes with the processing and interpretation of primary reflections. Processes such as migration and amplitude variation with offset (AVO) analysis assume that there are no multiple reflections. In areas of complex geology migration is increasingly being applied pre-stack and in depth, as opposed to in time, which means it is more difficult to obtain a well focused image and a reliable velocity structure if multiples are present. In the case of AVO, which seeks to detect subtle changes of reflection amplitude with offset, the presence of sea surface multiples severely limits the validity of any analysis.

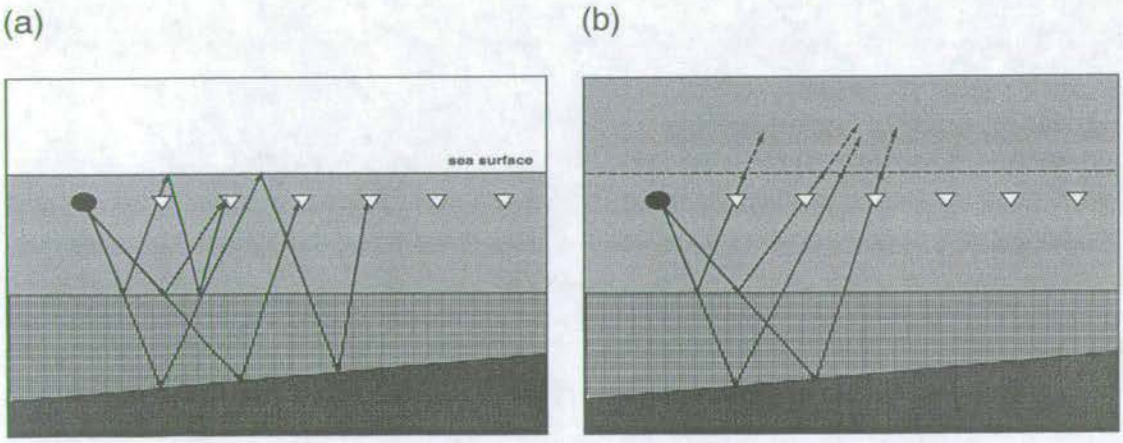


Figure 1: The problem of free surface multiple removal.

In recent years the literature has seen publication of several wave-theoretical approaches to the problem of free surface multiple elimination (Dragoset and MacKay, 1993, Fokkema and van den Berg, 1993, Berkhout and Verschuur, 1997, Verschuur and Berkhout, 1997, and Weglein et al., 1997). This work continues earlier studies on the wave-theoretical analysis of sea surface multiples and their removal (Riley & Claerbout, 1976, Kennett, 1979 and Berkhout, 1982). These methods, in principle, take account of the whole wavefield, in contrast to the more primitive methods of multiple attenuation based on moveout and periodicity which require relatively few data. Many of these wave-theoretical approaches developed to date use the data to *predict* the multiples, then use some kind of adaptive approach to *subtract* them from the recorded data. This is usually done iteratively to remove successively higher orders of multiples.

Unfortunately, the total recorded data comprise the incident field (direct plus ghost wave from sources to receivers) plus the scattered field. The multiple suppression algorithms require only the scattered field. Typically the part of the total field which includes the incident field is muted, removing part of the scattered field in the process. In addition, the theory requires that the source time function be known. These schemes are implemented such that any required knowledge of the source signature may be extracted in the form of an "effective wavelet" at the same time as suppressing the multiples (Riley & Claerbout, 1976; Verschuur, 1991). The effective wavelet is defined when the energy in the seismogram is a minimum; it is meant to account for both the source signature and any algorithmic deficiencies resulting from non-theoretically ideal acquisition conditions.

We present examples of an alternative method by Ziolkowski et al., (1998) wherein a full 3D wave-theoretical solution has been formulated. The problem of multiple elimination is solved by recovering the reflection response of the earth, by definition in the absence of the free surface. Our method deals with realistic extended (areal) sources, as opposed to point or dipole sources in the vicinity of the sea surface. It uses knowledge of the source time function at two stages in the formulation: to get the scattered field from the total field by subtracting the incident field; and in the construction of a downgoing plane wave.

The purpose of this paper is to present some synthetic examples for a one-dimensional stratified earth, to show that this concept works, at least in 1D. We begin by describing the concept of a plane wave reflection response in the frequency-wavenumber domain, first for a 1D earth with no sea surface, and progressing to a 3D earth with a free surface. Next, we go on to describe the processing steps necessary to calculate this response from marine seismic data. Finally, we give some examples for both towed streamer and ocean bottom cable (OBC) acquisition geometries using full-waveform synthetics.

**The plane wave reflection response**

Consider a plane wave propagating in a half-space of water above a horizontally-stratified medium, as shown in Figure 2(a). A downgoing incident wave, , is reflected from the stack of layers to create an upgoing scattered

wave, $U$. Both of these plane waves are characterised by a frequency, $\omega$, and wavenumbers, $k_x$ and $k_y$, which define the angle of propagation. The reflection response of this one-dimensional earth is defined in the frequency-wavenumber domain as

$$R(k_x,k_y,\omega)=\frac{U(k_x,k_y,\omega)}{I(k_x,k_y,\omega)}. \tag{1}$$

Note that, since there is no free surface, $U$ contains only primaries and internal multiples, and the division by $I$ essentially deconvolves for the source signature.

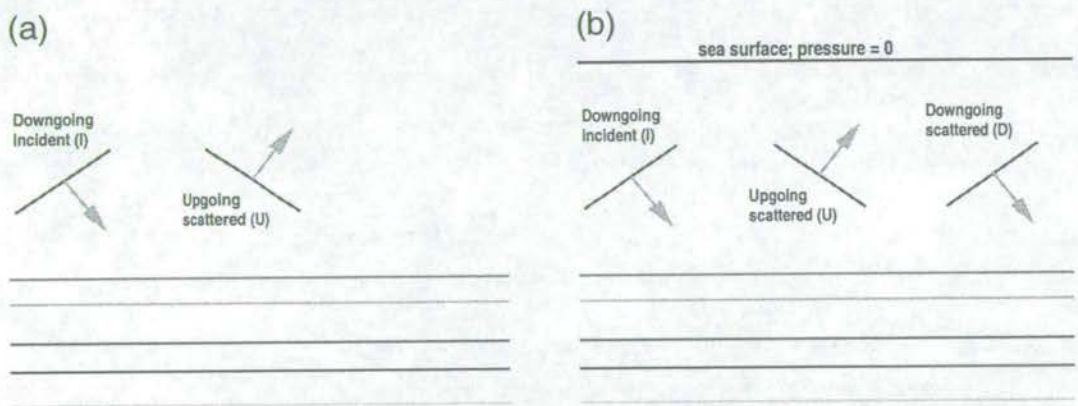


Figure 2: Plane waves propagating in a 1D earth.

When we introduce the free surface above the stack of layers, as depicted in Figure 2(b), we now have three types of plane waves in the water: The downgoing incident wave, $I$; the upgoing scattered wave, $U$; and now a downgoing scattered wave, $D$, which is the reflection of $U$ in the free surface. The reflection response is defined as

$$R(k_x,k_y,\omega)=\frac{U(k_x,k_y,\omega)}{I(k_x,k_y,\omega)+D(k_x,k_y,\omega)}. \tag{2}$$

Alternatively, we may express this as

$$U_i=R_i(I_i+D_i), \tag{3}$$

where the subscript $i$ denotes a unique combination of $(k_x,k_y,\omega)$. Because the earth is horizontally-stratified, Snell's law ensures that $i$ is the same for upgoing and downgoing plane waves. In this case, the scattered fields $U$ & $D$ both contain free-surface multiples, and recovering $R$ essentially deconvolves for the source signature while the multiples divide out.

Consider now the more complicated situation of a three-dimensional earth, with a plane wave propagating in a half-space of water, as shown in Figure 3(a). In this situation, the single downgoing incident wave $I$ is reflected by

the three-dimensional earth to yield a complicated upgoing scattered wave $U$. We assume that this non-plane scattered wave may be decomposed into plane wave components, $U_{ij}$, where the subscript $j$ denotes a unique combination of $(k_x^U, k_y^U, \omega)$, and, due to the discretisation of the data, ranges over $N$ discrete plane wave components. The superscript $^U$ on the wavenumber denotes upgoing waves which, in general, propagate with a different angle vis-à-vis the downgoing waves, except for the special case (see the 1D example above) where $i = j$. In the frequency-wavenumber domain the reflection response is defined as

$$U_{ij} = R_{ij}.I_i, \; j = 1,\ldots,N \,. \tag{4}$$

The reflection response is referred to a plane $z = z_w$ above the sea floor and below the source. The relationship between the upgoing and downgoing waves at this notional interface acts as a lower boundary condition to the problem. The 3D nature of the earth is obvious by comparison with the 1D case, since we need to recover $N$ plane wave reflection responses per incident wave. The upgoing scattered plane wave components contain only primaries and internal multiples, so recovering the $R_{ij}$ for the 3D earth once again essentially deconvolves for the source signature.

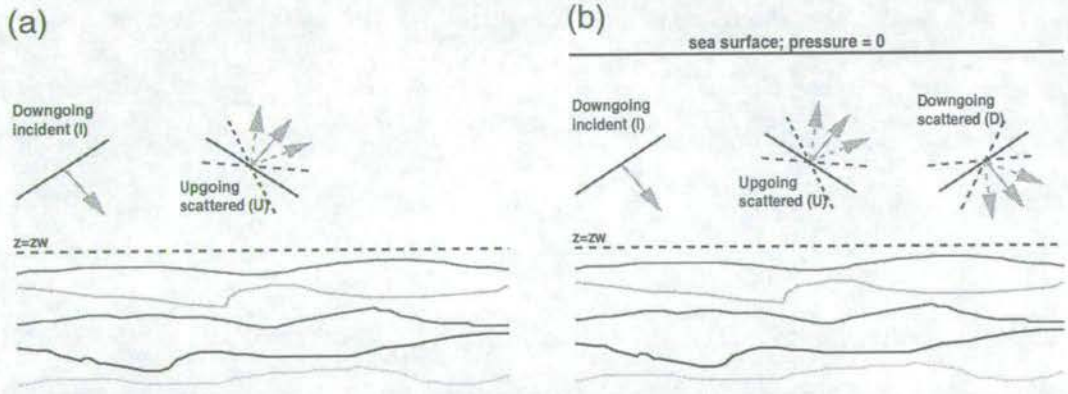


Figure 3: Plane waves propagating in a 3D earth.

When we introduce the free surface, we get a mixture of the previous two examples (Figure 3(b)). The downgoing incident wave is reflected from the 3D earth resulting in many upgoing scattered plane wave components $U_{ij}$, which are themselves reflected in the free surface, resulting in many downgoing scattered plane wave components $D_{ij}$. The reflection response is defined as

$$U_{ji} = R_{ji}.I_i + \sum_{k=1}^{N} R_{jk} D_{ki}, \; j = 1,\ldots,N \,, \tag{5}$$

where now we have fixed the upgoing wave, the $j$th of $N$ possible plane wave components, and we vary $i$ for all the possible downgoing incident plane waves, $i = 1,\ldots,N$. The subscript $i$ denotes a unique combination $(k_x^D, k_y^D, \omega)$,

and the superscript $^{D}$ on the wavenumber denotes downgoing waves. Considering a particular upgoing plane wave component, $j$, gives rise to a set of simultaneous equations which must be solved for the $R_{ji}$. Equations (5) may be rewritten in a matrix form, in which the structure is more obvious:

$$\begin{pmatrix} U_{j1} \\ U_{j2} \\ \vdots \\ U_{jN} \end{pmatrix} = \begin{pmatrix} I_1 + D_{11} & D_{21} & \cdots & D_{N1} \\ D_{12} & I_2 + D_{22} & \cdots & D_{N2} \\ \vdots & \vdots & \vdots & \vdots \\ D_{1N} & D_{2N} & \cdots & I_N + D_{NN} \end{pmatrix} \begin{pmatrix} R_{j1} \\ R_{j2} \\ \vdots \\ R_{jN} \end{pmatrix}. \qquad (6)$$

This is repeated for every upgoing plane wave component $j$. The 1D solution is found in the leading diagonal terms.

Figure 4(a) shows how we define downgoing wavenumbers by analysing receiver gathers, and reciprocally, Figure 4(b) shows how we define upgoing wavenumbers by analysing shot gathers. In both figures the closed circles represent source positions and the closed triangles represent receiver positions. The downgoing wavenumber is defined by the source interval, and the upgoing wavenumber is defined by the receiver interval (for 3D acquisition, in both $x$ and $y$).

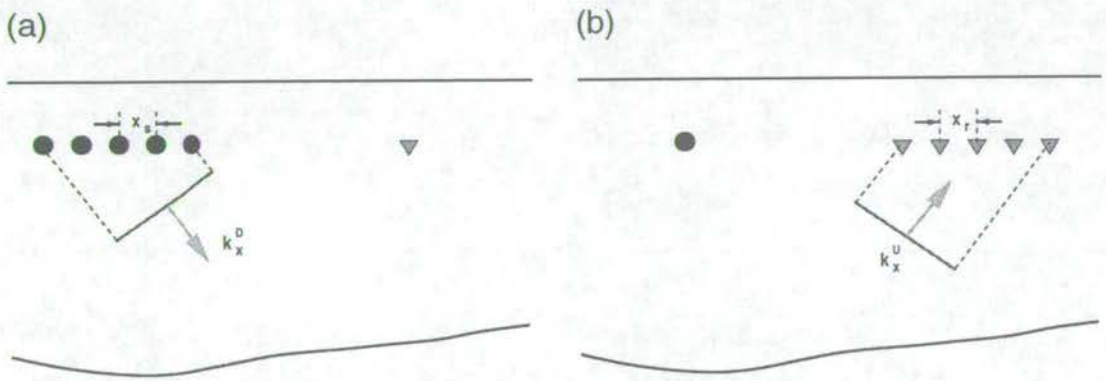


Figure 4: Defining wavenumbers in an up/down co-ordinate frame.

**Outline of the method**

In contrast to the recursive prediction-and-subtraction approach we calculate the multiple-free seismogram by computing the reflection response of the earth directly in the frequency-wavenumber domain, essentially as the ratio of the upgoing wavefield to the downgoing wavefield. The steps required to achieve this are summarised below:

1. Isolate the scattered field from the total field. This requires calculation of the incident field, using measurements of the source time function, so that it may be subtracted from the total field.

2. Construct the response of the earth to a plane wave. This requires ordering the data to common-receiver gathers and then transforming to frequency ($\omega$) and horizontal wavenumber ($k_x$ & $k_y$) to get plane wave

gathers. To each of these plane wave gathers two additional transforms are applied, over receiver coordinates, to get the frequency-wavenumber response of the earth to each plane wave.

3. Separate the transformed data into upgoing and downgoing waves using the condition that the pressure is zero at the free surface. If only pressure is available this involves deconvolution for the receiver ghost. If pressure and the vertical component of particle velocity are available this essentially involves an arithmetic combination of the two, but requires no information about the sea floor.

4. Express every upgoing plane wave component as the product of the incident plane wave with the reflection response plus a sum of the products of all the scattered downgoing plane wave components with their corresponding reflection responses. This gives rise to a set of simultaneous equations that must be solved for the reflection response for each upgoing plane wave.

5. Multiply an incident field, including the desired characteristics of an idealised source, with the reflection response, followed by transformation back to time and space and reordering.

**The Incident field**

The incident field is defined for these purposes by Ziolkowski et al. (1998) as that part of the wavefield which exists in the absence of the sea floor and the 3D earth below. This includes the reflection from the sea surface, and is calculated for a receiver location $(x_r, y_r, z_r)$ in response to a source placed at $(x_s, y_s, z_s)$. In the frequency-wavenumber domain it has the following form for one monopole source

$$\tilde{\tilde{I}}(k_x, k_y, z_r; z_s, \omega) = \frac{i}{2k_z} S(\omega)\left(\exp(ik_z \mid z_s - z_r \mid) - \exp(ik_z[z_s + z_r])\right), \qquad (7)$$

in which

$$k_z = \sqrt{\frac{\omega^2}{c^2} - k_x^2 - k_y^2}\,, \qquad (8)$$

$S(\omega)$ is the spectrum of the source signature, and we have assumed that the source is on the $z$-axis. The $i/2k_z$ factor is required to decompose the monopole source properly into plane waves. It is known as the "obliquity factor" from diffraction theory in optics. The two phase factors in brackets propagate the source signature to the correct location in space for the direct arrival and its ghost. We can accommodate areal sources and their associated anisotropic radiation patterns by making source signature measurements, and superposing the non-interacting "notional" monopole sources (Ziolkowski et al., 1982) which comprise the array. This would result in a summation over the many different $S(\omega)$ in equation (7), and additional

phase factors to reflect the relative positions of the different elements in the source array.

We subtract the incident field from the total field in the time-space domain to yield the scattered field. For the synthetic examples we present, we assume that this step has already been done by explicitly modelling the seismograms without the incident field. The right panel of Figure 5 shows an example of a calculated incident field when the source is near the surface and the receivers are on the sea bed. In this case the incident field is hyperbolic; were the receivers at the same depth as the source, the incident field would appear as a straight line in the time-space domain because the incident energy would be travelling horizontally. The left panel shows the scattered field only, modelled for a water layer over an elastic half-space, so that most of the events present are sea surface multiples. Normally a hydrophone would measure the sum of these two components, and subtraction of the incident field would be the first step.

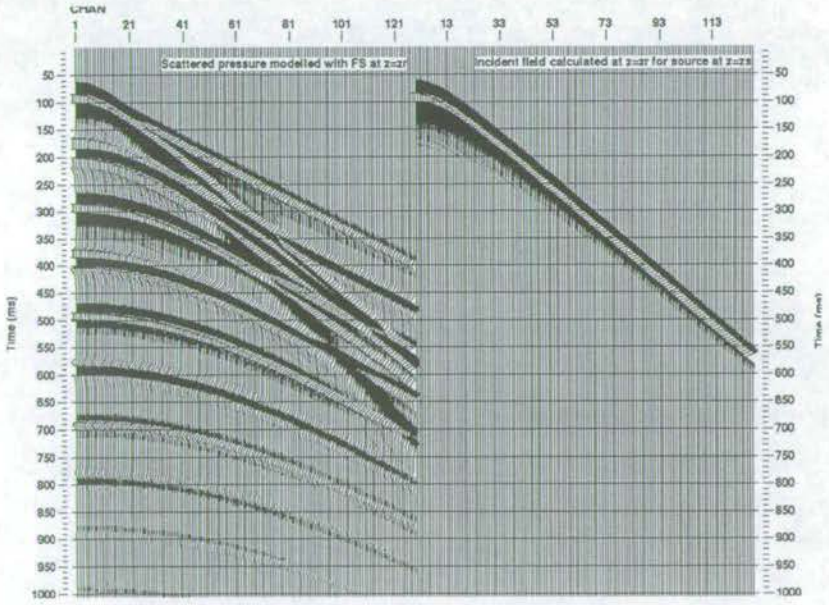


Figure 5: An example of incident and scattered fields separated.

**Response of the earth to plane waves**

The examples shown in this paper are for a one-dimensional earth model, and therefore all receiver gathers are the same. In this case the problem is greatly simplified since we are using a line source, and we simply need only transform to frequency and wavenumber. We adopt the convention that a pressure wavefield, $p(x_r, y_r, z_r; z_s, t)$, is recorded at a depth $z_r$, in response to a source at $z_s$. Applying a three-dimensional Fourier transform (over distance, $x$ & $y$, and time, $t$) we get

$$\tilde{\tilde{P}}(k_x, k_y, z_r; z_s, \omega) = \int_{-\infty}^{\infty}\int\int p(x_r, y_r, z_r; z_s, t)\exp\left(i[\omega t - k_x x_r - k_y y_r]\right)\mathrm{d}t\mathrm{d}x_r\mathrm{d}y_r. \qquad (9)$$

**Separation into upgoing and downgoing waves**

1) Pressure only (streamer):

If we have only hydrophone data we can extract the upgoing wave in the frequency-wavenumber domain by deconvolving for the receiver ghost, $1-\exp\left(ik_z[2z_r]\right)$. This factor becomes zero whenever $\exp\left(ik_z[2z_r]\right)$ equals +1, therefore, to remove the receiver ghost, we perform a stabilised division as follows

$$\tilde{\tilde{U}}^{scat}(k_x, k_y, z_r; z_s, \omega) = \frac{\tilde{\tilde{P}}^{scat}(k_x, k_y, z_r; z_s, \omega)\left[1-\exp\left(ik_z[2z_r]\right)\right]^*}{\left|1-\exp\left(ik_z[2z_r]\right)\right|^2 + \varepsilon}, \qquad (10)$$

where $^*$ indicates complex conjugation and $\varepsilon$ is a small real constant which ensures the denominator is never zero. The downgoing wave is obtained from the scattered field by subtracting the upgoing wave:

$$\tilde{\tilde{D}}^{scat}(k_x, k_y, z_r; z_s, \omega) = \tilde{\tilde{P}}^{scat}(k_x, k_y, z_r; z_s, \omega) - \tilde{\tilde{U}}^{scat}(k_x, k_y, z_r; z_s, \omega). \qquad (11)$$

2) Pressure and normal component of particle velocity (OBC):

If we have both hydrophone and the vertical component of particle velocity, as in dual sensor data, we can extract the upgoing and downgoing waves in the frequency-wavenumber domain using the following relations (Wapenaar & Berkhout, 1989)

$$2\tilde{\tilde{U}}^{scat}(k_x, k_y, z_r; z_s, \omega) = \tilde{\tilde{P}}^{scat}(k_x, k_y, z_r; z_s, \omega) - \frac{\rho\omega}{k_z}\tilde{\tilde{V}}_z^{scat}(k_x, k_y, z_r; z_s, \omega) \qquad (12)$$

$$2\tilde{\tilde{D}}^{scat}(k_x, k_y, z_r; z_s, \omega) = \tilde{\tilde{P}}^{scat}(k_x, k_y, z_r; z_s, \omega) + \frac{\rho\omega}{k_z}\tilde{\tilde{V}}_z^{scat}(k_x, k_y, z_r; z_s, \omega). \qquad (13)$$

Note that in doing so we require no properties of the sea floor, only the density and velocity of sound in the water.

**The reflection response of the whole earth**

In the case of a horizontally-stratified earth, the situation is greatly simplified from the general 3D case. Each upgoing plane wave component is simply the product of the incident plane wave with the reflection response plus the product of the downgoing wave with the reflection response.

$$\tilde{\tilde{U}}(k_x,k_y,z_r;z_s,\omega)=\tilde{\tilde{I}}(k_x,k_y,z_r;z_s,\omega).\tilde{\tilde{R}}(k_x,k_y,z_r;z_s,\omega)+ \\ \tilde{\tilde{D}}(k_x,k_y,z_r;z_s,\omega)\tilde{\tilde{R}}(k_x,k_y,z_r;z_s,\omega), \tag{14}$$

(in general, the second term on the right forms a summation over all possible downgoing scattered plane wave components, as described in equation (5)). Or, in other words, the reflection response of the whole earth is equal to the ratio of the upgoing wave to the downgoing wave:

$$\tilde{\tilde{R}}(k_x,k_y,z_r;z_s,\omega)=\frac{\tilde{\tilde{U}}(k_x,k_y,z_r;z_s,\omega)}{\tilde{\tilde{I}}(k_x,k_y,z_r;z_s,\omega)+\tilde{\tilde{D}}(k_x,k_y,z_r;z_s,\omega)}. \tag{15}$$

This division is stabilised in the same way as the division for the receiver ghost (equation (10)).

**Multiple-free seismograms**

An idealised incident field, $I_0$, with no ghost term is multiplied with the reflection response in the frequency-wavenumber domain to bandlimit it (both spatially, when areal sources are used, and temporally):

$$\tilde{\tilde{P}}_0(k_x,k_y,z_r;z_s,\omega)=\tilde{\tilde{I}}_0(k_x,k_y,z_r;z_s,\omega)\tilde{\tilde{R}}(k_x,k_y,z_r;z_s,\omega), \tag{16}$$

where

$$\tilde{\tilde{I}}_0(k_x,k_y,z_r;z_s,\omega)=\frac{i}{2k_z}Z(\omega)\left(\exp(ik_z\mid z_s-z_r\mid)\right), \tag{17}$$

and $Z(\omega)$ is some smooth desired wavelet spectrum. $Z(\omega)$ should be designed to have the same amplitude envelope as the original signature $S(\omega)$, as described in more detail in Ziolkowski et al., 1998, to improve resolution without sacrificing signal-to-noise ratio.

These data are then transformed back to time and space for easy interpretation:

$$p_0(x_r,y_r,z_r;z_s,t)=\left(\frac{1}{2\pi}\right)^3\int\int\int_{-\infty}^{\infty}\tilde{\tilde{P}}_0(k_x,k_y,z_r;z_s,\omega) \\ \exp\left(i[\omega t-k_x x_r-k_y y_r]\right)\mathrm{d}\omega\mathrm{d}k_x\mathrm{d}k_y \tag{18}$$

## Synthetic data examples

The data used to illustrate this scheme are computed over a layered elastic earth with the reflectivity method (Fuchs and Müller, 1971). The line source time function is a two-loop Ricker wavelet with a central frequency of 25 Hz (see Figure 6). The source depth is 7m and for the ocean bottom cable (OBC) geometry we calculated pressure and the vertical component of particle velocity at the acoustic/elastic interface at 75m depth. There are 128 receivers spaced 6.25m apart. The parameters for the layered earth are shown in Table 1.

| depth(m) | P-wave (m/s) | S-wave (m/s) | density (kg $m^3$) |
|---|---|---|---|
| 75 | 1500 | 0 | 1000 |
| 575 | 2000 | 1155 | 2200 |
| 1075 | 2500 | 1443 | 2150 |
| 1775 | 3000 | 1732 | 2200 |
| 2775 | 3500 | 2021 | 2200 |
| ∞ | 4000 | 2309 | 2400 |

Table 1: Earth parameters for the synthetic seismograms.

## Results

Figure 7 shows seismograms calculated for the OBC geometry with the free surface, for pressure and the vertical component of particle velocity. Figure 8 shows the upgoing and downgoing waves calculated using equations (12) & (13). Figure 9 shows a comparison of the seismogram modelled for pressure with no free surface alongside the result of processing the seismograms in Figure 6 to remove the multiples, following the procedure described above. Figures 10-12 show similar results for hydrophones only, where in this case the receivers are close to the surface as in streamer acquisition. Equations (10) & (11) were used to separate the waves shown in Figure 11. The agreement between modelled and processed synthetic data is very good for all reflected and refracted events. Moreover, there is little evidence of any multiple energy and the primary information is not affected by this procedure.

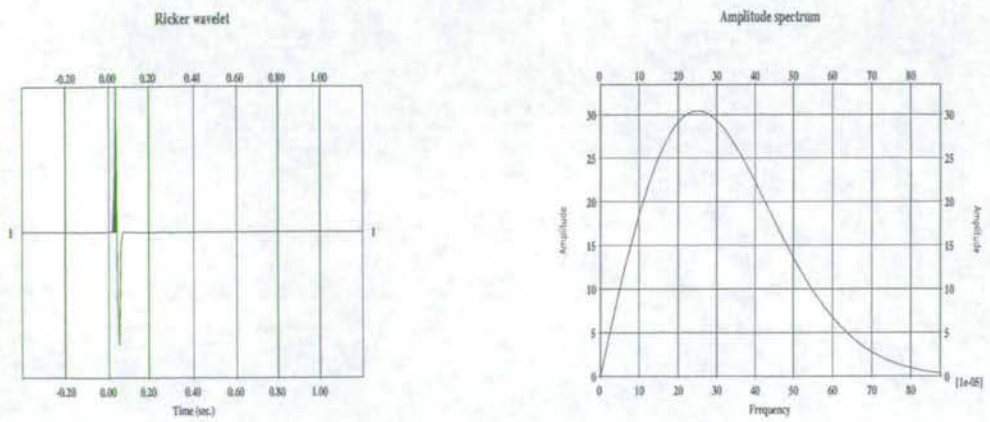


Figure 6: Ricker wavelet used as the source time function.

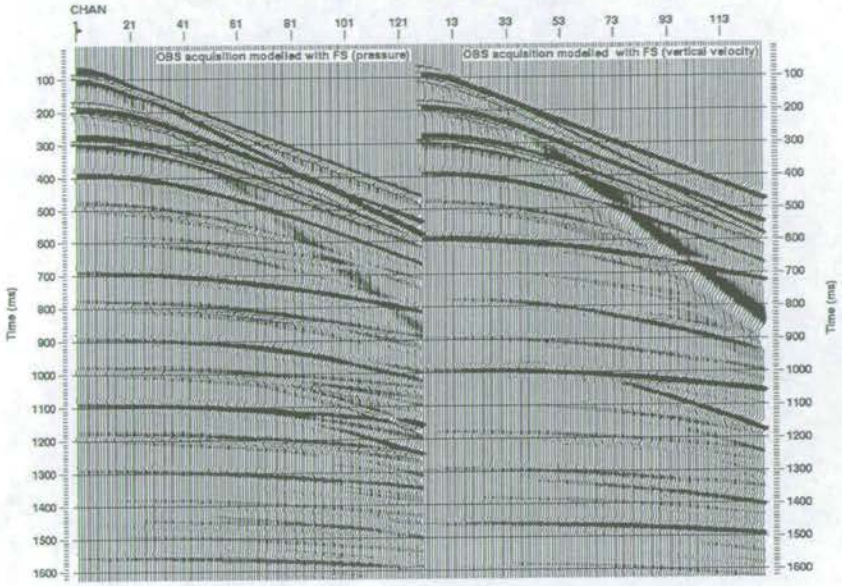


Figure 7: The gather on the left is the pressure; the gather on the right is the normal component of particle velocity (OBC).

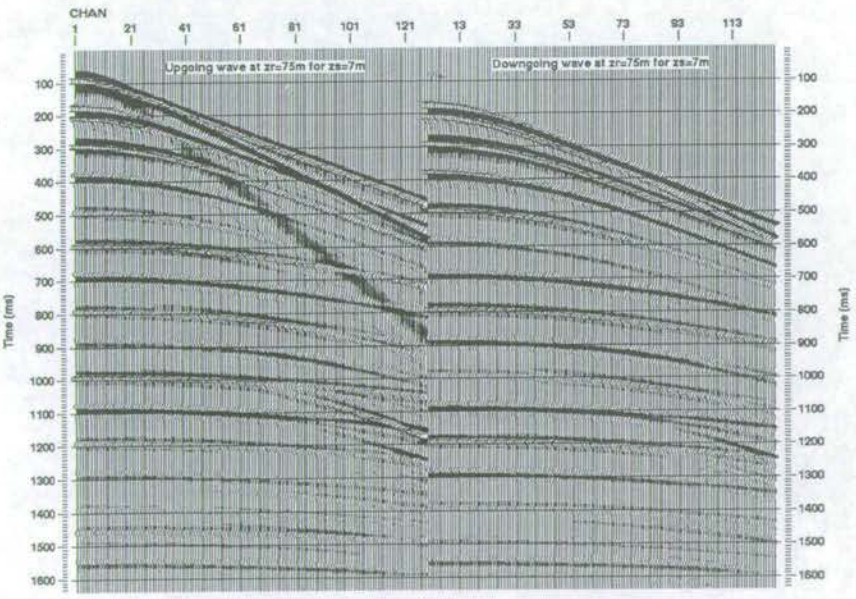


Figure 8: The gather on the left is the upgoing wavefield; the gather on the right is the downgoing wavefield (OBC).

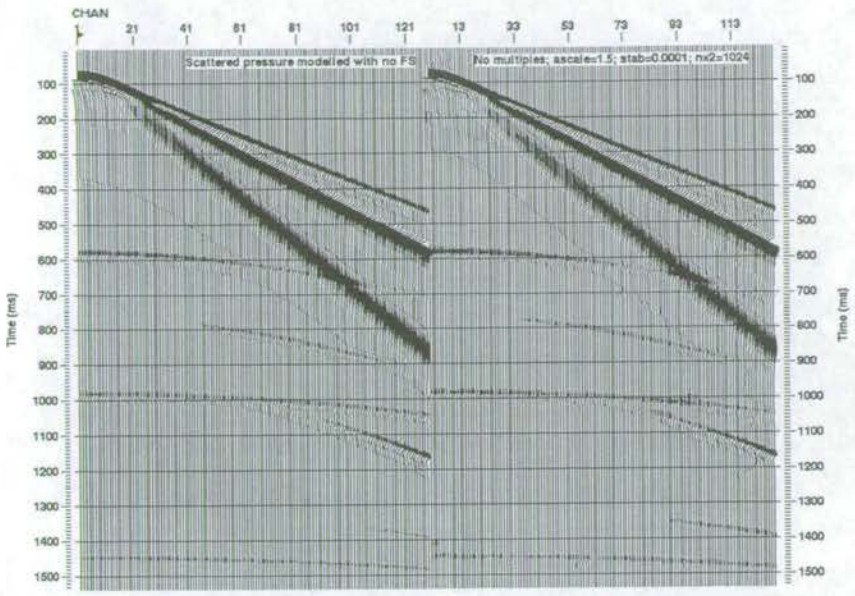


Figure 9: The gather on the left is modelled with no free surface; the gather on the right is the result of processing the seismograms with multiples to remove them (OBC).

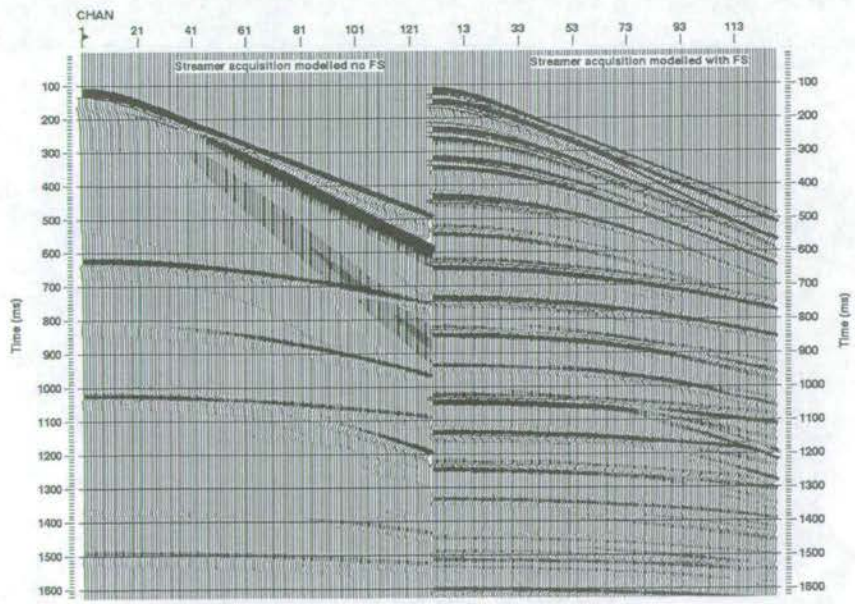


Figure 10: The gather on the left is modelled with no free surface; the gather on the right is modelled with the free surface (streamer).

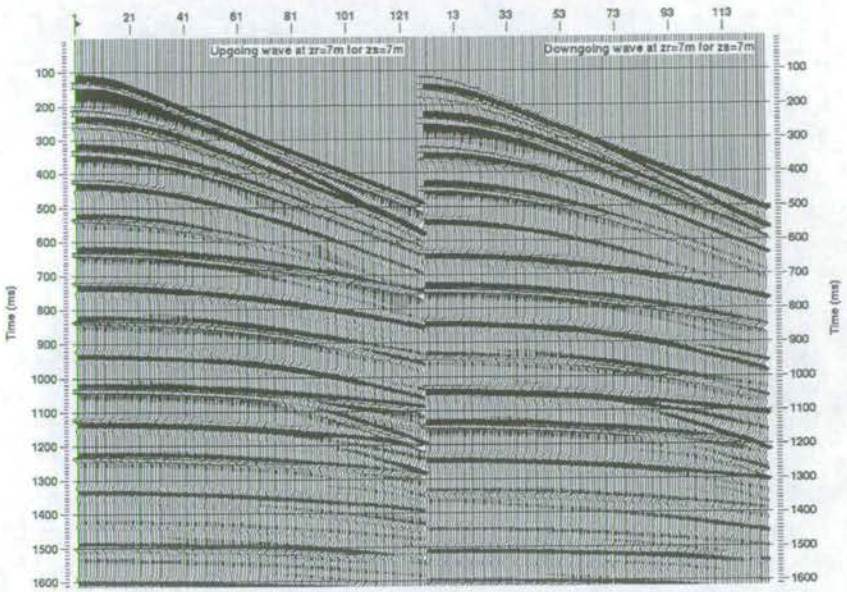


Figure 11: The gather on the left is the upgoing wavefield; the gather on the right is the downgoing wavefield (streamer).

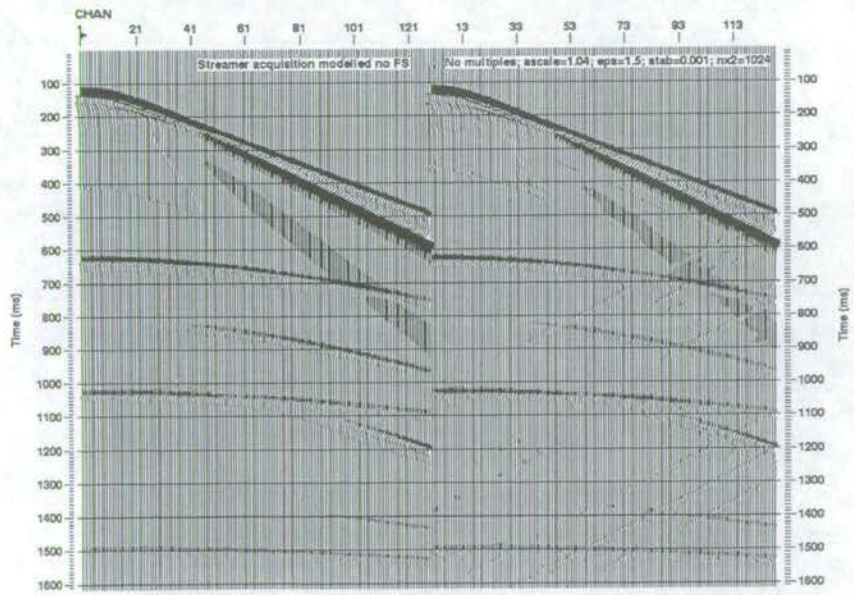


Figure 12: The gather on the left is modelled with no free surface; the gather on the right is the result of processing the seismograms with multiples to remove them (streamer).

## Discussion

We have demonstrated a scheme for free surface multiple removal which works well with hydrophone data alone or dual sensor data for a 1D earth. It requires that the total scattered field be decomposed into upgoing and downgoing waves which poses no problem for pressure alone or pressure and the normal component of particle velocity.


## Acknowledgements

We would like to thank BP, the DTI, Elf Geoscience Research, Mobil North Sea Ltd, PGS Exploration UK Ltd, Shell UK E&P and Western Geophysical for their sponsorship of the project "Processing of 3-component sea-floor seismic data", where some of this work was begun, and we also thank BHP Petroleum, Schlumberger Geco-Prakla, Saga Petroleum ASA, Texaco Britain Ltd and the Engineering and Physical Sciences Research Council (ROPA award no. GR/L73524) for their funding of our sea surface multiples consortium.


## References


Berkhout, A.J., 1982, *Seismic migration: Imaging of acoustic energy by wavefield extrapolation. A. Theoretical aspects*, 2nd edition, Elsevier Science Publ. Co. Inc., 211-218.

Berkhout, A.J. and Verschuur, D.J., 1997, Estimation of multiple scattering by iterative inversion, Part I: Theoretical considerations, *Geophysics*, **62**, 1586-1595.

Dragoset, W.H. and MacKay, S., 1993, Surface multiple attenuation and subsalt imaging, *Expl. Geophys.*, **24**, 463-472.

Fokkema, J.T. and van den Berg, P.M., 1993, *Seismic Applications of Acoustic Reciprocity*, Elsevier Science Publ. Co. Inc.

Fuchs, K. and Müller, G., 1971, Computation of synthetic seismograms with the reflectivity method and comparison with observations, *Geophys. J.R. astr. Soc.*, **23**, 417-433.

Kennet, B.L.N., 1979, The suppression of surface multiples on seismic records, *Geophysical Prospecting*, **27**, 584-600.

Riley, D.C. and Claerbout, J.F., 1976, 2-D Multiple reflections, *Geophysics*, **41**, 592-620.

Wapenaar, C.P.A. and Berkhout, A.J., 1989, *Elastic wavefield extrapolation*, Elsevier Science Publ. Co. Inc., 92.

Weglein, A.B., Araújo Gasparotto, F., Carvalho, P.M. and Stolt, R.H, 1997, An inverse scattering series method for attenuating multiples in seismic data, *Geophysics*, **62**, 1975-1989.

Verschuur, D.J., 1991, Surface-related multiple elimination: an inversion approach: PhD thesis, Delft University of Technology.

Verschuur, D.J. and Berkhout A.J., 1997, Estimation of multiple scattering by iterative inversion, Part II: Practical aspects and examples, *Geophysics*, **62**, 1596-1611.

Ziolkowski, A.M., Parkes, G.E., Hatton, L. and Haugland, T.-A., 1982, The signature of an air-gun array: Computation from near-field pressure measurements including interactions: *Geophysics*, **47**, 1413-1421.

Ziolkowski, A.M., Underhill, J.R. and Johnston, R.G.K., 1998, Wavelets, well-ties and the search for subtle stratigraphic traps: *Geophysics*, **63**, 297-313.

Ziolkowski, A.M., Taylor, D.B., and Johnston, R.G.K., 1998, A strategy for removing multiples from marine seismic reflection data: Presented at the 17th Mintrop Seminar, 27-29 April, Münster, Germany; published in GEOPHYSICAL PROSPECTING as "Marine seismic wavefield measurement to remove sea surface multiples", 1999, **47**, 841-870.